Investigation on the spectroscopic characteristics and electrical transport of boron doped graphene system

Thesis submitted by

Saikat Sarkar

Doctor of Philosophy (Science)

Department of Physics
Faculty Council of Science
Jadavpur University
Kolkata, India
2023

INDEX NO. 153/16/Phys/25

I. **Title of the thesis:**

Investigation on the spectroscopic characteristics and electrical transport of boron doped graphene system

II. **Name, Designation & Institution of the Supervisor:**

Prof. (Dr.) Kalyan Kumar Chattopadhyay
Professor
Department of Physics
School of Materials science & Nanotechnology
Jadavpur University
Kolkata-700032, India
e-mail: kalyan_chattopadhyay@yahoo.co.in/ kkc.juphy@gmail.com

III. **List of publications:**

Peer-reviewed international journal

1. Temperature-depended site selection of boron doping in chemically derived graphene. **Saikat Sarkar**, Rajarshi Roy, Bikram Das, Kalyan Kumar Chattopadhyay.
   ***Carbon**, 184, 253-265 (2021).*
2. Site specific nitrogen incorporation in reduced graphene oxide using imidazole as a novel reducing agent for efficient oxygen reduction reaction and improved supercapacitive performance.
   Dipayan Roy, **Saikat Sarkar**, Kaustav Bhattacharjee, Karamjyoti Panigrahi, Bikram Kumar Das, Kausik Sardar, Sourav Sarkar, Kalyan Kumar Chattopadhyay.
   ***Carbon**, 166, 361-373 (2020).*
3. Intimation of Charge Density Wave in out-of-plane Boron Doped Few-layer Graphene.
   Saikat Sarkar, Rajarshi Roy, Bikram Das, Kalyan Kumar Chattopadhyay.
   (under review) *(2023).*

4. $CH_3NH_3PbI_3$ as a radio frequency decoupling capacitor: interplay between Maxwell–Wagner polarization and a pseudo inductive response.

   Nripen Besra, Kausik Sardar, Nilesh Mazumder, Souvik Bhattacharjee, Anjan Das, Bikram Das, **Saikat Sarkar**, Kalyan Kumar Chattopadhyay.

   Journal of Physics D: Applied Physics, *54(17), 175105 (2021)*

5. Shape-Shifting via Salt Crystallization: Conversion of Nanostructured Polymer into Site-Selective Nitrogen-Doped Carbon Sheet with Enhanced Supercapacitive Performance.

   Partha Bairi, Kausik Sardar, Kausik Chanda, Madhupriya Samanta, Subhasish Thakur, Karamjyoti Panigrahi, **Saikat Sarkar**, Tufan Paul, Kalyan Kumar Chattopadhyay.

   ACS Appl. Energy Mater.*, 3 (6), 5984–5992(2020).*

6. Negative capacitance switching in size-modulated Fe_3O_4 nanoparticles with spontaneous non-stoichiometry: confronting its generalized origin in non-ferroelectric materials.

   S Bhattacharjee, A Banerjee, N Mazumder, K Chanda, **S Sarkar**, KK Chattopadhyay

   Nanoscale, *12, 1528-1540 (2020).*

7. Size-modulation of functionalized Fe_3O_4: Nanoscopic customization to devise resolute piezoelectric nanocomposites.

   Souvik Bhattacharjee, Nilesh Mazumder, Suvankar Mondal, Karamjyoti Panigrahi, Anibrata Banerjee, Dimitra Das, **Saikat Sarkar**, Dipayan Roy, and Kalyan Kumar Chattopadhyay.

   Dalton Transactions*,* ***49****, 7872-7890 (2020).*

8. Graphene wrapped organic nanotube: A promising material for Oxygen Reduction Reaction.

   M Mukherjee, M Samanta, **S Sarkar**, G. P. Das, K K Chattopadhyay.

   Materials Letters*, 248, 8-11 (2019).*

9. Geometrically intricate sheet-on-pillar/flake hierarchy embracing cobaltosic and manganese oxides over flexible carbon scaffold for binder-free high-energy-density supercapacitor.

S Thakur, S Maiti, T Paul, N Besra, **S Sarkar**, KK Chattopadhyay.

Cryst. Eng. Comm., *20 (40), 6183-6196 (2019).*

10. Tailored $CsPbX_3$ Nanorods for Electron-Emission Nanodevices.

    T Paul, S Maiti, N Besra, BK Chatterjee, BK Das, S Thakur, **S Sarkar**, NS Das, KK Chattopadhyay.

    ACS Applied Nano Materials, *2 (9), 5942-5951 (2019).*

11. $CsPbBrCl_2$/g-C_3N_4 type II heterojunction as efficient visible range photocatalyst.

    T Paul, D Das, BK Das, **S Sarkar**, S Maiti, KK Chattopadhyay.

    Journal of hazardous materials, *380, 120855 (2019).*

12. Tunable cathodoluminescence over the entire visible window from all-inorganic perovskite $CsPbX_3$ 1D architecture.

    T Paul, BK Chatterjee, S Maiti, **S Sarkar**, N Besra, BK Das, KJ Panigrahi, S Thakur, UK Ghorai, KK Chattopadhyay.

    Journal of Materials Chemistry C, *6 (13), 3322-3333 (2018).*

International conference proceedings

1. Enhancement of Electron Phonon Coupling by Modulation of Out-of-plane Oxygen Functional Groups in Thermally Annealed Few Layer Graphene.

   Saikat Sarkar, Rajarshi Roy, Kalyan Kumar Chattopadhyay.

   AIP Conference Proceedings, *(just accepted) (2022).*

2. Hierarchical heterostructure of MoS_2 flake anchored on TiO_2 sphere for supercapacitor application

   K Chanda, S Thakur, S Maiti, A Acharya, T Paul, N Besra, **S Sarkar**, A Das, K Sardar, KK Chattopadhyay.

   AIP Conference Proceedings *1953 (1), 030138 (2018).*

3. Room temperature solution processed low dimensional $CH_3NH_3PbI_3$ NIR detector.

   N Besra, T Paul, PK Sarkar, S Thakur, **S Sarkar**, A Das, K Chanda, K Sardar, KK Chattopadhyay.

***AIP Conference Proceedings** 1953 (1), 030210 (2018).*

4. Luminescence behavior of room temperature chemical processed all-inorganic $CsPbCl_3$ perovskite cubes.

   T Paul, BK Chatterjee, S Maiti, N Besra, S Thakur, **S Sarkar**, K Chanda, A Das, PK Sarkar, K Sardar, KK Chattopadhyay.

   ***AIP Conference Proceedings** 1953 (1), 030085 (2018).*
5. Efficient blue emission from ambient processed all-inorganic $CsPbBr_2Cl$ perovskite cubes.

   T Paul, BK Chatterjee, S Maiti, N Besra, S Thakur, **S Sarkar**, K Chanda, A Das, K Sardar, KK Chattopadhyay.

   ***AIP Conference Proceedings** 1942 (1), 120026 (2018).*
6. 3D hierarchical architecture based on 1D TiO_2 nanorod and 2D MnO_2 nanoflake for high performance supercapacitor electrode.

   S Thakur, S Maiti, A Acharya, T Paul, N Besra, **S Sarkar**, KK Chattopadhyay.

   ***AIP Conference Proceedings** 1942 (1), 140071 (2018)*
7. Low dimensional $CH_3NH_3PbBr_3$ cubes for persistent luminescence: Energy variation of electron excitation

   N Besra, T Paul, S Thakur, **S Sarkar**, K Sardar, K Chanda, A Das, KK Chattopadhyay.

   ***AIP Conference Proceedings** 1942 (1), 120027 (2018)*

IV. List of Patents: Nil

V. List of presentations in national/international conference/workshop:

1. **Hands-on training workshop** in INUP (Indian Nanoelectronics User Program), at CeNSE, IISc, Bengaluru supported by MeitY, Govt. of India. *(16th to 24th March, 2017)*
2. **Poster presentation** in a conference on Solid State of Physics organized by BARC, Mumbai sponsored by DAE, Govt. of India. *(18th to 22nd December, 2022)*

DECLARATION BY THE AUTHOR

This is to certify that this thesis, “Investigation on the spectroscopic characteristics and electrical transport of boron doped graphene system”, whis being submitted for the degree of Doctor of Philosophy (Science), contains only my original research and writing, and to the best of my knowledge and belief, neither the thesis nor any portion of it has been approved for the award of any other degree or certificate by the university or other institution of higher learning, with the exception of instances where appropriate credit has been given in the text.

Saikat Sarkar.
(Saikat Sarkar)
01.12.2023

CERTIFICATE FROM SUPERVISOR

This is to certify that the thesis entitled ***"Investigation on the spectroscopic characteristics and electrical transport of boron doped graphene system"*** submitted by **Mr. Saikat Sarkar** who got his name registered on **19.08.2016** for the award of Ph.D. degree (Department of Physics) of Jadavpur University is absolutely based upon his own work under the supervision of **Prof. (Dr.) Kalyan Kumar Chattopadhyay**, Jadavpur University and that neither his thesis nor any part of the thesis has been submitted for any degree/diploma or any other academic award anywhere before.

1.12.23

(Signature of Supervisor)

Dr. K. K. Chattopadhyay
Professor
Head, Department of Physics
Jadavpur University
Kolkata-700 032

Dedicated to my parents…

Acknowledgement

As I stand at the threshold of submitting my Ph.D. thesis, I am deeply honoured to take this moment to extend my heartfelt appreciation to the numerous individuals who have provided invaluable assistance at various stages of my research journey over the past few years. Their unwavering support and guidance have been pivotal in shaping the outcome of this work. First and foremost, I extend my sincere gratitude to my research supervisor, Prof. (Dr.) Kalyan Kumar Chattopadhyay, whose mentorship has been a constant source of inspiration, encouragement, and counsel throughout my Ph.D. tenure. I am particularly thankful for the trust he placed in me to tackle diverse physics challenges and for the illuminating discussions that enriched my academic experience. His profound scientific insights and scholarly approach have left an indelible mark on my intellectual growth. Furthermore, I appreciate his guidance in refining my skills to effectively present and elucidate my research findings.

This Ph.D. journey would have undoubtedly been less enriching and considerably more challenging were it not for the dedicated guidance, unwavering support, and constant encouragement from Rajarshi da. More than just my senior, he has been a consistent source of motivation for me, and this continues to be true till this day. His profound expertise in materials science, skill in crafting manuscripts, and effective communication have all contributed immensely to my personal growth. His boundless passion to research and consistency have aided in my personal development.

I would like to extend my gratitude to some of my senior lab mates, whose insightful discussions and remarkable skills significantly eased my work. These individuals are: Dr. Uttam Kumar Ghorai, Dr. Anuradha Mitra, Dr. Partha Bairi, Dr. Biplab Chatterjee.

I extend my appreciative acknowledgment to all the other members of our lab, including Tufan, Sarthak, Bikram, Subhashis, Kaushik Chanda, Kaushik Sardar, Nripen, Dimitra, Rimpa di, Mississippi, Madhupriya, Shabarni, Ratna, Anibrata, Arnab, Arya, Souvik who collectively create a warm and welcoming environment within our lab. A special thank you goes out to Karam, Dimitra, Bikram, Tufan and my juniors

Souvik, Anibrata, Arya for their significant support during my Ph.D. journey. I genuinely value the insightful discussions I shared with Souvik besides research.

I would like to extend my deepest regards and sincere most thanks to my esteemed mentors, Dr. Prashant Kumar and Dr. Surajit Ghosh. The insights acquired and the inspiration garnered from them have consistently guided me on this path. The companionship of my friends, Sangita, Subhankar, Anurup, Rimpa, Atanu, Debasmita, Ankur, has perpetually enveloped my life with a positive atmosphere. I truly appreciate the moments we've cherished together. Raja, who feels more like a friend than a brother, along with Bera (Suvajit), and their place, have been akin to a second home for me during this period. I still cherish all those awesome times I had with my school buddies.

I am indebted to my parents for prioritizing my education above everything else. Words can't do justice to how grateful I am for their endless love, care, and tireless support. They've been my ultimate inspiration, cheering me on at every step and keeping me in their prayers to succeed in life. I feel incredibly blessed and will forever be grateful for their sacrifices and encouragement that helped me reach this milestone. I'm equally grateful to my uncle Dr. Milan Sarkar and maternal uncle Subrata Koley, whose unwavering support has been instrumental in getting me to where I am today. I would like to express my deep gratefulness and affection for my beloved Minati Koley. Her unwavering love, wisdom, and support have been a constant source of strength and inspiration in my life. My brother, Bubai, consistently keeps me rooted and make me feel cherished by steadfastly supporting my choices and motivating me to pursue my aspirations. I am truly blessed to have such incredible sisters, and I want to acknowledge the immeasurable impact they have had on my personal and professional journey. Thank you, Moumita Sarkar Sau and Sangita Sarkar Das, for always being there for me. I want to extend my deepest thanks to my wife, Sangita Majumdar Sarkar, whose love and support have been the guiding light in my life. Your unwavering belief in me and your sacrifices have made all of this possible. I am profoundly grateful for your presence by my side.

Finally, I would like to express my gratitude to the Department of Science and Technology (DST), Government of India, for their invaluable support through the INSPIRE fellowship scheme. This support has been influential in enabling me to pursue my research and academic goals.

I would also like to extend my appreciation to the Department of Physics at Jadavpur University for their guidance, resources, and academic environment, which have greatly enriched my educational experience. The contributions of these organizations have played a pivotal role in my journey, and I am sincerely thankful for their support.

Contents

Chapter 1: Introduction 01-29

Chapter 2: Review of past work 30-62

Chapter 3: Experimental techniques 63-75

Chapter 4: Temperature-dependent site selection of boron doping in chemically derived graphene 76-108

Chapter 5: Intimation of Charge Density Wave in out-of-plane Boron Doped Few-layer graphene 109-129

Chapter 6: Grand conclusion and Future scope 130-133

Abstract

Condensed Matter Physics (CMP) displays captivating diversity through the interplay of energy and length scales. CMP's collaboration among theorists, experimentalists, and engineers has revolutionized finding exotic substances. Graphene, a single layer of carbon atoms in a hexagonal lattice, has drawn immense materials science attention with its exceptional properties — electrical/thermal conductivity, mechanical strength, and transparency — enabling diverse applications. One of the key aspects that make graphene versatile is its property tunability through a process called doping. Doping allows for precise adjustments of graphene's characteristics, opening up avenues for customizing its properties to suit specific needs in many applications. This thesis is focused on delving into the spectroscopic investigation of electronic and vibrational properties within doped graphene. This work also deals with the understanding the carrier transport properties in this modified two-dimensional system.

Introducing light elements to specific sites within the graphene lattice holds exciting potential, including adjustable bandgaps, heightened electron-phonon interaction, and unconventional transport characteristics. relevant to superconductivity (SC), ferromagnetism, and catalysis. However, this strategy can inadvertently introduce more defects and strain-related consequences as residual effects, leaving room for interpretation. Boron doping, the deliberate introduction of boron atoms into the graphene lattice, has emerged as a powerful strategy to modify and enhance graphene's properties. In this dissertation, various doping methods, including chemical vapor deposition, thermal treatment, and chemical synthesis, highlighting their advantages and limitations have been discussed. Boron-doped graphene exhibits fascinating properties, such as increased carrier concentration, improved catalytic activity, and enhanced stability under harsh conditions. These attributes make it highly promising for applications in electronic devices, energy storage, and catalysis. The challenges and opportunities associated with boron-doped graphene, including the need for precise control over doping levels, potential toxicity concerns, and the quest for scalable synthesis methods have been explored in this work. Moreover, it

elucidates emerging trends and future prospects, emphasizing the role of boron-doped graphene in advancing nanotechnology and materials science. Boron doping in graphene opens up exciting avenues for tailoring its properties, expanding its utility, and pushing the boundaries of what is possible in the world of two-dimensional materials.

In the initial phase of our research, a spectroscopic approach in conjunction with ab-initio results has been employed to unravel these intricacies. Through in-situ boron-doped reduced graphene oxide specimens, this work explored a range of hole doping concentrations, achieved by tuning annealing temperatures up to 1000°C. The thesis has shown, by varying the concentration and configuration (BC_3, BCO_2, BC_2O), a distinct interplay emerges, wherein the dopant competes with residual surface oxygen atoms. The study reveals a transition of preferred doping configuration from out-of-plane to in-plane (substitutional) with rising temperature. Additionally, as the doping concentration increases, the graphene lattice experiences both point defects and strain-induced effects. These factors lead to an anomalous bandgap crossover at elevated temperatures in boron-doped graphene, setting it apart from the thermally reduced counterpart. This observation bears significance for electronic and transport applications.

Moving forward in our research, the interaction between electrons and phonons in the subsequent phase has been inspected with assistance of some spectroscopic tools. While pristine graphene exhibits exceptional electrical conductivity, the induction of charge density wave (CDW) has been a challenging endeavour. CDW, periodic modulations of electron density accompanied by lattice distortions, are central in understanding novel phenomena in low-dimensional materials.

Traditionally, inducing CDW in graphene has proven elusive due to its inherent electronic structure. The direct application of in-plane perturbations or gating techniques often falls short of creating the conditions required for CDW formation. Recent research has highlighted the crucial role of out-of-plane doping, which involves introducing foreign atoms or molecules into the graphene lattice perpendicular to the carbon plane. In the literature, metal-intercalated graphene has already emerged as a promising strategy to induce symmetry-breaking phase transitions such as SC and CDW in two-dimensional layered materials. This approach capitalizes on the modified

vibrations and accumulating charges within the interlayer region of few-layer graphene, a potent carrier-lattice interaction and extensive charge ordering can be achieved, opening avenues for unique electronic phenomena. Furthermore, out-of-plane doping facilitates the emergence of a bandgap near the Fermi level, making CDW more attainable.

This thesis reviews experimental and theoretical studies that demonstrate the effectiveness of out-of-plane doping in realizing CDW in graphene. It discusses various doping techniques, such as chemical adsorption, intercalation, and substitution, and their impact on the electronic structure. The resulting CDW offer exciting possibilities for tailored electronic, thermal, and optical properties, with potential applications in advanced nanoelectronics and quantum technologies.

Overall, this abstract emphasizes the necessity of out-of-plane doping as a powerful tool for achieving charge density waves in graphene. By understanding and harnessing the role of out-of-plane dopants, researchers can unlock the full potential of graphene in the realm of emergent electronic phenomena and pave the way for next-generation graphene-based devices. In this context, boron-doped few-layered graphene stands out as a key player in realizing CDW phases at elevated temperatures (above T = 100K). The presence of out-of-plane boron groups proves instrumental in driving this transition. Ab-initio simulations unveil a distinctive CDW energy gap within the material's band structure, a finding corroborated by low-temperature electrical transport measurements. This study not only establishes a connection between the structural and vibrational characteristics of boron-doped few-layered graphene in the CDW ordering context, but also uncovers an intriguing electric field dependence on the CDW phase in this non-metallic, light-atom-doped graphene system.

Saikat Sarkar
01.12.23.

1.12.23

Dr. K. K. Chattopadhyay
Professor
Head, Department of Physics
Jadavpur University
Kolkata-700 032

List of abbreviations

Abbreviation	Descriptions
CMP	Condensed matter physics
2D	Two dimensional
CNT	Carbon Nanotube
TMD	Transition metal dichalcogenides
BZ	Brillouin zone
CVD	Chemical vapour deposition
GO	Graphene oxide
GIC	Graphite Intercalant compound
FLG	Few layered graphene
CDW	Charge density wave
EPI	Electron phonon interaction
EPC	Electron phonon coupling
GB	Grain boundary
SV	Single vacancy
SW	Stone-Wales
DV	Di-vacancy
A	Armchair
Z	Zigzag
FET	Field effect transistor
BG	Boron doped graphene
TG	Thermally reduced graphene
DOS	Density of state
XPS	X-ray photoelectron spectroscopy
VRH	Variable range hopping
XRD	X-ray Diffraction
OFG	Oxygen containing functional group
UHV	Ultra-high vacuum
SWCNT	Single wall carbon nanotube
rGO	Reduced graphene oxide
DMF	Dimethylformamide

TGA	Thermogravimetric analysis
STM	Scanning tunnelling microscopy
UV-VIS	Ultraviolet-Visible
NIR	Near infrared
PPMS	Physical properties measurement system
STS	Scanning tunnelling spectroscopy
FC-ZFC	Field cooling-zero field cooling
VASP	Vienna Ab initio Simulation Package
GGA	Generalized Gradient Approximation
PAW	projector augmented wave
HOMO	Highest occupied molecular orbital
LUMO	Lowest unoccupied molecular orbital
FWHM	Full width half maxima
O/P	Out-of-plane
I/P	In-plane
CB	Conduction band
VB	Valance band

Introduction

1

1.1. Introduction to graphene

Graphene, a remarkable two-dimensional carbon allotrope, stands at the forefront of scientific exploration and technological innovation. Carbon, as the elemental cornerstone of life and organic chemistry, exhibits unparalleled bonding versatility, enabling a vast array of structural diversity and an extensive range of physical properties in carbon-based systems. These distinctive characteristics are deeply rooted in the dimensional complexity of carbon structures. Graphene, a lattice of carbon atoms arranged in a hexagonal honeycomb pattern, has emerged as a central player in our quest to comprehend the electronic properties of various carbon allotropes. Despite its essential role as a forerunner to diverse carbon forms, graphene remained elusive for centuries, finally being isolated in 2004 [1]. The challenge lay not in its production but in its detection. The surprising revelation of free-standing graphene and the absence of suitable tools for identifying one-atom-thick flakes through macroscope delayed its discovery. This novel two-dimensional substance represents a fresh nanocarbon variant, consisting of carbon atoms organized into hexagonal rings. It stands apart from carbon nanotubes (CNTs) and fullerenes, showcasing distinctive attributes that have captivated the scientific community. Notably, graphene boasts remarkable characteristics, including the quantum Hall effect observed at room temperature [2,3] ambipolar electric field control combined with ballistic charge carrier conduction [1], adjustability of its band gap [4,5], and remarkable elasticity [6]. Graphene's electronic properties are a reflection of its structural adaptability. Its trigonal planar structure, arising from sp^2 hybridization, fosters the formation of robust carbon-carbon bonds, forming π and σ bands. These bands are critical in understanding graphene's behaviour, including its role in strongly correlated systems.

Graphene's electronic journey has been characterized by contrasting theoretical viewpoints, from Linus Pauling's resonant valence bond structure [7] to P. R. Wallace's semi metallic band structure [8]. While contemporary experimental data tend to support the latter, the influence of electron-electron interactions in graphene continues to be an active research area.

Notably, graphene consists of massless, chiral Dirac fermions, which lead to unique phenomena such as the anomalous quantum Hall effect [9]. These fermions disobey classical electrostatic potentials, a phenomenon known as the Klein paradox, and exhibit intriguing behaviours under disorder, allowing electron propagation over considerable distances [10].

The successful isolation of graphene from graphite has intrigued extensive exploration of the analogous layered transition metal dichalcogenides (TMDs) in solid state physics because of their flexible properties and feasible revolution in modern technology. Graphene is attracting much interest due to potential applications as a next generation electronic material as well as its unique physical properties. In particular, its superior thermal [11] and mechanical [12] properties, including high thermal conductivity and extremely high mechanical strength, make it a prime candidate material for heat control in high density, high-speed integrated electronic devices. The ground state electronic structure of graphene consists of a filled hexagonal first Brillouin zone (BZ), with an energy gap that goes monotonically to zero at the zone corners, from a maximum at the centres of the zone edges. This electronic configuration arises from the particular relationship between the number of conduction electrons per atom and the hexagonal atomic ordering.

Nonetheless, maintaining a uniform layer thickness, a critical factor in numerous applications [13,14], poses a formidable challenge when employing this approach. Moreover, addressing the increasing demand for graphene necessitates the implementation of large-scale production techniques. Chemical synthesis methods, such as chemical vapor deposition (CVD) and liquid-phase exfoliation, not only provide the scalability required for industrial applications but also enable precise control over the number of layers. Furthermore, in recent decades, efforts to enhance the versatility of graphene for a wide range of applications have included investigations on lattice modification through in-plane doping, surface functionalization, and intercalation between graphene layers.

1.2. Modification of graphene

In addition to its intrinsic electronic capabilities, graphene's adaptability extends to chemical and structural alterations, rendering it a highly promising candidate for a wide array of applications. The incorporation of foreign atoms into the graphene lattice brings about modifications in the electronic and phonon energy band structures. These alterations, whether occurring individually or in combination, can have diverse impacts on electronic and vibrational properties, as well as on phenomena associated with electron-phonon interactions. Moreover, the creation of defects, the introduction of strain, and variations in majority and minority carriers all contribute significantly to enhancing graphene's versatility.

1.2.1. Functionalisation of graphene

Functionalizing graphene is a multifaceted process that not only maintains its exceptional characteristics but also introduces novel functional groups, each contributing distinct properties. Various approaches exist for graphene functionalization, encompassing covalent functionalization [15], non-covalent functionalization [16], and elemental doping [17]. Among these, chemical functionalization of graphene stands out, offering the potential to induce a bandgap in graphene, thereby allowing precise control over its electrical properties, transitioning it from a semimetal to an insulator.

Functionalizing pristine graphene sheets with covalently-bonded functional groups is conducted to achieve several objectives. Enhanced dispersibility in common organic solvents is a primary goal, typically achieved by attaching specific organic groups, such as hydroxyl, carboxyl etc [18]. Achieving dispersion in organic solvents is crucial for creating nanocomposite materials involving graphene. Additionally, the introduction of organic functional groups introduces new properties, such as enhanced conductivity, which can be combined with graphene's inherent characteristics.

Non-covalent functionalization, in contrast, focuses on interactions such as hydrogen bonds and electrostatic forces between graphene and functional molecules. This approach maintains the bulk structure and outstanding properties of graphene but enhances its dispersibility and stability. Methods for non-covalent functionalization include bond interactions, hydrogen bonding, ionic bonding, and electrostatic interactions [19,20]. While non-covalent functionalization is relatively straightforward and gentle, it may introduce other components, such as surfactants.

Hence, functionalizing graphene is a versatile process that can fine-tune its properties for a wide range of applications, from electronics to energy storage and beyond. Different methods offer unique advantages, allowing us to tailor graphene's characteristics to fulfil specific needs.

1.2.2. Substitution doping in graphene

A significant emphasis in this chapter should be placed on the substitutional doping of graphene, a process wherein carbon atoms in the hexagonal honeycomb lattice of graphene are replaced by nitrogen or boron atoms. The resulting behaviour of doped graphene sheets, whether they exhibit n- or p-type characteristics, depends on the electrophilic nature of the substituting atoms. By precisely controlling the degree of doping, it becomes possible to potentially tailor the electrical properties of graphene. This opens up exciting possibilities for expanding the utility of graphene in nanoelectronics.

Nitrogen atoms are incorporated using their three sp^3 orbitals, allowing their lone pair electrons to conjugate with the graphitic π-system. Consequently, N-doped graphene sheets become electron-rich, leading to an anticipated n-type semiconducting behaviour. Typically, N-doped graphene sheets are generated by substituting O or C atoms with N during processes like reduction, annealing, or even in situ during graphene growth using methods such as chemical vapor deposition (CVD), arc discharge, or solvothermal techniques. During the reduction step, oxygen or sp^3 carbon atoms, often located at defect sites in graphene oxide (GO), can be substituted by nitrogen. This is achieved through the use of a nitrogen-rich reductive source, such as ammonia or hydrazine, at elevated temperatures.

Similarly, incorporating boron atoms, which possess one sp^3 orbital, leads to p-type behaviour and can be accomplished through procedures akin to those discussed in Chapter 2. Doping graphene with nitrogen or boron atoms is a widely adopted technique known for its substantial impact on altering the electrical properties of graphene. Authors conducted a detailed examination of the undisturbed graphene lattice, away from the dopant site, revealing that the centre of the triangular dopant structure aligns precisely with a carbon site, while the three apexes connect to the three nearest neighbouring carbon sites [27]. Interestingly, this experimentally observed shape of the graphitic B dopant closely matched theoretical predictions derived from Density Functional Theory (DFT) calculations. Despite both graphitic B and N dopants exhibiting an overall triangular symmetry, significant differences emerge when analysing their detailed structures. For B dopants, the maximum height is precisely observed at the B dopant site, whereas for N dopants, it occurs near the nearest carbon neighbours to the N dopant. Theoretical studies have elucidated that substitutional doping has the capacity to modulate graphene's band structure [21,22], resulting in a metal-semiconductor transition [23,24]. Consequently, this approach significantly enhances and broadens the potential applications of graphene. Doped graphene offers promising properties and finds application in various fields, including superconductivity [25], ferromagnetism [26], among others. As a result, intensive investigation is directed toward this area, leading to the advancement of range of applications for substitutionally doped graphene.

However, in contrast to the well-explored field of N-doped graphene, the study of B-doped graphene has been relatively limited in experimental research. Many fundamental questions regarding the nature of dopant structures, their distribution, and their impact on the electronic properties of graphene films have remained unanswered.

1.2.2. Intercalation in graphene

Intercalation offers a powerful means of tailoring graphene's properties for a wide range of applications, from energy storage to sensors and beyond [28]. In this scientific exploration, we delve into the concept of intercalation of graphene, its underlying mechanisms, and its potential applications.

Intercalation Mechanisms:

I. **Physical Intercalation:** Physical intercalation involves the insertion of foreign species between graphene layers without forming chemical bonds. Van der Waals forces are typically responsible for holding the intercalants in place. This process can be reversible, making it attractive for applications requiring tuneable properties. Gases like hydrogen and noble gases are common examples of physically intercalated species.

II. **Chemical Intercalation:** Chemical intercalation, on the other hand, involves the formation of strong covalent or ionic bonds between graphene layers and intercalants. This process often leads to irreversible changes in the graphene structure. Common chemical intercalants include metal atoms, metal ions, and organic molecules. The chemical nature of this interaction allows for precise control of graphene's electronic properties.

The introduction of metals into graphene sheets has garnered significant interest due to its profound alteration of the electronic and phonon structure and the emergence of novel properties not present in the host material [29,30]. Among the most intriguing phenomena within graphite intercalation compounds (GICs) is the induction of superconductivity in the amalgamation of typically non-superconducting graphite and metals [31,32]. Idea of intercalation of alkali metal have come from the structure of magnesium diboride, which

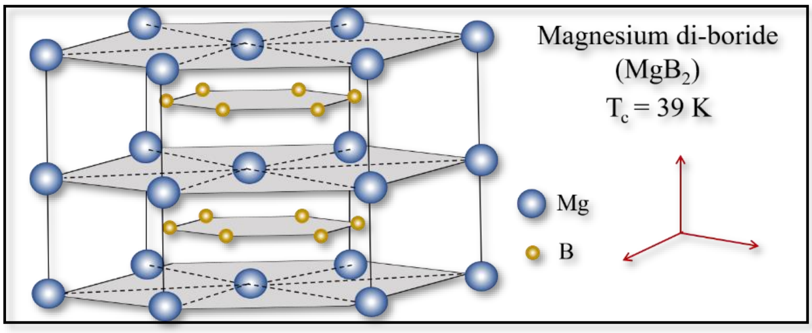

Figure 1: Structure of magnesium diboride

exhibits superconducting transition at 39 K. In this structure magnesium atoms are intercalated in between two layers of boron atoms as shown in figure 1. Shortly after the discovery of graphene, intensive efforts were launched to create superconducting graphene, driven by both fundamental scientific inquiry and practical applications. An especially promising candidate in this pursuit is calcium-intercalated bilayer graphene (C_6CaC_6), given that calcium-intercalated GIC (C_6Ca) boasts the highest recorded superconducting transition temperature of 11 K among the various metal-intercalated GICs [30]. Numerous theoretical [33,34] and experimental [35] investigations have proposed that C_6CaC_6 exhibits an electronic structure similar to that of superconducting GICs, thus suggesting the potential for superconductivity in C_6CaC_6. However, there have also been suggestions that the ground state may feature a charge-density wave (CDW), which could act to suppress or to trigger the superconducting behaviour in metal-intercalated bilayer graphene [36,37].

Few-layer graphene (FLG) can be chemically altered by inserting molecules into its structure. This intercalation process between layered graphene is governed by van der Waals interactions, imparting new chemical and physical attributes, such as superconductivity and quasi-low-dimensional magnetism [38,39]. An example of this phenomenon is the synthesis of FLG intercalate with $FeCl_3$ [40]. Notably, the electrical behaviour of this intercalated product is linked to a magnetic transition. This research marks the initial stride toward the creation of various functional bilayer intercalates, including sandwich-like structures. Beyond fundamental investigations into two-dimensional electron systems, FLG intercalation materials hold potential for diverse applications. For instance, the intercalation of ionic Li^+ into FLGs occurs during the electrochemical lithiation of FLGs. This phenomenon is of interest due to the reversible Li^+ intercalation/deintercalation capability within layered FLGs, which could potentially lead to increased Li-ion storage capacity. Furthermore, aside from ion batteries, FLG intercalates may find utility in hydrogen storage applications [41].

Hence, intercalation of graphene is a versatile and powerful technique for tailoring the properties of this remarkable material. It enables precise control over electronic, mechanical, and chemical characteristics, paving the way for a myriad of applications across diverse fields of science and technology. As research in this area continues to evolve, we can anticipate further innovations and breakthroughs that harness the full potential of intercalated graphene materials.

1.3 Necessity of doping in graphene

Doping emerges as an indispensable technique in the domain of graphene science, playing a pivotal role in the deliberate manipulation of its electronic and phonon properties. The necessity for doping in graphene research finds profound support in scientific literature. Geim et al. underscores the ability of doping to precisely regulate charge carrier concentration by shifting the Fermi level, thereby transforming pristine graphene into n-type semiconductors or metals [42]. Additionally, impact of doping on charge carrier mobility, and consequently on the electrical conductivity of graphene, is established [9]. Shifting of Fermi level (E_F), as depicted by figure 2, towards valance or conduction band of graphene results as change in type majority carriers for charge transport.

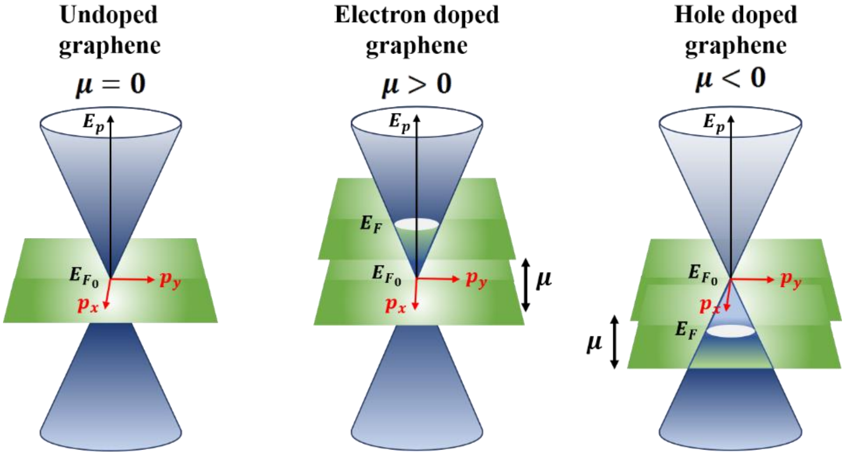

Figure 2: Shifting of Fermi level in terms of electron or hole doping

Beyond electronic properties, doping profoundly influences phonon characteristics within graphene. Interaction between dopants and the carbon lattice leads to alterations in phonon dispersion relations and impacts thermal conductivity, as documented in earlier report [43]. Doping-induced effects extend to enhanced chemical reactivity, vital for catalysis applications [44]. Moreover, doping enables customization of optical properties, introducing new absorption or emission spectral peaks [6]. Its role in constructing intricate heterostructures is also evident as described by Mishchenko et al. [45]. Precise control of charge carrier density via doping in the realm of the quantum Hall effect is crucial [2]. In essence, doping in graphene is a versatile tool enabling meticulous control over various properties, as substantiated by diverse scientific references spanning electronics and materials science.

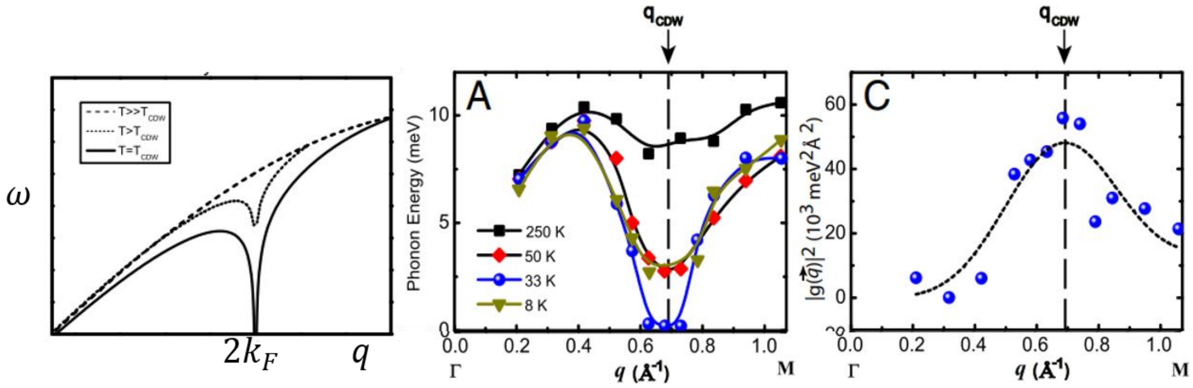

Figure 3: Softening of phonon involving with EPI [110]

Apart from substitution doping out-of-plane doping in graphene is an essential technique for enhancing electron-phonon interaction (EPI), a well-studied phenomenon supported by robust scientific evidence. The electron-phonon interaction plays a vital role in determining the electrical and thermal transport properties of graphene. Out-of-plane dopants, such as hydrogen (H), nitrogen (N), or other adatoms, significantly impact this interaction by altering graphene's electronic structure and phonon modes. Additionally, many authors emphasize the role of lighter atom as out-of-plane dopants in modulating electron-phonon interactions [46-49]. Out-of-plane dopants perturb the carbon lattice structure and electronic band structure, leading to enhanced scattering processes and modified electron-phonon coupling matrix elements. This influence extends to charge carrier mobility, thermal conductivity, and phonon lifetimes. Understanding and controlling EPI in graphene, facilitated by out-of-plane doping, have significant implications for obtaining correlated phases like CDW [110] or SC in graphene [figure 3].

1.4 Spectroscopic Investigation on effects of doping

Besides, the modulation of the type and density of charge carriers, two other major effects of doping in graphene are the formation of defects and the generation of strain. Doped as well as undoped Graphene contains various types of defects that profoundly impact its properties.

Apart from the process of mechanical exfoliation, other processes of graphene production induce different types of defects also in undoped graphene. These defects are categorized based on their dimensionality, comprising zero-dimensional defects, such as Stone–Wales defects, vacancies, adatoms, and substitutional impurities, as well as one-dimensional defects like line defects, grain boundaries (GBs), and edges. Due to inclusion of such constructional changes in graphene its lattice become strained. Depending upon the doping type and configuration, the type of strain occurred in graphene either compressive or tensile.

1.4.1. Defects in graphene:

Zero-dimensional Defects

Stone–Wales (SW) Defects: SW defects, as described, involve the rearrangement of carbon atoms within graphene, leading to pentagon-heptagon pairs. These defects can affect graphene's electronic properties by introducing localized states within the bandgap, influencing carrier concentration and electrical conductivity [14].

Vacancies: Single vacancies (SV) and double vacancies (DV) in graphene can distort the carbon lattice, leading to changes in electronic structure and magnetic properties [50-51]. SV defects, in particular, have been well-studied for their impact on the electronic properties of graphene [52].

Adatoms: Adatoms, when introduced onto graphene, can alter its electronic structure and create localized states within the bandgap [53]. The interaction between foreign atoms and graphene can vary, influencing the extent of charge transfer and chemical reactivity [54].

Substitutional Impurities: Substitutional impurities, such as transition metal atoms or boron/nitrogen doping, can modify graphene's electronic band structure [55]. For instance, boron or nitrogen doping can shift the Fermi level, resulting in p-type or n-type behaviour [56].

One-dimensional Defects

Line Defects: Line defects like dislocation lines can introduce strain in graphene and affect its electronic properties [57]. These defects can impact the mechanical strength and thermal conductivity of graphene [6].

Grain Boundaries: Grain boundaries in graphene, typically observed in polycrystalline samples, can lead to variations in electronic properties due to differences in orientation and lattice structure between adjacent grains [58].

Edges: The edge structure of graphene can dictate its reactivity and electronic properties [59]. Zigzag edges, for example, exhibit distinct electronic states, making them suitable for specific applications like nanoribbon-based devices [60].

Therefore, defects in graphene and doped graphene are not only fundamental aspects of its structure but also play a crucial role in tailoring its properties for various applications.

1.4.2. Investigation of defects using Raman Spectroscopy

Raman spectroscopy has become an indispensable tool in the field of graphene research due to its non-destructive nature and its ability to provide valuable insights into the atomic structure and electronic properties of graphene. This inelastic scattering process is illustrated in figure 4.

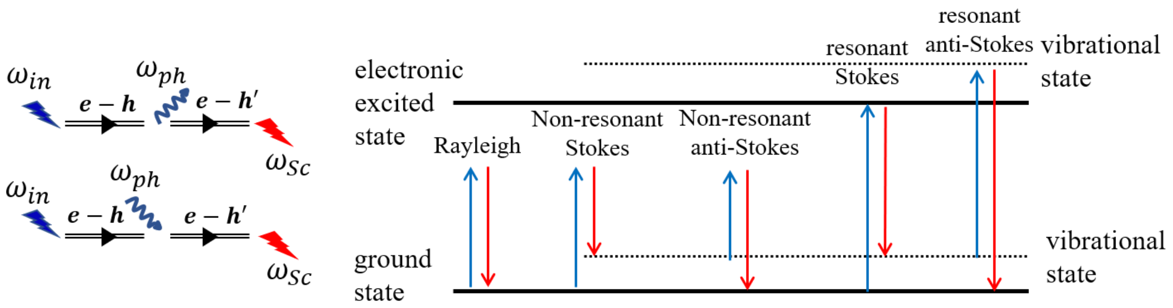

Figure 4: Raman Scattering. Stokes process (left up), anti-Stoke process (left down), Elastic Rayleigh scattering and inelastic Raman scattering (right), adapted from [61].

When analysing the Raman spectra of pristine and defective graphene, several distinct peaks can be observed, each offering unique information about the material's characteristics. These key peaks include G, D, D', 2D, 2D', D + D", and D + D' [61].

A. **G Peak (Graphitic Peak)**: Located at approximately 1580 cm^{-1}, the G peak corresponds to the E_{2g} phonon mode with a momentum close to zero at the Brillouin zone's Γ point. This peak is a signature of the crystalline, *sp*²-bonded carbon structure of graphene [62].

B. **2D Peak (Double Resonance Peak)**: Positioned around 2700 cm^{-1}, the 2D peak is another prominent feature in the Raman spectrum of graphene. It arises from the A'_1 phonon mode at the K point of the Brillouin zone and is associated with a double resonance process [62].

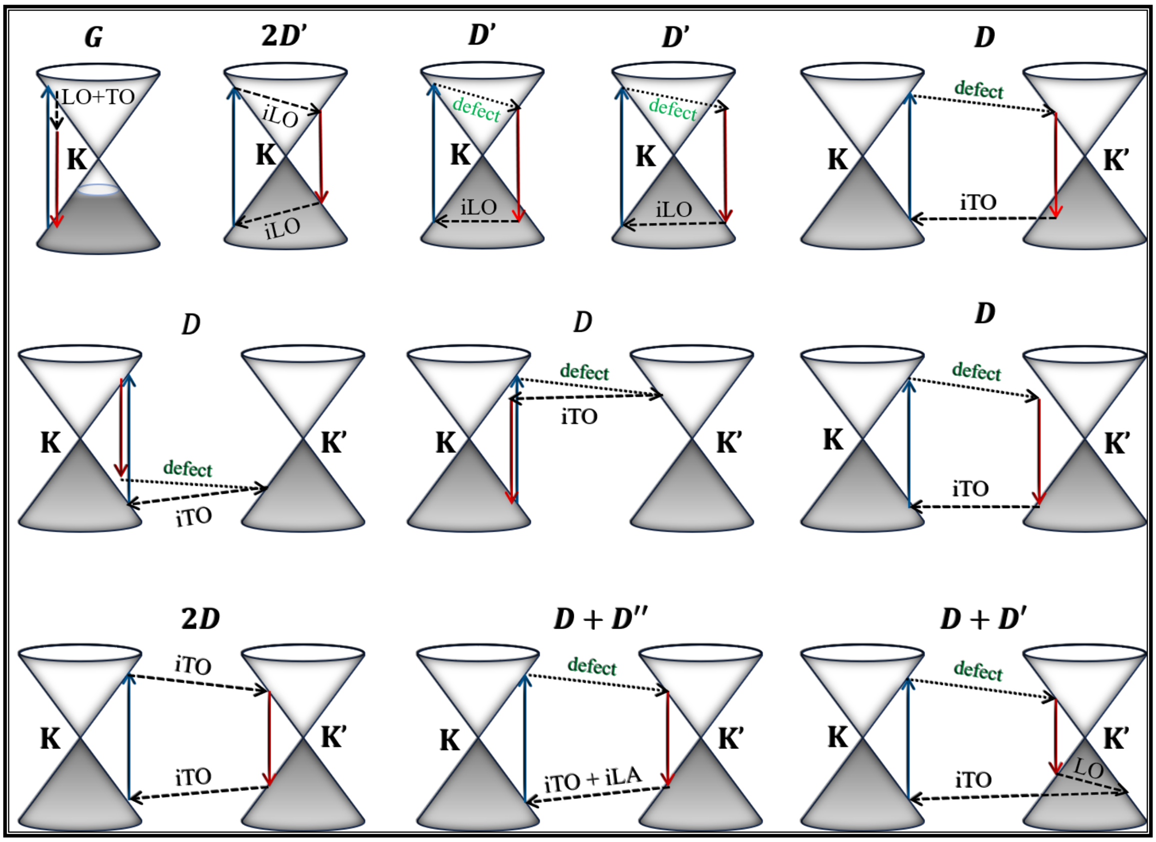

Figure 5: Schematic of Raman scattering processes

Defective graphene introduces additional peaks:

C. **D Peak (Disorder-Induced Peak)**: The D peak, located at approximately 1350 cm^{-1}, is a result of defects in the graphene lattice. It originates from A'$_1$ phonons near the K point of the Brillouin zone, with a nonzero momentum. Activation of the D peak requires a defect and involves an intervalley double resonant process [61].

D. **D' Peak**: The D' peak, at around 1620 cm^{-1}, is linked to E2g phonons with nonzero momentum. It results from an intravalley double resonant process connecting two points within the same cone around the K (or K') point [61].

E. **D + D' Peak**: The D + D' peak, observed at approximately 2950 cm^{-1}, arises when both intravalley and intervalley phonons are emitted together during the Raman scattering process. This peak is a clear indicator of the presence of defects in graphene [61].

These defect-induced Raman peaks (D, D', and D + D') offer valuable information about the nature and quantity of defects present in the graphene lattice. For instance, the intensity ratio of the D peak (I_D) to the G peak (I_G) is often used as a quantitative measure of defect density in graphene. It follows a power-law relationship with excitation energy, providing further insights into the defect-induced scattering processes [63-65]. One-phonon process for G peak, as described by Ferrari et al. [61], phonon-defect process for D, D’, 2D’, and phonon-phonon process for 2D peak are depicted in figure 5.

The distinct Raman peaks and their dependencies on excitation energy and intensity ratios offer researchers a comprehensive understanding of graphene's quality and the nature of defects, which is crucial for a wide range of applications.

Identification of the nature of defects in graphene:

When graphene undergoes treatments like thermal annealing or plasma irradiation, various types of defects emerge, such as vacancies and the introduction of sp^3 hybridization [66-67]. For instance, mild oxidation can lead to sp^3 defects, while Ar^+ bombardment, thermal reduction of oxidized graphene can create vacancy defects. Previous study illustrated evolution of the D peak, along with other defect-related Raman peaks, particularly D', increases in graphene with irradiation time [68]. Notably, graphene samples containing different defect types exhibit varying $I_D/I_{D'}$ ratios. Theoretical insights suggest that the $I_D/I_{D'}$ ratio can serve as a tool for identifying the nature of these defects in graphene [69]. The $I_D/I_{D'}$ ratio hinges on the defect potential (ΔV), where $\Delta V = V_D - V$. V_D represents the self-consistent potential of the defective graphene, while V is the corresponding value for pristine graphene. Notably, ΔV differs for SV, DV, SW, 555-777, and 5555-6-7777 defects in single-layer graphene [69]. Calculations indicate $I_D/I_{D'}$ ratios of approximately 1 for MV, ~11 for DV, ~17 for SW, ~4 for 555-777, and ~4 for 5555-6-7777 defects. Upon oxygen adsorption, these values shift to approximately 1, ~1, ~10, ~3, and ~6, respectively. This suggests that oxygen adsorption on a MV can mitigate the defect, reducing the intensity of the D and D′ peaks by about two orders of magnitude. Interestingly, different types of defective graphene share a common $I_D/I_{D'}$ ratio of around 13, including partially hydrogenated, fluorinated, and oxidized graphene [52]. Conversely, defective graphene samples generated via ion bombardment and anodic bonding, primarily featuring vacancy-like defects, exhibit a smaller $I_D/I_{D'}$ ratio of approximately 7. Polycrystalline graphite, where defects commonly manifest as grain boundaries, demonstrates an even smaller $I_D/I_{D'}$ ratio of about 3.5 [52]. These findings underscore the utility of Raman spectroscopy, particularly the $I_D/I_{D'}$ ratio, in discerning the nature of defects in graphene. However, it's essential to note that there can be disparities between experimental results and theoretical calculations. This inconsistency can be attributed to idealized descriptions of defects in ab initio calculations. In practice, defects are more complex and are not necessarily isolated, often forming dimers or clusters [70]

Quantification of the defects in graphene:

Raman spectroscopy provides a means to quantitatively assess the presence of defects in graphene [63,71]. When defects are introduced through Ar^+ bombardment, the relationship between the I_D/I_G and the average defect distance (L_D) can be understood in two stages [61,63]. In the first stage, I_D is nearly directly proportional to the total number of defects within the laser spot. Considering L_D and the laser spot size L, there are typically $(L/L_D)^2$ defects in the laser-probed region. Therefore, I_D scales as $(L/L_D)^2$ [72]. Conversely, I_G is proportionate to the total area illuminated by the laser, indicating $I_G \propto L^2$, leading to the relationship I_D/I_G proportional to $(1/L_D)^2$ [72]. This I_D/I_G ratio peaks when L_D is around 3 nm. In the second stage, as the number of defects increases and L_D becomes less than 3 nm, I_D decreases relative to I_G. In this stage, I_D/I_G proportional to the number of ordered hexagons, and the development of the D peak reflects the system's degree of ordering, which is the opposite of stage 1. Consequently, a new relation emerges: $I_D/I_G \propto (L_D)^2$ [72]. Thus, Raman spectroscopy provides an effective means to estimate the quantity of defects in graphene. As defects serve as scattering or trapping centres for charge carriers, they significantly impact graphene's electrical performance. A prior study elucidated the evolution of Raman peaks in graphene as the number of defects introduced by hydrogen plasma increased. The results demonstrated that the inverse of graphene's carrier mobility exhibits a linear correlation with the I_D/I_G ratio, underscoring that intervalley scattering can limit carrier mobility, and the scattering probability is proportionate to the defect density in graphene [65].

Identification edges and grain boundaries in graphene

Raman spectra hold the capability to discern the nature of edges in graphene, distinguishing between Zigzag (Z) and Armchair (A) edges [73]. Specifically, the Raman D peak remains inactive for Z-edges. This is because the momentum exchanged during scattering from Z-edges fails to bridge the adjacent Dirac cones K and K', thus not fulfilling the conditions for the double resonant process [75,76]. Conversely, the exchanged momentum from A-edges adequately satisfies the intervalley scattering between K and its adjacent K', leading to the activation of the D peak for A-edges [74].

Comparing the Raman images of different edge configurations in mechanically exfoliated single-layer graphene sheets, it's evident that the D peak intensity is higher for A-edges than Z-edges [74]. However, due to the inherent imperfections of Z-edges, the D peak intensity isn't entirely absent. Furthermore, investigations have revealed that both armchair and zigzag graphene edges are prone to modifications, even at relatively low temperatures of about 200 °C [77]. The D peak also demonstrates its sensitivity in identifying alignment configurations at edges for multi-layer graphene [78].

1.4.3. Strain in Graphene:

Doping can also induce strain in the graphene lattice. Strain refers to the deformation or stretching of the graphene sheet. This can occur when dopant atoms, such as hydrogen, are adsorbed on the graphene surface and induce local changes in the carbon-carbon bond lengths and angles. Strain in graphene can significantly alter its electronic band structure. Depending on the type and direction of strain, it can open or close bandgaps, change the electronic dispersion, and lead to the emergence of new electronic states. Strain engineering is used to tailor graphene's electronic properties for specific applications like flexible electronics, strain sensors, and mechanical actuators. It can also be applied to create pseudomagnetic fields in strained graphene, leading to novel quantum phenomena. In previous studies, Raman spectroscopy has been employed to assess strain in graphene [79]. Tensile strain causes shifts in the G and 2D peaks, with the 2D peak showing greater sensitivity and the ability to detect strains as low as 0.01%. These strain-induced shifts were mapped across sample areas with varying indentation depths, revealing increased strain with deeper indentations. It's important to note that strain distribution within the indentations was not uniform, and Raman spectroscopy provided an average strain measurement within the laser spot's diameter of approximately 500nm. Additionally, Raman spectroscopy allowed control over both the magnitude and direction of strain in graphene. By adjusting the polarization of the laser, researchers could probe strain in different directions, resulting in uniaxial or hexagonal strain patterns within graphene.

In summary, previous work demonstrated the utility of Raman spectroscopy for precise strain assessment in graphene, highlighting its sensitivity to small strains and its ability to manipulate strain patterns with control over direction and symmetry. Understanding and controlling defects and strain induced by doping are essential for harnessing the full potential of graphene in evolution of electronic phase transition.

1.5 Electrical properties of doped graphene

1.5.1. Transport properties of graphene

The remarkable electronic properties of graphene sheets have garnered global attention, both experimentally and theoretically, in recent years. Graphene's pivotal role in nanoelectronics stems from its adaptability for applications with its electronic properties finely controllable through diverse strategies. Carriers within pristine graphene exhibit massless Dirac fermion behaviour, validated through empirical experiments, facilitating the development of such devices like field-effect transistors (FETs) [80], spin filters [81], and nano sensors [82]. One particularly intriguing method involves the introduction of impurities, which inject electrons or holes into the system, thereby altering its electronic properties. Notably, these impurities can also serve as adsorption sites, facilitating the customization of nano-sensors. Our study focuses on boron impurities, a convincing choice due to their capacity to induce several effects on electronic characteristics, and transport properties of boron doped graphene (BG) systems. Substitutional boron atoms strategically occupy vacancy defect sites within the graphene. Literatures describe the presence of boron atoms at these edges of vacancy sites initiates a transition from metallic to semiconductor behaviour in the nanoribbon, concurrently breaking the symmetry between the spin-up and spin-down transmittance channels. Substitutional boron atoms effectively function as scattering centres, primarily impacting spin-up electrons until a critical width, estimated to be 6.6 nm, is reached. Beyond this critical point, both transmittance channels achieve parity. These findings underscore the feasibility of tailoring electronic currents along graphene nanoribbon through a judicious doping process.

In the high-temperature region, the resistance-temperature curve closely aligns with an Arrhenius-like temperature dependence. Here, the charge carriers have enough thermal activation energy to participate in conduction, and this behaviour can be described by the Arrhenius equation [83]:

$$R\ (T) = R_0 e^{\frac{E_A}{k_B T}}$$

,where R(T) is the measured resistance at different temperatures, R_0 is a pre-factor, k_B is the Boltzmann constant, and E_A is the activation energy barrier. This activation energy corresponds to the energy difference between the Fermi energy (E_F) and the energy level where the density of states (DOS) peak occurs.

For higher temperatures region, an extra energy is required for charge carriers to become active and participate in conduction, resulting in the Arrhenius-like behaviour. However, at lower temperatures region, the thermal activation energy is insufficient to activate a significant number of charge carriers, leading to a transition to a two-dimensional variable range hopping system. Different 2D models, such as Efros-Shklovskii variable range hopping (ES-VRH) [84,85] and Mott 2D-VRH [86], have been proposed to explain conduction mechanisms in disordered semiconductors.

In the Ohmic regime, the variable range hopping (VRH) conduction can be expressed as a power law:

$$R\ (T) = R_0 e^{\left(\frac{T_0}{T}\right)^p}$$

, where R_0 is a pre-factor, T_0 is a characteristic temperature, and p is a characteristic exponent distinguishing different conduction mechanism. The value of p depends on the dimensionality of the system, with p = 1/3 for 2D systems in the Mott VRH model. However, the ES-VRH model, applicable for doped graphene samples at low temperatures, considers a vanishing density of states (DOS) near the Fermi level, known as the Coulomb gap, leading to a different value of p (p = 1/2 in all dimensions). After finding the characteristics temperature in ES-VRH, localisation length for carriers can be estimated as,

$$T_0 \ = \ T_{ES} \ = \ \frac{2.8e^2}{4\pi\epsilon_0 k_B \xi}$$

The localization length (ξ) and characteristic temperature (T_{ES}) can vary with doping concentration as it depends on degree of graphitisation [88], which can be estimated analysing the X-ray photo electron spectroscopy (XPS) of doped or undoped graphene system. However, 3D-VRH model can be used for explaining conduction mechanism in oxygenated graphene [87].

After understanding of ES-VRH as transport mechanism for doped graphene sample, those parameters can shed light on the electron transport properties of graphene with varying degrees of doping. These findings contribute to a better understanding of the electrical behaviour of functionalized or doped graphene.

1.4.2. Signature of correlated phases in graphene

The phenomenon known as CDW involves a periodic modulation of electron density accompanied by lattice distortions, resulting in the emergence of unique properties in low-dimensional materials [figure 6]. Understanding the interplay and potential competition

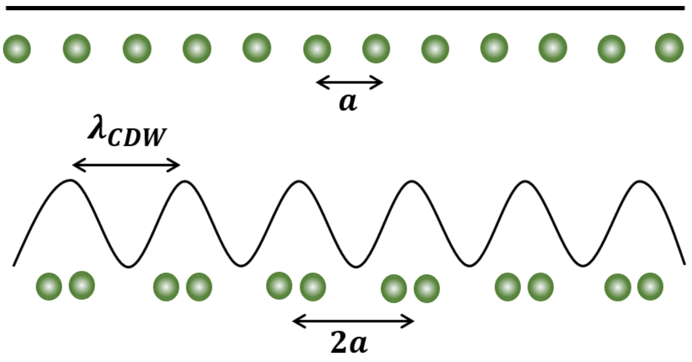

Figure 6: Periodic modulation of one-dimensional atomic arrangement

between superconductivity and CDW is a fundamental concern in low-dimensional systems, particularly in materials like transition metal dichalcogenides [111]. This issue becomes even more intriguing in the context of metal-intercalated bilayer graphene [37]. The occurrence of correlated phase like superconductivity and charge density wave (CDW) states in doped graphene has been a subject of significant interest in the field of condensed matter physics. Doping graphene, typically with foreign atoms or molecules, introduces charge carriers into its pristine hexagonal lattice, leading to various intriguing electronic phases [89,90].

Superconductivity in doped graphene refers to the correlated state where the state is achieved by mainly forming an interlayer state or by enhancing the electron-phonon interaction [91-94]. This remarkable property was long considered challenging to achieve in two-dimensional materials due to their low electron density. However, researchers have made significant progress in inducing superconductivity in graphene by introducing various dopants such as calcium (Ca) [93,95], lithium (Li) [89,91,96], or potassium (K) [97]. These dopants alter the electronic structure of graphene, creating a favourable environment for Cooper pairs of electrons to form and condense into a superconducting state. The discovery of superconductivity in doped graphene opens up possibilities for its utilization in advanced electronic and quantum computing applications.

On the other hand, CDW states in doped graphene involve periodic modulations in the electron density within the material. In a CDW state, the electrons arrange themselves into a repeating pattern, leading to regions of higher and lower charge density. These CDW phases can emerge in doped graphene when the electron-phonon interactions are strong enough to overcome the Coulomb repulsion between electrons. CDW states are associated with unique electronic properties, such as bandgap opening and enhanced electron-electron correlations. Understanding and controlling CDW states in doped graphene can have significant implications for the development of novel electronic devices and materials. The origin of

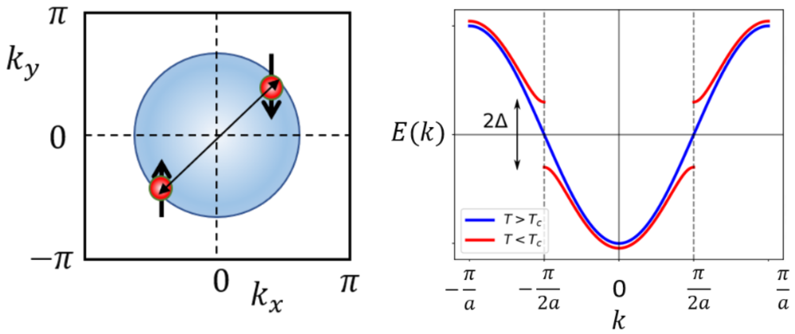

Figure 7: Pairing of electrons with opposite spin (left). Opening of band gap, also known as CDW gap, at Fermi level (right) [112]

CDWs is a complex and active area of research, but several mechanisms have been proposed to explain their formation. Here are some possible origins of CDWs:

(i) Peierls Instability: The Peierls instability is one of the most well-known mechanisms for CDW formation. It arises due to the coupling between electrons and lattice vibrations (phonons). When the electron-phonon interaction is strong enough, it can lead to an energy gap opening at the Fermi level (figure 7), creating a state of lower energy with a periodic distortion of the atomic lattice. This distortion forms a CDW and opens a gap in the electronic density of states, causing a partial or complete insulating behaviour [98].

(ii) Nesting of Fermi Surface: In some materials, the Fermi surface (the surface in momentum space that separates filled and empty electron states) can have specific nesting properties. Nesting occurs when parts of the Fermi surface can be mapped onto each other by a wavevector associated with a CDW [figure 8]. Electrons near the Fermi surface can then undergo a collective, periodic motion, leading to the formation of a CDW [99].

(iii) Competing electronic interaction: In some cases, competing electronic interactions like the on-site Coulomb repulsion and the electron-phonon interaction [93,105,110] can result in the formation of CDWs [figure 3]. These interactions can lead to a delicate balance between CDW and other ordered phases like superconductivity or magnetic order, giving rise to complex phase diagrams [100,109].

(iv) Quantum Criticality: CDWs can also be driven by quantum criticality, where the system is on the brink of a phase transition at absolute zero temperature. Fluctuations in the electronic density can become enhanced as the system approaches a quantum critical point, leading to the emergence of CDWs [101].

(v) Dimensionality and Reduced Dimensional Systems: CDWs are more prevalent in low-dimensional materials, such as 1D or 2D systems, where electronic correlations and interactions can be more pronounced. Reduced dimensionality can enhance the susceptibility to CDW formation [102].

(vi) External factors like pressure, magnetic fields, and chemical substitutions can also induce or suppress CDWs by modifying the balance between competing interactions in the material [103,104].

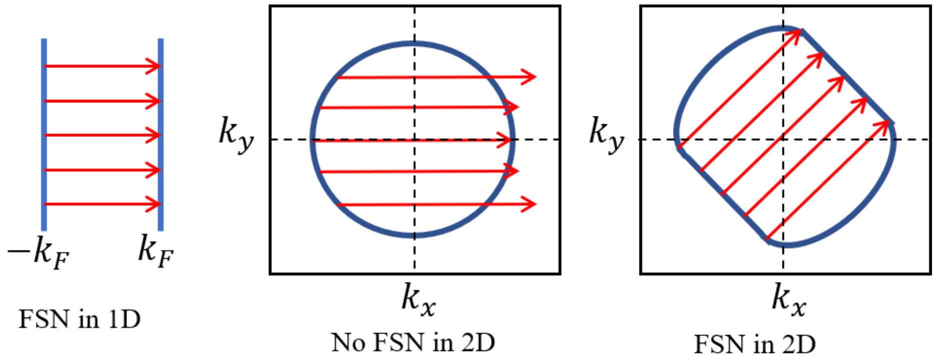

FSN in 1D

No FSN in 2D

FSN in 2D

Figure 8: Nesting of Fermi surface in 1D and 2D

Understanding the origin of CDWs is essential for harnessing their properties for technological applications and advancing our understanding of condensed matter physics. Different materials may exhibit CDWs due to different underlying mechanisms, making it a rich and diverse field of study. Researchers continue to investigate these phenomena to uncover the underlying physics and potential practical applications.

1.6 Aims and Objectives

The proposed research work aims to achieve several key objectives:

1. Synthesis Strategy Development: The primary goal is to establish a robust and efficient synthesis strategy for producing BG systems on a large scale. This involves the development of a method that can be readily scaled up for practical applications.

2. Precise Control of Boron Doping: To achieve the desired properties, the research seeks to attain a high degree of control over the boron doping level. By manipulating synthesis parameters, the research aims to precisely modulate the boron content and explore various doping configurations within the graphene lattice.

3. Spectroscopic Characterizations: The research will employ advanced spectroscopic techniques such as XPS and Raman spectroscopy to comprehensively characterize the BG systems. These analyses will provide critical insights into the chemical composition, structural integrity, and electronic properties of the materials.

4. Electrical Transport Property Investigation: The study will focus on elucidating the electrical transport properties of the BG systems. This involves measuring parameters like electrical conductivity, charge carrier mobility, and resistivity, which are crucial for understanding the materials' electronic behaviour and potential applications.

5. Exploration of Quantum Phenomena: Another important objective is to explore intriguing quantum phenomena that may manifest in these two-dimensional BG systems. Specifically, the research aims to investigate phenomena such as superconductivity and CDWs. Understanding and harnessing these quantum effects could lead to groundbreaking advancements in electronic and quantum device technologies.

In summary, this research project seeks to develop a scalable synthesis method for BG, precisely control doping levels and configurations, comprehensively characterize the materials using advanced spectroscopic techniques, investigate their electrical transport properties, and explore quantum phenomena within these two-dimensional systems. Achieving these objectives will contribute significantly to the fundamental understanding and practical utilization of BG materials.

References

1. K. S. Novoselov, A. K. Geim, S. V. Morozov, D. Jiang, Y. Zhang, S. V. Dubonos, I. V. Grigorieva, and A. A. Firsov, Electric Field Effect in Atomically Thin Carbon Films, Science, **306**, 666-669 (2004).
2. Novoselov, K., Geim, A., Morozov, S. *et al.* Two-dimensional gas of massless Dirac fermions in graphene, Nature, **438**, 197–200 (2005).

3. K. S. Novoselov, Z. Jiang, Y. Zhang, S. V. Morozov, H. L. Stormer, U. Zeitler, J. C. Maan, G. S. Boebinger, P. Kim, and A. K. Geim, Room-Temperature Quantum Hall Effect in Graphene, Science, **315**, 1379-1379, (2007).
4. M. Y. Han, B. Özyilmaz, Y. Zhang, and P. Kim, Energy Band-Gap Engineering of Graphene Nanoribbons, Phys. Rev. Lett., **98**, 206805, (2007).
5. L. Liu, Z. Shen; Bandgap engineering of graphene: A density functional theory study, Appl. Phys. Lett., **95 (25),** 252104 (2009).
6. C. Lee, X. Wei, J. W. Kysar, and J. Hone, Measurement of the Elastic Properties and Intrinsic Strength of Monolayer Graphene, Science, **321**, 385-388 (2008).
7. Pauling, L., The Nature of the Chemical Bond, Cornell University Press, Ithaca, NY (1972).
8. P. R. Wallace, The Band Theory of Graphite, Phys. Rev., **71**, 622, (1947).
9. Zhang, Y., Tan, YW., Stormer, H. *et al.* Experimental observation of the quantum Hall effect and Berry's phase in graphene, Nature, **438**, 201–204 (2005).
10. M. Katsnelson, K. Novoselov, A. Geim, Chiral tunnelling and the Klein paradox in graphene, Nature Phys**., 2**, 620–625 (2006).
11. A. Balandin, Thermal properties of graphene and nanostructured carbon materials, Nature Mater., **10**, 569–581 (2011).
12. Y. W. Sun, D. G. Papageorgiou, C. J. Humphreys, D. J. Dunstan, P. Puech, J. E. Proctor, C. Bousige, D. Machon, A. San-Miguel, Mechanical properties of graphene, Applied Physics Reviews, **8 (2)**, 021310 (2021).
13. A. Dimiev, Layer-by-layer removal of graphene for device patterning, Science, **331**, 1168 (2011).
14. A. H. Castro Neto, F. Guinea, N. M. R. Peres, K. S. Novoselov, A. K. Geim, The electronic properties of graphene, Rev. Mod. Phys., **81**, 109 (2009).
15. C. K. Chua and M. Pumera, Covalent chemistry on graphene, Chem. Soc. Rev., **42(8),** 3222 (2013).
16. D. W. Lee, T. Kim and M. Lee, An amphiphilic pyrene sheet for selective functionalization of graphene, Chem. Commun., **47(29),** 8259 (2011).
17. X. Duan, S. Indrawirawan, H. Sun, et al., Effects of nitrogen- , boron-, and phosphorus-doping or co-doping on metal free graphene catalysis, Catalysis, **249**, 184–191 (2015).

18. X. Zhao, Q. Zhang, Y. Hao, Y. Li, Y. Fang, and D. Chen, Alternate Multilayer Films of Poly(vinyl alcohol) and Exfoliated Graphene Oxide Fabricated via a Facial Layer-by-Layer Assembly, Macromolecules, **43 (22),** 9411-9416 (2010).
19. J. Xu, L. Wang, and Y. Zhu, Decontamination of Bisphenol A from Aqueous Solution by Graphene Adsorption, Langmuir, **28 (22),** 8418-8425 (2012).
20. Z.-H. Huang, X. Zheng, W. Lv, M. Wang, Q.-H. Yang, and F. Kang, Adsorption of Lead(II) Ions from Aqueous Solution on Low-Temperature Exfoliated Graphene Nanosheets, Langmuir, **27 (12),** 7558-7562 (2011).
21. R. Roldán, M. P. López-Sancho, and F. Guinea, Effect of electron-electron interaction on the Fermi surface topology of doped graphene, Phys. Rev. B, **77**, 115410 (2008).
22. T. O. Wehling, K. S. Novoselov, S. V. Morozov, E. E. Vdovin, M. I. Katsnelson, A. K. Geim, and A. I. Lichtenstein, Molecular Doping of Graphene, Nano Letters, **8 (1)**, 173-177 (2008).
23. M. Deifallah, P. F. McMillan, and F. Corà, Electronic and Structural Properties of Two-Dimensional Carbon Nitride Graphenes, The Journal of Physical Chemistry C, **112 (14),** 5447-5453 (2008).
24. F. Cervantes-Sodi, G. Csányi, S. Piscanec, and A. C. Ferrari, Edge-functionalized and substitutionally doped graphene nanoribbons: Electronic and spin properties, Phys. Rev. B, **77**, 165427 (2008).
25. B. Uchoa and A. H. Castro Neto, Superconducting States of Pure and Doped Graphene, Phys. Rev. Lett. **98**, 146801 (2007).
26. N. M. R. Peres, F. Guinea, and A. H. Castro Neto, Coulomb interactions and ferromagnetism in pure and doped graphene, Phys. Rev. B, **72**, 174406 (2005).
27. L. Zhao, M. Levendorf, S. Goncher, T. Schiros, L. Pálová, A. Zabet-Khosousi, K. T. Rim, C. Gutiérrez, D. Nordlund, C. Jaye, M. Hybertsen, D. Reichman, G. W. Flynn, J. Park, and A. N. Pasupathy, Local Atomic and Electronic Structure of Boron Chemical Doping in Monolayer Graphene, Nano Letters, **13(10)**, 4659-4665 (2013).
28. M. S. Dresselhaus & G. Dresselhaus, Intercalation compounds of graphite, Advances in Physics, **51(1)**, 1-186 (2002).
29. J. T. Xu, Y. H. Dou, Z. X. Wei, J. M. Ma, Y. H. Deng, Y. T. Li, H. K. Liu, S. X. Dou, Adv. Sci., **4**, 1700146 (2017).
30. T. Weller, M. Ellerby, S. Saxena *et al.*, Superconductivity in the intercalated graphite compounds C_6Yb and C_6Ca, Nature Phys**, 1**, 39–41 (2005).

31. M. Xue, G. Chen, H. Yang, Y. Zhu, D. Wang, J. He, and T. Cao, Superconductivity in Potassium-Doped Few-Layer Graphene, J. Am. Chem. Soc., **134 (15)**, 6536-6539 (2012).
32. J. Chapman, Y. Su, C. Howard, *et al.*, Superconductivity in Ca-doped graphene laminates. Sci. Rep., **6**, 23254 (2016).
33. M. Calandra and F. Mauri, Theoretical Explanation of Superconductivity in C_6Ca, Phys. Rev. Lett. **95**, 237002 (2005).
34. I. I. Mazin and A. V. Balatsky, Superconductivity in Ca-intercalated bilayer graphene, Philosophical Magazine Letters, **90(10),** 731-738 (2010).
35. K. Kanetani, K. Sugawara, T. Sato, R. Shimizu, K. Iwaya, T. Hitosugi, and T. Takahashi, Ca intercalated bilayer graphene as a thinnest limit of superconducting C_6Ca, **109 (48),** 19610-19613 (2012).
36. R. Shimizu, K. Sugawara, K. Kanetani, K. Iwaya, T. Sato, T. Takahashi, and T. Hitosugi, Charge-density wave in Ca-intercalated bilayer graphene induced by commensurate lattice matching, Physical Review Letters, **114**, 146103 (2015).
37. K. Rahnejat, C. Howard, N. Shuttleworth et al., CDWs in the graphene sheets of the superconductor CaC_6. Nat. Commun., **2**, 558 (2011).
38. G. E. Grechnev, A. A. Lyogenkaya, Y. A. Kolesnichenko, Y. I. Prylutskyy, R. Hayn, Electronic structure and magnetic properties of graphite intercalated with 3d-metals, Low Temperature Physics, **40**, 450–453 (2014).
39. T. P. Kaloni, M. Upadhyay Kahaly, and U. Schwingenschlögl, Induced magnetism in transition metal intercalated graphitic systems, J. Mater. Chem., **21**, 18681-18685 (2011).
40. D. Wehenkel, T. Bointon, T. Booth *et al.*, Unforeseen high temperature and humidity stability of $FeCl_3$ intercalated few layer graphene. Sci. Rep., **5**, 7609 (2015).
41. X. Qi, J. Qu, H.-B. Zhang, D. Yang, Y. Yu, C. Chia, and Z.-Z. Yu, $FeCl_3$ intercalated few-layer graphene for high lithium-ion storage performance, J. Mater. Chem. A, **3**, 15498-15504 (2015).
42. A. Geim, K. Novoselov, The rise of graphene, Nature Mater., **6**, 183–191 (2007).
43. R. R. Nair, P. Blake, A. N. Grigorenko, K. S. Novoselov, T. J. Booth, T. Stauber, N. M. R. Peres, And A. K. Geim, Fine Structure Constant Defines Visual Transparency of Graphene, Science, **320**,1308-1308 (2008).

44. X. Wang, X. Li, L. Zhang, Y. Yoon, P. K. Weber, H. Wang, J. Guo, And H. Dai, N-Doping of Graphene Through Electrothermal Reactions with Ammonia, Science, **324**, 768-771 (2009).
45. A. Mishchenko, J. S. Tu, Y. Cao, R. V. Gorbachev, J. R. Wallbank, M. T. Greenaway, V. E. Morozov, S. V. Morozov, M. J. Zhu, S. L. Wong, F. Withers, C. R. Woods, Y-J. Kim, K. Watanabe, T. Taniguchi, E. E. Vdovin, O. Makarovsky, T. M. Fromhold, V. I. Fal'ko, A. K. Geim, L. Eaves & K. S. Novoselov, Twist-controlled resonant tunnelling in graphene/boron nitride/graphene heterostructures. Nature Nanotech., **9**, 808–813 (2014).
46. K. Noori, S. Y. Quek, and A. Rodin, Hydrogen adatoms on graphene: The role of hybridization and lattice distortion, Phys. Rev. B, **102**, 195416 (2020).
47. F. Gargiulo, G. Autès, N. Virk, S. Barthel, M. Rösner, L. R. M. Toller, T. O. Wehling, and O. V. Yazyev, Electronic Transport in Graphene with Aggregated Hydrogen Adatoms, Phys. Rev. Lett., **113**, 246601 (2014).
48. A. Grüneis, C. Attaccalite, A. Rubio, D. V. Vyalikh, S. L. Molodtsov, J. Fink, R. Follath, W. Eberhardt, B. Büchner, and T. Pichler, Electronic structure and electron-phonon coupling of doped graphene layers in KC_8, Phys. Rev. B., **79**, 205106 (2009).
49. D. K. Efetov and P. Kim, Controlling Electron-Phonon Interactions in Graphene at Ultrahigh Carrier Densities, Phys. Rev. Lett., **105**, 256805 (2010).
50. Lehtinen, P. O., Foster, A. S., Ma, Y., Krasheninnikov, A. V., & Nieminen, R. M. (2010). Irradiation-induced magnetism in graphene. ACS Nano, 4(1), 519–532.
51. Yazyev, O. V., & Louie, S. G. (2010). Electronic transport in polycrystalline graphene. Nature Materials, 9(10), 806–809.
52. R. R. Nair, W. Ren, R. Jalil, I. Riaz, V.G. Kravets, L. Britnell, P. Blake, F. Schedin, A. S. Mayorov, S. Yuan, M. I. Katsnelson, H.-M. Cheng, W. Strupinski, L. G. Bulusheva, A. V. Okotrub, I. V. Grigorieva, A. N. Grigorenko, K. S. Novoselov, A. K. Geim, (2012). Fluorographene: A Two-Dimensional Counterpart of Teflon. Small, 8(11), 1808–1813.
53. Bieri, M., Treier, M., Cai, J., Aït-Mansour, K., Ruffieux, P., Gröning, O. et al. (2009). Porous Graphene as an Atmospheric Nanofilter. Small, 5(21), 2398–2402.
54. Girit, Ç. Ö., Meyer, J. C., Erni, R., Rossell, M. D., Kisielowski, C., Yang, L., et al., (2009). Graphene at the Edge: Stability and Dynamics. Science, 323(5922), 1705–1708.

55. Balandin, A. A., Ghosh, S., Bao, W., Calizo, I., Teweldebrhan, D., Miao, F., et al., (2008). Superior Thermal Conductivity of Single-Layer Graphene. Nano Letters, 8(3), 902–907.
56. Elias, D. C., Nair, R. R., Mohiuddin, T. M. G., Morozov, S. V., Blake, P., Halsall, M. P., et al., (2009). Control of Graphene's Properties by Reversible Hydrogenation: Evidence for Graphane. Science, 323(5914), 610–613.
57. Mounet, N., & Marzari, N. (2005). First-principles determination of the structural, vibrational and thermodynamic properties of diamond, graphite, and derivatives. Physical Review B, 71(20), 205214.
58. Huang, P. Y., Ruiz-Vargas, C. S., van der Zande, A. M., Whitney, W. S., Levendorf, M. P., Kevek, J. W., … Muller, D. A. (2011). Grains and grain boundaries in single-layer graphene atomic patchwork quilts. Nature, 469(7330), 389–392.
59. Ritter, K. A., & Lyding, J. W. (2009). The influence of edge structure on the electronic properties of graphene quantum dots and nanoribbons. Nature Materials, 8(3), 235–242.
60. Kosynkin, D. V., Higginbotham, A. L., Sinitskii, A., Lomeda, J. R., Dimiev, A., Price, B. K., et al., (2009). Longitudinal Unzipping of Carbon Nanotubes to Form Graphene Nanoribbons. Nature, 458(7240), 872–876.
61. A. C. Ferrari, D. M. Basko, Raman spectroscopy as a versatile tool for studying the properties of graphene, Nat nanotechnol., **8**, 235–46 (2013).
62. A. C. Ferrari, J. C. Meyer, V. Scardaci et al., Raman spectrum of graphene and graphene layers. Phys. Rev. Lett, **97**, 187401 (2006).
63. J. F. Rodriguez-Nieva, E. B. Barros, R. Saito, M. S. Dresselhaus, Disorder-induced double resonant Raman process in graphene, Phys. Rev. B, **90**, 235410 (2014).
64. P. Venezuela M. Lazzeri, F. Mauri, Theory of double-resonant Raman spectra in graphene: intensity and line shape of defect-induced and two-phonon bands, Phys. Rev. B, **84**, 035433 (2011).
65. Z. H. Ni, L. A. Ponomarenko, R. R. Nair et al., On resonant scatterers as a factor limiting carrier mobility in graphene, Nano Lett., **10**, 3868 (2010).
66. X. T. Guo, A. Zafar, H. Y. Nan, et al., Manipulating fluorescence quenching efficiency of graphene by defect engineering, Appl. Phys. Express, **9**, 055502 (2016).
67. H. Y. Nan, Z. H. Ni, J. Wang, Z. Zafar, Z. X. Shi, Y. Y. Wang, The thermal stability of graphene in air investigated by Raman spectroscopy, J. Raman Spectrosc., **44**, 1018–1021 (2013).

68. X. T. Guo, A. Zafar, H. Y. Nan, et al., Manipulating fluorescence quenching efficiency of graphene by defect engineering, Appl. Phys. Express, **9**, 055502 (2016).
69. J. Jiang, R. Pachter, F. Mehmood, A. E. Islam, B. Maruyama, J. J. Boeckl, A Raman spectroscopy signature for characterizing defective single-layer graphene: defect-induced I (D)/I (D′) intensity ratio by theoretical analysis, Carbon, **90**, 53–62 (2015).
70. T. Moldt, A. Eckmann, P. Klar, et al., High-yield production and transfer of graphene flakes obtained by anodic bonding, ACS Nano, **5,** 7700–7706 (2011).
71. M. M. Lucchese, F. Stavale, M. E. H. Ferreira, et al., Quantifying ion-induced defects and Raman relaxation length in graphene, Carbon, **48**, 1592-1597 (2010).
72. L. G. Cançado, A. Jorio, E. H. M. Ferreira, F. Stavale, C. A. Achete, R. B. Capaz, M. V. O. Moutinho, A. Lombardo, T. S. Kulmala, and A. C. Ferrari, Nano Lett. 11, 3190 (2011).
73. C. Casiraghi, A. Hartschuh, H. Qian, et al., Raman spectroscopy of graphene edges. Nano Lett., **9**, 1433-1441 (2009).
74. Y. M. You, Z. H. Ni, T. Yu, Z. X. Shen, Edge chirality determination of graphene by Raman spectroscopy, Appl. Phys. Lett., **93**, 3112 (2008).
75. R. Saito, A. Jorio, A. G. Souza, G. Dresselhaus, M. S. Dresselhaus, M. A. Pimenta, Probing Phonon Dispersion Relations of Graphite by Double Resonance Raman Scattering, Phys. Rev. Lett., **88**, 027401 (2002).
76. M. A. Pimenta, G. Dresselhaus, M. S. Dresselhaus, L. G. Cancado, A. Jorio, R. Saito, Studying Disorder in Graphite-Based Systems by Raman Spectroscopy, Phys. Chem. Chem. Phys., 9, 1276–1291 (2007).
77. Y. N. Xu, D. Zhan, L. Liu, et al., Thermal dynamics of graphene edges investigated by polarized Raman spectroscopy, ACS Nano, 5, 147-152 (2010).
78. Q. Q. Li, X. Zhang, W. P. Han, et al., Raman spectroscopy at the edges of multilayer graphene, Carbon, **85,** 221-224 (2015).
79. P. Nemes-Incze, G. Kukucska, J. Koltai, J. Kürti, C. Hwang, L. Tapasztó, L. P. Biró, Preparing local strain patterns in graphene by atomic force microscope based indentation, Sci. Rep., **8**, 3035 (2017).
80. M. T. Hwang, M. Heiranian, Y. Kim, *et al.* Ultrasensitive detection of nucleic acids using deformed graphene channel field effect biosensors. Nat. Commun., **11**, 1543 (2020).
81. H. Yu, J. F. Liu, Perfect Spin-filtering in graphene monolayer-bilayer superlattice with zigzag boundaries. Sci. Rep., **6**, 25361 (2016).

82. L. Zhang, D. Peng, R.-P. Liang, J.-D. Qiu, Graphene-based optical nanosensors for detection of heavy metal ions, TrAC Trends in Analytical Chemistry, **102**, 280-289 (2018).
83. B. Muchharla et al., Tunable electronics in large-area atomic layers of boron–nitrogen–carbon, Nano Lett., **13(8)**, 3476–3481 (2013).
84. A. L. Efros and M. Pollak, Electron-Electron Interactions in Disordered Systems, 1st ed., vol. 10. Amsterdam, The Netherlands: North Holland, (1985).
85. B. I. Shklovskii and A. L. Efros, Electronic Properties of Doped Semiconductors. Heidelberg, Germany: Springer, (1984).
86. A. Lösche, "N. F. MOTT, E. A. DAVIS. Electronic processes in non-crystalline materials, clarendon-press, oxford 1971 437 seiten. £7,50, Kristall Technik Banner, **7(4)**, 55–56 (1972).
87. D.J. Sánchez-Trujillo, L. V. Osorio-Maldonado, & J. J. Prías-Barragán, Temperature dependence of electrical conductivity and variable hopping range mechanism on graphene oxide films, *Sci. Rep.,* **13**, 4810 (2023).
88. A. Haque, M. A. -A. Mamun, M. F. N. Taufique, P. Karnati and K. Ghosh, Temperature Dependent Electrical Transport Properties of High Carrier Mobility Reduced Graphene Oxide Thin Film Devices, IEEE Transactions on Semiconductor Manufacturing, **31(4)**, 535-544, (2018).
89. Nandkishore, R., Levitov, L. S. &Chubukov, A. V. Chiral superconductivity from repulsive interactions in doped graphene. Nature, Phys. 8,158–163 (2012).
90. B. Uchoa and A. H. Castro Neto, Superconducting States of Pure and Doped Graphene, Phys. Rev. Lett., **98**, 146801 (2007).
91. Profeta, G., Calandra, M. &Mauri, F. Phonon-mediated superconductivity in graphene by lithium deposition. Nature Phys. 8, 131–134 (2012).
92. Csányi, G., Littlewood, P. B., Nevidomskyy, A. H., Pickard, C. J. & Simons, B. D. The role of the interlayer state in the electronic structure of superconducting graphite intercalated compounds. Nature Phys. 1,42–45 (2005).
93. S. L. Yang, et al., Superconducting graphene sheets in CaC_6 enabled by phonon-mediated interband interactions. Nature commun. 5, 3493, (2014).
94. H. Liang, X. Ma, Z. Yang, P. Wang, X. Zhang, Z. Ren, M. Xue, G. Chen, Emergence of superconductivity in doped glassy-carbon, Carbon, **99**, 585-590 (2016).

95. Weller, T. E., Ellerby, M., Saxena, S. S., Smith, R. P.. & Skipper, N. T. Superconductivity in the intercalated graphite compounds C_6Yb and C_6Ca. Nature Phys. 1,39–41 (2005).
96. Ludbrook, B. M. et al. Evidence for superconductivity in Li-decorated monolayer graphene. Proc. Natl. Acad. Sci. USA 112, 11795–11799 (2015).
97. Xue, M., Chen, G., Yang, H., Zhu, Y., Wang, D., He, J., Cao, T. Superconductivity in Potassium-Doped Few-Layer Graphene. J. Am. Chem. Soc., 134, 6536−6539 (2012).
98. Choi, J.-H., Liu, S., Zhang, W., Liu, Z. F., Rummeli, M. H., CDWs Driven by Peierls Instability at the Interface of Two-Dimensional Lateral Heterostructures, Small, **14**, 1803040 (2018).
99. Rahnejat, K., Howard, C., Shuttleworth, N. *et al.* CDWs in the graphene sheets of the superconductor $CaC_{6,}$ Nat. Commun., **2**, 558 (2011).
100. Lee, J., Wong, D., Velasco Jr, J. et al., Imaging electrostatically confined Dirac fermions in graphene quantum dots. Nature Phys**.,** **12**, 1032–1036 (2016).
101. Gruner, T., Jang, D., Huesges, Z. *et al.*, CDW quantum critical point with strong enhancement of superconductivity, Nature Phys, **13**, 967–972 (2017).
102. Lin, D., Li, S., Wen, J. *et al.*, Patterns and driving forces of dimensionality-dependent CDWs in 2*H*-type transition metal dichalcogenides, Nat. Commun., **11**, 2406 (2020).
103. Guo, Z., Hao, X., Dong, J. *et al.* Observation of pressure induced CDW order and eightfold structure in bulk VSe_2. Sci. Rep. **11**, 18157 (2021).
104. Fuchs, J., Lederer, P., CDW in graphene: Magnetic-field-induced Peierls instability, Eur. Phys. J. Spec. Top., **148**, 151–158 (2007).
105. M. L. Adam, A. A. Bala, Prediction of phonon-mediated superconductivity and CDW in charge doped 1T-HfTe2, Computational Condensed Matter, 26, e00527 (2021).
106. L. G. Cançado, K. Takai, T. Enoki, M. Endo, Y. A. Kim, H. Mizusaki, A. Jorio, L. N. Coelho, R. Magalhães-Paniago, and M. A. Pimenta, Appl. Phys. Lett. 88, 163106 (2006).
107. F. Tuinstra, and J. L. Koenig, J. Chem. Phys. 53, 1126 (1970).
108. M. M. Lucchese, F. Stavale, E. H. M. Ferreira, C. Vilani, M. V. O. Moutinho, R. B. Capaz, C. A. Achete, and A. Jorio, Carbon 48, 1592 (2010).
109. R. Shimizu, K. Sugawara, K. Kanetani, K. Iwaya, T. Sato, T. Takahashi, and T. Hitosugi, Charge-density wave in Ca-intercalated bilayer graphene induced by commensurate lattice matching, Physical Review Letters 114, 146103.

110. X. Zhu, Y. Cao, J. Zhang, E. W. Plummer, J. Guo, Classification of charge density waves based on their nature, Proc. Natl. Acad. Sci., **112(8),** 2367-71 (2015).
111. Naito M., Tanaka S., Electrical transport properties in 2H-NbS_2, 2H-$NbSe_2$, 2H-TaS_2 and 2H-$TaSe_2$. J. Phys. Soc. Jpn., **51(1),** 219–227 (1982).
112. Ewen Bellec, Study of charge density wave materials under current by X-ray diffraction (2019).

Review of past work

2

2.1. Introduction

In this chapter, we surveyed details about process of boron doping in graphene to set a proper controllable synthesis strategy. Initially, we went through few literatures about the X-ray photoelectron spectroscopic properties of graphene to ensure the proper configuration of boron doping in graphene. Then to interpret the spectroscopic behaviour of doped as well as undoped graphene samples, we reviewed some literatures about the structural analyses like X-ray diffraction of doped graphene. We performed an extensive survey on Raman analyses of both doped and undoped graphene to investigate different properties like defects, strain, type of doping, electron phonon interaction etc. Finally, we studied a number of articles related to the electrical properties of graphene and other two-dimensional materials to understand the electrical behaviour of boron doped graphene (BG) samples.

2.2. Synthesis strategy of boron doped graphene

2.2.1. Synthesis of graphene oxide

In 1859, British scientist B.C. Brodie took the first attempt to prepare graphite oxide using potassium chlorate ($KClO_3$) as oxidising agent [1]. As he found some interesting and unique properties of graphite oxide researcher from all around the world had become interested in this process of oxidation. In his method, he mixed graphite and $KClO_3$ with fuming nitric acid (HNO_3) at 60°C for 4 days. In 1898, L. Staundenmaier modified this method of oxidation sulfuric acid (H_2SO_4) with that mixture of graphite, $KClO_3$ and fuming HNO_3 [2]. This method did not require repetition of oxidation process to obtain the desired degree. But, both of these processes were very lengthy and were not safe because of hazardous and explosive chlorine dioxide gas. However, Hofmann proposed a similar method, where all the aforementioned steps were followed by slightly change in precursor. Here, instead of fuming HNO_3, aqueous solution of HNO_3 having 68% concentration was added to concentrated H_2SO_4 (98%) and mixture was kept in an ice bath to advance further procedure [3]. Finally, almost after a century, Hummer and Offeman proposed most effective and popular method to synthesize graphite oxide in 12 h [4]. In this method, graphite powder and sodium nitrate ($NaNO_3$) are mixed with H_2SO_4 (98%). Strong oxidising agent potassium permanganate ($KMnO_4$) are used in that solution which is kept under an ice bath. Here, $NaNO_3$ acted as the required nitrate source instead of fuming nitric acid, whereas $KMnO_4$ removed all the disadvantages of chlorate process. With this process, graphite layers are also become exfoliated and a good quality of few-layered graphene oxide (GO) is produced is produced within a very less amount time as compared to the Brodie's method. Moreover, Hummer's method increases the degree of oxidation in graphite lattice. To enhance the quality of oxidised graphene layers Cote et al. prescribed a modified method which has been followed in this research work [5]. In this method, 1 g of graphite and 1 g of $NaNO_3$ are mixed well using a mortar pestle. Then 46 mL of H_2SO_4 are added to that mixture after placing the reaction beaker in an ice bath. Thereafter, 6 g of $KMnO_4$ is added in a careful and unhurried way. After that, the solution is moved to a 40 °C water bath and stirred well for about 1 h until it forms a thick brownish paste. Next, 100 mL of water is added very slowly where brown fume is observed to come out of that solution. Then, the solution is stirred for 30 min maintaining the temperature of the water bath at 90 °C. Afterwards, 100 mL of water is poured, followed by subsequent addition of 3 mL of H_2O_2 (30%) slowly. The colour of the solution changes from dark brown to yellow immediately. Then, the solution is filtered and washed with 5% HCl solution at first and then with the deionised water for several times until the pH becomes neutral. After that thick, brown, slurry GO is redispersed in water by sonication employing a table-top ultrasonic cleaner and a clear dispersion of few-layer exfoliated GO is obtained. Finally, fine powder GO sample is obtained after drying this dispersion in a vacuum oven at 60 ℃ for 48 h. However, this method also has some disadvantages, as it produces a toxic gas NO_2 (brown) and a toxic liquid N_2O_4. To avoid the production of those toxic materials Marcano et al. [6] added a mixture of acids, H_2SO_4 and H_3PO_4 (9:1), replacing $NaNO_3$ and named this process as Improved Hummes' method. Though, this improved method causes more degree of oxidation in a less hazardous way, the yield of GO is not much as in the modified method described by Cote et al [5].

Oxidation technique	Degree of oxidation
Brodie's method	C/O = 2.2
Staudenmaier method	C/O = 2.52
Hofmann method	C/O = 1.77

Hummers' method	Oxidised carbon: 61% Graphitic carbon: 39%
Modified Hummers' method	Oxidised carbon: 63% Graphitic carbon: 37%
Improved Hummers' method	Oxidised carbon: 69% Graphitic carbon: 31%

2.2.2. Reduction of GO

GO contains oxygen-containing functional groups (OFGs), such as carboxyl, epoxy, carbonyl and carboxyl groups. Being attached with in-plane carbon atoms they are mainly responsible for the hydrophilicity of GO. So as to obtain few layer graphene sheets, there are many different ways to remove the OFGs, i.e., to reduce the GO. Some of those techniques are studied here to optimize a strategy for reduction of graphene and for doping of boron simultaneously.

Thermal Reduction and its effects:

Thermal reduction of GO involves annealing the oxidised samples at higher temperature in an inert atmosphere. Generally, argon (Ar) or nitrogen (N_2) is used to make the atmosphere inert, though some reducing gas like hydrogen (H_2) is also applied inside the reduction chamber for get better reduction [7,8,9]. The process of reduction a high temperature is considered as an easy, linear and large-scale synthesis technique of graphitisation of GO layers. In this method, good quality graphene powder is obtained that exhibits high electrical and thermal conductivity essential to many devices.

Considering the effect of reduction atmosphere inside the furnace, heating temperature is found to be the prime regulating factor for removal of OFGs. [45,55,66,71,72,76]. Along with the composition structural, chemical and electrical properties are also evolved with the annealing temperature. Schniepp et al. [10] investigated different stages of thermal treatment in terms of C/O ratio. The C/O ratio was less 7 when the temperature reached to 500℃. The C/O ratio higher than 13 was obtained while temperature is increased to 750℃. Finally, the C/O ration of 73.1 had been achieved by the Shen et al. [11]. Cao et al. demonstrated the dependency of C/O ratio on temperature as well as the duration of time [12]. In their work, C/O ratio enhanced to 6.0 by the reduction at 550°C for a duration of 10 minutes. This ratio continued to elevate, reaching 16.5 as the temperature was further elevated to 1000°C. The influence of temperature on GO reduction was strongly affirmed by the remarkable increase in the C/O atomic ratio, reaching a substantial 44.2 at 1200°C. On the other hand, the duration of heating notably contributed to the degree of de-oxygenation. The C/O atomic ratio exhibited an intensified enlargement as the duration of heating is extended, culminating in a value of 499 upon reaching a heating time of 120 minutes. Yang et al. thermally treated the GO sample on Si_3N_4/Si Substrate and demonstrated the effect of atmosphere of the reduction chamber [13]. In inert (Ar) atmosphere, C/O ratios were found as 3.9, 6.8 and 11.36 for annealing temperatures 200°C, 500°C and 1000°C respectively. Whereas, in presence of reducing gas, i.e., in Ar/H_2 atmosphere, these ratios became 3.9, 7.3 and 12.4 for the samples annealed at 200°C, 500°C and 1000°C respectively. Further enhancement in the degree of reduction was observed when the ultra-high vacuum (UHV) condition was maintained during reduction. The C/O ratios were 8.9, 13.2 and 14.1 for the samples reduced at 500°C, 700°C and 900°C respectively. In their report, the dependency of reduction was clearly manifested as the C/O ratios obtained at 500°C, showed the increasing trend from 6.8 to 7.3 and then to 8.9 while the reduction atmosphere was changed from Ar to Ar/H_2 and then to UHV respectively. Moreover, they also compared those results with the graphene samples reduced chemically by hydrazine hydrate for which C/O ratio was 8.8.

Wan et al. introduced an interesting technique for reduction of GO at lower temperature utilizing aluminium (Al) [14]. They performed the reduction within a two-zone furnace at temperatures ranging from 100 to 200°C, to reduce GO. The molten Al metal effectively removes oxygen, resulting in the production of well-crystallized graphene papers characterized by a notably high C/O ratio as 18.8, in contrast to the thermally treated graphene at high temperatures. During the aluminium reduction process, highly reactive hydrogen atoms originating from water react with the molten aluminium, facilitating effective removal of oxygen. Another low- temperature driven reduction method was followed by Zhu et al. [15]. However, in this case, GO was dispersed in propylene carbonate and this dispersion was reduced at 150 °C. The C/O ratio of 8.3 was achieved in this method.

Furthermore, Punckt et al. modified this process of thermal reduction a little which helped them to improve the degree of reduction much prominently [16]. The enhancement of C/O ratio from 7.3 to 24 obtained by increasing temperature from 500 °C to 1100 °C. Though this amount was raised to 65 by changing the reduction time from 60 s to 10 min. After that, when the reduction was done at 1100°C followed by another annealing treatment of samples in Ar atmosphere for 1 h at the same temperature, the C/O ratio was drastically changed to 170. Maximum C/O was confirmed by this work was 340 while the samples were reannealed with 1500°C for 1 h under Ar environment.

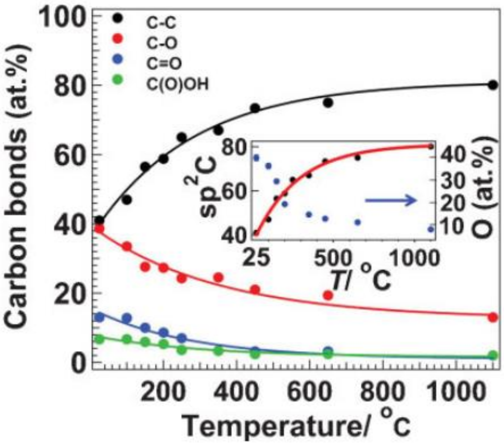

Figure 1 : Variation of different OFGs and carbon-carbon bonds [inset: percentages of sp^2 carbon and oxygen] present at graphene samples thermally annealed at different temperatures [31].

Now, the different degree of reduction affects other properties of graphene such as its chemical structure, carrier type, electrical conductivity, band gap etc. Li et al. conducted an investigation into the alteration of chemical structure based on annealing temperature [17]. The evolution of XPS spectra underscores the necessity of elevated temperatures to achieve effective reduction of GO. Through density functional theory (DFT) calculations, Kim et al. [18] determined the binding energies of epoxy and hydroxyl groups to a 32-carbon-atom graphene unit. Their findings suggested greater stability of epoxy groups compared to hydroxyl groups in GO. Gao et al. [19] further divided epoxy and hydroxyl groups into two types based on their positions within GO's aromatic domains, revealing differences in stability. Gao's work indicated that the dissociation of hydroxyl groups attached to GO's edges occurs at a critical temperature (T_{OH}) of 650°C, while carboxyl groups slowly reduce at 100–150°C and carbonyl groups are stable until a high $T_{C=O}$ of 1730°C. Experimental observations sometimes deviate from simulations, such as Jeong et al.'s work [20], which found that annealing at 200°C in low-pressure argon removed most oxygen-containing groups.

In order to enable the utilization of graphene across diverse nanoelectronics applications, it becomes imperative to establish methodologies for the scalable production of graphene with finely tuned electrical properties. In this context, Tu et al. presented the findings of an essential investigation concerning the remarkable transition between n-type and p-type graphene accomplished through variations in the thermal annealing temperature [21]. This study reveals that at temperatures ranging from 300 to 450°C and 800 to 1000°C, the charge carriers in graphene are electrons (n-type), while within the temperature range of 450 to 800°C, they are holes (p-type). This behaviour stems from the influence of distinct OFGs on reduced graphene, which are determined by the annealing temperature. They ascertained that the prevalence of electron-withdrawing groups (namely, carboxyl, carbonyl, and sp^3-bonded hydroxyl, ether, and epoxide groups) yields p-type graphene, while a dominance of electron-donating groups (sp^2-bonded hydroxyl, ether, and epoxide groups) results in n-type graphene. Furthermore, as an illustrative example, authors constructed a flexible thermoelectric device comprising GO-700 and GO-1000 as p-type and n-type constituents, respectively. This device, comprising eight pairs of these components, exhibited an output voltage of 4.1 mV and an output power of 41 nW for a temperature difference (ΔT) of 80 K. These outcomes provide compelling evidence that the carrier characteristics of graphene can be significantly modulated by manipulating the specific functional groups present on its surface. This adaptability opens avenues for a broad spectrum of applications, including the incorporation of graphene into flexible thermoelectric devices.

Wang et al. [22] examined GO thin films annealed at different temperatures, revealing that the volume electrical conductivity of reduced graphene oxide (rGO) films was 50 S/cm at 500°C, 100 S/cm at 700°C, and 550 S/cm at 1100°C. Wu et al. [23] employed arc-discharge treatment to exfoliate graphite oxide and create graphene, capitalizing on temperatures exceeding 2000°C in a brief span. However, thermal exfoliation exhibited a notable drawback: structural harm to graphene sheets due to carbon dioxide release [25]. Approximately 30% of the graphite oxide mass was lost during exfoliation, causing lattice defects throughout the sheet [24]. These defects influence electronic properties by reducing ballistic transport path lengths and introducing scattering centres. Consequently, the electrical conductivity of graphene sheets averages 10–23 S/cm, significantly lower than that of pristine graphene, indicating a weak effect on carbon plane electronic structure reduction and restoration.

The introduction of OFGs is recognized to modulate graphene's bandgap. A gradual reduction in the oxygen content of GO also customizes the bandgap via an alternate route. Consequently, understanding the nature of oxygen is crucial for tailoring bandgaps, particularly in the specific cases addressed in this section. For nonstoichiometric and hygroscopic compounds like GO, a proportional relationship between bandgap and molar oxygen concentration has been established [26], and theoretical studies predict a proportional rise in the bandgap with an increased oxygen-to-carbon ratio [27]. Huang et al. similarly demonstrated that the material's bandgap increases with heightened oxygen coverage density [28]. In-depth DFT analyses employing Vienna Ab initio simulations revealed that local minima at oxygen-to-carbon ratios of 11.1% and 25% introduce simultaneous bandgap openings of 0.780 and 0.354 eV. Employing a combination of hydrazine and ammonia treatment in water offered an alternative route to tailor the bandgap of graphene. Gradual functional group removal led to the transformation from sp^3 to sp^2 transitions, reducing the bandgap from 2.8 eV to 0.02 eV for few-layered graphene sheets [29].

Nevertheless, conventional reduction methods exhibit rapid kinetics, posing challenges in controlling the chemical organic moieties during reduction due to their aggressive mild chemical behaviour. To mitigate this, a slower reduction kinetics becomes necessary to tame hydrazine's reactivity. Employing gas-based hydrazine reduction of GO instead of wet chemistry protocols offers better control over moiety and reduction sequence. Employing a stepwise hydrazine treatment in a controlled, gradual manner facilitates the tuning of the optical bandgap from 3.5 eV to 1.0 eV [30]. While chemical approaches provide insights into bandgap tuning, accurately determining the oxygen content in oxidized sheets remains challenging. Out-of-plane oxygen presence not only expands interlayers but also contributes to expansion and exfoliation. However, uneven sheet dispersion, uncontrollable sheet size, and shape hinder process optimization and reproducibility. Each individually modified material exhibits distinct physical and electronic characteristics. Thus, establishing a fundamental grasp of surface modification and interlayer chemistry for multiple layers of rGO becomes crucial.

Subsequent sections will initially explore GO's application in various chemical and physical approaches, as well as in pure thermal treatments. Subsequently, the focus will shift to factors influencing oxygen removal and, consequently, the bandgaps calculated during gradual thermal treatments. Lowering thermal treatment temperatures minimizes defect formation and varies oxygen concentration in the sheets during reduction, a subject that will be explored further. Finally, new techniques for GO exfoliation without necessitating heat or chemical treatments will also be discussed.

In sum, elevated temperatures are essential for GO reduction, as corroborated by both experimental and simulated studies. The complex interplay of functional group densities and interactions with graphene's lattice presents challenges in achieving complete GO reduction through thermal annealing, even at high temperatures.

Solvothermal Reduction: Various chemical agents can be used to reduce GO, such as hydrazine [13,18,19,32,38], sodium borohydride [33] etc. These agents donate electrons to the OFGs, leading to their reduction. Care must be taken with some of these reagents, as they can be hazardous.

Gao et al. reported a very simple and effective process consists of two steps: deoxygenation and dehydration [34]. This approach likely helps in a controlled reduction process and in minimizing the presence of functional groups. The first step involves the use of sodium borohydride ($NaBH_4$) as a reducing agent for deoxygenation. The second step involves dehydrating the material using concentrated sulfuric acid. This step further reduces remaining functional groups and promoting the restoration of the graphene structure that results in graphene with fewer functional groups, high conductivity, larger crystallite size, and good solubility. An important aspect of their process is that it avoids the use of highly toxic reagents, making it globally approachable.

2.2.3. Boron doping in graphene

Boron doping in graphene has emerged as a significant avenue for tailoring its electronic and structural properties, rendering it suitable for a wide range of applications. Several techniques have been explored to introduce boron atoms into the graphene lattice, each offering distinct advantages and challenges.

Solvothermal process:

Hydrothermal doping of boron involves the incorporation of boron ions during the hydrothermal synthesis of GO. This technique results in boron oxide bonding with oxygen-containing groups in GO, yielding boron-doped graphene with enhanced electric, chemical and structural properties.

To begin with, BG was synthesized using a straightforward hydrothermal technique as previously outlined [35-37,52]. A solution of H_3BO_3 was introduced into an aqueous dispersion of GO that was obtained through ultrasonication. This mixture was subjected to stirring for 1 hour before being transferred to a Teflon-lined stainless autoclave. The autoclave was sealed and then heated to 180°C, maintaining this temperature for a duration of

12 hours. Following the completion of the hydrothermal process, the system was allowed to cool to room temperature, and the resulting precipitate was isolated through centrifugation, followed by thorough rinsing with distilled water. The final BG product was subsequently subjected to freeze-drying overnight to facilitate its preservation for subsequent applications.

Tang et al. described a straightforward reflux method to synthesize BG samples utilizing GO and borane-THF adduct [39]. Here, borane-THF adduct was introduced to the suspension of GO, which was then heated to 100°C within an oil bath while being stirred magnetically for a duration of 96 hours. Following this, the final product was obtained by cooling, washing and drying subsequently.

Microwave assisted method:

Umrao et al. designed a microwave assisted way to synthesize multilayered BG samples [40]. Initial step involved dispersing GO in ethanol using both a bath and an ultrasonicator for thorough dispersion. Simultaneously, a clear solution of boric acid in water was prepared. The boric acid solution was then introduced into the GO dispersion while stirring. This mixture was maintained at 60°C for 8 hours to allow the reaction to proceed fully, under microwave-assisted conditions. Subsequently, the reaction mixture was cooled to room temperature. To eliminate any residual unreacted boric acid, the mixture underwent a hot DI water wash, after which it was dried at 80°C. The resulting solid material was then subjected to exfoliation using a microwave oven set at 700 W for 40 seconds.

Solid-State Reaction: Boron doping can be achieved by exposing graphene to boron-rich solid materials at elevated temperatures. The boron atoms migrate into the graphene lattice through a solid-state reaction. This technique offers control over doping levels but requires careful optimization of reaction parameters.

Here In this process [41], incorporating boron into graphene involved thermal annealing of GO in the presence of boron oxide (B_2O_3). Boron atoms originating from B_2O_3 vapor were introduced to replace carbon atoms within the graphene structure at higher temperatures within a custom-built tubular furnace. The typical synthesis procedure involved placing GO powder onto the surface of B_2O_3 within a corundum crucible. This crucible was subsequently positioned at the centre of a corundum tube while maintaining a continuous flow of argon, ensuring an inert atmosphere within the tube furnace. The furnace's central temperature was gradually raised to 1200°C at a heating rate of 5°C per minute. Following a 4-hour dwell time at this temperature, the sample was slowly cooled down to room temperature under an argon atmosphere. Subsequently, the resulting product underwent refluxing in a 3M NaOH aqueous solution for 2 hours to eliminate any unreacted boron oxide. After filtration and thorough water washing, the product was vacuum-dried at 60°C. In this process, almost 3.2 at.% boron was achieved.

Using similar process, clusters of single-walled carbon nanotubes (SWCNTs) doped boron and containing up to 10 At. % of boron were successfully synthesized with high efficiency through a thermo-chemical treatment process as reported by authors [42-45]. This method involved subjecting pure SWCNT bundles and B_2O_3 to controlled conditions within a flowing nitrogen (N_2) atmosphere. The influence of synthesis temperature (ranging from 1503 K to 1773 K) and duration (varying between 30 and 240 minutes) on the content of both boron and nitrogen, as well as the overall yield of the SWCNT bundles, was thoroughly investigated. Notably, the highest yield of SWCNT bundles doped with both B and N was achieved by conducting the synthesis at 1553 K for a period of 30 minutes.

Arc discharge:

This method utilizes a high-energy electrical arc discharge between graphite electrodes submerged in a boron-rich environment, such as a boron-containing gas or vapor. The arc discharge generates high temperatures and pressures, causing the vaporized boron species to interact with the graphite electrodes, leading to the incorporation of boron atoms into the resulting graphene sheets. With this method of doping, 1 to 5 at.% boron in carbon nanotubes was achieved by an electric arc-discharge between an anode made of homogeneous BC_4N and a cathode made of graphite [46]. Suenaga et al. applied another combination of electrodes like, boron containing HfB_2 as anode against a graphite cathode in a nitrogen atmosphere [47]. Nitrogen- or boron-doped graphene has also been produced using this arc discharge technique. As described by Panchokarla et al., N-doped graphene sheets are produced by carrying out the arc discharge between carbon electrodes in the presence of hydrogen and pyridine or ammonia. To produce boron-doped graphene, it was necessary to use boron-stuffed graphite electrodes or a mixture of hydrogen and diborane vapor; the B-doped graphene showed a p-type semiconductor behaviour [48].

Chemical Vapor Deposition (CVD): In this widely employed technique, boron-containing precursors are introduced during the growth of graphene through CVD. Boron atoms are carried by a carrier gas and get incorporated into the lattice as graphene grows on a suitable substrate. CVD allows precise control over the doping level and spatial distribution of boron atoms, enabling the creation of tailored electronic structures.

B-doped SWCNTs were obtained by Liu et al. through a high-temperature chemical reaction subsequent to the growth process [49]. They subjected SWCNTs, produced via arc discharge, to this treatment in direct contact with B_2O_3 within a flowing NH_3 environment. The mixture of SWCNTs and B_2O_3 was subjected to heating at 900 °C for a duration of 4 hours within a quartz tube reactor, with NH_3 flowing as the carrier gas. Excess boron precursor was removed by utilizing hot deionized water (at 100 °C).

Another literature showed that the surface of the carbon coated aluminium had been modified involving a mixture of 3.2 vol % benzene and 3.2 vol % boron trichloride (BCl_3) under a N_2 flow at 725°C for 20 minutes [50]. In a study by Wu et al., it was observed that boron doping of graphene could be attained through heat treatment with BCl_3 gas [51]. However, the effectiveness of this approach was limited, resulting in a modest doping efficiency of only 0.88 at % boron incorporation.

2.3 Spectroscopic overview

XPS analyses

The utilization of X-ray photoelectron spectroscopy (XPS) analysis was conducted to delve into the arrangement and presence of boron doping within the graphene structure. The comprehensive examination of the resulting sample, comprising boron-doped graphene (BG), revealed the clear presence of boron (B), carbon (C), and oxygen (O), with corresponding atomic proportions. The B1s, C1s, and O1s peaks were centred at 190.4 eV, 283.9 eV, and 531.6 eV [41]. Conversely, the survey scan of pristine graphene solely indicated the core levels of C1s (284.2 eV) and O1s (531.6 eV). Through deconvolution, both the amount and arrangement of doping were investigated. Sheng et al. identified the atomic percentages of B, C, and O as 3.2%, 87.7%, and 9.1%, respectively.

Furthermore, the B1s peak was observed at a higher binding energy (B1s peak: 190.4 eV, in contrast to 187 eV for pure boron), indicating the integration of boron atoms from B_2O_3 vapor into the graphene structure. In higher-resolution spectra, the distinctive C1s peak of BG, featuring an asymmetrical shape, experienced a shift toward lower binding energy when compared to pristine graphene. This phenomenon can be attributed to the formation of B–C bonds, which influences the Fermi level by redistributing p-electrons within the graphene structure.

Upon applying the Shirley algorithm to the intensive C1s peak of BG, it could be deconvoluted into four constituents. The most prominent peak at 283.9 eV corresponded to sp^2 hybrid carbon atoms, while signals at higher binding energies indicated the presence of C–O groups after thermal annealing. However, the minor signal at 281.8 eV, indicative of carbon adjacent to boron atoms as in the B_4C system, was absent due to low boron content.

In the high-resolution B1s spectrum, an observed upward shift in the B1s signal suggested the integration of boron into the sp^2 carbon networks. Subsequent curve fitting indicated that peaks centred at 187.7 eV and 189.0 eV likely corresponded to B_4C and BC_3 structures, respectively. The peak at 190.4 eV indicated boron atoms bonding with carbon and oxygen (BC_2O). The signal at 191.9 eV suggested the presence of oxidized boron atoms (BCO_2), indicating that boron atoms were enclosed by carbon and oxygen atoms. Cumulatively, these findings affirmed the development of B–C bonds during the annealing process [41].

Sahoo et al. obtained 5.93 atomic percent of boron doped into the graphene sample [53]. The inclusion of boron into the graphene lattice was understood through the relative shift of the B1s peak from 188 eV to 192 eV [54]. In this study, researchers performed deconvolution of the C1s, revealing four distinct peaks at 290.79 eV, 288.47 eV, 285.63 eV, and 284.65 eV. The presence of 284.65 eV signified the existence of C - C sp^2 bonded graphite-like carbon, indicating a predominant arrangement of carbon atoms within BG in a conjugated honeycomb structure. The less pronounced peaks at higher binding energies suggested the presence of functional groups bonded with the graphene structure, even post reduction. The deconvolution of the B1s peak also offered insights. BC_3 (191.28 eV), BC_2O (192.6 eV), and BCO_2 (193.5 eV) each corresponded to distinct doping states of boron within the graphene sheets. Two higher energy deconvoluted peaks provided information regarding the bonding of boron with both carbon and oxygen. Specifically, the peak at 191.28 eV resulted from 'graphitic' boron, indicating the substitution of carbon atoms with boron within the graphene layers. Wu et al. indicated the contribution of BC_3 with the boron peak at approximately 191.8 eV and the contribution of both BC_2O alongside BCO_2 at around 192.8 eV [35]. In certain studies, the B1s spectrum was fitted with four components: BC_3 (188.9 eV), BC_2O (190.1 eV), BCO_2 (192.1 eV), and BO_3 (193.4 eV) [50, 55]. Kwon et al. achieved 0.6 atomic percent of boron, while Ozaki et al. reported 0.8 atomic percent of boron in graphene.

Umrao et al. noted an additional peak at 283.8 eV while deconvoluting the core level spectra of C1s, representing a C−B bond [40]. This bond exhibited a lower binding energy in comparison to sp^2 C−sp^2 C bonding. In this study, the B1s core level spectra were fitted with two distinct components centred at 191.9 eV and 193.1 eV, corresponding to B−C and B−O bonds, respectively.

XRD analyses

The X-ray Diffraction (XRD) pattern reveals a significant peak at 2θ = 26°, indicating an interlayer spacing of approximately 3.4 Å between the (002) graphitic crystal planes induced by laser treatment, as documented by Peng et al. Additionally, a graphitic crystal phase (100) was identified at 2θ = 43° [60]. The remarkable degree of graphitization of BG is further corroborated through thermogravimetric analysis (TGA) measurements conducted under argon, demonstrating BG's stability even beyond 900°C [60]. Yeom et al. employed amorphous glass-like B_2O_3 as a precursor for boron doping through a thermal process [56]. The identification of this phase was confirmed via XRD measurements. Generally, three crystalline phases of boron (III) oxide—α-B_2O_3, β-B_2O_3, and a glass-like g-B_2O_3 phase—are acknowledged to exist, with the local structure of g-B_2O_3 resembling that of α-B_2O_3 [57, 58]. The XRD data of g-B_2O_3 show two distinct wide halos shifting towards lower 2θ positions with rising temperature. Specifically, the interplanar spacings of g-B_2O_3 derived from the initial halo expand from 4.00Å (2θ = 22.2°) at 25°C to 4.48Å (2θ = 19.8°) at 1000°C. Furthermore, TGA of g-B_2O_3 demonstrates weight loss beyond 500°C, likely resulting from partial g-B_2O_3 decomposition rather than boiling, considering g-B_2O_3's boiling temperature is roughly 1500°C. At 1000°C, around 6% by weight of g-B_2O_3 undergoes decomposition. Consequently, during the synthesis of doped graphene nanoplatelets, the elimination of oxygen groups from GO and the decomposition of g-B_2O_3 occur as the annealing temperature escalates to 1000°C. The defects arising from oxygen group removal can serve as active sites for the chemical substitution of carbon atoms by boron atoms. Notably, boron atoms stemming from g-B_2O_3 decomposition can easily react with carbon atoms at these sites. The interlayer spacing of BG measures approximately 3.7–3.8Å, as calculated from the 2θ = 23°–24° peak in the XRD data, slightly larger than the (002) graphite spacing of 3.36Å, indicating a structure akin to graphite with additional defects due to boron doping.

Another literature identified a distinct peak around 25.8° for (002) plane of BG lattice with an interlayer spacing of 0.35 nm [41]. The diffraction patterns of graphite, graphite oxide (GO), pristine graphene, and boron-doped graphene (BG) were assessed. The sharp (002) peak at 26° in Fig. 2(a) underscores the high crystalline nature of the utilized graphite. The shift of this peak to 11° signifies the expansion of the carbon basal plane upon incorporating oxygen-containing functional groups, causing the interlayer spacing to increase from the graphitic 0.34 nm to 0.84 nm and thus forming GO. The diffraction pattern for pristine graphene reveals an interlayer spacing of 0.36 nm. The broadening of the (002) peak implies the amorphous nature of the synthesized PG and BG. The absence of an additional peak at 2θ = 14° and 28° indicates the lack of B_2O_3 [53]. TGA demonstrates the thermo-oxidative stability of all samples up to 500°C in air, confirming the well-ordered structures of the graphitic networks. XRD patterns present peaks (interlayer d spacing) at 26.018° (3.42 Å) for Graphene, 25.888° (3.44 Å) for BG, and 25.948° (3.43 Å) for BN-Graphene. These measurements are all lower (indicating larger d spacing) than the 26.548° (3.34 Å) for pristine graphite [61].

Moreover, the relative peak intensities of (002) for graphene, BG, and BN-graphene were 0.72, 0.30, and 0.48% of that of pristine graphite, implying that solvothermally synthesized graphene adopts crumpled and wrinkled forms. Consequently, efficient stacking is limited, in contrast to pristine graphite, which forms numerous stacked layers [59]. Umrao et al. exhibited clear variations in lattice parameters and interplanar spacings between undoped and doped graphene, as outlined in table 1.

Table 1 : Lattice parameters, interplanar spacing for reduced, B-doped, N-doped and B-N co-doped graphene [40]

Parameters	Reduced Graphene	B-doped graphene	N-doped graphene	B-N co-doped graphene
a (nm)	0.23805	0.23759	0.23748	0.23930
c (nm)	0.68278	0.68098	0.67970	0.68073
d_{100} (nm)	0.20616	0.20575	0.20566	0.20724
d_{002} (nm)	0.34139	0.34049	0.33985	0.34036

UV-VIS (band gap) absorbance spectra analyses

The optical bandgap analysis of BG samples was conducted utilizing ultraviolet-visible (UV-Vis) absorption spectroscopy and Tauc plots [62]. The UV-Vis spectra of all BG samples exhibit absorption peaks at 375, 382, and 386 nm, attributed to π to π* transitions, indicative of a direct optical bandgap ranging from ~2.91 to 3.05 eV. The observed diminished light absorption between 450 and 800 nm can be attributed to the maximization of sp2 domains within the BG structure. Additionally, an extra shoulder in the UV-Vis spectra within the range of 375 to 386 nm for BG samples corresponds to n to π* transitions involving C=O bonds [64]. This signifies the electron transition from boron states to π* states, suggesting a heterogeneous distribution of boron atoms within the rGO's carbon network. Notably, the UV-Vis absorption spectra of BG samples display strong light absorption in the UV spectrum that extends toward the visible range.

The determined bandgaps for BG samples with boron concentrations of 4.8, 5.53, and 6.51 at. % were found to be 3.05, 2.94, and 2.91 eV, respectively. Thus, it is observed that the BG sample with the highest boron doping concentration of 6.51 at. % exhibits the lowest optical bandgap value of 2.91 eV. Furthermore, the relationship between direct optical bandgap and boron doping concentration was explored, revealing a decrease in the bandgap with increasing doping concentration. This phenomenon is attributed to the reduction of oxygen-related functional groups within the carbon network and the compensation of energy states associated with the incorporation of boron dopant atoms, resulting in a shift in the conduction band edges [65].

Theoretical studies offered a different perspective on bandgap opening upon boron doping [63]. Although the doping was purely substitutional, the bandgaps were measured at approximately 0.19, 0.32, 0.42, and 0.54 eV for boron concentrations of around 3.6, 7.3, 11.3, and 13.8 at. %, respectively. This finding highlights the potential for controlling graphene's bandgap through this doping method.

Raman analyses

Raman spectroscopy serves as a highly effective and non-destructive tool for assessing the structure and quality of carbon materials, particularly in discerning defects, disordered arrangements, and graphene layer counts [66]. In this regard, the Raman spectra of freshly prepared BG were collected using a micro-Raman spectrometer with an excitation wavelength of 514 nm, under ambient conditions, and by depositing DMF dispersions on Si substrates, as conducted by Sheng et al. [41] For reference, the Raman spectrum of pristine graphene obtained through the thermal annealing of GO under identical conditions was also presented. In the Raman spectrum of BG, distinct features emerge, including a prominent G peak at 1576 cm^{-1} and a broad 2D peak at 2696 cm^{-1}, which affirm the graphitic structure of BG with a few layers. The highly intense D band at 1347 cm^{-1} in BG samples serves as unequivocal evidence of numerous defects within the graphene layers. These defects are commonly attributed to rigorous graphite oxidation and the incorporation of boron into the carbon hexagonal lattice. In contrast, for pristine graphene, the G band and 2D band are positioned at 1579 cm^{-1} and 2694 cm^{-1}, respectively. The absence of significant shifts or line broadening strongly suggests the preservation of graphene structure after boron doping. Moreover, a slightly elevated I_D/I_G value (0.87) in BG compared to pristine graphene (I_D/I_G = 0.8) underscores BG's higher defect density due to boron doping under similar conditions. When compared to the peak position and morphology of single-layer graphene [67], BG exhibits a broader and upward-shifted band around 2696 cm^{-1}, indicating the production of few-layer BG through thermal annealing.

Umrao et al. conducted Raman spectroscopy on microwave-synthesized undoped graphene, N-doped graphene, B-doped graphene, and BN-doped graphene using 532 nm laser excitation [40]. The 2D contour matrix plot in the Raman measurements revealed distinctive bands, including the D band at approximately 1359 cm^{-1}, the G band at around 1586 cm^{-1}, the 2D band at approximately 2700 cm^{-1}, and the D+D′ band at about 2945 cm^{-1}. The D band arises from the breathing mode of A_{1g} symmetry, indicative of disorder in graphene sheets. The G band signifies the doubly degenerate phonon mode (E_{2g} symmetry) of the sp^2 carbon network, highlighting its graphitic nature [68]. The 2D band, an overtone of the D band, is highly sensitive to the stacking order of graphene layers. In multilayer graphene, the 2D band consists of two sub-bands around 2688 ± 0.70 cm^{-1} and 2720 ± 0.20 cm^{-1}, attributed to contributions from 2D graphite and the highly oriented 3D structure of graphite, respectively [69]. Unlike the 2D band, which doesn't necessitate defects for activation, the D+D′ band arises from the combination of phonons with different momenta around K and Γ, requiring the presence of defects [70]. Interestingly, BN-doped graphene exhibited a lower defect density, resulting in the absence of the D+D′ band and an increased distance between defects (L_D) compared to other samples.

When considering B and/or N doping, two significant observations arise. Firstly, a subtle shift in the D band and G band of doped graphene is evident: shifting from 1342 and 1586 cm^{-1} for undoped graphene to 1354 and 1592 cm^{-1} for N-doped graphene, 1345 and 1587 cm^{-1} for B-doped graphene, and 1345 and 1592 cm^{-1} for BN-doped graphene. This shift reflects structural distortion due to varying bond distances of C-C, C-N, and/or C-B post-doping. Secondly, the intensity ratio of the D band to the G band (I_D/I_G) increases from 1.05 for undoped graphene to 1.14 for N-doped graphene, 1.12 for B-doped graphene, and 1.19 for BN-doped graphene. This augmentation signifies increased structural disorder upon N and/or B doping [35].

The staging of graphene often relies on the G peak position (Pos (G)) [72,73]. Particularly in graphene, the Fermi energy shift has two primary effects: (1) variations in the equilibrium lattice parameter, influencing phonon softening/stiffening [71,74,75], and (2) effects surpassing the adiabatic Born-Oppenheimer approximation, affecting phonon dispersion near Kohn anomalies [71,75-80]. Born-Oppenheimer approximation effects lead to a G band upward shift for hole doping (p-type) and a downward shift for electron doping (n-type) [71,74,75]. Thus, BN-doped graphene demonstrates an excess of electron carriers due to B and N co-doping, distinguishing it from other doped materials. Calculations of defect density (n_d) and L_D help to elucidate the role of defects, ultimately influencing charge carrier mobility.

2.4 Electrical properties

Electrical study

The electrical characteristics of graphene, as well as the impact of doping on these properties, can be effectively assessed through specific parameters and measurements. Common metrics such as carrier mobility and the on/off ratio are employed to gain insights into the nature of transport within graphene. To delve deeper into the comprehension of phase transitions, temperature-dependent transport studies provide valuable insights.

Tang et al. explored the utilization of boron-doped graphene as a gate material in FETs, revealing its distinctive p-type conductivity characterized by a remarkable current on/off ratio exceeding 10^2 [63]. By varying the boron content, they effectively tuned the band gap of graphene from 0 to 0.54 eV, leading to modulated transport properties. This controlled doping approach, with predictable effects on transport, holds significant promise for the development of graphene-based devices. Jung et al. worked on FETs based on BN-doped graphene, successfully achieving an on/off current ratio of 10.7, a clear indication of its semiconducting behaviour [59]. The optical band gap was corroborated to be approximately

3.3 eV, further affirming its semiconducting characteristics. The presence of nitrogen (2.66 atom%) and its higher electronegativity relative to boron (2.38 atom%) drove the Dirac point to -10 V, resulting in n-type behaviour. In this context, boron and nitrogen played the roles of acceptor and donor centres within the graphene plane [83]. Intriguingly, boron, akin to nitrogen, predominantly integrated into the graphitic structure of the carbon lattice, contributing around 0.5 carriers per dopant [82]. One of the pivotal parameters in understanding the electronic transport properties of graphene, whether doped or undoped, is carrier mobility. Pristine graphene, due to its zero band gap and susceptibility to oxygen and water absorption, exhibits a low on/off ratio and p-type behaviour [84,87,89]. Wei et al.'s work on N-doped graphene showcased relatively lower conductivity and a larger on/off ratio, ultimately transitioning to n-type behaviour after nitrogen doping [81]. Their findings revealed mobility values of about 300-1200 cm^2 V^{-1} s^{-1} for pristine graphene and 200-450 cm^2 V^{-1} s^{-1} for N-doped graphene. These values are consistent with varying mobility reports in CVD-grown graphene, spanning from 100-2000 cm^2 V^{-1} s^{-1} [86]. In contrast, chemically exfoliated graphene nanoribbons exhibited mobility in the range of 100-200 cm^2 V^{-1} s^{-1} [84], while Gomez-Navarro et al. reported lower mobility (2-200 cm^2 V^{-1} s^{-1}) for rGO [88]. These differences in mobility can be attributed to doping defects, growth imperfections, and the formation of grain boundaries during the CVD process. Notably, in the case of N-doped graphene, nitrogen atoms acted as scattering centres, leading to decreased conductivity [85,88]. Moreover, these doping atoms integrated into the graphene lattice, forming covalent bonds with carbon atoms and altering the lattice structure. By N or B doping significant modification of the graphene's electronic structure suppressed the density of states near the Fermi energy level (E_F), resulting in the opening of a band gap between the valence and conduction bands. Additionally, the introduction of substituted nitrogen atoms near EF contributed strong electron donor states. Consequently, N-doped graphene exhibited n-type semiconductor behaviour, resulting in reduced conductivity and an improved on/off ratio. On contrast, Panchakarla et al. reported higher conductivity in case of B and N- doped graphene sample as compared to pristine graphene [48].

The temperature-dependent conductivity of doped graphene provides valuable insights into transport mechanisms and phase transitions within the graphene lattice. Reduced graphene samples exhibited a substantial drop in conductivity of over three orders of magnitude when cooled from 298 K to 4 K, in contrast to undoped graphene whose conductivity was reduced by less than one order of magnitude [90]. Temperature-dependent data was best fitted by plotting ln(I/A) against $T^{(-1/3)}$, suggesting VRH as the primary charge transport mechanism within the rGO sheets [91]. Despite differences in conductivity-temperature relationships, rGO monolayers displayed ambipolar behaviour similar to pristine graphene in gate dependence of resistance [92]. Resistance maxima were observed near zero gate voltage within a cryostat under low helium pressure. Extended exposure to the ambient environment caused a notable shift in maxima towards positive gate voltages, which could be reversed by vacuum treatment. Similar shifts have been attributed to doping by oxygen and/or water absorption [92]. Room-temperature field-effect mobilities of 2-200 cm^2/Vs for holes and 0.5-30 cm^2/Vs for electrons were extracted from the gate dependence of resistance for the rGO samples. These values were approximately two orders of magnitude lower than those reported for pristine graphene, which exhibited mobilities between 3000 and 10000 cm^2/Vs [93]. The introduction of nitrogen (N) atoms induced atomic-scale structural deformations within graphene, resulting in new chemical structures like pyridinic, pyrrolic, and graphitic nitrogen. This phenomenon was verified through XPS. N acted as an electron donor, enhancing the n-type conductivity of graphene, while boron (B) introduced holes, effectively diminishing the density of states near the Fermi level and creating a band gap [94,95]. The co-doping of N and B further enhanced conductivity by introducing free electrons and holes into the graphene's π-conjugation systems, possibly forming nanojunctions within graphene layers [96]. Electrical properties were investigated across a temperature range of 20-300 K, revealing nonlinear resistance behaviour. At higher temperatures ($T > 50$ K), thermal activation mechanisms were predominant, following the Arrhenius law. Activation energies were calculated as 3.283 meV for undoped graphene, 2.378 meV for B-doped graphene, 3.08 meV for N-doped graphene, and 1.98 meV for BN-doped graphene [40]. Below 50 K, the electric conduction model developed by Mott for disordered materials described the resistivity behavior due to variable range hopping of polarons. The Mott variable range hopping model (Mott VRH) fittingly explained the data in the low-temperature region. The resistivity confirms adherence to the Mott 2D VRH model. Below 50 K, the influence of Coulomb interactions between electrons became significant, resulting in a soft energy gap known as the Coulomb gap (CG) and aligning with the Efros−Shklovskii (ES)-VRH model for 2D materials at lower temperatures [40]. The study also calculated various Mott parameters using both the 2D VRH model and the ES-VRH model. These findings collectively contribute to our understanding of the complex electrical behaviours and transport mechanisms in doped graphene and its derivatives, offering insights into potential applications in nanoelectronics and beyond.

Charge Density Wave in graphene:

CDW represent a ground state with reduced symmetry, commonly observed in layered materials. Many materials, including metal intercalated graphene system [98], transition-metal dichalcogenides [97], organometallic compounds [99,100], and high-temperature superconductors like cuprates [101], exhibit both superconductivity and CDW simultaneously. Given the prevalence of these phenomena, it's a natural question to inquire whether graphene, the simplest 2D material, can host a CDW or striped state.

The most direct approach to investigate the potential existence of a CDW in graphene is by introducing carriers through a field-effect gate and subsequently examining the material's properties. Various experimental techniques, such as electrical measurements, thermodynamic analyses, and local probes like scanning tunnelling microscopy (STM) and spectroscopy (STS), can shed light on these properties. In the case of graphene intercalated with calcium atoms, significantly higher electron doping of the graphite host occurs, with around 0.2 electrons per carbon atom donated to the graphitic π^* band in CaC_6. This system also exhibits exceptional superconducting behaviour with a remarkably high transition temperature (T_c=11.5 K) compared to other intercalated graphite materials [98].

Another significant indicator of CDW behaviour is the opening of a bandgap at the Fermi level [102]. Several methods can induce a bandgap in graphene, including charge transport with adsorbed atoms or molecules, interactions with substrates, and the application of perpendicular electric fields. In the specific case discussed here, the bandgap arises from substitutional doping, a mechanism akin to substitutionally doped graphene, aligning with theoretical predictions. In most conventional physical systems, such as metals and semiconductors, non-interacting electrons are sufficient to describe their behaviour, as the Coulomb interaction energy among electrons is significantly smaller than their kinetic energy. However, certain systems deviate from this norm, where electron-electron interactions play a pivotal role in shaping the system's properties.

Table 2 : Some previous results of SC and CDW in graphene

Graphene system	Superconductivity		CDW		
	T_C (K)	Ref.	T_{CDW} (K)	(meV)	Ref.
CaC_6 (Bulk)	11.5	[103]	250	450	[98]
CaC_6 (FLG)	7	[111]			
CaC_6 (BLG)	4	[108]	5 - 70	77	[102]
CaC_6 (laminates)	12	[109]			
CaC_6 (laminates BN)	4.4 - 6.4	[109]			
CaC_6 (rGO laminates)	4	[109]			
YbC_6 (Bulk)	6.5	[103]			
KC_6 (FLG)	4.5	[106]			
LiC_6 (SLG)	8.1	[104]			
LiC_6 (SLG)	5.9	[105]			
Ion-C_6 (MLG)	-		100	-	[107]
Boron doped Graphene*			100*	240*	*This work

By introducing donor intercalants like metals into graphite, the material undergoes a transition towards a more metallic character, leading to an increase in the density of states at the Fermi level. This transition can give rise to strongly correlated phenomena, including superconductivity, as observed in various Graphite Intercalation Compounds (GICs) like CaC_6, YbC_6, and BaC_6 [103]. Similar effects and the emergence of a superconducting state upon doping-induced intercalation have also been documented in other layered 2D materials.

Indication of charge density wave in temperature dependent resistivity measurement:

The temperature-dependent resistivity of a material provides several indications or signatures of the presence of a CDW phase. One of the primary indicators of a CDW is an anomalous temperature dependence of resistivity. At a critical temperature (T_{CDW}), which is typically associated with the Peierls transition, the resistivity may exhibit a sharp increase or a kink in its temperature dependence, as seen in figure 2.

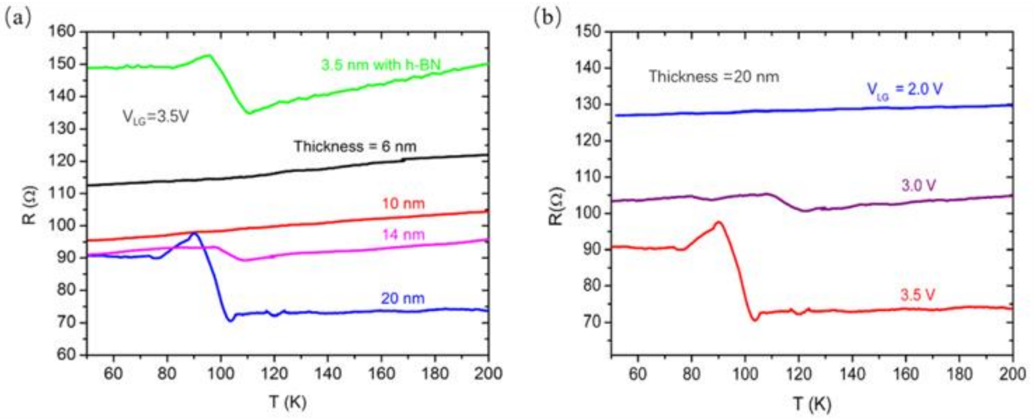

Figure 2: Kink in resistivity at T_{CDW} in electrostatically doped graphene [107]

This abrupt change is often a clear indication of the formation of the charge density wave. The presence of a CDW leads to the opening of an energy gap in the electronic band structure of the material. This gap manifests itself in the resistivity as a decrease in conductivity at temperatures below T_{CDW}. As the temperature decreases, the resistivity rises sharply due to the energy gap, which restricts electron motion. In materials with a well-defined CDW, the resistivity may exhibit periodic oscillations with temperature [112]. These oscillations are associated with the periodic modulation of the charge density. The amplitude of these oscillations can provide information about the strength of the CDW. When the CDW transition is first order, there can be hysteresis in the resistivity-temperature curve [113]. This means that the resistivity may have different values for increasing and decreasing temperature, and the transition from the CDW state to the normal state (and vice versa) occurs at different temperatures. Below the critical temperature T_{CDW}, the material may exhibit non-metallic behaviour in its resistivity-temperature curve. This includes a decrease in electrical conductivity and the development of an insulating-like behaviour as the CDW forms [114].

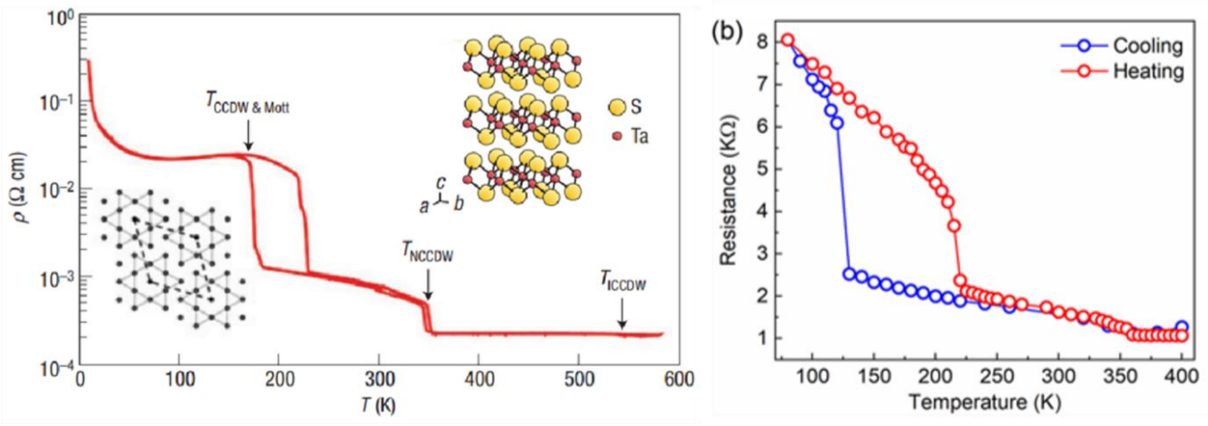

Figure 3: Non-metallic behaviour of NbSe$_2$ below T_{CDW} (left) as reported by Sipos et al. [114]. Hysteresis in resistivity curve of TaS$_2$ (right) as recognised by Balandin group [113].

It's important to note that the exact behaviour of resistivity in the presence of a CDW can vary depending on the specific material and its characteristics. Researchers use temperature-dependent resistivity measurements, along with other experimental techniques, to study and confirm the existence of CDW and to gain insights into their properties. These measurements are valuable for both fundamental research and potential applications in electronic materials.

References

1. B. Brodie, “On the Atomic Weight of Graphite,” Philos. Trans. R. Soc. London, vol. **149**, 249–259, 1859.
2. L. Staudenmaier, Ber. Dtsch. Chem. Ges., **31**, 1481 (1898).
3. (a) U. Hofmann and E. Konig., Z. Anorg. Allg. Chem., **234**, 311 (1937); (b) U. Hofmann and R. Hoist., Ber. Dtsch. Chem. Ges., **12**, 754 (1939).
4. W. S. Hummers and R. E. Offeman, J. Am. Chem. Soc., **80**, 1339 (1958).
5. L. J. Cote, F. Kim, and J. Huang, Langmuir–Blodgett Assembly of Graphite Oxide Single Layers, J. Am. Chem. Soc. **131**, 1043 (2009).

6. D. C. Marcano, D. V Kosynkin, J. M. Berlin, a Sinitskii, Z. Z. Sun, a Slesarev, L. B. Alemany, W. Lu, and J. M. Tour, “Improved Synthesis of graphene oxide,” ACS Nano, **4 (8),** 4806–4814 (2010).
7. H. A. Becerril, J. Mao, Z. Liu, R. M. Stoltenberg, Z. Bao, Y. Chen, Evaluation of Solution-Processed RGO Films as Transparent Conductors, ACS Nano, **2 (3)**, 463-470 (2008).
8. X. Wang, L. Zhi, K. Mullen, Transparent, Conductive Graphene Electrodes for Dye-Sensitized Solar Cells, Nano Letters, **8 (1)**, 323-327 (2008).
9. B. Shen, W. Zhai, and W. Zheng, Ultrathin Flexible Graphene Film: An Excellent Thermal Conducting Material with Efficient EMI Shielding. Adv. Funct. Mater., **24**, 4542-4548 (2014).
10. H. C. Schniepp, J.-L. Li, M. J. McAllister, H. Sai, M. Herrera-Alonso, D. H. Adamson, R. K. Prud'homme, R. Car, D. A. Saville, and I. A. Aksay, Functionalized Single Graphene Sheets Derived from Splitting Graphite Oxide, The Journal of Physical Chemistry B, **110 (17)**, 8535-8539 (2006).
11. B. Shen, W. Zhai, W. Zheng, Ultrathin Flexible Graphene Film: An Excellent Thermal Conducting Material with Efficient EMI Shielding, Advanced Functional Materials, **24(28)**, 4542–4548 (2014).
12. J. Cao, G. Q. Qi, K. Ke, Y. Luo, W.Yang, B.-H. Xie and M.-B. Yang, Effect of temperature and time on the exfoliation and de-oxygenation of graphite oxide by thermal reduction, J. Mater. Sci., **47**, 5097–5105 (2012).
13. D. Yang, A. Velamakanni, G. Bozoklu, S. Park, M. Stoller, R. D. Piner, S. Stankovich, I. Jung, D. A. Field, C. A. Ventrice, R. S. Ruoff, Chemical analysis of graphene oxide films after heat and chemical treatments by X-ray photoelectron and Micro-Raman spectroscopy, Carbon, **47 (1)**, 145-152 (2009).
14. D. Wan, C. Yang, T. Lin, Y. Tang, M. Zhou, Y. Zhong, F. Huang, and J. Lin, Low-Temperature Aluminum Reduction of graphene, Electrical Properties, Surface Wettability, and Energy Storage Applications, ACS Nano, **6 (10)**, 9068-9078 (2012).
15. Y. Zhu, M. D. Stoller, W. Cai, A. Velamakanni, R. D. Piner, D. Chen, and R. S. Ruoff, Exfoliation of Graphite Oxide in Propylene Carbonate and Thermal Reduction of the Resulting graphene Platelets, ACS Nano, **4 (2)**, 1227-1233 (2010).

16. C. Punckt, F. Muckel, S. Wolff, I. A. Aksay, C. A. Chavarin, G. Bacher, and W. Mertin, The effect of degree of reduction on the electrical properties of functionalized graphene sheets, Applied Physics Letters, **102**, 023114 (2013).
17. X. Li, H. Wang, J. T. Robinson, H. Sanchez, G. Diankov, H. Dai, Simultaneous nitrogen doping and reduction of graphene oxide, J. Am. Chem. Soc., **131(43),** 15939–44 (2009).
18. M. C. Kim, G. S. Hwang, R. S. Ruoff, Epoxide reduction with hydrazine on graphene: a first principles study, J. Chem. Phys. **131(6),** 064704, (2009).
19. X. Gao, J. Jang, S. Nagase, Hydrazine and thermal reduction of graphene: reaction mechanisms, product structures, and reaction design, J. Phys. Chem. C, **114(2),** 832–42 (2009).
20. H-K. Jeong, Y.P. Lee, M. H Jin, E. S. Kim, J. J. Bae, Y. H. Lee, Thermal stability of graphite oxide, Chem. Phys. Lett., **470**, 255–8 (2009).
21. N. D. K. Tu, J. Choi, C. R. Park, H. Kim, Remarkable Conversion Between n- and p-Type RGO on Varying the Thermal Annealing Temperature, J. Chemistry of Materials, **27,** 7362-7369 (2015).
22. X. Wang, L. Zhi, K. Mullen, Transparent, conductive graphene electrodes for dye-sensitized solar cells, Nano Lett., **8(1),** 323–7 (2008).
23. D. Pan, J. Zhang, Z. Li, M. Wu, Hydrothermal route for cutting graphene sheets into blue-luminescent graphene quantum dots, Adv. Mater., **22(6),** 734–8 (2010).
24. H. C. Schniepp, J. L. Li, M. J. McAllister, H. Sai, M. Herrera-Alonso, D. H. Adamson, et al., Functionalized single graphene sheets derived from splitting graphite oxide, J Phys Chem B, **110(17),** 8535–9 (2006).
25. K. N. Kudin, B. Ozbas, H. C. Schniepp, R. K. Prud’homme, I. A. Aksay, R. Car, Raman spectra of graphite oxide and functionalized graphene sheets, Nano Lett., **8(1),** 36–41 (2007).
26. I. Jung, D. A. Field, N. J. Clark, Y. Zhu, D. Yang, R. D. Piner, S. Stankovich, D. A. Dikin, H. Geisler, C. A. Ventrice Jr., R. S. Ruoff, Reduction Kinetics of graphene oxide Determined by Electrical Transport Measurements and Temperature Programmed Desorption, J. Phys. Chem. C, **113**, 18480-18486 (2009).
27. D. W. Boukhvalov, and M. I. Katsnelson, Modelling of Graphite Oxide, J. Am. Chem. Soc., **130**, 10697, (2008).
28. H. Huang, Z. Li, J. She, W. Wang, Oxygen density dependent band gap of rGO, J. Appl. Phys., **111**, 054317 (2012).

29. Y. Shen; P. Zhou; Q. Q. Sun; L. Wan; J. Li; L. Y. Chen; D. W. Zhang; X. B. Wang, Optical investigation of rGO by spectroscopic ellipsometry and the band-gap tuning, J. Appl. Phys. Lett., **99**, 141911 (2011).
30. A. Mathkar, D. Tozier, P. Cox, P. Ong, C. Galande, K. Balakrishnan, A. L. M. Reddy, and P. M. Ajayan, Controlled, Stepwise Reduction and Band Gap Manipulation of graphene, The Journal of Physical Chemistry Letters, **3** (8), 986-991 (2012).
31. C. Mattevi, G. Eda, S. Agnoli, S. Miller, K. A. Mkhoyan, O. Celik, et al, Evolution of electrical, chemical, and structural properties of transparent and conducting chemically derived graphene thin films, Adv. Funct. Mater., **19(16)**, 2577–83 (2009).
32. D. Li, M. B. Mu¨ller, S. Gilje, R. B. Kaner, G. G. Wallace, Processable aqueous dispersions of graphene nanosheets, Nat. Nanotechnol. **3(2),** 101–105 (2008).
33. H.-J. Shin, K. K. Kim, A. Benayad, S.-M. Yoon, H. K. Park, I.-S. Jung, et al., Efficient reduction of graphite oxide by sodium borohydride and its effect on electrical conductance, Adv. Funct. Mater, **19(12),** 1987–1992 (2009).
34. W. Gao, L.B. Alemany, L. Ci, P. M. Ajayan, New insights into the structure and reduction of graphite oxide, Nat. Chem. **1(5),** 403–8 (2009).
35. Wu, Z.-S., Winter, A., Chen, L., Sun, Y., Turchanin, A., Feng, X. and Müllen, K., Three-Dimensional Nitrogen and Boron Co-doped Graphene for High-Performance All-Solid-State Supercapacitors. Adv. Mater., 24: 5130-5135 (2012).
36. Qingli Hao, Xifeng Xia, Wu Lei, Wenjuan Wang, Jieshan Qiu, Facile synthesis of sandwich-like polyaniline/boron-doped graphene nano hybrid for supercapacitors, Carbon, 81, 552-563 (2015).
37. Yujuan Xu, Wu Lei, Zhen Han, Tianyi Wang, Mingzhu Xia, Qingli Hao, Boron-doped graphene for fast electrochemical detection of HMX explosive, Electrochimica Acta, 216, 219-227 (2016).
38. Hailiang Wang, Joshua Tucker Robinson, Xiaolin Li, and Hongjie Dai, Solvothermal Reduction of Chemically Exfoliated Graphene Sheets, Journal of the American Chemical Society, **131 (29),** 9910-9911 (2009).
39. Z.-R.Tang, Y. Zhang, N. Zhangab and Y.-J. Xu, New insight into the enhanced visible light photocatalytic activity over boron-doped rGO, Nanoscale,**7**, 7030-7034 (2015).
40. S. Umrao, T. K. Gupta, S. Kumar, V. K. Singh, M. K. Sultania, J. H. Jung, I.-K. Oh, and A. Srivastava, Microwave-Assisted Synthesis of Boron and Nitrogen co-doped RGO for the Protection of Electromagnetic Radiation in Ku-Band, ACS Applied Materials & Interfaces, **7 (35),** 19831-19842 (2015).

41. Z.-H. Sheng, H.-L. Gao, W.-J. Bao, F.-B. Wang and X.-H. Xia, Synthesis of boron doped graphene for oxygen reduction reaction in fuel cells, J. Mater. Chem., **22**, 390-395 (2012).
42. D. Golberg, Y. Bando, L. Bourgeois, K. Kurashima, T. Sato, Large-scale synthesis and HRTEM analysis of single-walled B- and N-doped carbon nanotube bundles, Carbon, **38(14),** 2017-2027 (2000).
43. Fuentes, G. G.; Borowiak-Palen, E.; Knupfer, M.; Pichler, T.; Fink, J.; Wirtz, L.; Rubio, A., Formation and electronic properties of BC_3 single-wall nanotubes upon boron substitution of carbon nanotubes, Phys. ReV. B: Condens. Matter Mater. Phys, **69**, 245403/1 (2004).
44. Golberg D, Bando Y, Kurashima K, Sato T., Nanotubes of boron nitride filled with molybdenum cluster, J. Nanosci. Nanotechnol., **1(1)**, 49-54 (2001).
45. Golberg, D., Han, W., Bando, Y., Bourgeois, L., Kurashima, K., & Sato, T., Fine structure of boron nitride nanotubes produced from carbon nanotubes by a substitution reaction, Journal of Applied Physics, ***86*****(4),** 2364-2366 (1999).
46. Ph. Redlich, J. Loeffler, P.M. Ajayan, J. Bill, F. Aldinger, M. Rühle, B C N nanotubes and boron doping of carbon nanotubes, Chemical Physics Letters, 260(3-4), 465-470 (1996).
47. K. Suenaga, C. Colliex, N. Demoncy, A. Loiseau, H. Pascard, And F. Willaime, Synthesis of Nanoparticles and Nanotubes with Well-Separated Layers of Boron Nitride and Carbon, *Science*, **278**, 653-655 (1997).
48. L. S. Panchokarla, K. S. Subrahmanyam, S. K. Saha, A. Govindaraj, H. R. Krishnamurthy, U. V. Waghmare, C. N. R. Rao, Synthesis, Structure, and Properties of Boron- and Nitrogen-Doped Graphene,tang Adv. Mater., **21**, 4726 (2009).
49. X. M. Liu, H. E. Romero, H. R. Gutierrez, K. Adu, and P. C. Eklund, Transparent Boron-Doped Carbon Nanotube Films, Nano Letters, **8(9)**, 2613-2619 (2008).
50. T. Kwon, H. Nishihara, H. Itoi, Q.-H. Yang, and T. Kyotani, Enhancement Mechanism of Electrochemical Capacitance in Nitrogen-/Boron-Doped Carbons with Uniform Straight Nanochannels, Langmuir, **25 (19),** 11961-11968 (2009).
51. Z.-S. Wu, W. Ren, K. Xu, F. Li, & H.-M. Cheng, Doped graphene sheets as anode materials with super-high rate and large capacity for lithium ion batteries, ACS Nano, **5**, 5463–5471 (2011).

52. Xing, M., Shen, F., Qiu, B. *et al.* Highly-dispersed Boron-doped Graphene Nanosheets Loaded with TiO_2 Nanoparticles for Enhancing CO_2 Photoreduction. *Sci Rep* **4**, 6341 (2014).,52
53. M. Sahoo, K.P. Sreena, B.P. Vinayan, S. Ramaprabhu, Green synthesis of boron doped graphene and its application as high performance anode material in Li ion battery, Materials Research Bulletin, **61**, 383-390 (2015).
54. L. S. Panchakarla, A. Govindaraj, and C. N. R. Rao, Nitrogen- and Boron-Doped Double-Walled Carbon Nanotubes, ACS Nano, **1 (5)**, 494-500 (2007).
55. J-i. Ozaki, N. Kimura, T. Anahara, A. Oya, Preparation and oxygen reduction activity of BN-doped carbons, Carbon, **45(9)**, 1847-1853 (2007).
56. DY. Yeom, W. Jeon, N. Tu, *et al.*, High-concentration boron doping of graphene nanoplatelets by simple thermal annealing and their supercapacitive properties, Sci. Rep., **5**, 9817 (2015).
57. J. D. Mackenzie, & W. E. Claussen, Crystallization and phase relations of boron tridioxide at high pressures, J. Am. Ceram. Soc., **44**, 79–81 (1961).
58. A. Takada, Modeling of B_2O_3 glass structure by coupled MD/MC simulation, Phys. Chem. Glass., **47**, 493–496 (2006).
59. S.-M. Jung, E.K. Lee, M. Choi, D. Shin, I.-Y. Jeon, J.-M. Seo, H.Y. Jeong, N. Park, J.H. Oh, and J.-B. Baek, Direct Solvothermal Synthesis of B/N-Doped Graphene. Angew. Chem. Int. Ed., **53,** 2398-2401 (2014).
60. Zhiwei Peng, Ruquan Ye, Jason A. Mann, Dante Zakhidov, Yilun Li, Preston R. Smalley, Jian Lin, and James M. Tour, Flexible Boron-Doped Laser-Induced Graphene Microsupercapacitors, ACS Nano, **9 (6),** 5868-5875 (2015).
61. I.-Y. Jeon, H.-J. Choi, M. J. Ju, I. T. Choi, K. Lim, J. Ko, H. K. Kim, J. C. Kim, J.-J. Lee, D. Shin, S.-M. Jung, J.-M. Seo, M.-J. Kim, N. Park, L. Dai, J.-B. Baek, Direct nitrogen fixation at the edges of graphene nanoplatelets as efficient electrocatalysts for energy conversion. Sci Rep**, 3**, 2260 (2013).
62. Junaid, M.; Khir, M.H.M.; Witjaksono, G.; Tansu, N.; Saheed, M.S.M.; Kumar, P.; Ullah, Z.; Yar, A.; Usman, F. Boron-Doped RGO with Tunable Bandgap and Enhanced Surface Plasmon Resonance. *Molecules* **2020**, *25*, 3646.
63. Tang, Yong-Bing; Yin, Li-Chang; Yang, Yang; Bo, Xiang-Hui; Cao, Yu-Lin; Wang, Hong-En; Zhang, Wen-Jun; Bello, Igor; Lee, Shuit-Tong; Cheng, Hui-Ming; Lee, Chun-Sing, Tunable Band Gaps and p-Type Transport Properties of Boron-Doped

Graphenes by Controllable Ion Doping Using Reactive Microwave Plasma, ACS Nano, **6(3)**, 1970–1978 (2012).

64. A. T. Habte, D. W. Ayele, M. Hu, Synthesis and Characterization of reduced graphene oxide (rGO) Started from graphene oxide (GO) Using the Tour Method with Different Parameters, Adv. Mater. Sci. Eng., **2019** (2019).
65. Marschall, R.; Wang, L. Non-metal doping of transition metal oxides for visible-light photocatalysis. Catal. Today, **225**, 111–135 (2014).
66. A. Das, S. Pisana, B. Chakraborty, S. Piscanec, S. K. Saha, U. V. Waghmare, K. S. Novoselov, H. R. Krishnamurthy, A. K. Geim, A. C. Ferrari and A. K. Sood, Monitoring dopants by Raman scattering in an electrochemically top-gated graphene transistor, Nat. Nanotechnol., **3**, 210 (2008).
67. C. H. Lui, L. Liu, K. F. Mak, G. W. Flynn and T. F. Heinz, Ultraflat graphene, Nature, **462**, 339 (2009).
68. A. Ferrari, J. Robertson, Interpretation of Raman spectra of disordered and amorphous carbon, Phys. Rev. B: Condens. Matter Mater. Phys., **61**, 14095 (2000).
69. E. Barros, N. Demir, A. S. Filho, J. M. Filho, Jorio, G. Dresselhaus, M. Dresselhaus, Raman spectroscopy of graphitic foams, Phys. Rev. B: Condens. Matter Mater. Phys., **71**, 165422 (2005).
70. L. G. Cancado, A. Jorio, E. M. Ferreira, F. Stavale, C. Achete, R. Capaz, M. Moutinho, A. Lombardo, T. Kulmala, A. Ferrari, Quantifying defects in graphene via Raman spectroscopy at different excitation energies. Nano Lett., **11**, 3190−3196 (2011).
71. A. Das, B. Chakraborty, S. Piscanec, S. Pisana, A. Sood, A. Ferrari, Phonon renormalization in doped bilayer graphene, Phys. Rev. B: Condens. Matter Mater. Phys., **79**, 155417 (2009).
72. T. Enoki, M. Endo, M. Suzuki, Graphite Intercalation Compounds and Applications., Oxford University Press: Oxford, 2003.
73. M. S. Dresselhaus, G. Dresselhaus, Intercalation compounds of graphite, Adv. Phys., **51**, 1−186 (2002).
74. L. Pietronero, S. Strassler, Bond-length change as a tool to¨determine charge transfer and electron-phonon coupling in graphite intercalation compounds, Phys. Rev. Lett., , **47**, 593 (1981).
75. A. Das, S. Pisana, B. Chakraborty, S. Piscanec, S. Saha, U. Waghmare, K. Novoselov, H. Krishnamurthy, A. Geim, A. Ferrari, Monitoring dopants by Raman

scattering in an electrochemically top-gated graphene transistor, Nat. Nanotechnol., **3**, 210−215 (2008).

76. M. Lazzeri, F. Mauri, Nonadiabatic Kohn anomaly in a doped graphene monolayer, Phys. Rev. Lett., 97, 266407 (2006).
77. D. M. Basko, Theory of resonant multiphonon Raman scattering in graphene, Phys. Rev. B: Condens. Matter Mater. Phys., **78**, 125418 (2008).
78. S. Piscanec, M. Lazzeri, F. Mauri, A. Ferrari, J. Robertson, Kohn anomalies and electron-phonon interactions in graphite, Phys. Rev. Lett., **93**, 185503 (2004).
79. D. Basko, S. Piscanec, A. Ferrari, Electron-electron interactions and doping dependence of the two-phonon Raman intensity in graphene, Phys. Rev. B: Condens. Matter Mater. Phys., **80**, 165413 (2009).
80. S. Pisana, M. Lazzeri, C. Casiraghi, K. S. Novoselov, A. K. Geim, A. C. Ferrari, F. Mauri, Breakdown of the adiabatic Born− Oppenheimer approximation in graphene, Nat. Mater., **6**, 198− 201 (2007).
81. D. Wei, Y. Liu, Y. Wang, H. Zhang, L. Huang, and G. Yu, Synthesis of N-Doped Graphene by Chemical Vapor Deposition and Its Electrical Properties, Nano Letters, **9 (5),** 1752-1758 (2009).
82. L. Zhao, M. Levendorf, S. Goncher, T. Schiros, L. Pálová, A. Zabet-Khosousi, K. T. Rim, C. Gutiérrez, D. Nordlund, C. Jaye, M. Hybertsen, D. Reichman, G. W. Flynn, J. Park, and A. N. Pasupathy, Local Atomic and Electronic Structure of Boron Chemical Doping in Monolayer Graphene, Nano Letters, **13(10)**, 4659-4665 (2013).
83. M. Telychko, P. Mutombo, P. Merino, P. Hapala, M. Ondráček, F. C. Bocquet, J. Sforzini, O. Stetsovych, M. Vondráček, P. Jelínek, and M. Švec, Electronic and Chemical Properties of Donor, Acceptor Centers in Graphene, ACS Nano, **9 (9)**, 9180-9187 (2015).
84. Xiaolin Li et al., Chemically Derived, Ultrasmooth Graphene Nanoribbon Semiconductor, Science, **319**, 1229-1232 (2008).
85. T. B. Martins, R. H. Miwa, Antônio J. R. da Silva, and A. Fazzio, Electronic and Transport Properties of Boron-Doped Graphene Nanoribbons, Phys. Rev. Lett., **98**, 196803, (2007).
86. A. Reina, X. Jia, J. Ho, D. Nezich, H. Son, V. Bulovic, M. S. Dresselhaus, and J. Kong, Large Area, Few-Layer Graphene Films on Arbitrary Substrates by Chemical Vapor Deposition, Nano Letters, **9 (1)**, 30-35 (2009).

87. F. Schedin, A. Geim, S. Morozov, *et al.*, Detection of individual gas molecules adsorbed on graphene, Nature Mater**.**, **6**, 652–655 (2007).
88. C. Gómez-Navarro, R. T. Weitz, A. M. Bittner, M. Scolari, A. Mews, M. Burghard, and K. Kern, Electronic Transport Properties of Individual Chemically RGO Sheets, Nano Letters, **7 (11)**, 3499-3503 (2007).
89. L. Fu, Y. Liu, Z. Liu, B. Han, L. Cao, D. Wei, G. Yu, and D. Zhu, Carbon Nanotubes Coated with Alumina as Gate Dielectrics of Field-Effect Transistors, Adv. Mater., **18(2),** 181-185 (2006).
90. Y.-W. Tan, Y. Zhang, K. Bolotin, Y. Zhao, S. Adam, E. H. Hwang, S. Das Sarma, H. L. Stormer, and P. Kim, Measurement of Scattering Rate and Minimum Conductivity in Graphene, Phys. Rev. Lett., **99**, 246803 (2007).
91. J. Robertson, Amorphous carbon, Advances in Physics, **35(4)**, 317-374 (1986).
92. R. Martel, V. Derycke, C. Lavoie, J. Appenzeller, K. K. Chan, J. Tersoff, and Ph. Avouris, Ambipolar Electrical Transport in Semiconducting Single-Wall Carbon Nanotubes, Phys. Rev. Lett., **87**, 256805 (2001).
93. M. C. Lemme, T. J. Echtermeyer, M. Baus and H. Kurz, A Graphene Field-Effect Device, IEEE Electron Device Letters, 28(4), 282-284 (2007).
94. S. Watcharotone, D. A. Dikin, S. Stankovich, R. Piner, I. Jung, G. H. B. Dommett, G. Evmenenko, S.-E. Wu, S.-F. Chen, C.-P. Liu, S. T. Nguyen, and R. S. Ruoff, Graphene−Silica Composite Thin Films as Transparent Conductors, Nano Lett., **7(7)**, 1888-1892 (2007).
95. Dikin, D., Stankovich, S., Zimney, E. *et al.*, Preparation and characterization of graphene oxide paper. Nature, **448**, 457–460 (2007).
96. Quan-Hong Yang, Peng-Xiang Hou, Masashi Unno, Seigo Yamauchi, Riichiro Saito, and Takashi Kyotani, Dual Raman Features of Double Coaxial Carbon Nanotubes with N-Doped and B-Doped Multiwalls, Nano Letters, **5 (12),** 2465-2469 (2005).
97. Naito M., Tanaka S., Electrical transport properties in 2H-NbS_2, 2H-$NbSe_2$, 2H-TaS_2 and 2H-$TaSe_2$. J. Phys. Soc. Jpn., **51(1),** 219–227 (1982).
98. Rahnejat, K., Howard, C., Shuttleworth, N. *et al.* Charge density waves in the graphene sheets of the superconductor CaC_6, Nat. Commun., **2**, 558 (2011).
99. Yoshida, M., Zhang, Y., Ye, J. *et al.* Controlling charge-density-wave states in nano-thick crystals of 1T-TaS_2. *Sci Rep* **4**, 7302 (2014).
100. Singh O, Curzon A, An electron diffraction evidence of charge density wave instability in 2H-NbSe2. Phys Lett A, **56(1),** 63–64 (1976).

101. Hoffman JE, et al., A four unit cell periodic pattern of quasi-particle states surrounding vortex cores in $Bi_2Sr_2CaCu_2O_{8+\delta}$. Science, **295(5554),** 466–469 (2002).
102. R. Shimizu, K. Sugawara, K. Kanetani, K. Iwaya, T. Sato, T. Takahashi, and T. Hitosugi, Charge-density wave in Ca-intercalated bilayer graphene induced by commensurate lattice matching, Physical Review Letters 114, 146103.
103. Weller, T. E., Ellerby, M., Saxena, S. S., Smith, R. P.. & Skipper, N. T. Superconductivity in the intercalated graphite compounds C_6Yb and C_6Ca. Nature Phys. 1,39–41 (2005).
104. Profeta, G., Calandra, M. &Mauri, F. Phonon-mediated superconductivity in graphene by lithium deposition. Nature Phys. 8, 131–134 (2012).
105. Ludbrook, B. M. et al. Evidence for superconductivity in Li-decorated monolayer graphene. Proc. Natl. Acad. Sci. USA 112, 11795–11799 (2015).
106. Xue, M., Chen, G., Yang, H., Zhu, Y., Wang, D., He, J., Cao, T. Superconductivity in Potassium-Doped Few-Layer Graphene. J. Am. Chem. Soc., 134, 6536−6539 (2012).
107. G. Long, S. Xu, T. Zhang, Z. Wu, W. K. Wong, T. Han, J. Lin, Y. Cai, N. Wang; Charge density wave phase transition on the surface of electrostatically doped multilayer graphene, Appl. Phys. Lett., **109 (18),** 183107 (2016).
108. S. Ichinokura, K. Sugawara, A. Takayama, T. Takahashi, and S. Hasegawa, Superconducting Calcium-Intercalated Bilayer Graphene, ACS Nano, **10 (2),** 2761-2765 (2016).
109. Chapman, J.et al., Superconductivity in Ca-doped graphene laminates. Sci. Rep., **6**, 23254 (2016).
110. M. Calandra and F. Mauri, Theoretical Explanation of Superconductivity in C_6Ca, Phys. Rev. Lett., **95**, 237002 (2005).
111. K. Li, X. Feng, W. Zhang, Y. Ou, L. Chen, K. He, L.-L. Wang, L. Guo, G. Liu, Q.-K. Xue, X. Ma, Superconductivity in Ca-intercalated epitaxial graphene on silicon carbide, *Appl. Phys. Lett.*, **103 (6),** 062601 (2013).
112. Liao, M., Wang, H., Zhu, Y. *et al.*, Coexistence of resistance oscillations and the anomalous metal phase in a lithium intercalated $TiSe_2$ superconductor. *Nat Commun*, **12**, 5342 (2021).
113. S. Baraghani, Z. Barani, Y. Ghafouri, A. Mohammadzadeh, T. T. Salguero, F. Kargar, and A. A. Balandin, Charge-Density-Wave Thin-Film Devices Printed with Chemically Exfoliated 1T-TaS_2 Ink, ACS Nano, **16 (4),** 6325-6333 (2022).

114. Sipos, B., Kusmartseva, A., Akrap, A. *et al.* From Mott state to superconductivity in 1T-TaS_2. *Nature Mater* **7**, 960–965 (2008).

Experimental techniques

3

In this chapter we briefly describe the sample preparation method and different experimental techniques employed for this work. We prepared a batch of graphene powder samples by a chemical method followed by thermal treatment at different temperatures. We employed X-ray diffraction for structural analyses of samples. We investigated spectroscopic properties of samples by exploring the X-ray Photoelectron Spectroscopy, Raman spectroscopy and Ultraviolet-Visible (UV-Vis) spectroscopy in detail. We studied electrical properties of samples by using the Physical Property Measurement System (PPMS).

3.1 Sample preparation

Preparation of few-layer pristine graphene samples can be performed mainly in two particular steps. Initially, separation of layers of highly purified graphite flakes is done by proper oxidation of each layer using suitable oxidising agents. Then those oxygen functional groups from graphene lattice are removed by thermal reduction process at inert atmosphere. In this work, graphene or doped graphene samples are synthesized in large scale effectively at lower cost.

3.1.1 Preparation of few-layer GO with the modified Hummers' method

In modified Hummers' method [1], oxidation of graphite layers mainly exfoliates the layers of graphite by incorporation of different OFGs preceded by intercalating an oxidising agent. Detail procedure for preparation of few-layer GO is described in previous chapter. In the first step, $NaNO_3$ and H_2SO_4 are added to graphite flakes which helps to insert the oxidizer at interplanar sites of graphite. However, H_2SO_4 can also execute the oxidation process with the following reaction [2]:

$$\mathrm{C + H_2SO_4 \overset{\Delta}{\rightarrow} CO_2 + 2SO_2 + 2H_2O}$$

But it is challenging to intercalate H_2SO_4 molecules into the graphite layers as the interplanar spacing of the graphite (0.34 nm) is smaller than the diameter of H_2SO_4 molecules (0.39 nm) in ionic form. It also requires heat to react with carbon atoms. That is the reason for combining the $NaNO_3$ with concentrated H_2SO_4 which can generate the HNO_3 in presence of light followed by the production of smaller O_2 molecules.

$$4HNO_3 \xrightarrow{\text{light}} 4NO_2 + O_2 + 3H_2O$$

Now, this abovementioned reaction is responsible for oxidation of the carbon atoms at the edge of graphite planes that leads to opening a gap between graphite layers. Thereafter, H_2SO_4 along with HNO_3 can easily diffuse to the interplanar sites by making the interlayer gap 0.798 nm and can go for exfoliation via further oxidation of in-plane carbons.

Nevertheless, this process of oxidation is quite slow. For vigorous rate of oxidation $KMnO_4$ is added to that mixture at below 4°C. Reaction of $KMnO_4$ with excess H_2SO_4 turns the colour of that mixture into green by producing Mn_2O_7 having diameter of 0.671 nm which is lesser than the interplanar spacing of intercalated graphite layers.

$$KMnO_4 + 3H_2SO_4 \rightarrow K^+ + MnO_3^+ + H_3O^+ + 3HSO_4^-$$

$$MnO_4^- + MnO_3^+ \rightarrow Mn_2O_7$$

This Mn_2O_7 is a strong oxidant which breaks the C=C and results in proper exfoliation of graphite layers. These exfoliated oxygenated layers of graphite are termed as GO. Successive production permanganic acid ($HMnO_4$) in reaction of Mn_2O_7 with H_2SO_4 and then H_2O makes the colour of solution purplish-red as shown in figure 1(left).

$$Mn_2O_7 \overset{\Delta}{\rightarrow} 6MnO_2 + 3O_2 + O_3$$

$$MnO_2 + 2H_2SO_4 \rightarrow 2MnSO_4 + O_2 + + 2H_2O$$

$$Mn_2O_7 + H_2O \rightarrow 2HMnO_4 \text{ (Purplish-red)}$$

Oxidation process is then stopped by adding some DI water into that mixture. As the water is added to the mixture the temperature become high while diluting the H_2SO_4. This H_2O molecules also help to produce other OFGs from C=O in lattice plane. After that temperature of that mixture comes down to 60°C.

Further purification of GO is performed by adding H_2O_2 and washing with 5% HCl solution and then with plenty of DI water. H_2O_2 breaks the MnO_4^- ion into Mn^{2+} ions which have been removed by washing with HCl solution. At this stage, the colour of the solution becomes yellowish as shown in figure 1(right).

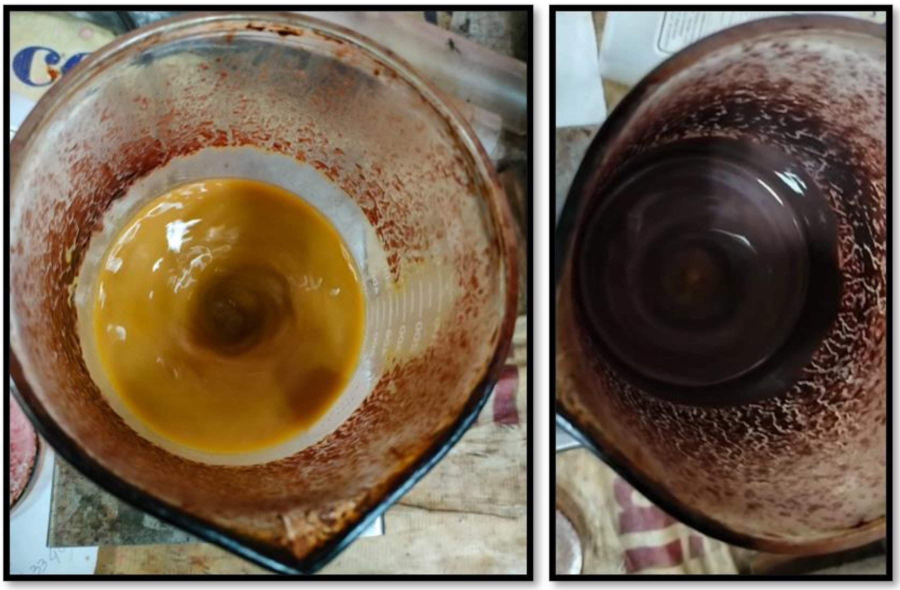

Figure 1 : Synthesis of GO; during reaction with $KMnO_4$ (left), after adding H_2O_2 (right)

This HCl solution also produces Cl^- ions which have been removed by repeated washing with DI water.

$$2MnO_4^- + 5H_2O_2 + 6H^+ \rightarrow 2Mn^{2+} + 5O_2 + 8H_2O$$

$$2MnO_4^- + 16HCl \rightarrow 2Mn^{2+} + 6Cl^- + 5Cl_2 + 8H_2O$$

Finally, after washing several times with water complete removal of chlorine ions is confirmed by checking the pH level of that as obtained brown slurry thick solution of few-layer GO.

3.1.2 Reduction of GO

Reducing GO is a process by which we reinstate graphene structures from oxidized form of graphene. GO contains OFGs, such as epoxides (C-O-C), hydroxyls (-OH), carbonyls (-CO) and carboxyls (-COOH), which give it a higher degree of hydrophilicity and ease of dispersion in water and other solvents. However, these groups also disrupt the excellent electronic and mechanical properties of pristine graphene.

The reduction process aims to remove or reduce these oxygen functional groups, thereby restoring some of the original properties of graphene. There are several methods for reducing GO. Thermal reduction and chemical reduction are two popular methods to obtain graphene from GO samples. Other methods like electrochemical reduction, photochemical reaction, microwave reduction, microbial reduction etc are also effective ways where the electric potential, photon with a particular wavelength and enzymes of certain bacteria respectively reduce the GO samples.

Thermal Reduction:

In this method, dried powder sample GO is pestled very well in a mortar. Then this brown coloured GO powder is mounted on a quartz crucible and introduced into a quartz tube. Thereafter this arrangement is place into a tube furnace for heating at desired temperature up to 1000 °C. To make the atmosphere inert inside the tube 99.999% pure nitrogen (N_2) or argon (Ar) gas is flowed maintaining the flow rate 60 ml/min. To confirm the uniform heating of sample, slow heating, i.e., 5 °C/min heating rate is preferred. Fig. 2. describes the schematic of such arrangement for thermal reduction of GO.

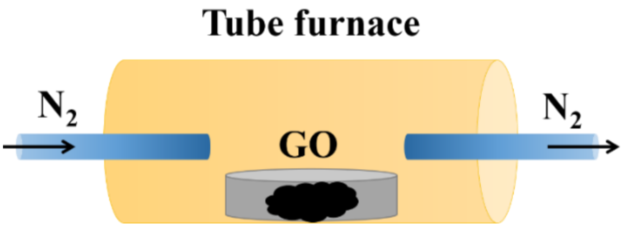

Figure 2: Schematic of the arrangement for thermal reduction of GO

When GO samples are heated to 150 °C, most of the H_2O molecules are removed from the interplanar sites by vaporisation. This phenomenon leads to contraction of interlayer spacings of GO crystals. Within the temperature range of 150-200°C, layers of GO are partially exfoliated owing to the extreme vaporization of intercalated H_2O molecules. When the samples are heated up to 600°C temperature, mainly -COOH groups are eliminated at first. Further lowering of inter-planar spacing (d_{002}) is occurred because of the removal of -COOH groups. When temperature is elevated to 800°C, some of -C-O-C- groups are wiped out and resulted as relaxation of in-plane lattice. At 1000°C, complete removal of -C-O-C- groups along with the partial removal of -OH groups give rise to the formation of point type defects. After heating above the temperature of 1000°C, reduced graphene layers begin to restack over one another and a crystal growth is observed where defects are also disappeared due to self-diffusion of carbon atoms inside lattice. All those outcomes of annealing of GO samples at different temperatures are investigated by the analyses of X-ray Diffraction patterns collected from the X-ray diffractometer. The details of this instrument will be discussed later in this chapter.

Advantages:

- Relatively simpler process that requires minimal equipment like tube furnace, inert gas etc. and it does not need any chemical reagent.
- If GO is thermally annealed at temperature above 1000°C, defects are also minimised owing to self-diffusion of carbon atoms.
- Degree of graphitisation is very high; hence C/O ratio is very high.

Challenges:

- Generation of defects specially divacancy defects are obvious byproducts of this type of reduction.
- May not achieve complete reduction, and residual oxygen functional groups may still be present.
- Lack of fine control over the reduction process, which can result in variations in the degree of reduction.
- It can lead to restacking of graphene layers at higher temperature, i.e., around 2000 °C.
- Thermally reduced graphene treated above 600°C becomes very hydrophobic and insoluble to water.

3.2 Experimental Procedure

3.2.1 X-ray Diffraction (XRD):

XRD stands as a crucial technique in comprehending the atomic arrangements within materials, providing valuable insights into their properties and purity. This phenomenon arises from the interaction between X-rays and the atoms in the materials. The initial step following the synthesis of a nanomaterial involves confirming its phase purity. XRD analysis aids in accurately identifying the phases present in the newly synthesized nanomaterials. After Roentgen's discovery of X-rays in 1895, progressive research led to the comprehension of the diffraction patterns resulting from a crystal's atomic planes. This breakthrough paved the way for precise investigations into matter's structural properties. Matter can generally be categorized as follows:

(i) Amorphous: Solid matter characterized by randomly oriented constituent atoms, lacking long-range order. Examples include glasses, (ii) Crystalline: Solid materials with well-ordered and repeatable arrangements of constituent atoms. The crystalline structure is represented by the simplest repeating unit known as the unit cell. Repeating this unit cell in all three dimensions forms the complete crystal structure. The periodic alignment of atoms within the crystal structure creates a consistent diffraction pattern. Analysing this XRD pattern yields information about the crystal's structure and lattice parameters. Consequently, the XRD measurement technique holds a prominent role in characterizing crystal structure, plane orientation, texture variations, grain size, and other lattice properties. Now, the fundamental principles of XRD can be summarized as follows: When monochromatic X-rays strike a crystal lattice, atomic planes cause reflection of these X-rays, with each atom acting as a scattering centre. When the X-ray wavelength is comparable to the distance between two crystal planes, the X-rays are elastically scattered by atomic electrons. These scattered waves interfere constructively in specific directions dictated by Bragg's law [3]:

$$2d\, sin\, \theta \;=\; n\lambda \tag{3.1}$$

,where d is the interplanar distance, θ is the angle of incidence, n is the diffraction order, and λ is the X-ray wavelength. Bragg's law outlines the necessary conditions for XRD in real space. In reciprocal space, this law can be simply transformed into a geometric representation known as the Ewald sphere.

Figure 3: X-ray diffractometer

For the XRD analysis of the synthesized graphene materials, a Rigaku Benchtop model X-ray diffractometer was utilized (as depicted in Figure 3). The diffraction pattern was recorded using a $\theta - 2\theta$ configuration, with Cu Kα X-rays (λ = 1.5404 Å) serving as the irradiation source. The diffractometer operated at 40 kV voltage and 10 mA current. Data collection occurred at a scanning rate of 0.2s/steps. Following data collection, the XRD pattern underwent background correction for subsequent analysis. Additionally, the observed peaks were cross-referenced with the International Centre for Diffraction Data (ICDD) resource.

3.2.2 X-ray Photoelectron Spectroscopy (XPS):

XPS is a spectroscopic technique that involves the interaction of a sample's surface with monochromatic soft X-rays, leading to the ejection of core electrons. The underlying principle of XPS is based on the photoelectric effect discovered by Hertz in 1887, and its development was advanced in the mid-1960s by Kai Siegbahn and his research group at the University of Uppsala, Sweden. This technique allows for the determination of the chemical state, chemical composition, atomic percentage, and electronic state of sample components [2]. The interaction between an X-ray photon and a core electron in the sample is described by the equation [5];

$$K.E. = h\nu - B.E - \varphi \tag{3.2}$$

, where K.E. represents the kinetic energy of the ejected photoelectron, $h\nu$ is the characteristic energy of the X-ray photon, B.E. is the binding energy of the orbital, and φ is the work function energy of the spectrometer. The kinetic energy of the emitted photoelectrons provides information about the presence of elements in the sample, while the intensity of the photoelectron signal corresponds to the atomic percentage of each element within the material. XPS is particularly effective in determining the chemical state of elements through variations in binding energy or chemical shifts of the photoelectron line. Each element exhibits a characteristic binding energy associated with its core atomic orbital, resulting in distinct photoelectron spectra featuring binding energy peaks. This robust surface analytical method is capable of qualitatively analysing all elements except hydrogen and helium, quantifying composition, and determining valence states. The experimental setup [Figure 4] encompasses an X-ray source, an electron energy analyser, a detection system, and a sample stage. Analysis takes place on the SPECS system utilizing a hemispherical energy analyser (HSA 3500). Photoelectrons are excited using monochromatic Mg K_α X-rays (1253.6 eV) or Al K_α X-rays (1486.6 eV) as the excitation sources, operating at 10 kV with an anode current of 17 mA. XPS measurements necessitate a vacuum pressure of 10^{-8} to 10^{-9} Torr. For powder samples, a small pallet with a 6 mm diameter is prepared using a pelletizer to enhance the signal-to-noise ratio (SNR). During the analysis, a pass energy of 40 eV is

Figure 4: Experimental set up of XPS

maintained for survey scans, and for high-resolution scans, the pass energy is adjusted to 20 eV. We used CasaXPS software to analyse the data further [6].

3.2.3 UV-VIS Spectroscopy:

UV-VIS spectroscopy is a valuable technique employed to investigate the optical characteristics of materials. This method encompasses the study of absorption, transmittance, and reflectance spectroscopy within the UV, visible, and near-infrared regions of the electromagnetic spectrum. At its core, the technique revolves around the phenomenon of materials absorbing photon energy at specific UV or visible wavelengths, which in turn gives rise to distinct spectral patterns in the UV-visible realm. This absorbed photon energy corresponds to a material's band gap energy, a significant property. Upon the absorption of photons, materials undergo a fascinating process: electrons are excited to higher energy states or molecular orbitals, creating what is known as excited states. This is particularly prominent in organic materials, where different electronic transitions occur, such as π to π*, n to π*, σ to σ*, and n to σ* transitions. These transitions involve specific types of molecular orbitals, namely non-bonding (n), bonding (π and σ), and anti-bonding (π* and σ*) orbitals.

The concept of how materials absorb light can be deciphered through the lens of two fundamental laws: Lambert's law and Beer's law. When dealing with UV-vis measurements of materials dissolved in solvents, this is typically carried out using a quartz cuvette. Photons

Figure 5: UV-VIS spectrometer

with a certain intensity (I_0) are directed at the cuvette. In this scenario, a portion of the photon energy is absorbed by the material, while the rest passes through, resulting in a reduced intensity (I). The ratio of these intensities, (I/I_0), is termed transmittance (T). The absorbance (A) of a material is quantified as (-log10T), signifying the quantity of photon energy absorbed by the material's molecules. Lambert's law establishes a direct relationship between absorbance and the cuvette's thickness (path length of 10 mm), essentially dictating the path traversed by light. On the other hand, Beer's law delineates that the concentration of the material in the solution is directly proportional to its absorbance. Combining these laws leads to the formulation of the Beer-Lambert law [7], as expressed in equation (3.3), where α represents molar absorptivity, 'c' signifies the concentration of the solution, and 'd' denotes the path length.

$$\log\frac{I_0}{I} = A = \alpha cd \tag{3.3}$$

In terms of instrumentation, a UV-vis spectrometer comprises several essential components: a light source, a monochromator (comprising entrance and exit slits as well as a dispersive element), and a detector. The primary purpose of conducting UV-vis measurements is to compute a material's band gap, which offers insights into its optoelectronic properties. Depending on the nature of the samples—such as liquids, homogenous solutions, uniformly dispersed solid samples, and thin-film samples—UV-vis measurements in absorbance or transmittance mode are employed to determine their respective band gaps, typically using the Bardeen equation [8] (3.4).

$$\alpha h\nu = A\,(h\nu - Eg) \tag{3.4}$$

This equation involves a range of parameters including constants, light-wave frequency (υ), band gap (E_g), and α. n is indicative of the electronic transition's nature—whether it is direct or indirect. Different values of 'n', such as 1/2, 3/2, 2, and 3, correspond to various types of transitions. Tauc's plot is an illustrative representation taking n = 1/2, with $(\alpha h\upsilon)^{1/n}$ plotted against ($h\upsilon$). A tangent drawn through the linear portion of this plot intersects the x-axis at the precise band gap value. One of the prominent UV instruments utilized in research is the Shimadzu 3600 UV-Vis-NIR spectrophotometer, employing a deuterium lamp for the UV range and a halogen lamp for the visible and near-infrared ranges [Figure 5]. Absorbance measurements of samples dispersed in solvents, the solvent alone, without the sample, is utilized as the reference.

3.2.4 Raman Spectroscopy:

The origins of the term "Raman spectroscopy" pay tribute to its inventor, C.V. Raman, who, in partnership with K.S. Krishnan, authored the seminal paper introducing this technique [9]. This method is rooted in the fundamental Raman effect, which postulates that the frequency of a fraction of scattered radiation diverges from that of the monochromatic incident radiation. Raman spectroscopy stands out as a widely embraced and extensively used technique for investigating the vibrational, rotational, and other low-frequency modes within different materials. This analytical approach, rooted in the Raman Effect, hinges on the interaction of monochromatic light—typically generated by a laser—with molecules in a material. This interaction results in inelastic scattering, causing the photons' energy to shift either higher or lower than the initial incident energy. This phenomenon is known as the Raman Shift.

In the process of conducting Raman Spectroscopy, an intense monochromatic radiation source, often a laser, is directed onto the material under examination. A Raman spectrum is essentially a graphical representation illustrating the intensity of scattered radiation across different frequencies. This deviation in frequency from the incident radiation is often expressed in wavenumbers (cm^{-1}) and is referred to as the Raman shift. Practically, Raman spectroscopy involves directing a monochromatic laser beam onto the sample. As the beam interacts with the vibrating molecules within the material, inelastic scattering occurs, leading to the creation of scattered light and the subsequent formation of a Raman spectrum [10,11]. The variance in frequency from the incident radiation provides valuable insights into low-

Figure 6: Raman spectrometer

frequency transitions involving vibrational, rotational, and other molecular characteristics [12].

A pivotal application of Raman spectroscopy lies in the exploration of the vibrational properties of nanostructured materials. It's a powerful tool for extracting information about various aspects, including structural attributes, phases, grain sizes, and phonon confinement. For the specific Raman spectra in this study, the WiTec Alpha 300 instrument was employed, featuring a 532nm emitting Nd: YAG LASER source [Figure 6]. These spectra were refined through Rayleigh correction to enhance their interpretability.

3.2.5 Electrical Resistivity Measurement:

In this study, we utilized an electrical measurement configuration in conjunction with the Physical Property Measurement System (PPMS) from Cryogenic Ltd., UK, to perform resistivity measurements and various direct current (dc) magnetic investigations. These magnetic studies encompassed the assessment of magnetic hysteresis loops, minor loops, as well as the acquisition of field-cooled and zero field-cooled (FC-ZFC) magnetization curves. To achieve the required cooling to liquid helium temperatures, we employed a CP1000 series He-compressor manufactured by Cryomech, USA, which was integrated with the electrical measurement setup. Additionally, a water chiller sourced from Dai-Chi Cooling Solutions Pvt. Ltd. was connected to the compressor for cooling purposes.

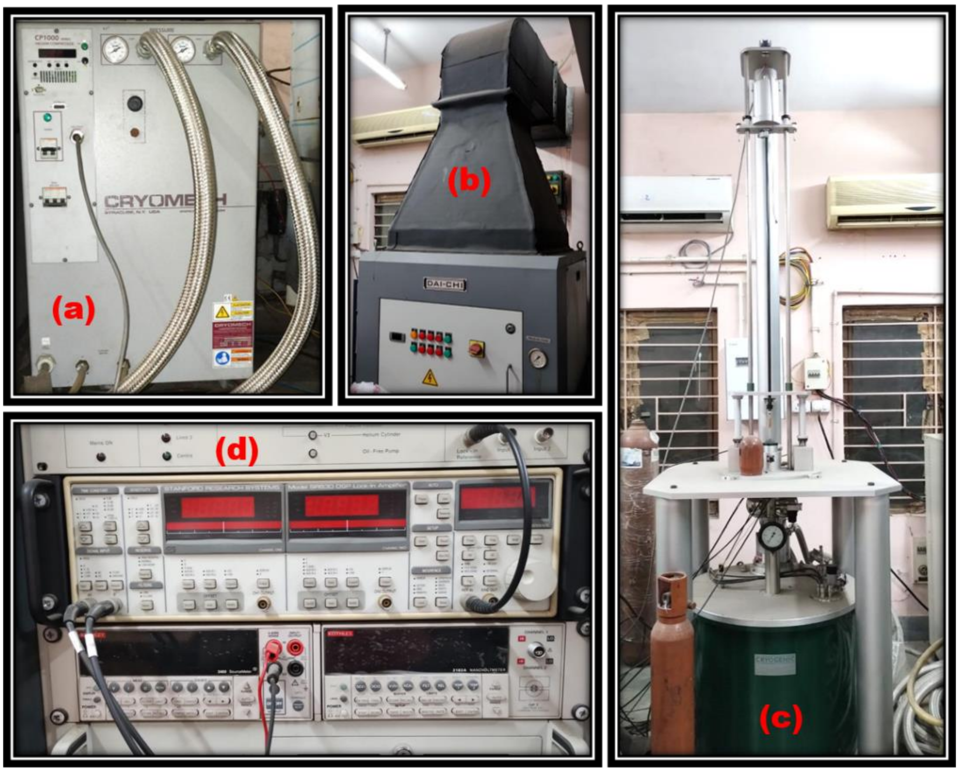

Figure 7: Experimental set up for measurement of electric properties. (a) Helium compressor, (b) Water chiller, (c) VSM Sample chamber, (d) Source meter and nanovoltmeter

Figure 7 illustrates the electric measurement setup connected to our Physical Property Measurement System (PPMS). For the experiments, pellet samples with specific geometries, were linked to both a current source meter (Keithley, 2400) and a nanovoltmeter (Keithley, 2182A). Data collection and control of the various system components during data acquisition were automated using Labview software. The collected data were subsequently processed, graphed, and plotted on a computer for analysis.

References

1. L. J. Cote, F. Kim, and J. Huang, Langmuir−Blodgett Assembly of Graphite Oxide Single Layers, J. Am. Chem. Soc. **131**, 1043 (2009).
2. X. Chen, Z. Qu, Z. Liu, and G. Ren, Mechanism of Oxidization of Graphite to Graphene Oxide by the Hummers Method, ACS Omega **7** (27), 23503-23510 (2022)
3. K.J. Buschow, R.W. Cahn, M.C. Flemings, B. Ilschner, E.J. Kramer and S. Mahajan, Science and technology 2001, 1, 11.
4. B.V. Crist and D.B. Crisst, Handbook of monochromatic XPS spectra; Wiley New York, 2000; Vol. 1.

5. Lefebvre, J.; Galli, F.; Bianchi, C. L.; Patience, G. S.; Boffito, D. C. Experimental methods in chemical engineering: X-ray photoelectron spectroscopy-XPS. The Canadian Journal of Chemical Engineering 2019, 97, 2588-2593, DOI: 10.1002/cjce.23530.
6. http://www.casaxps.com/help_manual/casaxps2316_manual/xps_spectra.pd,Casa XPS.
7. Swinehart, D. F. The beer-lambert law. Journal of chemical education 1962, 39, 333.
8. Bardeen, J.; Blatt, F. J.; Hall, L. H. Proc. Atlantic City Photoconductivity Conf., 1954. 1956.
9. Raman, C. V.; Krishnan, K. S. A new type of secondary radiation. Nature 1928, 121 (3048), 501-502.
10. Sherman, C. P., In Handbook of Instrumental Techniques for Analytical Chemistry, chapter 15; Settle, F., Ed. Prentice-Hall Inc., New Jersey: 1997.
11. Chalmers, J. M.; Edwards, H. G. M.; Hargreaves, M. D. Infrared and Raman spectroscopy in forensic science, John Wiley & Sons: 2012.
12. Bumbrah, G. S.; Sharma, R. M. Raman spectroscopy–Basic principle, instrumentation and selected applications for the characterization of drugs of abuse. Egyptian Journal of Forensic Sciences 2016, 6, 209-215.

Temperature-dependent site selection of boron doping in chemically derived graphene

4

Abstract:

Site dependent light element doping in graphene can lead to exciting phenomenological prospects such as tunable bandgap, enhanced electron phonon coupling and anomalous transport properties for superconductivity, ferromagnetism and catalysis. However, they can lead to more additional defect sites and strain dependent effects as a residual fallout of the process and remains open to interpretations. In this work, we delineate a spectroscopic approach combined with ab-initio results to decipher these factors by using a prototypical in-situ boron doped reduced graphene oxide sample specimens and tuning them from low to moderate hole doping concentrations. The selectivity of doping configurations (BC_3, BCO_2 and BC_2O) as well as their concentration is varied by regulating the annealing temperature (up to 1000 °C). We find a competitive relationship between the dopant and the residual surface oxygen atoms with gradual transformation of favourable doping configuration from out of plane to in-plane (substitutional) with increasing temperature. Furthermore, simultaneous induction of point defects and strain related effects in graphene lattice were also observed with increase in doping concentration. This led to anomalous bandgap crossover at high temperatures in boron doped graphene in comparison to the thermally reduced counterpart which could be important for electronic and transport applications.

4.1 Introduction

Since the discovery of graphene [1,2], the aspect of doping has been the most challenging in order to open the bandgap for electronic applications [3]. It is well-known that substitutional doping in graphene can pose considerable difficulties due to sp^2 bonded network of carbon atoms [4,19]. During the last decade, there has been consistent effort to control the doping in graphene using two different strategies, the physical process which includes ion bombardment [5,71], plasma or CVD based techniques [6,13,15,39] and the chemical route [7-10]. The idea was mainly to have controlled dope with either heavy or lighter elements for interstitial or substitution depending for potential applications. As it turns out, doping heavier elements (e.g. TMs, Eu, Ln, Sr) can lead to potential magnetic applications as graphene lacks any d or f orbitals in its outer shell [11,12]. On the other hand, doping of lighter elements is very useful in energy [13] and catalysis [14], optoelectronics [15] and even in superconductivity applications [16,17] when out of plane dopants are intercalated substantially to enhance the electron-phonon coupling constant. Among most dopants, boron and nitrogen are the well investigated [6,10,14,21,22,33,40] and have proven to be fruitful due to their matching atomic radii with carbon, implying easier substitution of atoms under the right conditions.

In fact, nitrogen which can be doped in pyrrolic, pyridinic and graphitic configuration have been significantly important for optoelectronic, energy and catalysis applications [14,18]. On the contrary for boron, the research focus has been far more limited to energy and catalysis [10,14,15,34,35]. While the structure of boron atom very well lends itself to replace carbon and open up the bandgap in graphene, the impetus to investigate the site selectivity of boron atoms and probing into the electronic properties is somewhat elusive in literature. One of the reasons for that can be attributed to the fact the doping process is difficult to carry out by simple top-down reaction as it requires high energy to break the stable C sp^2 network of host material [19]. However, starting from few layer graphene or reduced graphene oxide it is possible to incorporate boron [20,21] or nitrogen [22] atom in graphitic configuration by thermal annealing process at high temperature. Furthermore, there have been recent reports where inclination has been to test magnetic properties in boron doped graphene derivatives such as quantum dots [23,24]. Hence, this suggests some untapped territories for boron doped graphene and requires further exploration to understand the underlying intricacies of the system better for novel applications.

It is noticeable that boron doping can lead to many interesting electronic properties if tuned properly but can also produce other unintended effects such as strain and defects. Hence, doping should be investigated in correlation with its unintentional counter consequence (defects, strain, etc.). Furthermore, the synthesis strategy can have significant impact on doping configuration (site selectivity) and how that affects the graphene structure and its properties formulate needs to be addressed.

In this article, we investigate a simple system boron doping in reduced graphene oxide synthesized by a physiochemical process to identify the energetically favourable doping sites. We further investigate the effect of synthesis temperature for boron doping in graphene using a combined approach of spectroscopy and ab-initio methods. Furthermore, the competitive evolution from substitutional to intercalation boron doping with the in-situ reduction of the oxygenated groups is observed. This enabled us additionally to elucidate the role of defects and strain generated within the system as a function of temperature gradient and doping. Moreover, we attempt to understand the influence of different boronic configurations on the electronic and optical properties of thermally reduced graphene for fundamental understanding and novel electronic applications.

4.2 Methods

4.2.1 Synthesis of Thermally Reduced Graphene Oxide (TG):

All solvents and reagents are of analytical grade and directly used without further purification. Few-layer Graphene oxide was synthesized from bulk graphite powder by Modified Hummer's method [25,26]. In a typical synthesis, 1.0 g of graphite powder was added into the mixture of 45 ml concentrated sulphuric acid (H_2SO_4, 98 %) and 5 ml of phosphoric acid (H_3PO_4) at room temperature. After overnight stirring, the mixture was cooled to 4 °C using an ice bath. 6.0 g of $KMnO_4$ was then added very slowly under continuous stirring maintaining the temperature of the mixture below 10 °C. After 3 h, 120 ml of distilled water was added into the mixture. After 1 h of continuous stirring 8 ml of 30 % H_2O_2 was added to the mixture followed by dilution of the solution and adding 250 ml of de-ionized water. Yellowish solid precipitation was then filtered out and subsequently washed with 5 % HCl aqueous solution to remove any excess metal ions and further distillation with de-ionized water was undertaken to neutralize until the pH was about 6. Finally, the solution was kept under probe sonication with a power rating of 500 W for 30 min to get better exfoliation results. The resulting graphene oxide (GO) was dried at 40 °C. Finally, TG500, TG700, TG900, and TG1000 samples were all obtained by annealing the GO powder at 500 °C, 700 °C, 900 °C and 1000 °C respectively using a tube furnace under N_2 atmosphere for 1 h.

4.2.2 Synthesis of Boron doped reduced Graphene Oxide (BG):

100 ml of an aqueous dispersion of as-prepared GO with a concentration of 0.5 mg.ml^{-1} was well mixed with 50 mg of boron oxide (B_2O_3) using an ultrasonicator for 1 h. Next, the dispersed solution was dried at 50 °C for 24 h and subjected to thermal annealing at 500 °C, 700 °C, 900 °C and 1000 °C, respectively using a tube furnace under N_2 atmosphere for 1 h. Obtained black powder was washed with hot distilled water to remove the residual boron oxide and then filtered several times. Finally, dried samples were collected as boron doped few-layer graphene sheet (BG) annealed at different temperatures. Samples are designated as BG500, BG700, BG900, BG1000 are the boron doped samples synthesized by maintaining the furnace temperatures 500 °C, 700 °C, 900 °C and 1000 °C respectively.

4.2.3 Experimental details:

Powder X-ray diffraction (XRD) patterns of the synthesized samples were recorded by Bruker D8 diffractometer with Cu-K_α radiation at room temperature. An X-ray of wavelength 1.5404 Å (Cu-Kα) was projected to a Quartz holder containing powder sample. To find proper d-spacing and crystallite size (L_{002}) along the direction of (002) plane, obtained spectra were fitted with Voigt function as shown in figure A4(a) [see appendix A]. Deconvoluted parameters such as exact values of 2θ, Full width half maxima (β) values were used calculate the value of d-spacing and crystallite size for all samples. Employing the deconvoluted peak parameters, d_{002} for all samples were calculated using the Bragg's equation : $2d_{002}\sin\theta = n\lambda$, considering only first order diffraction i.e. $n = 1$ and λ is the wavelength of the applied X-ray. Crystallite size of each sample were measured by Debye-Scherrer equation as,

$$L = \frac{K\lambda}{\beta\cos\theta} \tag{1}$$

Where, K is Debye-Scherrer constant with the value of 0.89 for crystallite considered along the direction of (002) plane and 1.84 for the in-plane crystallite of sample. To find in plane crystallite sizes, peaks around $2\theta=43.2^{\circ}$ were fitted with two Voigt peak functions and parameters were measured using Eq.1 taking K value 1.84 [Figure A4(b) ; appendix A].

Two-dimensional layered structure of BG and TG sheets was observed by High Resolution Transmission Electron Microscope (JEM-2100) operated in 200 KeV (appendix A; figure A1).

Absorption spectra of TG and BG samples were obtained from UV-Vis spectrometer (Shimazdu-3600). For UV-Vis measurement samples were dispersed in ethanol with similar concentrations of 0.5 mg.ml^{-1}. Xenon lamp having spectral range from 185 nm to 3000 nm was used to carry out the absorption measurement. Tauc plot was used to determine the optical band gap for BG and TG samples (figure A6 & A7; appendix A).

X-ray photoelectron spectra (XPS) of various doped samples together with undoped samples were characterized by X-ray Photoelectron Spectrometer (SPECS, HSA 3500), to confirm doping into graphene system. To find out the percentage of dopants survey spectra were taken using a monochromatic Al-K$_{\alpha}$ X-ray source of 1486.61 eV. To calculate the boron to carbon ratio (B/C), survey spectra were analysed through CasaXPS providing proper Relative Sensitivity factor (R.S.F.) value for each component i.e. 1 for carbon, 0.482 for boron and 2.93 for oxygen atom. To probe the types of bond present from individual atomic spectra with certain energy value, high resolution scan for C1s and B1s were performed lowering the pass energy and adjusting the step size, dwell time to count electrons that were coming to the hemispherical analyser during measurement. All high-resolution spectra of C1s and B1s for all the samples were deconvoluted with Lorentzian asymmetric line shape with tail damping [$LF(\alpha, \beta, w, m)$; equivalent to asymptotic theoretical Doniach-Sunjic asymmetric line shape] using CasaXPS software. Background subtractions were also done with Shirley algorithm using the same.

Raman Spectra of all samples were obtained by Raman Spectrometer (WITEC, alpha 300 R) to observe different phonon modes present in the samples. An argon laser of wavelength 532 nm was used to excite the sample to higher excited state with 100X objective with 600 grooves/mm. All spectra were deconvoluted using nine Lorentzian functions. The first order D and G peaks were deconvoluted with five components as D*, D, D”, G, D’ and the second order defect induced peaks were deconvoluted with four components as G*, 2D, D+D’ and 2D’ peaks for BG and TG samples. The maxima of intensities corresponding to D, G, D’, D* and 2D peaks have been designated as I_D, I_G, $I_{D'}$, I_{D*} and I_{2D} respectively in later analysis.

Full-width-half maxima (FWHM) of those peaks have been ascribed as FWHM (D), FWHM (G), FWHM (D') and FWHM (2D) respectively. Raman frequencies, in terms of wave number, of the peaks under consideration are nominated as Pos (D), Pos (G), Pos (D') and Pos (2D) on an individual basis. Here, Raman shift, or Raman frequencies have been represented in terms of wavenumber with the units of cm^{-1}. These Raman shifts in terms of wavenumber have also been assigned with ν_x in some cases, where x corresponded to first and second order peaks D, D', 2D, D+D' and 2D' peaks respectively. Crystallite size, and defect density of the samples were calculated for all samples using the above-mentioned components of the Raman spectra.

4.2.4 Computational details:

The Density functional theory (DFT) simulations were performed using Vienna ab-initio simulation package (VASP) [27,28] using projector-augmented-wave approach (PAW) [29]. During, geometry optimization, the Perdew–Burke–Ernzerhof (PBE) [30] functional was utilized to deal with the exchange-correlation terms within the generalized gradient approximation (GGA). Plane wave basis set with energy cut-off 500 eV and Γ centered k-point mesh of (1×1×1) was implemented throughout the calculations as the considered structures were sufficiently large with lateral dimension greater than 15 Å. The structural relaxation processes were allowed to continue until the total energies converged below 1×10^{-5} eV/ atom. The effect of dispersive forces was taken into account using the PBE+D2 forcefield (Grimme's) method [31]. As the GGA method typically underestimates the band gap value, the Heyd–Scuseria–Ernzerhof (HSE06) hybrid functional [32] was used during the density of states (DOS) calculations.

4.3 Results and Discussion

4.3.1 XPS analyses:

Survey spectra for all BG samples are shown in figure 1(a) and those for TG samples are supplied in figure 1(b). C1s, B1s, and O1s peaks are prominently observed at 284 eV, 189 eV and 532 eV respectively. Presence of core level B1s peaks in the survey spectra indicate the presence of boron atoms in all the BG samples whereas there was no sign of boron in any of the TG sample specimen. From this figure, it can be estimated that the percentage of B1s contribution increases for the BG samples with increasing annealing temperature. Figure 1(c) shows the deconvolution of C1s spectra in all the BG and TG samples.

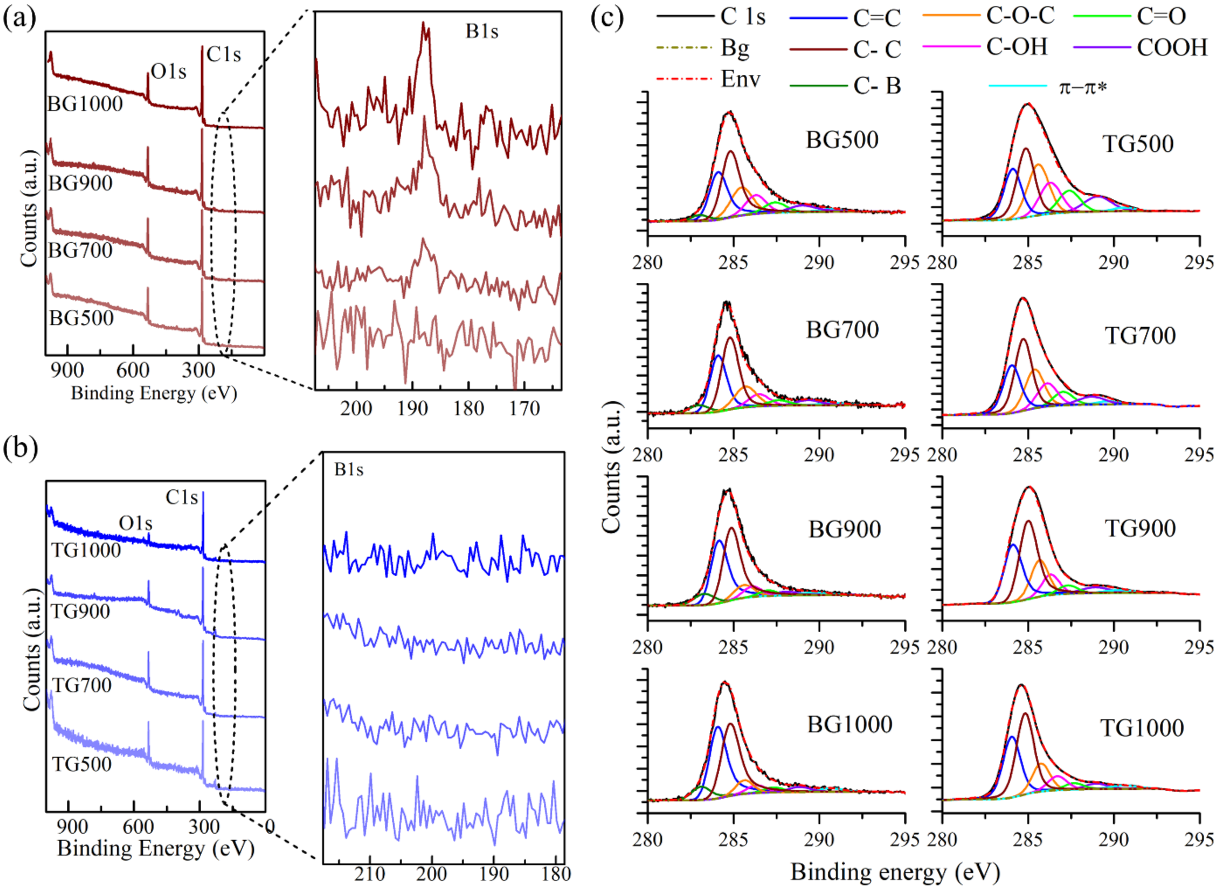

Figure 1. XPS spectra of (a) BG and (b) TG samples synthesized under annealing temperature varied from 500°C to 1000°C (magnified at B1s region to detect the presence of boron). C1s is assigned to carbon 1s peak and that of O1s is assigned to oxygen 1s peak (c) Deconvoluted spectra for BG (eight components) and TG (seven components; C-B contribution absent) samples used for XPS analysis.

From overall line shape of C1s peaks, it is clearly seen that the peak profiles are becoming narrower as more amount of C sp^2 bonds start to dominate the graphene lattice with increase in temperature as more removal of oxygenated moieties takes place. From the C1s profile, contributions from different functional groups or atoms, bonded with in-plane carbon atoms, are detected having the binding energies of 283.0 ± 0.2 eV, 284.0 ± 0.1 eV, 284.7 ± 0.1 eV, 285.6 ± 0.1 eV, 286.3 ± 0.1 eV, 287.3 ± 0.1 eV, 288.8 ± 0.1 eV, 290.4 ± 0.2 eV, which are attributed to the binding energies of C-B [33-35], C=C, C-C, C-O-C, C-OH, C=O, O-C=O bonds, and $\pi - \pi^*$ shake-up satellites corresponding to the hexagonal C sp^2 honeycomb network, respectively [36-38]. Binding energies corresponding for all bonds in BG and TG samples are provided in detail in the table A1 [appendix A]. Obviously in case of the TG samples, contribution from the C-B was not found during the deconvolution profiling. -C-

OH, -C-O-C-, -C=O, -O-C=OH are the Oxygen Functional Groups (OFG) which are bonded along the out of plane and at the edges forming the sp^3 hybridization network with hexagonal carbon atoms, present in both TG and BG systems.

In order to identify the amount and configuration of boron atoms into graphene network, detailed analysis of XPS was conducted for all the BG together with TG samples. In figure 2(a), deconvolution of B1s peaks, composed of five peaks centered at around 186.9 ± 0.1 eV, 188.6 ± 0.2 eV, 190.0 ± 0.2 eV, 191.8 ± 0.2 eV, 193.0 ± 0.1 are attributed to B-B, BC_3, BC_2O, BCO_2, and B-O respectively (detail in table. A2 ; appendix A) [39,40]. Among these five configurations, boron atoms in B-B and BC_3 configuration are expected to substitute carbon atoms from the plane of lattice, whereas in BC_2O, BCO_2, and B-O configurations, the boron atoms are oriented along the out of plane direction assembled with the OFGs already present in sample during annealing and form such boronic groups. Interestingly, two major classifications of boron incorporation, i.e. substitutional and out of plane-incorporation, evolved with annealing temperature in opposite fashion as shown in Figure 2(b). It is revealed that the substitutional boron doping configuration, mostly as BC_3, increases with the annealing temperature whereas, the total amount of the out of plane boron atoms (BC_2O + BCO_2) decay to almost 70 % of its initial value found in the BG500 sample. This further implies that the in-plane doping effect is more likely to occur for the BG900 and BG1000 samples and one can achieve the out of plane boron population easily in the BG500 and BG700 samples. Variation of the percentage of sp^2 carbon (C=C), sp^3 carbon (C-C), and $\pi - \pi^*$ transitions with the annealing temperature is shown for both BG and TG samples in figure 2(c). More restoration of sp^2 carbon ring was observed in both the samples BG, TG, owing to more removal of sp3 bonded boron configuration from BG samples, and sp^3 bonded OFGs in TG samples with increasing annealing temperature. It is found that the amounts of sp^2 carbons in the BG samples are greater than that of the TG as boron diffusion in carbon lattice makes the lattice more graphitized than carbon self-diffusion does. Details about this diffusion process of boron and carbon in graphene lattice is discussed in next section. Due to restoration of hexagonal rings, the resonance of π- electrons is also reinforced as indicated in figure 2(c). Even after possessing better graphitization BG samples have lesser π-electron densities in comparison to the TG samples. This is because some of the π-conjugated electron densities are compromised during sharing of the electrons with the in-plane boron atoms located within the hexagonal ring with vacant P_z orbital.

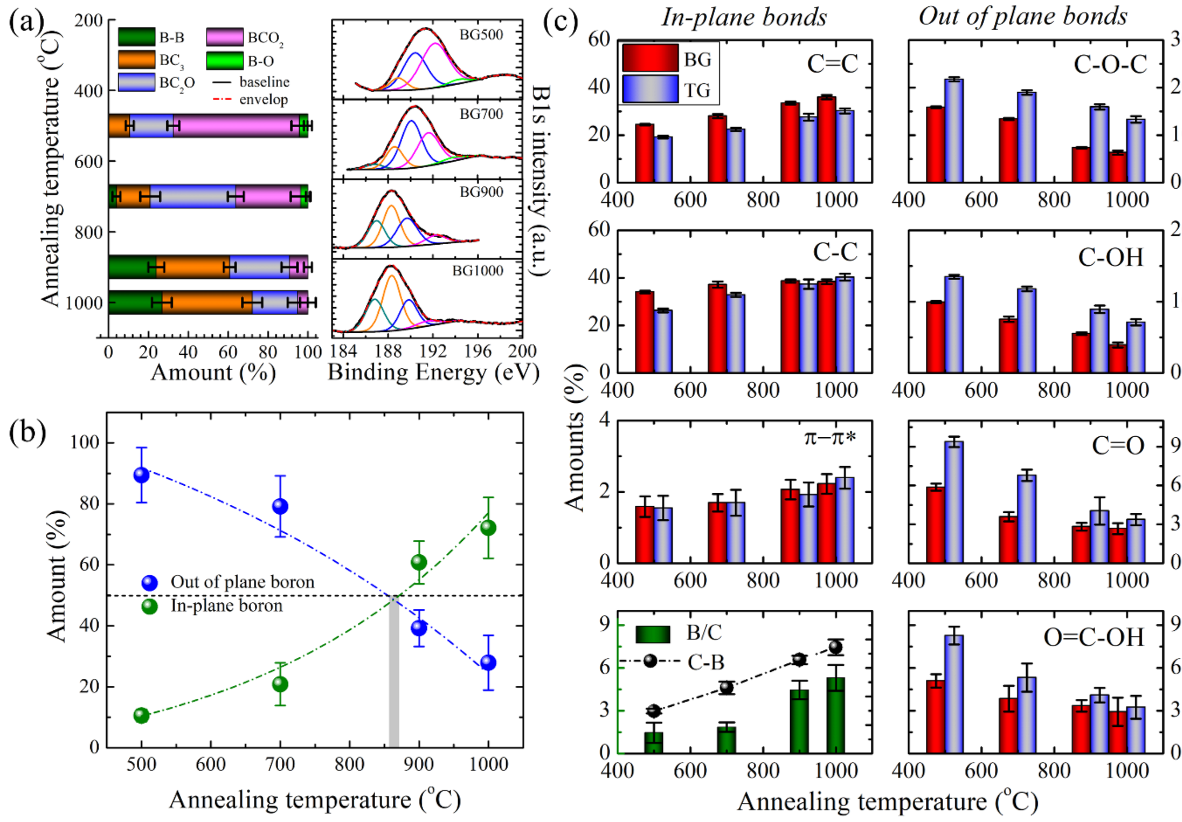

Figure 2. Derived parameters obtained for the BG and TG samples after deconvolution of the B1s, C1s peaks. (a) Amount of different components of boron groups present in BG samples and Deconvoluted spectra of B1s for all the BG samples, consisting of five component boronic configurations e.g. B-B, BC$_3$, BC$_2$O, BCO$_2$ and B-O.] (b) Left column; Evolution in amounts of the sp^2 and sp^3 hybridized carbon, π-electron transitions, carbon-boron (C-B) bonds and boron to carbon (B/C) ratio in BG and TG samples with the annealing temperatures. Right column; Degradation of the epoxy groups (C-O-C), hydroxyl groups (C-OH), ketone groups (C=O) and carboxyl groups (O-C=O) in respective samples with annealing temperatures. (c) Variation in amount of the in-plane boron and the out of plane configurations of boron with increasing annealing temperature.

Hence, π-electron densities in the BG samples are increasing at a slow pace in comparison to that of the TG samples. This increment of reconstructed π electron densities was hindered during the synthesis process temperatures of 900-1000 °C because of more inclusion of the boron atoms in the graphene plane. In our experiment, during the interplay between increasing graphitization and more inclusion of in-plane boron with increase of the annealing temperature, the percentage of *C-C* remain unaltered for BG samples. Whereas for TG samples, the percentage of *C-C* is high due to restoration of hexagonal ring at higher annealing temperature. Also, the percentage of the overall C-B percentage (%) in the C1s core level spectra for all BG samples, increase prominently with the rise of the annealing temperature, as shown in the figure 2(c). Scattered point representation shows the change in the atomic percentages (at.%) of boron present in the BG samples relative to the at.% of the carbon atoms, as indicated by the B/C ratio. The values of B/C ratio for BG500, BG700, BG900 and BG1000 are 1.5, 1.9, 4.5 and 5.3 respectively, are all in increasing order, ensuring more boron content in BG systems with increasing temperature

To probe the favourable site for the out of plane boron attachment in TG lattice, degradation of the OFGs through the reduction process was further observed in detail. Figure 2(c); right column, displays the temperature dependent removal of the OFGs for the BG and TG samples. In comparison to the TG samples, the C-O-C and C-OH functional groups have almost a similar rate of degradation in case of the BG samples during the annealing process. But the percentage of the C=O and O-C=O moieties in the BG samples are much lower than that of the TG samples at lower annealing temperature where out of plane doping occurs significantly. At higher annealing temperature, during substitutional doping, removal rate of the C=O and O-C=O groups in the BG samples become identical to that of the TG samples. Therefore, it can be predicted that the C=O and O-C=O bonds are more preferable sites for boron atoms to be attached over the lattice plane. Removal of OFGs by thermal treatment for both BG and TG samples indicate the proper reduction of both doped and undoped samples. Hence, lowering of the out of plane boron groups (BC_2O, BCO_2) and increasing of the in-plane boron (BC_3) with the elevation of annealing temperature along with the selection of site for out of plane boron attachment at lower annealing temperatures have been found through XPS analysis. To further understand the reduction level and the interaction with the doped graphene layers, XRD analysis has been discussed in next section.

4.3.2 XRD analysis:

In figure 3, the contraction of this interlayer spacing (d-spacing) primarily occurs because of the rearrangement of the out of plane boron atoms by substitutional boron atoms. Further lowering of the gap in doped sample takes place as the repulsive π-electron densities between the two adjacent layers are compromised with an increasing trend of the boron substitutional doping at higher annealing temperatures. Apart from the van der Waals interaction which helps to re-stack the exfoliated graphene layers [41], interaction between the π-electron densities of adjacent layers and the Poisson contraction effect [42,43] also play important role in changing the d-spacing value due to doping in graphene lattice after re-stacking. The van der Waal term is usually responsible for the contraction of adjacent layers in few-layer graphene whereas in the doped lattice this attractive interaction can be altered by π-electron interactions and change in lattice parameters. Besides this, the doping configuration of boron atoms in BG system can vary the interlayer distance. For substitution, incorporation of boron causes reduction of interlayer distance and reverse phenomenon can be observed for interstitial occupancy [44]. On the other hand, for the TG samples, d_{002} spacing is decreasing initially when samples were heated up to 700 °C, as most of the oxygen containing groups were removed at this annealing temperature. In figure 3(inset), the exponential decay curve (shown in black dashed line) has been plotted with the same decay constant as applied for the fitting of the exponential decrement of the oxygen content (O/C ratios) in the TG samples starting from graphene oxide during annealing (appendix A; figure A2). After that, d-value increases due to thermal expansion between graphene layers at very high temperatures [45] and then starts to saturate. Figure 3(inset) depicts that the interlayer distance of the TG samples obtained at higher temperatures are in good agreement with a linear term (red dashed line in figure 3 (inset)) proposed by Nelson & Riley [46], later modified [47] as,

$$d\ (nm) = 0.3328 + 8.63 \times 10^{-6} T + 5.538 \times 10^{-10} T^2 \tag{2}$$

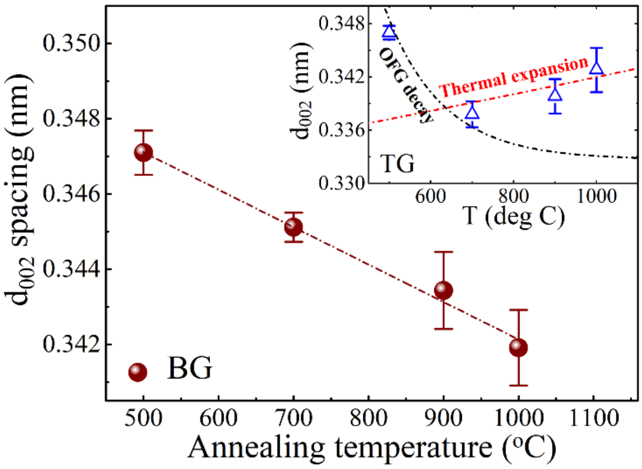

Figure 3. *d_{002}* spacing between graphene plane oriented with turbostratic layer in BG samples after deconvolution of the spectra (appendix A; figure A4(a)); [inset: d_{002} spacing for the TG samples. Red dashed line shows the thermal exfoliation curve and the blue dashed line shows the OFGs removal trend (appendix A; figure A2)].

, where T is the annealing temperature in °C. Another difference between the BG and TG lattice regarding the XRD spectra is the presence of the sharp graphitic peak found for the BG samples also at lower annealing temperatures, although they are absent for the TG samples (appendix A; figure A3). This observation validates the process of the atomic diffusion towards the vacancies present in the graphitic lattice through the thermal process. Some authors have commented both from experimental [48] and simulated results [49] that the diffusion constant of boron atom in hexagonal carbon lattice along the in-plane direction is much higher than the self-diffusion of carbon with lower the activation energy [49]. Hence, the degree of graphitization is substantially enhanced due to the presence of the boron atoms in graphene even at lower annealing temperature. However, the XRD results, in terms of interlayer distance, support the substitution doping of boron atoms into graphene lattice and also imply the removal of the out of plane boron groups in BG samples and OFGs in TG samples at lower annealing temperature. Moreover, along with the d-spacing, lack of π-electron density in BG lattice also plays a key role in bandgap reduction which is discussed in the context of the absorption spectra in the next section.

4.3.3 UV-Vis spectra analysis and ab-initio simulations:

Figure 4(a) shows the variation of the optical bandgap for all the samples. In case of Graphene Oxide (GO), presented in figure A5 [appendix A], a peak near 236 nm corresponding to $\pi - \pi^*$ transition is clear evidence of perfect oxidation in the graphite system [50]. A shoulder peak near 296 nm can also be observed for the GO sample due to the transition of the non-bonding electrons from n–level (non-bonding) to π^* (anti-bonding state) [51,52]. Non-bonding electrons are congregated here due to the presence of the OFGs in the system. However, this peak originated from the $\pi - \pi^*$ transition in GO, and then further blueshifts ~ 272 nm due to the reduction process [50,53]. This peak is attributed to the C=C bonding present in the graphene sample. Absorption peaks near 272 nm for all the BG and TG samples, as shown in figure A6 [appendix A] & figure 7 respectively, confirm the proper reduction of the graphene structure. Now for the TG samples, the peak corresponding to the $\pi - \pi^*$ transition is red-shifted with more degree of reduction which indicates more removal of the OGFs from the system at higher annealing temperature. To understand the red-shifting of absorption band maxima and hence the reduction of bandgap for TG samples one can consider Woodward-Fisher rule where more conjugated graphene system can lead to the shifting of absorption maxima to higher wavelength [54]. Physical interpretation of this rule can be elucidated considering one dimensional quantum well problem, mostly applied for nano-crystallites. In such systems, bandgaps are inversely proportional of the crystallite sizes, i.e. the sizes of the sp^2 cluster [55].

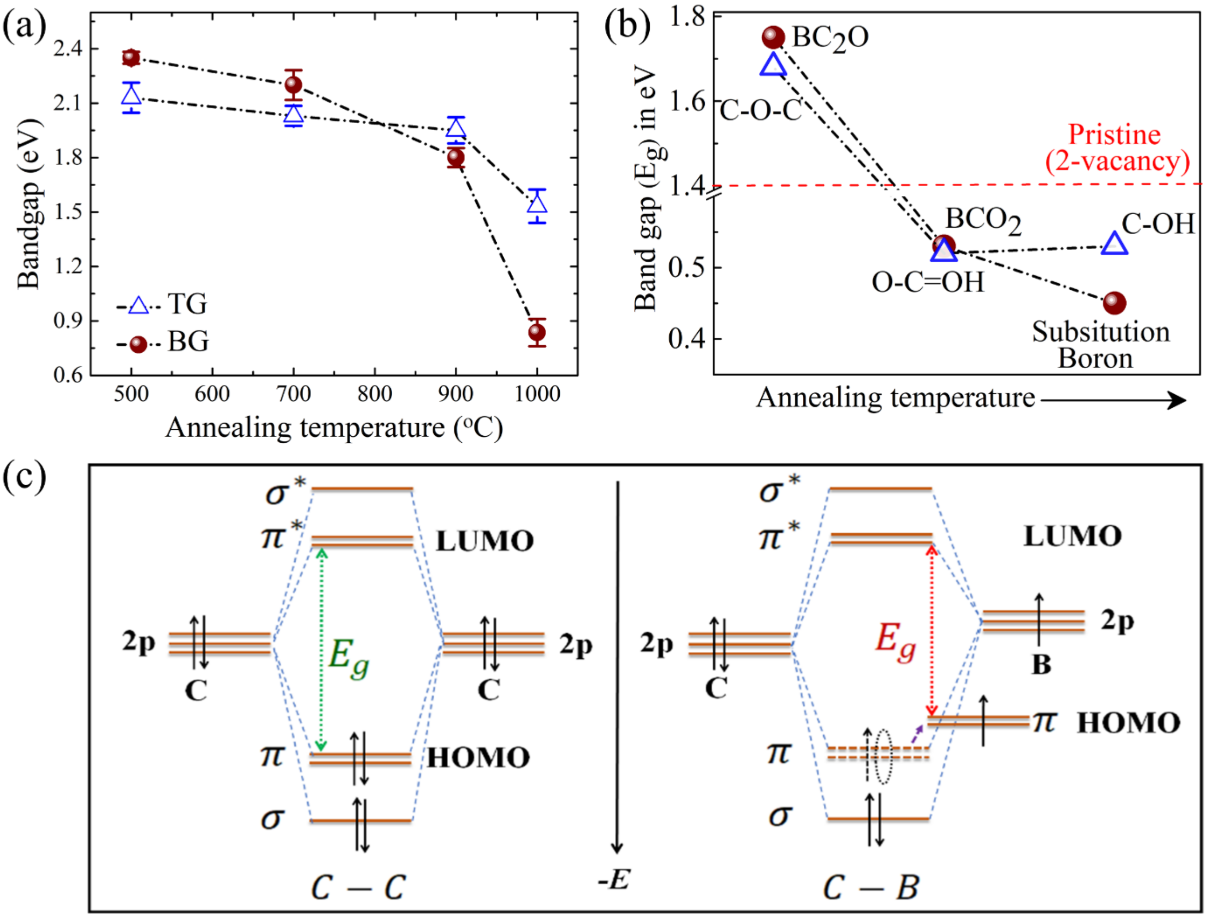

Figure 4. (a). Variation of bandgaps obtained by analyzing the UV-VIS absorption spectra for BG and TG samples while maintaining uniform concentrations (appendix A; figure A6 & A7). (b) Theoretically obtained bandgap from DOS for each system (bonding configurations) as considered. (c) Schematic diagram comparing the molecular orbital structures considering C-C and C-B bonding configurations independently. Only 2p orbital of Boron and Carbon atoms has been considered here. E_g represents the bandgap between energy states the HOMO and LUMO states.

Here in case of the TG samples, more withdrawal of the OFGs reinstates sp^2 clusters with more dominance of $\pi - \pi^*$ conjugated electrons, as depicted in figure 2(c), that finally reduces the π-π^* bandgap. For BG samples, similar diminution of the bandgap with the elevation of the annealing temperature can be observed due to the removal of the out of plane boron groups in conjunction with oxygen atoms, i.e. BC$_2$O and BCO$_2$. More substitutional doping, however less, re-develops the Csp^2 domain, as demonstrated in figure 2(c), which causes the reduction of the bandgap in BG samples. In spite of the similar variation of bandgaps for both doped and undoped samples endorsed well by the amount of π-conjugations and sp^2 cluster sizes, anomalous criss-cross nature of bandgap variation between

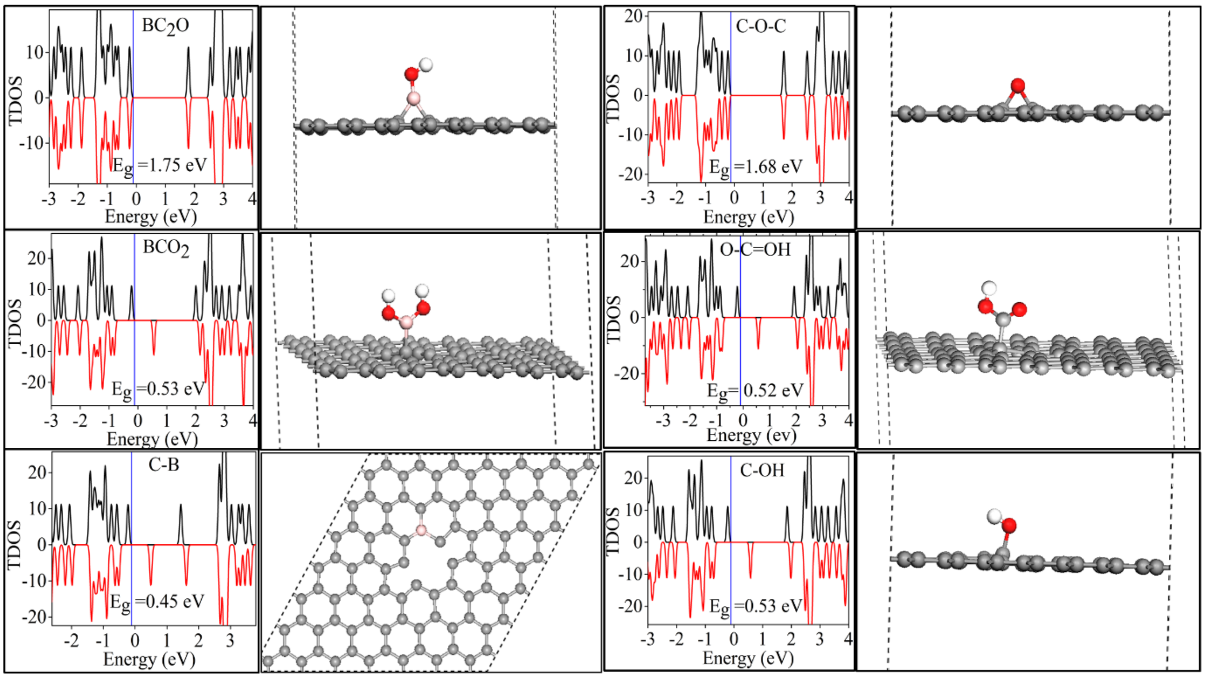

Figure 5. TDOS for the BG and TG lattices with the different boronic (BC_2O, BCO_2, C-B) and OFG (C-O-C, O-C=OH, C-OH) bonding configurations. Corresponding crystal structure is shown at the right side of each TDOS plot where pink, gray, red & white spheres in the figure are for boron, carbon, oxygen & hydrogen atoms respectively. (DOS for the pristine graphene lattice with double vacancy is demonstrated in figure A8 [appendix A]).

TG and BG samples has been detected. This anomaly can be explained by estimating the shift of the Highest Occupied Molecular Orbital (HOMO) state due to boron substitution. Much lowering of optical bandgap value for BG sample at higher temperature can also be explained by considering the upshifting of HOMO level due to inadequacy of one electron in π-orbital (bonding) in boron atom while bonded with only carbon atom, as explained in fig 4(c). Here, for carbon-carbon bond, *2p* valance shell of each carbon atoms shares two electrons to completely fill the σ level and half-fill π level. For the in-plane C-B bond, B-*2p* having only one electron making a deficiency of electron in π-level, which compel to up-shift that π level assigned as HOMO and ends up with reduction of $\pi - \pi^*$ transition gap [56]. In contrast, sufficient number of electrons in HOMO levels restored due to the carbon-carbon bond formation in TG900 and TG1000 lattices partially ceases the bandgap reduction. To validate the above explanation, the bandgaps of BG samples containing major boron group configurations as well as of TG samples containing OFGs have been calculated by plotting the DOS with the help of ab-initio simulation. As the boron groups attached to the graphene lattice evolved with temperature, it can be assumed that each boron group based on major occupancy plays significant role to attenuate the bandgap of the whole system. Hence from XPS analysis, majority of the boron group (OFG) with the elevation of annealing temperature has been estimated. For example, at lower temperature BC_2O group takes the lead and after that BCO_2 and finally the substitution of boron has the majority inside the lattice (figure 2(a)). On the other hand, TG lattice are populated with epoxy groups at lower temperature and then with the C=O groups at the mid-range of annealing temperature and finally at 1000 °C the TG lattices are left with some hydroxyl (-OH) groups as amount of this functional moiety is increasing with temperature as shown in figure 2(c). So, on that basis, DOS calculations of graphene containing those particular groups have been performed as demonstrated in figure 5. From these calculations, bandgaps of corresponding configurations are plotted with increasing annealing temperature in figure 4(b). These bandgap values obtained from the ab-initio simulation reveal a similar trend, maintaining the criss-cross nature as seen in experimental curves from figure 4(a). Another aspect of this trend can be explained by XRD results, where a sharp graphitization peak was obtained for the BG samples (figure A3 ; appendix A). As the boron atoms help to re-develop the in-plane crystallization due to the higher diffusion rate of boron than carbon as discussed in XRD section. This causes more reduction of bandgap of BG lattice than TG samples. Hence, all the arguments simply indicate that the out-of-plane boron configurations have higher optical bandgaps which exceed the reference level made by TG samples. While with the elevation of annealing temperature, BG samples containing more in-plane boron atoms reduce the bandgap of the doped graphene sample below the reference level (TG samples).

4.3.4 Raman analyses:

Full Raman spectra for both doped and the undoped samples are demonstrated in figure 6 (a) & (b) respectively. The D and G peaks are prominent here, ensuring the presence of defects in all samples. To know the defect type these first order peaks of all samples are deconvoluted into five components, as depicted in figure 6(c). Furthermore, four-component deconvolutions of the 2D band are also observed for all the samples (figure 6(d)), which confirm the few-layered structure of the graphene samples. Genesis of phonon-defect bands such as D and D’ can be understood by defect-induced Double Resonance (DR) process [57,58,61]. Under excitation, electron-hole pairs are generated with a momentum $q \neq 0$ (at the corner of Brillouin zone; K or K’) due to defects present in lattice and scattered twice in the DR process.

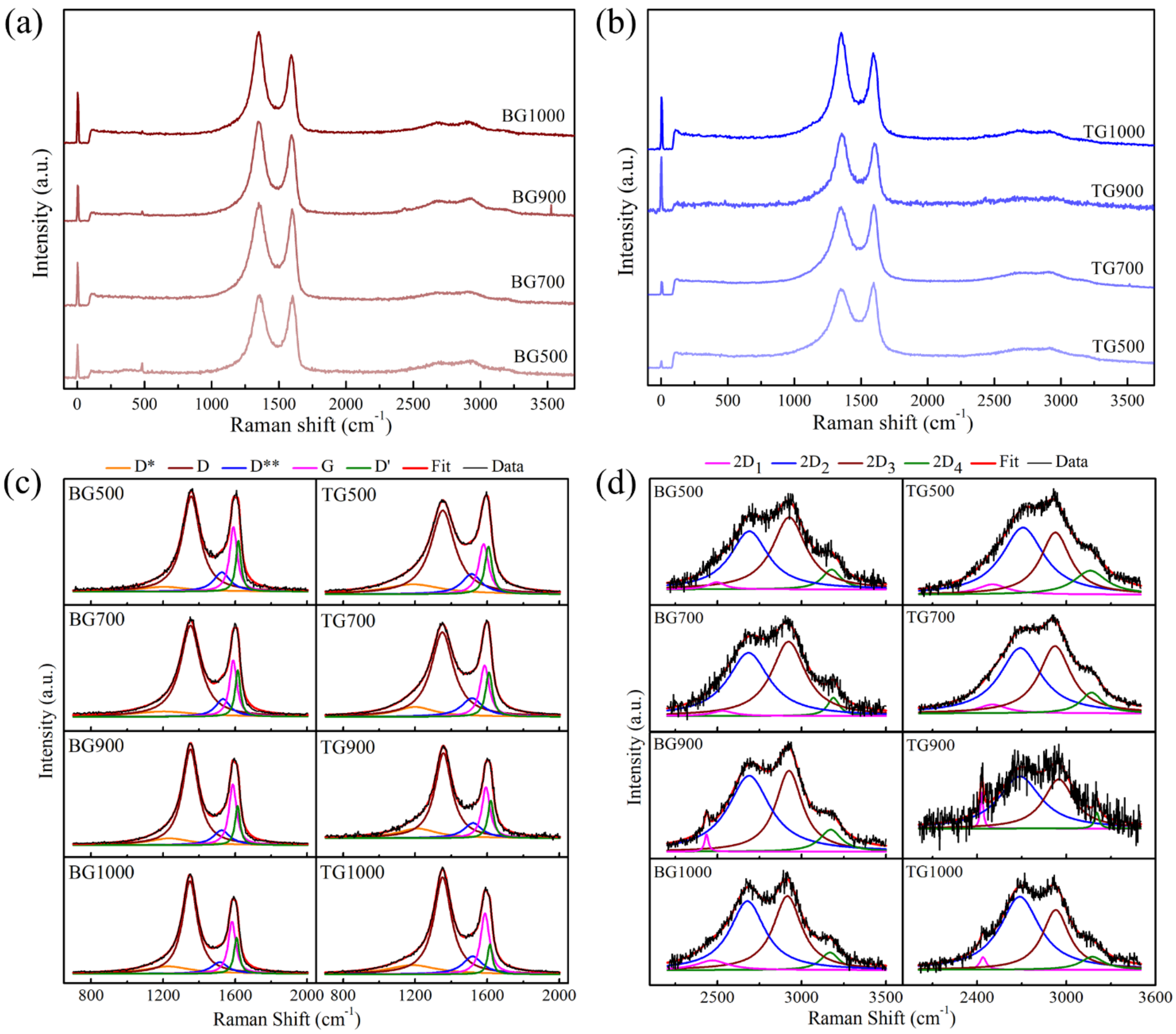

Figure 6. Full range Raman spectra for (a) BG and (b) TG lattice derived with different annealing temperatures varied from 500^{o}C to 1000^{o}C. Deconvoluted Raman spectra consist of (c) first order and (d) second order components for all BG and TG samples. Black lines are the original line shape as obtained from spectrometer and rest of the colors represent the contributions of different bands.

For the first time, they are scattered with phonons with exchange of their momenta, which leads to creation of phonons. After that, another secondary scattering process occurs due to collision with defects, which recombines the electron hole pairs in the system. This process is called phonon-defect process that out-turns as phonon-defect bands i.e. D (Intervalley DR process) and D’ (Intravalley DR process) bands in only defected system [59,60]. This process is found in defected system only. Another DR process, called phonon–phonon process can be found in graphene lattice by scattering of those pairs twice where the phonons are emerged with opposite wave vector $+q$ and $-q$, keeping resultant $q = 0$, both times. In pure crystal this process can always occur and 2D peak arises consequently [61]. Later in this paper, the evolution of 2D peaks due to doping of boron atoms has been discussed. Now, to analyse the defect concentration and defect type in those BG and TG samples, phonon-defect lines are considered for discussion.To know the types of defects and quantification of the same due to boron incorporation into graphene lattice and also to understand the effect of annealing treatment on oxygenated graphene, one should take the ratios of maximum intensities of the D and G peaks (I_D/I_G), and the ratios of the maximum intensities of the D and D' peaks ($I_D/I_{D'}$) into account. As reported by Venezuela et. al., there are three types of defects found in graphene system [61]. One of them is the hopping defect that describes the deformation of the carbon-carbon bonds while retaining the sp^2 hybridization intact. This type of defect can be seen in graphene lattice due to the presence of vacancies or point defects [62,64]. Another example of the hopping defect is the Stone-Wales (SW) defect that requires a rotation of the two sp^2 bonded carbon atoms by 90° with respect to the midpoint of this bond [63]. Finally, there is the on-site defect which is related to the out of plane atoms bonded to the carbon atoms lying in-plane to the lattice with sp^3 hybridization [64]. In this system, some atoms or some functional groups can be chemically bonded with sp^3 hybridization which could be aligned mainly outside to the graphene plane. Contributions from these two types of defects are quantified by the intensities of the D peaks in most cases. Additionally, one more type of defect can be observed in graphene system termed as the Coulomb impurities which are basically some charged particles getting adsorbed at some height above the graphene sheets [61,64]. These coulomb impurities cannot affect the D peaks as the potential remains maximum near to the Γ point in the momentum space, where the phonons corresponding to the D peaks are closer to the K point in graphene's Brillouin zone (BZ) [65,66]. It is reported that the phonons associated with the D' peaks are closer to Γ point in BZ and are more interactive with the charged impurities, though undetectable, present within graphene samples [61]. Therefore, the I_D/I_G ratios can be used to observe the variation of the defect concentrations where the type of defects can be probed by measuring the ratios of the intensities of D and D' peaks ($I_D/I_{D'}$). The intensities of the G peaks are considered here to be the reference intensities and remained unaltered compared to the defect band intensities as it comes from simply the in-plane E_{2g} mode of vibration of the carbon atoms [67,68].

Here the variations of the I_D/I_G ratio of all TG and BG samples have been plotted in figure 7(a). The I_D/I_G ratios for the doped BG samples are clearly increasing, whereas for the undoped TG samples these are decreasing. In this scenario, one can expect

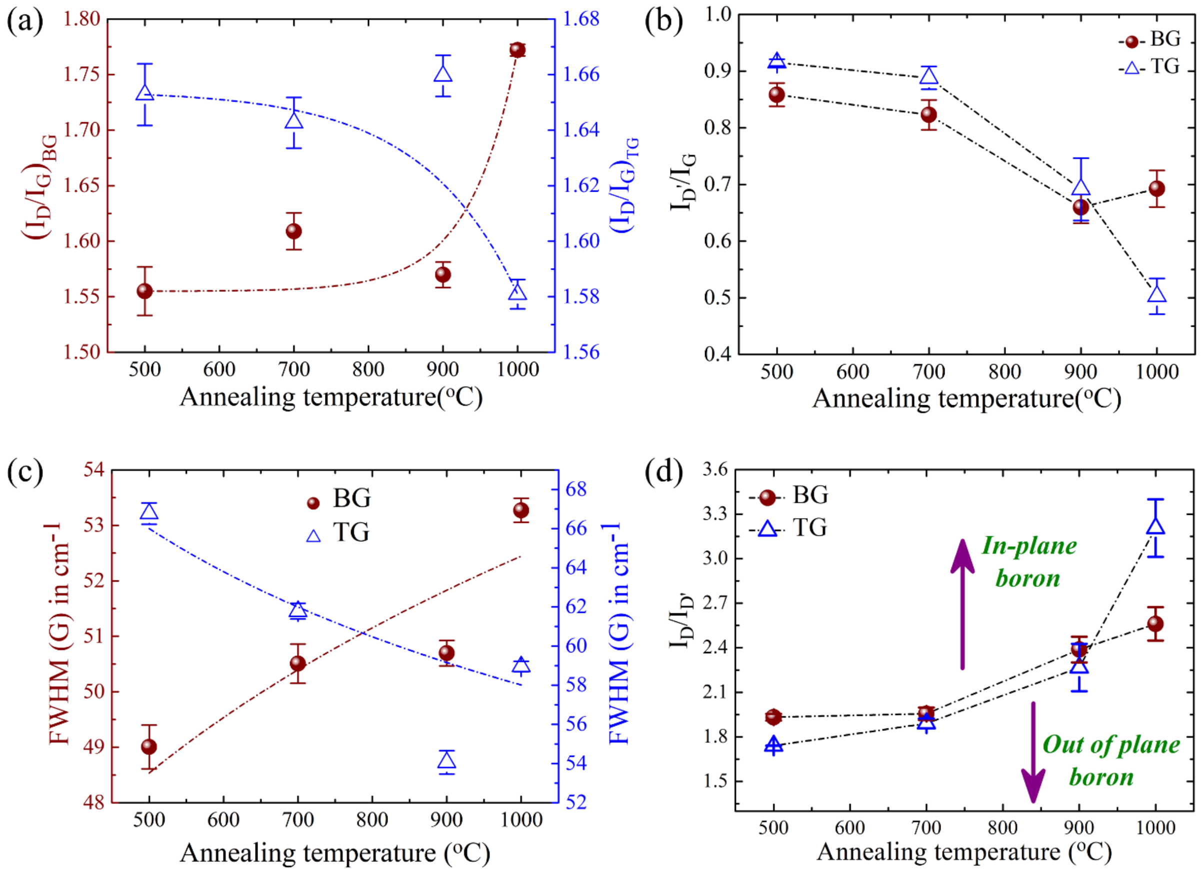

Figure 7. Raman analysis for BG and TG samples. (a) Variations of I_D/I_G ratios for BG and TG samples synthesized at different temperatures is plotted. (b) Decrement of $I_{D'}/I_G$ ratios for BG and TG samples synthesized with increasing temperatures is shown. (c) FWHM of G band is plotted after deconvolution for TG and BG samples in y-axis against annealing temperature (d) Shifting of the $I_D/I_{D'}$ values for the different doped and undoped samples is shown as a function of annealing temperature.

that the increment, clearly observable for the BG samples with higher doping concentration, is due to more defects induced in graphene network at higher annealing temperatures. On the other hand, in case of the TG systems, having an exponential fall of the I_D /I_G ratios with annealing temperature, are supposed to have less disorder in comparison. To verify this notion, the values of the FWHM (G) are also plotted against the annealing temperature for both BG and TG samples. It is well known that the FWHM (G) always increases with increasing disorder [69,70]. Decrement of FWHM (G) for the TG samples, as observed in figure 7(c), attributes to the narrowing of the G bands which implies the reconstruction of defect-free lattices during annealing process at higher temperatures. Obviously in the BG lattices, broadening of G peaks indicates the enhancement of disorder with increasing boron content annealed at higher temperatures. However, enhancement of I_D/I_G and broadening of FWHM (G) confirms more inclusion of defects into BG lattice, with the elevation of annealing temperature.

For further realization of complexity of boron doping, the intensity ratios between the D’ and G peaks ($I_{D'}/I_G$) have been plotted against the annealing temperature in figure 7(b). As it is already stated that the D’ peaks are sensitive to the charged impurities in the system, the deviation of the $I_{D'}/I_G$ ratios help to comment about the third type of defects as mentioned earlier. From figure 7(b), it is evident that in the TG samples, thermal treatment at higher temperatures contributes to lower occupation of the OFGs, acting as Coulombic impurities that reside over the graphene sheets, with $I_{D'}/I_G$ ratios sharply falling with temperature. On the contrary, for the BG samples, there are also decrement in the $I_{D'}/I_G$ ratios, indicating the replacement of the out of plane boron groups by in-plane graphitic boron. Interestingly, for the BG samples decrement of the $I_{D'}/I_G$ ratio is almost linear, rather than exponential, due to slow removal of the BCO_2, BC_2O and C-O-B groups and induction of the BC_3 configuration in the lattice. Consequently, it can be stated that, with changing of the doping configurations with respect to the temperatures is not specified by any kind of distinct transition, but rather as a continuous process of substitution in this case.

Previous reports have shown mainly two stages of evolution in the I_D/I_G ratios for the graphene samples based on defect concentration [71,72]. For low defect concentration, the I_D/I_G ratio varies inversely to the square of average of inter-defect length, in short, defect length (L_D) in *sp*^{2} carbon lattice (stage-I). For higher concentration of defects, these I_D/I_G ratios become proportional to the $(L_D)^2$ (stage-II). In other words, the I_D/I_G ratio is proportional with defect density (n_D) for stage-I and varies inversely with $(n_D)^2$ for stage-II. In this regard, increasing I_D/I_G ratio, as well as the FWHM (G) with more boron doping follows the evolution of those parameters as indicated for stage-I [64,72,57]. Eventually, defects in the TG samples describe the same path of evolution and thereby aligning our interest to both TG and BG systems with lower density of defects as obtained.

In their Seminal work, Tuinstra and Koenig introduced an equation for the graphitic carbon system with lower defect concentration, where in-plane crystallite size (L_a) depends on the I_D/I_G ratio in a particular manner as follows: $I_D/I_G = C(\lambda)/L_a$, where $C(\lambda = 515.5\text{ nm}) = 4.4\text{ nm}$ [73,57]. This relation was modified later by Lucchese et. al. for point defect like vacancies created in graphene lattice by ion bombardment where the I_D/I_G ratio is inversely proportional to the square of the inter defect distance (L_D) [71]. In this model, the defect sites are termed as impact points which are surrounded by two circular areas with radii r_A and r_S. The inner circular region, where defects are formed, is called the structurally disordered region (characterized by r_S) and the outer part where lattice structure remains unperturbed but mixing of the Bloch states takes place near K and K' valleys in BZ of graphene lattice due to proximity of impact points, is called the activated region (characterized by r_A). This phenomenal model, in particular, is fitted well for higher concentration of defects where Tuinstra-Koenig (T-K) relation fails to explain the decrement of I_D/I_G ratios with increasing defect densities. However, for lower concentration of defects, Lucchese's model comes into a good agreement with the T-K relation when only considering the line defects e.g. edge defects, rather than point defects, where L_a is in nanometer scale [71].

Another approach for estimating the defect types is illustrated in the figure 7(d), where the $I_D/I_{D'}$ ratios, associated with both the doped and the undoped samples, are plotted against the annealing temperature. As per our interest at stage-I, both defect-phonon peaks D and D' commensurate with the defect density, n_d. as $I_D \sim A_d n_d$ and $I_{D'} \sim B_d n_d$, where A_d and B_d both are constants and depend upon the type of perturbations introduced through the defects inside the lattice [64]. Hence, the $I_D/I_{D'}$ ratios become $I_D/I_{D'} \sim A_d/B_d$, independent of concentration of defects and only depend on type of defects inside the crystal. As per report, for onsite defects, the $I_D/I_{D'} \approx 13$, becomes maximum and for hopping defects, the $I_D/I_{D'} \approx 7$, and for boundary defects, the $I_D/I_{D'} \approx 3.5$, becomes minimum [64]. Here Eckmann. et. al. suggest that in graphene system lattice with sp^3 bonds like OFGs and out of plane boron groups are not only create the on-site defects but also produce a crystal deformation which changes the hopping parameters. Therefore, these types of defects persist in the lattice as a combination of both on-site and hopping defects. In addition, the charges present in those groups can contribute as coulomb impurities in the lattice. In that case, theoretical calculation claimed that value of $I_D/I_{D'}$ ratio of about 1.3 describes the onsite defects and the value of about 10.5 describes the hopping defects [61,64]. In our study, the value of $I_D/I_{D'}$ ratio for TG system this value shifts from 1.7 to 3.2 with increasing annealing temperature while the BG system shifts from 1.8 to 2.6 with increasing the doping density or annealing temperature. This increment of the $I_D/I_{D'}$ ratios with the annealing temperatures clearly indicates that the out of plane boron atoms (as on-site defects) are being removed and more in-plane boron atoms (as hopping defects) are substituting in the BG samples with increasing annealing temperature. For the TG samples, it is similar to the OFGs are removed from the systems at high temperature and some hopping defects e.g. vacancies dominate the lattice structure, obtained after the removal of the OFGs. Finally, in TG1000, maximum I_D /$I_{D'}$ implies the least amount of on-site defects as expected. So, we can summarize the facts regarding the defects in the BG and TG samples as: (1) Evolution of the I_D/I_G with temperature, henceforth with doping concentrations, follow stage-I, which indicates that the samples contain lower density of defects. (2) Evolution of the $I_{D'}/I_G$ similarly with the doping density confirms that out of plane boron atoms are having Coulombic contributions as defects to the BG lattices, whereas the OFGs have the same for the TG lattices. (3) $I_D/I_{D'}$ ratios are suggesting that the on-site defects are replaced by hopping defects for both BG and TG samples, where the onsite defects for BG samples are the out of plane boron configurations, i.e. BC_2O, BCO_2, C-O-B and for the TG samples those are the oxygen functional groups. On the other hand, the in-plane BC_3 graphitic boron configuration is categorized as hopping defects in the BG samples while the vacancies are playing the main role as hopping defects in the TG samples. (4) T-K relation defining the I_D/I_G as a function of crystallite size, L_a, still should be satisfied for corresponding parameters of our samples. As the relation between the I_D/I_G and L_D, as mentioned for stage-I, matches well with the T-K relation for lower concentration of one-dimensional defect (line defect) as we have obtained in the TG lattices.

To verify the last statement, the in-plane crystallite sizes are calculated for all samples from the XRD pattern considering the peaks near $2\theta = 43^\circ$. Those peaks are deconvoluted into two with the values of $2\theta = 42.5^\circ$ and $2\theta = 43.2^\circ$ by Voigt functions as presented in figure A4(b) [appendix A]. These two peaks correspond to the (100) and (101) planes respectively [74]. As graphitic substitution of boron in the BG samples and vacancies in the TG samples mainly affect the in-plane lattice in the direction of normal to the (100) plane, crystallite sizes of the BG and the TG lattices were measured (using Eq. 1) considering only these (100) planes for all samples. Figure 8(a) demonstrates the compatibility of the values of the crystallite sizes obtained from the XRD spectra for the TG and the BG samples with those values calculated from the T-K relation theoretically using the following equation which is moderately improved by Cancado et. al. [75] as:

$$L_a(nm) = \frac{(2.4\times10^{-10})\lambda^4}{\left(\frac{I_D}{I_G}\right)} \tag{3}$$

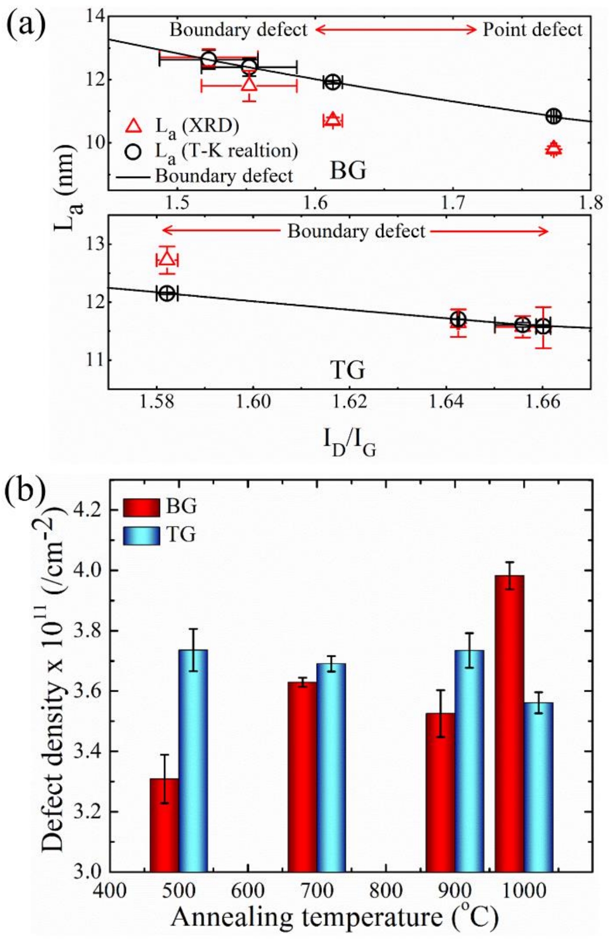

Figure 8. (a) Correlation between the in-plane crystallite sizes (L_a) to the I_D/I_G ratios for the BG and TG samples is shown. Values of L_a are calculated from the XRD measurements (figure A4 (b) ; appendix A) and the I_D/I_G ratios are considered from the Raman spectra. (b) Different values of defect concentrations measured for the BG and TG samples using Eq. 4.

In our experiment, the BG900 and BG1000 samples have deviated from the T-K equation and this disagreement is less in case of the BG500 and BG700. Overall slope for the experimentally collected L_a values is slightly steeper than those for the theoretically calculated using the T-K equation. From this observation, one can say intuitively that the defects due to boron incorporation into graphene plane are more like point defects (as deviated from the T-K equation) which may have some intention to follow the relation, I_D/I_G = $1/(L_D)^2$, proposed by Lucchese et.al. On the contrary, In TG samples, experimentally obtained L_a values are fitted well with T-K equation as most of the defects in the TG samples are boundary defects due to remaining of hydroxyl groups (C-OH) attached at the edges of graphene sheets even at 1000°C. Considering the boron incorporation into graphene lattice as point defect, we have calculated the defects densities, $n_{D,}$ using equation [72],

$$n_D(cm^{-2}) = \frac{(1.8\pm0.5)\times10^{22}}{\lambda^4}\left(\frac{I_D}{I_G}\right) \tag{4}$$

for all samples as shown in figure 8(b). From this figure, it is noticed that the defect densities in the BG samples are increasing with annealing temperature according to our intension. while for the TG samples doping concentrations are decreasing inevitably with increasing annealing temperatures.

Effects of boron doping in graphene can be probed with another perspective by comparing the G and 2D band frequencies of the BG and the TG samples. For nitrogen-doped graphene, the authors have come up with a consensus that doping with nitrogen atoms increases the electron density (n-type) and introduces a compressive strain in graphene lattice [76]. On the contrary, incorporation of boron as foreign atoms can have different outcomes. In brief, proposed consequences due to doping of the boron atoms into graphene lattice are as follows: (1) some have demonstrated that this doping phenomenon as a simple method to incorporate p-type charge carriers in graphene lattice as boron contains single deficiency of electron while bonded with sp^2 hybridization in its excited state [77]. In case of doped graphene, the Fermi surface changes according to non-adiabatic Born-Oppenheimer Approximation (ABO) and that shifts the Kohn anomaly from Γ and K point as well in reciprocal space. So, changes of the Fermi surface from that anomalous lowest point (Kohn anomaly) with $q = 0$ results as stiffening of E_{2g} mode, hence the G peak [78]. Authors have plotted the G band frequencies as a function of electron and hole concentration due to doping [78]. In their work, Pos(G) is shifted up because of increasing both electron and hole concentration in graphene. Similarly, boron doping can be considered as a source of hole gas, thus Pos(G) value can increase with increasing doping concentration. This type of doping can also be achieved by intercalating electron acceptor or electron donor molecules over graphene surface. Charge transfer between graphene sheets and intercalated molecules can make the surface hole or electron doped [79]. (2) On a separate note, Kim et. al. investigated the substitutional boron doping that causes tensile strain generated inside the lattice [80]. Several Raman analyses of strained two-dimensional lattices, especially, graphene, claim the redshifting of G band frequencies with increasing tensile strain while boron percentage was increased [19,81]. Longer bond length of C-B in boron doped graphene than that of C-C in pristine sample also induces this tensile strain within the lattice.

In our case, to eliminate the above conflict, investigation of the doping effects is performed by a simple relative study of the G and the 2D band frequency. Here in figure 9, ΔPos (2D) vs. ΔPos (G) for BG and TG samples are plotted where the actual shift in

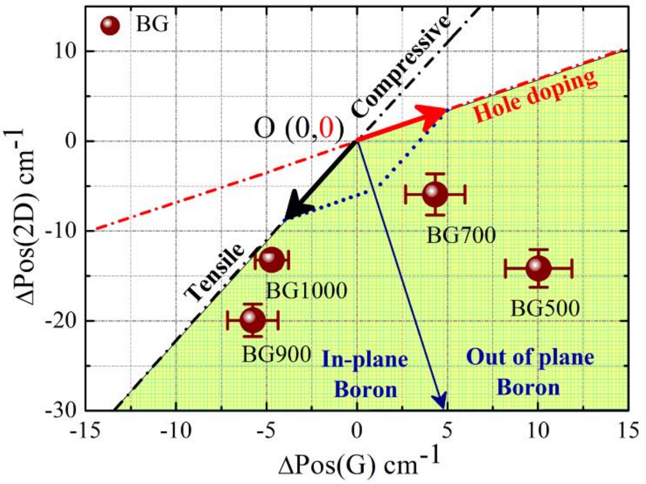

Figure 9. Representation of ΔPos (2D) vs. ΔPos (G) plot for BG samples. ΔPos (2D or G) is obtained by considering the real shift found in BG samples with respect to TG system at a particular annealing temperature. Black dashed line is the axial representation of the effect of strain and red dashed line is the same of effect of hole doping. Corresponding black and red arrows are the representation of unit vectors [81] for those effect's directions respectively. Blue solid line shows the resultant effect of hole as well as tensile strain on frequency shifts, where effects of both hole and strain are equal.

frequencies of G and 2D bands are obtained by taking the differences between the frequencies of BG samples and those values for the reference TG samples at corresponding temperature. Now, it is fact that effect of elemental doping in graphene can be decomposed in two consequences as variation in hole concentration and formation of strain lattice. Previous report also states that two consequences individually display a steady variation of ΔPos (2D) w.r.t. to ΔPos (G) with a particular slope, i.e. for hole, it is ~ 0.7 and for strain, it is ~ 2.2 [81,82]. Therefore, for boron doping, the combined effect (the frequency shift) can be deconvoluted in two compositions along the direction of variations of the frequency shifts due to hole and strain as the axes. In figure 7(a), boron doped samples are found in the fourth quadrant (color shaded area) in axial representation of hole doping and strain effect. This confirms the p-type doping of graphene associated with small amount of tensile strain due to boron inclusion where the strain contribution in lattice is due to enlarged C-B bond length. Therefore, doping of boron atoms can induce defect as well as strain in graphene lattice apart from its charge carrier contribution. From this result, apart from the doping related analysis, It is also justified that strain dominancy in shifting the G and 2D comes into picture for higher number substituted boron atoms into graphene lattice, as claim in ref. [80]

4.4 Conclusion

In summary, boron doped graphene sheets were synthesized and the aspect of doping density as well as their different configurations have been analysed as a function of increasing annealing temperature. Additionally, transition from on-site to hopping configuration of defects was also observed with increasing doping concentration. Thermal annealing of the samples was done mainly to substitute the carbon by boron atoms for achieving the desirable BC_3 configuration. However, other configurations of boron atoms i.e, BCO_2 and BC_2O, mostly situated at the edge or the out of the plane lattice, have been achieved by simply tuning the annealing temperature. Higher annealing temperature created higher population of BC_3 configurations i.e., graphitic substitution in the lattice, while at lower temperatures other BCO_2 and BC_2O groups were accumulated in out of plane sites.

Henceforth, by using simple spectroscopic techniques, the effect of boron doping on reduced graphene can be summarized as; The C=O & -O-C=O groups have been identified for out of plane boron attachments as the most favourable sites among the OFGs. Furthermore, anomalous ‘squeezing’ of the bandgap for the BG samples is in good agreement with the occurrence of the substitutional doping produced at temperatures higher than 900 °C. The contrasting relationship between the undoped (TG) and the doped (BG) samples regarding the amount of C sp^2 and π-conjugated domains become more prominent in case of the substitution doping than the out of plane boron attachment due to more presence of the C-B bond in the BG samples when prepared at higher temperature.

Estimation of the in-plane crystallite sizes, d- spacing in the BG and TG samples have been utilized to substantiate the low defect concentration present in the samples. Finally, Raman spectroscopy measurements confirmed the p-type charge contribution of the doped samples by inspecting the slope of ΔPos (2D) vs. ΔPos (G).

Finally, next to the type of charge carrier, point defects have also appeared as an added effect with subtle manifestation of strain. More inclusion of boron into lattice produced more defects within graphene system. Hence, for future purposes and novel applications, many aspects such as the band structure, phonon dispersion and the defect profile, can be adjusted with these p-type BG systems consisting of point defects and explored further.

References

[1] H. P. Boehm, A. Clauss, G. Fischer, and U. Hofmann, Surface properties of extremely thin graphite lamellae, *In Proceedings of the Fifth Conference on Carbon, Pergamon* (1962) pp. 73-80. DOI : 10.1016/B978-0-08-009707-7.50013-3

[2] K. S. Novoselov, A. K. Geim, S. V. Morozov, D. Jiang, Y. Zhang, S. V. Dubonos, I. V. Grigorieva, and A. A. Firsov, Electric Field Effect in Atomically Thin Carbon Films, Science **306**, 666 (2004). DOI : 10.1126/science.1102896

[3] D. Usachov, O. Vilkov, A. Grüneis, D. Haberer, A. Fedorov, V. K. Adamchuk, A. B. Preobrajenski, P. Dudin, A. Barinov, M. Oehzelt *et al.* Nitrogen-Doped Graphene: Efficient Growth, Structure, and Electronic Properties, Nano Lett. **11**, 5401 (2011). DOI: 10.1021/nl2031037

[4] L. Tsetseris and S. T. Pantelides, Graphene: An impermeable or selectively permeable membrane for atomic species?, Carbon **67**, 58 (2014). DOI: 10.1016/j.carbon.2013.09.055

[5] M. Telychko, P. Mutombo, M. Ondráček, P. Hapala, F. C. Bocquet, J. Kolorenč, M. Vondráček, P. Jelínek, M. Švec, Achieving High-Quality Single-Atom Nitrogen Doping of Graphene/SiC(0001) by Ion Implantation and Subsequent Thermal Stabilization, Acs Nano, **8** 7318 (2014). DOI: 10.1021/nn502438k

[6] L. Zhao, M. Levendorf, S. Goncher, T. Schiros, L. Pálová, A. Zabet-Khosousi, K. T. Rim, C. Gutiérrez, D. Nordlund, C. Jaye *et al.* Local Atomic and Electronic Structure of Boron Chemical Doping in Monolayer Graphene, Nano Lett. **13**, 4659 (2013). DOI: 10.1021/nl401781d

[7] S. -M. Jung, E. K. Lee, M. Choi, D. Shin, I. -Y. Jeon, J. -M. Seo, H. Y. Jeong, N. Park, J. H. Oh, and J. -B. Baek, Direct Solvothermal Synthesis of B/N-Doped Graphene, Angew. Chem. Int. Ed. **53**, 2398 (2014). DOI: 10.1002/anie.201310260

[8] D. Deng, X. Pan, L. Yu, Y. Cui, Y. Jiang, J. Qi, W.-X. Li, Q. Fu, X. Ma, Q. Xue *et al.* Toward N-Doped Graphene via Solvothermal Synthesis, Chemistry of Materials **23**, 1188-1193 (2011). DOI: 10.1021/cm102666r

[9] Q. Zhu, J. Yu, W. Zhang, H. Dong, and L. Dong, Solvothermal synthesis of boron-doped graphene and nitrogen-doped graphene and their electrical properties, Journal of Renewable and Sustainable Energy **5**, 021408 (2013). DOI: 10.1063/1.4798484

[10] J. Han, X. Zhao, L. Zhang, S. Lee, J. Oh, K. S. Lee, J. R. Potts, J. Ji, X. Zhao, R. S. Ruoff and S. Park, Generation of B-doped graphene nanoplatelets using a solution process and their supercapacitor applications, ACS Nano **7**, 19 (2013). DOI: 10.1021/nn3034309

[11] E. Santos, A. Ayuela, S. Fagan, J. Filho, D. Azevedo, A. Filho, and D. Sánchez-Portal, Switching on magnetism in Ni-doped graphene: Density functional calculations, Phys. Rev. B **78**, 195420 (2008). DOI: 10.1103/PhysRevB.78.195420

[12] E. J. G. Santos, D. Sánchez-Portal, and A. Ayuela, Magnetism of substitutional Co impurities in graphene: Realization of single π vacancies, Phys. Rev. B **81**, 125433 (2010). DOI: 10.1103/PhysRevB.81.125433

[13] L. Qu, Y. Liu, J.-B. Baek, and L. Dai, Nitrogen-Doped Graphene as Efficient Metal-Free Electrocatalyst for Oxygen Reduction in Fuel Cells, ACS Nano **4**, 1321 (2010). DOI: 10.1021/nn901850u

[14] Y. Zheng, Y. Jiao, L. Ge, M. Jaroniec, and S. Z. Qiao, Two-Step Boron and Nitrogen Doping in Graphene for Enhanced Synergistic Catalysis, Angew. Chem. Int. Ed. **52**, 3110 (2013). DOI: 10.1002/anie.201209548

[15] X. Li, L. Fan, Z. Li, K. Wang, M. Zhong, J. Wei, D. Wu, and H. Zhu, Boron Doping of Graphene for Graphene–Silicon p–n Junction Solar Cells, Adv. Energy Mater. **2**, 425 (2012). DOI: 10.1002/aenm.201100671

[16] G. Profeta, M. Calandra, and F. Mauri, Phonon-mediated superconductivity in graphene by lithium deposition, Nat. Phys. **8**, 131 (2012). DOI: 10.1038/nphys2181

[17] J. Chapman, Y. Su, C. A. Howard, D. Kundys, A. N. Grigorenko, F. Guinea, A. K. Geim, I. V. Grigorieva, and R. R. Nair, Superconductivity in Ca-doped graphene laminates, Sci. Rep. **6**, 23254 (2016). DOI: 10.1038/srep23254

[18] T. Lin, I. W. Chen, F. Liu, C. Yang, H. Bi, F. Xu, and F. Huang, Nitrogen-doped mesoporous carbon of extraordinary capacitance for electrochemical energy storage, Science **350**, 1508 (2015). DOI: 10.1126/science.aab3798

[19] S. Agnoli, and M. Favaro, Doping graphene with boron: a review of synthesis methods, physicochemical characterization, and emerging applications, J. Mater. Chem. A **4**, 5002 (2016). DOI: 10.1039/C5TA10599D

[20] L. Wang, Z. Sofer, P. Šimek, I. Tomandl, and M. Pumera, Boron-Doped Graphene: Scalable and Tunable p-Type Carrier Concentration Doping, J. Phys. Chem. C **117**, 23251 (2013). DOI: 10.1021/jp405169j

[21] D. –Y. Yeom, W. Jeon, N. D. K. Tu, S. Y. Yeo, S. –S. Lee, B. J. Sung, H. Chang, J. A. Lim, and H. Kim, High-concentration boron doping of graphene nanoplatelets by simple thermal annealing and their supercapacitive properties, Sci. Rep. **5**, 9817 (2015). DOI: 10.1038/srep09817

[22] X. Wang, X. Li, L. Zhang, Y. Yoon, P. K. Weber, H. Wang, J. Guo, and H. Dai, N-Doping of Graphene Through Electrothermal Reactions with Ammonia, Science **324**, 768 (2009). DOI: 10.1126/science.1170335

[23] H. Wang, R. Revia, K. Wang, R. J. Kant, Q. Mu, Z. Gai, K. Hong, and M. Zhang, Paramagnetic Properties of Metal-Free Boron-Doped Graphene Quantum Dots and Their Application for Safe Magnetic Resonance Imaging, Adv. Mater. **29**, 1605416 (2017). DOI: 10.1002/adma.201605416

[24] H. Wang, R. Revia, Q. Mu, G. Lin, C. Yena, and M. Zhang, Single-layer boron-doped graphene quantum dots for contrastenhanced in vivo T1-weighted MRI, Nanoscale Horiz. **5**, 573 (2020). DOI: 10.1039/C9NH00608G

[25] W. S. Hummers, and R. E. Offeman, Preparation of Graphitic Oxide, Carbon **80**, 1339 (1958). DOI: 10.1021/ja01539a017

[26] L. J. Cote, F. Kim, and J. Huang, Langmuir−Blodgett Assembly of Graphite Oxide Single Layers, J. Am. Chem. Soc. **131**, 1043 (2009). DOI: 10.1021/ja806262m

[27] G. Kresse, and J. Hafner, *Ab initio* molecular dynamics for liquid metals, Phys. Rev. B **47**, 558 (1993). DOI: 10.1103/PhysRevB.47.558

[28] G. Kresse, and J. Hafner, *Ab initio* molecular-dynamics simulation of the liquid-metal–amorphous-semiconductor transition in germanium, Phys. Rev. B **49**, 14251 (1994). DOI: 10.1103/PhysRevB.49.14251

[29] P. E. Blöchl, Projector augmented-wave method, Phys. Rev. B **50**, 17953 (1994). DOI: 10.1103/PhysRevB.50.17953

[30] J. P. Perdew, K. Burke and M. Ernzerhof, Generalized Gradient Approximation Made Simple, Phys. Rev. lett. **77**, 3865 (1996). DOI: 10.1103/PhysRevLett.77.3865

[31] S. Grimme, Semiempirical GGA-type density functional constructed with a long-range dispersion correction, J. comput.chem. **27**, 1787 (2006). DOI: 10.1002/jcc.20495

[32] A. V. Krukau, O. A. Vydrov, A. F. Izmaylov and G. E. Scuseria, Influence of the exchange screening parameter on the performance of screened hybrid functionals, J. Chem. Phys. **125**, 224106 (2006). DOI: 10.1063/1.2404663

[33] S. Wang, E. Iyyamperumal, A. Roy, Y. Xue, D. Yu, and L. Dai, Vertically aligned BCN nanotubes as efficient metal-free electrocatalysts for the oxygen reduction reaction: a synergetic effect by co-doping with boron and nitrogen, Angew. Chem. Int. Ed. **50**, 11756 (2011). DOI: 10.1002/anie.201105204

[34] C. Wang, Z. Guo, W. Shen, Q. Xu, H. Liu, and Y. Wang, B-doped Carbon Coating Improves the Electrochemical Performance of Electrode Materials for Li-ion Batteries, Adv. Func. Mater. **24**, 5511 (2014). DOI: 10.1002/adfm.201401006

[35] W. Shen, H. Li, C. Wang, Z. Li, Q. Xu, H. Liu, and Y. Wang, Improved electrochemical performance of the Na3V2(PO4)3 cathode by B-doping of the carbon coating layer for sodium-ion batteries, J. Mater. Chem. A **3,** 15190 (2015). DOI: 10.1039/C5TA03519H

[36] F. J. Sonia, H. Kalita, M. Aslam, and A. Mukhopadhyay, Correlations between preparation methods, structural features and electrochemical Li-storage behavior of reduced graphene oxide, Nanoscale **9**, 11303 (2017). DOI: 10.1039/C7NR03348F

[37] M. Fan, C. Zhu, Z. -Q. Feng, J. Yang, L. Liu, and D. Sun, Preparation of N-doped graphene by reduction of graphene oxide with mixed microbial system and its haemocompatibility, Nanoscale **6**, 4882 (2014). DOI: 10.1039/C3NR06657F

[38] M. C. Davies, R. A. P. Lynn, J. Hearn, A. J. Paul, J. C. Vickerman, and J. F. Watts, Surface Chemical Characterization Using XPS and TOF-SIMS of Latex Particles Prepared by the Emulsion Copolymerization of Functional Monomers with Methyl Methacrylate and 4-Vinyl Pyridine, Langmuir **11**, 4313 (1995). DOI: 10.1021/la00011a024

[39] Y. -B. Tang, L. -C. Yin, Y. Yang, X. -H. Bo, Y. -L. Cao, H. -E. Wang, W. -J. Zhang, I. Bello, S. -T. Lee, H. -M. Cheng *et al.* Tunable Band Gaps and p-Type Transport Properties of Boron-Doped Graphenes by Controllable Ion Doping Using Reactive Microwave Plasma, ACS Nano **6**, 1970 (2012). DOI: 10.1021/nn3005262

[40] J. -i. Ozaki, N. Kimura, T. Anahara, and A. Oya, Preparation and oxygen reduction activity of BN-doped carbons, Carbon **45**, 1847 (2007). DOI: 10.1016/j.carbon.2007.04.031

[41] V. V. Gobre, and A. Tkatchenko, Scaling laws for van der Waals interactions in nanostructured materials, Nat. Commun. **4**, 2341 (2013). DOI: 10.1038/ncomms3341

[42] Y. Hishiyama, and M. Inagaki, Lattice parameter changes in graphite with boron doping, Carbon **39**, 150 (2001). DOI: 10.1016/S0008-6223(00)00207-4

[43] O. Hod, Graphite and Hexagonal Boron-Nitride have the Same Interlayer Distance. Why?, J. Chem. Theory Comput. **8**, 1360 (2012). DOI: 10.1021/ct200880m

[44] G. Wang, X. Li, Y. Wang, Z. Zheng, Z. Dai, X. Qi, L. Liu, Z. Cheng, Z. Xu, P. Tan *et al.* Interlayer Coupling Behaviors of Boron Doped Multilayer Graphene, J. Phys. Chem. C **121**, 26034 (2017). DOI: 10.1021/acs.jpcc.7b05771

[45] E. G. Steward, and B. P. Cook, X-Ray Measurement of Thermal Expansion Perpendicular to the Layer Planes of Artificial and Natural Graphites, Nature **185**, 78 (1960). DOI: 10.1038/185078b0

[46] J. B. Nelson, and D. P. Riley, The thermal expansion of graphite from 15 c. to 800 c.: part I. Experimental, Proc. Phys. Soc. **57**, 477 (1945). DOI: 10.1088/0959-5309/57/6/303

[47] B. Marsden, A. Mummery, and P. Mummery, Modelling the coefficient of thermal expansion in graphite crystals: implications of lattice strain due to irradiation and pressure, Proc. R. Soc. A **474**, 20180075 (2018). DOI: 10.1098/rspa.2018.0075

[48] M. A. Kanter, Diffusion of Carbon Atoms in Natural Graphite Crystals, Phys. Rev. **107**, 655 (1957). DOI: 10.1103/PhysRev.107.655

[49] I. Suarez-Martinez, A. A. El-Barbary, G. Savini, and M. I. Heggie, First-Principles Simulations of Boron Diffusion in Graphite, Phys. Rev. Lett. **98**, 015501 (2007). DOI: 10.1103/PhysRevLett.98.015501

[50] D. Li, M. B. Müller, S. Gilje, R. B. Kaner, and G. G. Wallace, Processable aqueous dispersions of graphene nanosheets, Nat. Nanotechnol. **3,** 101 (2008). DOI: 10.1038/nnano.2007.451

[51] J. Chen, B. Yao, C. Li, and G. Shi, An improved Hummers method for eco-friendly synthesis of graphene oxide, Carbon **64**, 225 (2013). DOI: 10.1016/j.carbon.2013.07.055

[52] Q. Lai, S. Zhu, X. Luo, M. Zou, and S. Huang, Ultraviolet-visible spectroscopy of graphene oxides, AIP Advances **2**, 032146 (2012). DOI: 10.1063/1.4747817

[53] F. Li, Y. Bao, J. Chai, Q. Zhang, D. Han, and L. Niu, Synthesis and Application of Widely Soluble Graphene Sheets, Langmuir **26**, 12314 (2010). DOI: 10.1021/la101534n

[54] S. S. Zade, and M. Bendikov, From Oligomers to Polymer: Convergence in the HOMO−LUMO Gaps of Conjugated Oligomers, Org. Lett. **8**, 5243 (2006). DOI: 10.1021/ol062030y

[55] J. Robertson, and E. P. O'Reilly, Electronic and atomic structure of amorphous carbon, Phys. Rev. B **35**, 2946 (1987). DOI: 10.1103/PhysRevB.35.2946

[56] G. Yang, C. Wu, X. Luo, X. Liu, Y. Gao, P. Wu, C. Cai, and S. Scott Saavedra, Exploring the Emissive States of Heteroatom-Doped Graphene Quantum Dots, J. Phys. Chem. C **122**, 6483 (2018). DOI: 10.1021/acs.jpcc.8b01385

[57] C. Thomsen, and S. Reich, Double Resonant Raman Scattering in Graphite, Phys. Rev. Lett. **85**, 5214 (2000). DOI: 10.1103/PhysRevLett.85.5214

[58] A. C. Ferrari, and D. M. Basko, Raman spectroscopy as a versatile tool for studying the properties of graphene, Nat. Nanotechnol. **8**, 235 (2013). DOI: 10.1038/nnano.2013.46

[59] D. M. Basko, Theory of resonant multiphonon Raman scattering in graphene, Phys. Rev. B **78**, 125418 (2008). DOI: 10.1103/PhysRevB.78.125418

[60] R. Saito, A. Jorio, A. G. Souza Filho, G. Dresselhaus, M. S. Dresselhaus, and M. A. Pimenta, Probing Phonon Dispersion Relations of Graphite by Double Resonance Raman Scattering, Phys. Rev. Lett. **88**, 027401 (2001). DOI: 10.1103/PhysRevLett.88.027401

[61] P. Venezuela, M. Lazzeri, and F. Mauri, Theory of double-resonant Raman spectra in graphene: Intensity and line shape of defect-induced and two-phonon bands, Phys. Rev. B **84**, 035433 (2011). DOI: 10.1103/PhysRevB.84.035433

[62] S. Ghosh, K. Ganesan, S. R. Polaki, T. R. Ravindran, N. G. Krishna, M. Kamruddin, and A. K. Tyagi, Evolution and defect analysis of vertical graphene nanosheets, J. Raman Spectrosc. **45**, 642 (2014). DOI: 10.1002/jrs.4530

[63] J. Ma, D. Alfè, A. Michaelides, and E. Wang, Stone-Wales defects in graphene and other planar sp^2-bonded materials, Phys. Rev. B **80**, 033407 (2009). DOI: 10.1103/PhysRevB.80.033407

[64] A. Eckmann, A. Felten, A. Mishchenko, L. Britnell, R. Krupke, K. S.Novoselov, and C. Casiraghi, Probing the Nature of Defects in Graphene by Raman Spectroscopy, Nano Lett. **12**, 3925 (2012). DOI: 10.1021/nl300901a

[65] L. M. Malard, M. A. Pimenta, G. Dresselhaus, and M. S. Dresselhaus, Raman spectroscopy in graphene, Phys. Rep. **473**, 51 (2009). DOI: 10.1016/j.physrep.2009.02.003

[66] R. Beams, L. G. Cançado, and L. Novotny, Raman characterization of defects and dopants in graphene, J. Phys.: Condens. Matter **27**, 083002 (2015). DOI: 10.1088/0953-8984/27/8/083002

[67] R. J. Nemanich, G. Lucovsky, and S. A.Solin, Infrared active optical vibrations of graphite, Solid State Commun. **23**, 117 (1977). DOI: 10.1016/0038-1098(77)90663-9

[68] R. Saito, M. Hofmann, G. Dresselhaus, A. Jorio, and M. S. Dresselhaus, Raman spectroscopy of graphene and carbon nanotubes, Adv. Phys. **60**, 413 (2011). DOI: 10.1080/00018732.2011.582251

[69] E. H. Martins Ferreira, M. V. O. Moutinho, F. Stavale, M. M. Lucchese, R. B. Capaz, C. A. Achete, and A. Jorio, Evolution of the Raman spectra from single-, few-, and many-layer graphene with increasing disorder, Phys. Rev. B **82**, 125429 (2010). DOI: 10.1103/PhysRevB.82.125429

[70] A. C. Ferrari, Raman spectroscopy of graphene and graphite: Disorder, electron–phonon coupling, doping and nonadiabatic effects, Solid State Commun. **143**, 47 (2007). DOI: 10.1016/j.ssc.2007.03.052

[71] M. M. Lucchese, F. Stavale, E. H. M. Ferreira, C. Vilani, M. V. O. Moutinho, R. B. Capaz, C. A. Achete, and A. Jorio, Quantifying ion-induced defects and Raman relaxation length in graphene, Carbon **48**, 1592 (2010). DOI: 10.1016/j.carbon.2009.12.057

[72] L. G. Cançado, A. Jorio, E. H. M. Ferreira, F. Stavale, C. A. Achete, R. B. Capaz, M. V. O. Moutinho, A. Lombardo, T. S. Kulmala, and A. C. Ferrari, Quantifying Defects in Graphene via Raman Spectroscopy at Different Excitation Energies, Nano Lett. **11**, 3190 (2011). DOI: 10.1021/nl201432g

[73] F. Tuinstra, and J. L. Koenig, Raman Spectrum of Graphite, J. Chem. Phys. **53**, 1126 (1970). DOI: 10.1063/1.1674108

[74] K. S. Subrahmanyam, S. R. C. Vivekchand, A. Govindaraj, and C. N. R. Rao, A study of graphenes prepared by different methods: characterization, properties and solubilization, J. Mater. Chem. **18**, 1517 (2008). DOI: 10.1039/B716536F

[75] L. G. Cançado, K. Takai, T. Enoki, M. Endo, Y. A. Kim, H. Mizusaki, A. Jorio, L. N. Coelho, R. Magalhães-Paniago, and M. A. Pimenta, General equation for the determination of the crystallite size La of nanographite by Raman spectroscopy, Appl. Phys. Lett. **88**, 163106 (2006). DOI: 10.1063/1.2196057

[76] Z. Zafar, Z. H. Ni, X. Wu, Z. X. Shi, H. Y. Nan, J. Bai, and L. T. Sun, Evolution of Raman spectra in nitrogen doped graphene, Carbon **61**, 57 (2013). DOI: 10.1016/j.carbon.2013.04.065

[77] D. J. Late, A. Ghosh, K. S. Subrahmanyam, L. S. Panchakarla, S. B. Krupanidhi, and C. N. R. Rao, Characteristics of field-effect transistors based on undoped and B- and N-doped few-layer graphenes, Solid State Commun. **150**, 734 (2010). DOI: 10.1016/j.ssc.2010.01.030

[78] S. Pisana, M. Lazzeri, C. Casiraghi, K. S. Novoselov, A. K. Geim, A. C. Ferrari, and F. Mauri, Breakdown of the adiabatic Born–Oppenheimer approximation in graphene, Nat. Mater. **6**, 198 (2007). DOI: 10.1038/nmat1846

[79] N. Jung, N. Kim, S. Jockusch, N. J.Turro, P. Kim, and L. Brus, Charge Transfer Chemical Doping of Few Layer Graphenes: Charge Distribution and Band Gap Formation, Nano Lett. **9**, 4133 (2009). DOI: 10.1021/nl902362q

[80] Y. A. Kim, K. Fujisawa, H. Muramatsu, T. Hayashi, M. Endo, T. Fujimori, K. Kaneko, M. Terrones, J. Behrends, A. Eckmann *et al.* Raman Spectroscopy of Boron-Doped Single-Layer Graphene, ACS Nano **6**, 6293 (2012). DOI: 10.1021/nn301728j

[81] J. E. Lee, G. Ahn, J. Shim, Y. S. Lee, and S. Ryu, Optical separation of mechanical strain from charge doping in graphene, Nat. Commun. **3**, 1024 (2012). DOI: 10.1038/ncomms2022

[82] O. Frank, J. Vejpravova, V. Holy, L. Kavan, M. Kalbac, Interaction between graphene and copper substrate: The role of lattice orientation, Carbon. **68** 440 (2014). DOI: 10.1016/j.carbon.2013.11.020

Intimation of Charge Density Wave in out-of-plane Boron Doped Few-layer Graphene

5

Abstract:

To achieve some symmetry-breaking phase transition like superconductivity (SC), charge density wave (CDW) etc. in two-dimensional layered materials, metal-intercalated graphene has become a suitable agency because of its modified electronic and phonon structure as compared to pure graphene. Strong carrier-lattice interaction followed by a long-range charge ordering can be obtained through incorporation of adequate soft vibrations and accumulation of charges at the interlayer region of few-layer graphene. In this work, we employ boron doped few layered graphene to acquire the CDW phase above T_{CDW} = 100K, where the out-of-plane boron groups are playing a significant role for such transition. Distinct CDW energy gap in band structure is identified using ab-initio simulations and the transition is also verified from low temperature electrical transport measurements. Thus, we elucidate on the correlation between the structural and the vibrational properties on our boron doped few-layered graphene system in the context of the CDW ordering. Furthermore, we find interesting electric field dependency on the CDW phase in this non-metallic, light-atom doped graphene is also depicted here.

5.1 Introduction

Recent advancement of doped graphene systems towards obtaining a strongly correlated electron system unfolds a promising field for graphene as well as for other two-dimensional (2D) materials [1-9]. Particularly since the last decade, intercalation of alkali metals [1,10,11], and other alkaline earth elements [12,13] in few-layered graphene systems (FLGs) has become an area of interest for inducing macroscopic quantum phenomena like superconductivity (SC) [10-13], charge density wave (CDW) [14,15] in low-dimensional materials. For CDW phase, the system acquires a periodic accumulation of electronic charges on account of few popular microscopic events such as Fermi surface nesting [16-18], electron-phonon coupling [19-21], formation of exciton pair [22-24] and in some cases exciton-phonon interaction [25]. In fact, in some cases the electron-electron interactions weigh heavily as a considerable term in the CDW ordering process [26-28]. All these situations, either separately or collectively, decrease the energy due to correlation of electrons and thereby opens up a band gap level near the Fermi level. Alteration of the periodicity of the electronic charges built up by charge localization essentially results in the commensurable and/or incommensurable changes of the lattice constants. Similar to superconductivity, origin of the charge density wave in different materials is still ambiguous since several microscopic factors collectively assist together to construct such correlated phases. Interestingly, coexistence of these phases is found in various layered materials, mostly in transition metal dichalcogenides (TMD), either in or out of favor of each other. It is truly difficult to explain this coexistence of two collective phenomena; however, it is found that the electron-phonon coupling (EPC) plays an important role in both cases. This fermion-boson interaction develops an attractive term to surmount the Coulombic part between the charges and constructs a highly correlated electronic structure in layered materials. Thus, several studies explain the occurrence of CDW phase by using the EPC mechanism in materials such as $NbSe_2$, $TaSe_2$ etc. [29-32]. In general, the description of the EPC is given by an equation as,

$$\lambda = \frac{N(E_F)D^2}{M\omega_{ph}^2} \tag{1}$$

, where $N(E_F)$ is the electronic density of states (DOS) per spin at Fermi level (E_F), D is the deformation potential, M is the effective atomic mass, ω_{ph} is the phonon frequency [33]. Hence to achieve enhanced EPC, one can aim for manipulating these contributing factors in equation (1) that includes the phonon frequency, DOS at Fermi level and the atomic mass in some cases. We may exclude the effect of the deformation potential as this remains invariant with either electron or hole doping, though we should not ignore this term in case of intercalation. Few studies demonstrate the enhancement of deformation potential by intercalating out-of-plane electrons closer to the plane [33,34]. However, electron or hole doping of graphene directly increases the DOS near Fermi level by shifting the Fermi level to the conduction band or valance band respectively. But doping in the plane of lattice of the graphene, i.e., in-plane doping cannot elevate the value of the EPC, as extremely energetic in-plane phonons amplify the ω_{ph} term in the denominator of equation (1). Intercalation of graphene can contribute to reinforce the EPC in two ways, by increasing the DOS at E_F and then involving a considerable amount to the out-of-plane vibrations associated with the softer phonon modes. Ca-intercalated graphene platelet (bulk) shows a phase transition with commensurable lattice deformation from normal to the CDW state at transition temperature $T_{CDW} = 240K$ with an energy gap, $\Delta_{CDW} = 450\, meV$ appearing due to the correlated fermions [14]. Whereas, bilayer graphene achieves the CDW phase at $T_{CDW} = 78K$ with an energy gap, $\Delta_{CDW} = 70\, meV$ [15]. Here, the interlayer (IL) states and dependency of the deformation potential on the interlayer distance, both play a key role to suppress the CDW phase while reducing symmetry from the bulk to the layered structure. Interestingly, almost destruction of the SC phase due to nesting of the π^* bands for the Ca-intercalated bilayer graphene provide evidence of the competing SC and the CDW phases. However, proper explanation for the CDW phase transition in 2D systems and its exact origin is yet to be fully understood.

This work deals with a signature of the CDW phase in non-metallic, boron doped FLG where some boronic and borinic configuration of the boron atoms hold the interlayer positions along out-of-plane (z-axis) direction from lattice plane. Boron atoms are intentionally opted to incorporate between the graphene layers due to its light weight (small atomic mass, M) which is essential for the soft vibrations along the out-of-plane of lattice followed by an enhanced EPC. Generation of IL states associated with those out-of-plane doping configurations and the transfer of charges between the IL states and graphene layer provide extra benefits towards obtaining such instability. Moreover, Dresselhaus predicted the superconducting state in boron doped graphene and commented about unusual defect properties and localized electron density [35], which are also regulating factors for EPC and hence for CDW, as discussed later in this literature.

5.2 Methods

To achieve our objective, we prepared several sample specimens of few-layered graphene systems having different doping configurations of boron. Boron doped graphene samples, labelled as BG500, BG700, BG900 and BG1000, were achieved by standard chemical vapor deposition method performed at 500 ℃, 700 ℃, 900 ℃, 1000 ℃ respectively [36].

5.3 Results and Discussion

5.3.1 Theoretical analysis:

In search of the origin of CDW phase in boron doped FLG, we optimized our few-layered graphene systems with different doping configurations for ab-initio study. Fig 1(a), 1(b) & 1(c) show the optimized structure of doped graphene consisting of the in-plane BC_3, out-of-plane BC_2O and BCO_2 groups respectively. Choice of the di-vacancy defect is made to emulate the real system as prepared by annealing treatment at high temperatures [37,38]. There are several advantages to boron groups along the out-of-plane direction since, *(a)* they can generate relatively softer vibration perpendicular to the lattice plane, *(b)* they can imitate the intercalated graphite structure accumulating electrons closer to the lattice plane that essentially increase the deformation potential in FLG system. *(c)* Generation of the interlayer states that participate in charge transfer to the antibonding π^* bands. Fig. 1(e) & 1(f) exhibit that electrons are transferred to the out-of-plane boron groups from the lattice plane as the localization of the charges are seen at out-of-plane dopant sites. Enhancement of the population of the electrons at the interlayer region is the most suitable arrangement for the excitation of those interlayer electrons to the antibonding state easily as well as for improvement of the lattice vibrations. Some metal intercalated graphite compounds procure the SC states using this charge transfer process [39]. On the other hand, electrons are more localized around boron itself for the in-plane doping as shown in fig 1(d). There is another viewpoint for the charge transfer process as the lacking of charge from the lattice for the out-of-plane doping leaves the system more hole doped, we provide a different approach explained later in this letter. Now, to find the gap in the valance band owing to the energy reduction of the periodic density of charges, the total density of states (DOS) of all the doped systems are shown in Fig. 1(g), 1(h) & 1(i) respectively. For the in-plane doping of the boron, the Fermi level shifts down inside the valance states by an amount of 470 meV, as seen in fig 1(g).

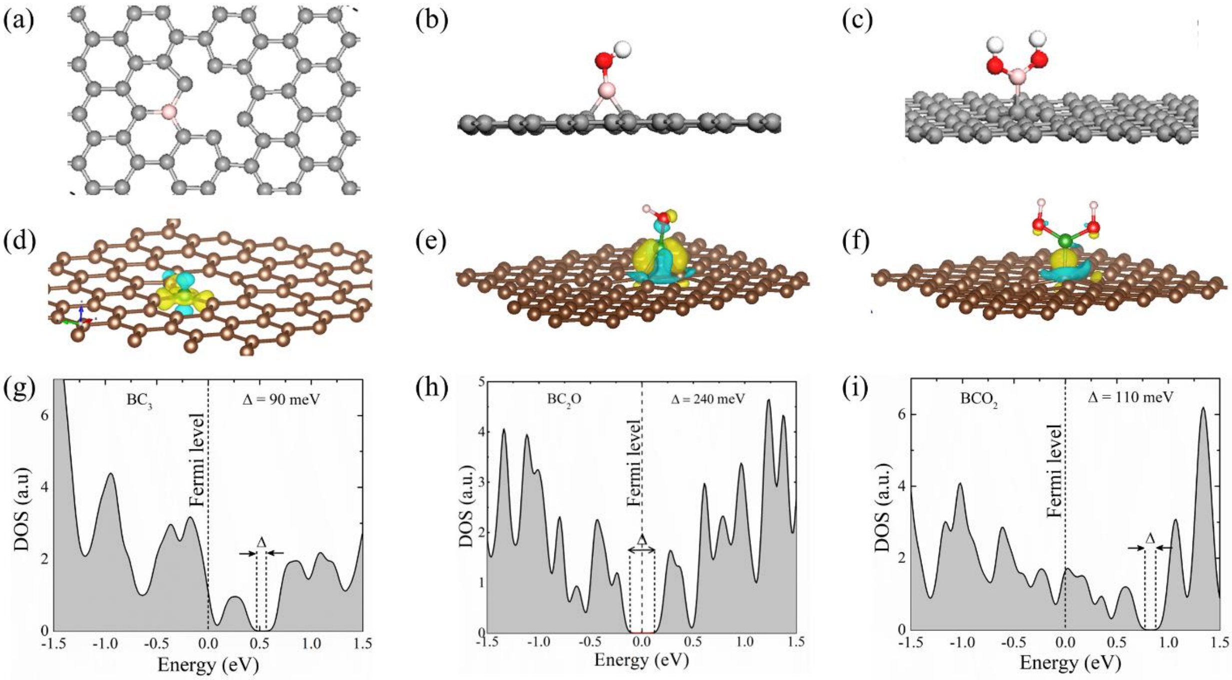

Figure 1: Theoretical study: (a) – (c) optimized structure of boron doped supercell where boron atoms are configured as (a) BC_3, (b) BC_2O, and (c) BCO_2. Transfer of charges between in-plane carbon lattice and the (d) doped boron in plane, (e) BC_2O group, (f) BCO_2 group. Yellow shows the accumulation of electrons where cyan indicates deficiency of electrons after equilibrium. DOS vs. energy plot of (g) BC_3, (h) BC_2O, and (i) BCO_2 [Appendix B] Δ is the energy gap appeared at Fermi level at ground state.

This shift clearly indicates that the boron doping produces a hole concentration in the graphene lattice. The gap between the conduction band (CB) and the valance band (VB) is found here to be about 90 meV. This gap is expected here due to the di-vacancy of graphene as well as the defect present in the lattice and the interstitial sites of graphene. On the extreme side, for BCO_2 configurations, this shift of the Fermi level to the VB is much larger and this shift of the Fermi level from the top of the valance band, simply designated as the valance band maxima (VBM), is about 770 meV. Hence much higher percentage of the hole doping is expected here, which also substantiate the experimental results. Bandgap for this structure is also increased to 110 meV as compared to the BC_3 configuration. Now, for the BC_2O configurations, instead of the shifting of the Fermi level towards the valance band, a wide bandgap of about 240 meV opened up at the Fermi level. Hence, the band separation at the

Fermi level followed by a divergence of density of states near the saddle points emphasize the possibility of charge ordering below T_{CDW}. In addition, we observe Van Hove Singularity (VHS) slightly away from the Fermi level ~0.5eV for this BC_2O configuration as seen in figure 1(h). Furthermore, a flat like band near the Fermi level is also observed for the BCO_2 configuration as well [Fig. B8; appendix B]. Therefore, to achieve further evidence of the CDW phase in graphene, more focused measurements are done for the BG samples which we demonstrate below.

5.3.2 Properties of BG samples:

Fig. 2(a) depicts the XPS results obtained for all of the BG samples. Peaks associating with the other out-of-plane configurations of boron atoms are found above B.E. 190 eV. As the synthesis temperature goes to 1000 ℃, most of these out-of-plane groups are removed and thereby substitutional doping (mostly BC_3) in-plane of the lattice is ensued in majority as depicted in Fig. 2(a). We obtained the actual amount of the in-plane and the out-of-plane boron groups present in the graphene samples physically by deconvoluting the B1s peak for each sample [Fig. B1; Appendix B]. Evolution of the doping configuration from the out-of-plane to the in-plane is shown in Fig. 2(b). Out-of-plane boron groups own maximum occupancy about 90% of the total doping for then BG500, which then falls gradually to 30% for the BG1000 sample [Table B2; appendix B]. Amounts in percentages are fit with the cubic function that show the two distinct stages, by means of doping, separated by an inflection point (Fig. 2b). It is noteworthy that the BG500 and the BG700 samples mostly contain the out-of-plane boron and have different pattern of variation below the inflection point as compared to the BG900 and BG1000 samples which are typically consisting of in-plane boron atom as dopants. At the point of inflection, the out-of-plane boron groups holds around 60% occupancy, which is found to be the mid-value of the entire range of the doping variation. Hence this current state of affairs distinguishes two different stages modulated by the in-plane (I/P) and the out of plane (O/P) boron doping in few-layered graphene systems. Therefore, some contrastive physical, electrical, vibrational properties are distinctly observed throughout the whole study of BG samples prepared by annealing. In connection with the electronic instabilities those properties are found to be either collectively manipulating these instabilities or be a by-product of this phase transition.

First of all, the interlayer distances of these doped graphene samples, specified by d_{002} in Fig. 2(c), demonstrates the obvious trend that shows that the layer gap increases with increase in doping occupancy for the out of plane sites. d_{002} for the BG samples are obtained from the X-ray diffraction patterns [Fig. B2; appendix B].

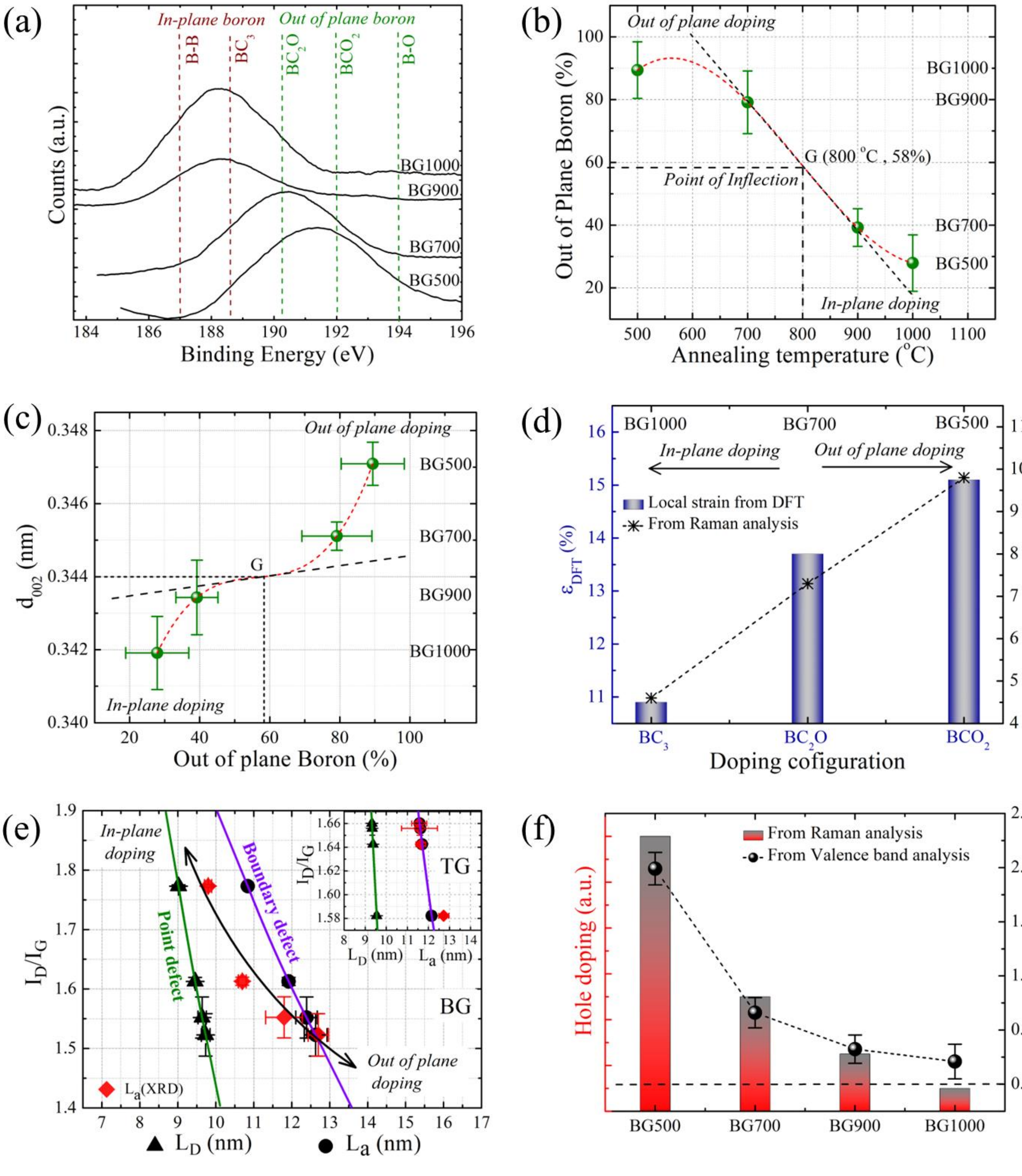

Figure 2: Manipulating factors of boron doped FLG in order to achieve CDW state: (a) XPS study of all BG samples. (b) Real measures of out of plane boron and in-plane boron in BG samples. (c) variation of interlayer distances with the amounts of out-of-plane groups present in BG samples. (d) Strain produced due to inclusion of differently configured boron groups in graphene lattice. Bars represent the result obtained from DFT, and stars demonstrate the

strain amounts as realized from Fig. 9 in ref. 36. (e) Types of defects produced in graphene lattice as a result of boron doping. $\frac{I_D}{I_G}$ ratios as a function of experimentally obtained in-plane crystallite sizes, $L_a(XRD)$, of BG samples considering T-K relation and modified-T-K relation for boundary (characterized by crystallite size, L_a) and point defects (characterized by defect length, L_D) respectively [appendix B]. (f) Degree of hole hoping in all BG samples analyzed by measuring the shift of valance band maxima from Fermi level as well as from the Raman analysis [36; Fig. 9]

BG1000 has the shortest interlayer distance among all the BGs due to several factors like removal of the O/P boron groups, deficiency of the π-electron densities, van der Waals forces etc. which were clearly discussed in ref. 36. On the other hand, BG500 has the maximum interlayer distance because of the O/P boron groups. We believe, in the case accumulation of the electrons inside the layers definitely helps to enhance the lattice deformation potential and modifies the vibrational states in achieving CDW states. Another stimulating factor for the acquisition of the CDW phase in two-dimensional materials is tensile strain produced along the in-plane direction of the lattice [40,41]. Some two-dimensional TMDs such as 2H-$NbSe_2$ [40] 1T-VSe_2 [42] and rare-earth ditelluride like $CeTe_2$ [43] have shown their CDW transition where tensile strain directly helps in the charge ordering. Tensile strain, particularly uniaxial one (as biaxial strains have little contribution to it) enlarges the momentum separation q_{CDW} in Fermi pockets around the Γ point by softening the phonon energies and thereby altering the carrier hopping parameter [40]. It is now established that the boron doping in hexagonal carbon lattice induces tensile strain [35, 44]. Moreover, negative thermal coefficient of graphene is also a considerable factor at low temperatures, as it stretches the carbon rings during the cooling down of the temperature [45]. Our earlier literature gives an estimation of the tensile strain due to the boron groups in BG samples [Ref. 36; fig. 9]. Fig. 2(d) depicts that O/P boron groups develop more strain than I/P boron groups inside the graphene lattice which evidently assists the CDW phase at lower temperatures. To ensure the validity of the experimental analysis about strain, theoretical data of the effective strain induced in the graphene planes due to external boron atom doping are investigated using ab-initio simulations [Table B3; appendix B.]. This theoretical result is specific for the particular boron groups that is found to be comparable with the experimentally calculated strain [Methods; Appendix B] as described in Fig. 2(d). Since the out-of-plane (BC_2O & BCO_2)

boron groups take the utmost responsibility to produce tensile strain in the plane of BG700 & BG500 lattice as compared to the BG1000 as noted previously. Therefore, BG500 and BG700 samples are considered to be more suitable systems for CDW formation. Furthermore, the role of defects in CDW phase transition are unexplained till date. Weitering et al. clearly describe how point defects acts as nucleation centers for the CDW phase in germanium lattice [46]. Fig. 2(e) reveals the types of defects occurring in our boron doped graphene samples. After calculating the $\frac{I_D}{I_G}$ values from the deconvoluted Raman spectra of BG samples [Fig. B5; appendix B], two distinct reference lines for point and boundary defects are drawn using the modified T-K relation [47]. Point defects and boundary defects are characterized by their defect length (L_D) and crystallite size (L_a) respectively in the figure. For two dimensional lattices, both of these parameters reveal similar range of crystallinity. Therefore, a comparative analysis is performed by evaluating the mean in-plane crystallite sizes (L_a) of BG samples as revealed in Fig. 2(e). Thermally treated undoped graphene (TG samples) is employed here for the comparative analysis [Fig. 2(e); inset]. After analyzing the XRD peaks along in-plane (001) direction, experimental measures of crystallite sizes are cumulated [Fig. B3; appendix B]. Thus, it becomes clear that the variation of the crystallite sizes in the BG samples indicate that the O/P doping creates the boundary type defects inside the lattice whereas, I/P substitution of boron creates the point type defects in the same. On the other hand, undoped TG samples, annealed at high temperature, are prone to have boundary defects for its different functional groups attached in the out-of-plane configuration. However, we believe that for one-dimensional defects in our O/P doped system divides the whole lattice into several grains and the possibility of incommensurate CDW (IC-CDW) arises since commensurable phase transition requires lesser dimension of defects [48,49]. Absence of loop for the heating and cooling cycle at low temperature transport measurements also indicate a transition is likely to be from normal to IC-CDW states in BG500 and BG700 samples [8, 50, 51]. Thus, in present scenario, all those factors like, tensile strain, hole doping, line defects etc. are directly or indirectly trigger the O/P boron doped BG system to have greater EPC that allow for the charge ordering and periodic modulation of electron density in one dimension.

5.3.3 Electrical Properties:

Now to observe the charge transport phenomenon particularly in the low temperature regime, resistance vs. temperature (R-T) measurements were performed for all the BG samples

[Appendix B]. Fig. 3(a) reveals the semiconducting nature of all BG samples with long range disorder as the resistance for all the sample increase exponentially at low temperatures.

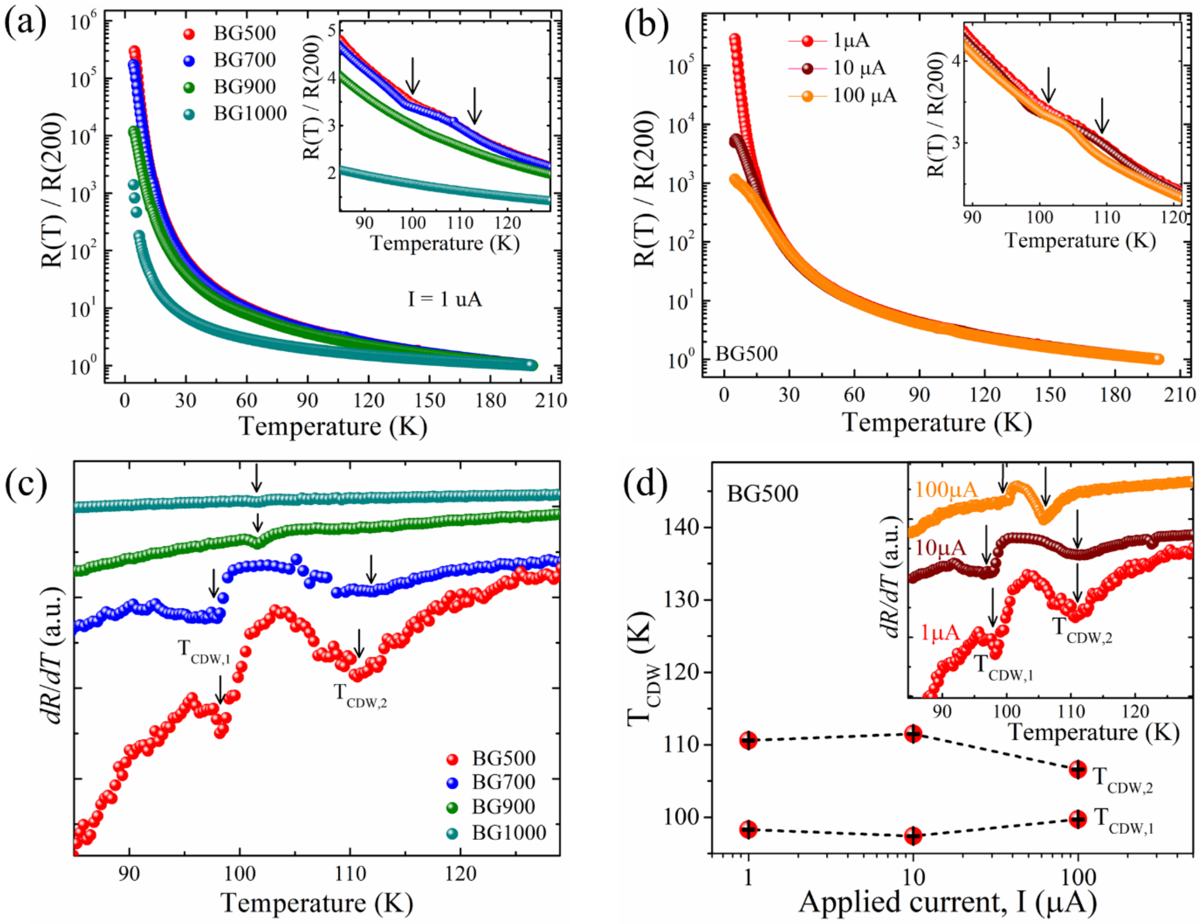

Figure 3: (a) Temperature dependent resistances (R) of all BG samples under a bias current I = 1μA. (b) Temperature dependent resistances of BG500 sample under various bias currents (c)Corresponding first derivative of resistance curve for all BG samples at bias current I = 1μA. (d) Influence of applied bias current on transition temperatures, $T_{CDW,1}$ and $T_{CDW,\,2}$. Corresponding first derivative of resistance curve for BG500 sample at different bias currents (inset).

An observable kink near 100 K can be identified for both the BG500 and BG700 samples under applied I = 1μA (inset: fig. 3(a)). These small elevations in resistance values just above 100K are expected due to reconstruction of in-plane superlattice leading to a charge density wave (CDW) phase transition in the BG system. Transition from normal to CDW phase are more prominent in the derivative plots for the BG samples in fig. 3(c). Interestingly, in *dR/dT* representation, two points of inflections clearly infers that the formation of superlattice takes place by two sets of transitions in samples. Two distinct temperatures separated by nearly 10K are designated as $T_{CDW,1}$ and $T_{CDW,2}$ in Fig. 3(c). It is obviously unconventional to have such pair of minima in the way of achieving CDW phase transition in other TMDs, but still for few-layer, boron-doped graphene comprised with large amounts of defects it can be predicted due to few dissimilar aspects compared to normal TMDs. Effect of the applied electric field in achieved CDW phase set another perspective to the understanding of this collective phenomena. Different R-T curves and first order derivative with respect to the temperature in absolute scale are obtained for BG500 at I = 1 μA, 10 μA and 100 μA, to probe the influence of the electric field in CDW phase transition, as depicted in Fig. 3(b) and 3(d) respectively. As the intensity of applied electric field increases, destruction of the CDW phase occurs. It is possible that pinning of the electric field strengthens the coulombic interactions so much, and also harden the vibration of the phonons by significant amount, that yields in vanishing of the CDW phase because of the weaker EPC. Similar observation is reported by Balandin group [53], where higher electric field redirects the sample 1T-TaS_2 from IC-CDW to metallic state. For BG500 sample, variation of the onset points for CDW transition by altering the applied bias field are shown in Fig. 3(d), which delineates the evolutions of both $T_{CDW,1}$ and $T_{CDW,2}$. Two transition points have a clear tendency to converge to a single point and that is leading to the destruction of CDW phase with increasing electric field. Some rare earth tritellurides holding two CDW transition points showed this type of shrinkage of CDW signatures under increasing pressure [54,55].

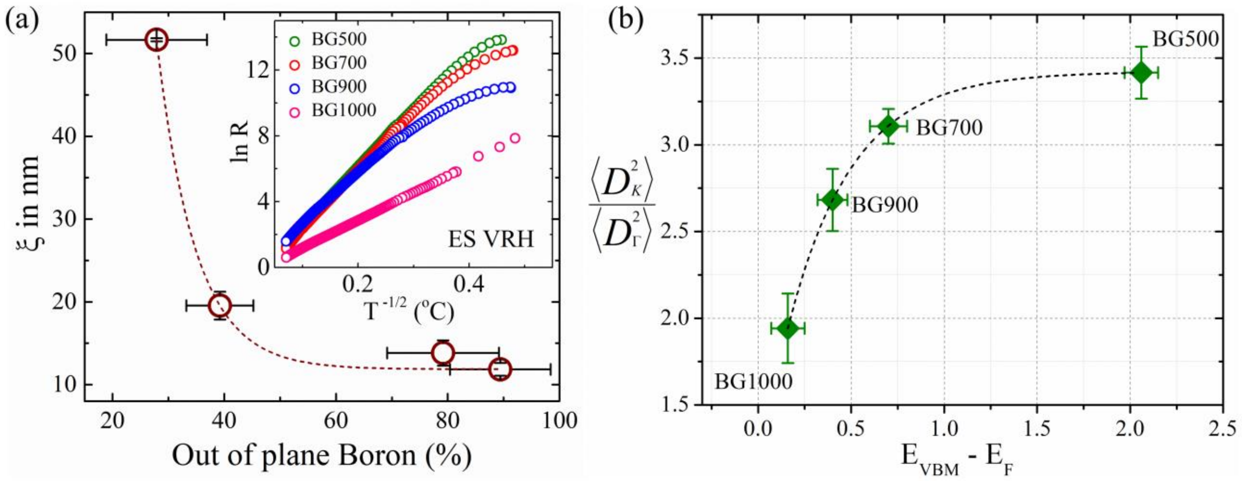

Figure 4: (a) Variation of localization length (ξ) with different amounts of O/P boron. (b) Ratio of the average of the square of EPC parameters, averaged on the Fermi surface,

associated with the K and Γ points, represented as $\frac{\langle D_K^2 \rangle}{\langle D_\Gamma^2 \rangle}$ vs. Degree of hole doping in terms of the shift of VBM from E_F. E_{VBM} stands for energy of valance band maxima and E_F is the Fermi energy level.

Considering aforementioned the coulombic interactions near to the Fermi level and the isotropic nature of the system, these samples are best fit [Fig. B7; appendix B] to the Efros-Shklovskii variable range hopping (ES-VRH) model [56,57] of conduction of charge carrier. Localization of electron wave function can be understood as a by-product of the enhanced EPC as stronger EPC indicates more localization of charge i.e., smaller localization length, ξ. Fig. 4(a) indicates that the BG samples with more out-of-plane boron groups are having shorter localization length. Hence, due to strong EPC in BG500 and BG700, electrons are much localized here. To understand the origin of this CDW phase in BG, two most discussed mechanisms are brought into this picture. Firstly, Fermi surface nesting (FSN) which is characterized by a wave vector q_{CDW} that connects the Fermi contours. Secondly, momentum dependence of electron-phonon coupling (EPC) matrix induces CDW phases as observed in case of 2H-$NbSe_2$. There is another mechanism of charge ordering (CO), mostly found in some cuprates, termed as unconventional density wave [59]. Unlike $NbSe_2$, TaS_2, $TaSe_2$ etc. CO in cuprates cannot be explained by FSN or q-depended EPC, rather influences of anti-ferromagnetism and coulomb interaction are anticipated [60]. As present work deals with mainly light atom doped graphene system, the possibility of unconventional charge density waves can be discarded. Possibility of FSN is mostly seen in one dimensional lattice [19] or some TMDs like VSe_2 etc. [58]. q-depended EPC involves an inelastic scattering interaction of electrons in the lattice. Thus, to assess the momentum dependency and possibility of the EPC at higher symmetry points, second order Raman peaks $2D$ and $2D'$ originating from the interaction of the phonons at K and Γ points are precisely examined [Appendix B] [34, 61]. Moreover, fig. 4(b) dictates that the EPC near K-point is amplified in graphene containing the O/P boron groups. Hence, the enhancement of the EPC terms definitely plays the utmost role in the genesis of CDW phase in BG500 and BG700.

Starting from a non-metallic ground state, the first CDW transition occurs near $T_{CDW,1}$ = 100K are obtained by modulation of charge periodicity as traditionally occurs. Now, a possible reason for subsequent transition, at $T_{CDW,2}$ = 110K, is anticipated as the enormous incorporation of O/P boron can modify the surface of graphene layer by generating a pseudo-periodicity of superficial atoms as boron has a greater self-diffusive property in carbon lattice at higher temperature [52]. It is noteworthy, that the BG900 and BG 1000 samples containing mostly in-plane boron atoms have single transition temperature as there is no such surface boron which can contribute to this pseudo-periodicity. Fluctuations of onset transition temperatures for differently doped BG systems are elucidated in Fig. 5.

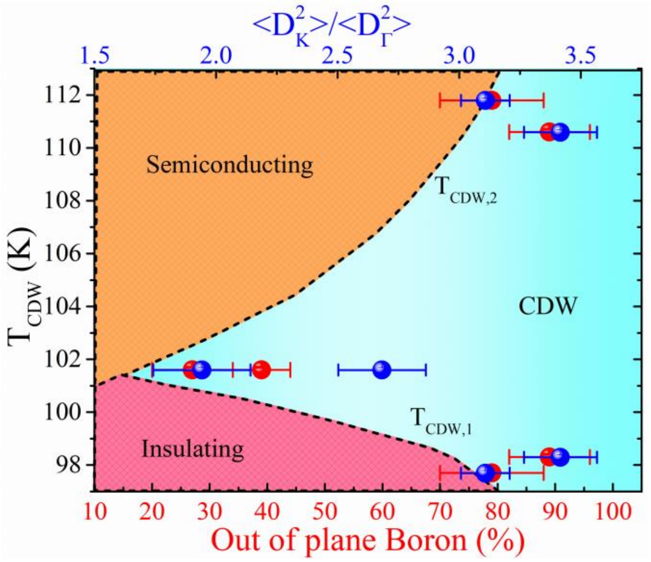

Figure 5: Temperature vs. O/P boron (%) phase diagram: Elucidating the effect of O/P doping and associated EPC parameter $\frac{\langle D_K^2 \rangle}{\langle D_\Gamma^2 \rangle}$ [as calculated in Fig. 4(b)] on transition temperatures, $T_{CDW,1}$ and $T_{CDW,2}$.

This phase depicts the final result precisely, as the signatures of CDW phases are found to be more profound in the samples with greater number of O/P groups. Strength of EPC induced by out-of-plane vibrations is also affecting the transition from insulating to CDW and CDW to semiconducting state in similar fashion as represented this figure. Therefore, the significance of O/P boron groups as a modulating factor in order to attain strongly correlated system of particles followed by the lattice reconstruction at this particular temperature (T_{CDW}) is understood as predicted from theoretical analyses.

5.4 Conclusion

In the conclusion, we have shown that out-of-plane boron doped few-layer graphene undergoes a quantum-mechanical collective phenomena described by a periodic distribution of correlated charges inside the lattice. Origin of this reconstruction of lattice at transition temperature is mostly enhancement of EPC and interaction of interlayer states with π electron density. Spectroscopic results show excellent validation for explaining the CDW phase in BG system. Finally, the ab-initio based theoretical simulations upholds the allied electronic behaviour of these systems. However, the dependency of CDW phase with applied electric field offers a new perspective towards apprehension of such instabilities.

References

1. N. Ehlen, M. Hell, G. Marini, E. H. Hasdeo, R. Saito, Y. Falke, M. O. Goerbig, G. D. Santo, L. Petaccia, G. Profeta, and A. Grüneis, Origin of the Flat Band in Heavily Cs-Doped Graphene, ACS Nano **2020**, 14 (1), 1055-1069. https://doi.org/10.1021/acsnano.9b08622
2. X. Wang, N. Liu, Y. Wu, Y. Qu, W. Zhang, J. Wang, D. Guan, S. Wang, H. Zheng, Y. Li, C. Liu, and J. Jia, Strong Coupling Superconductivity in Ca-Intercalated Bilayer Graphene on SiC, Nano Lett. **2022**, 22 (18), 7651-7658. https://doi.org/10.1021/acs.nanolett.2c02804
3. G. Long, S. Xu, T. Zhang, Z. Wu, W. K. Wong, T. Han, J. Lin, Y. Cai, and N. Wang, Charge density wave phase transition on the surface of electrostatically doped multilayer graphene, Appl. Phys. Lett. **2016** ,109, 183107. https://doi.org/10.1063/1.4966953
4. J. J. Gao, W. H. Zhang, J. G. Si, X. Luo, J. Yan, Z. Z. Jiang, W. Wang, H. Y. Lv, P. Tong, W. H. Song, X. B. Zhu, W. J. Lu, Y. Yin, and Y. P. Sun, Chiral charge density waves induced by Ti-doping in 1T-TaS_2, Appl. Phys. Lett. **2021,** 118, 213105. https://doi.org/10.1063/5.0052240
5. R. Zhang, I-L. Tsai, J. Chapman, E. Khestanova, J. Waters, and I. V. Grigorieva, Superconductivity in Potassium-Doped Metallic Polymorphs of MoS_2, Nano Lett. **2016** 16 (1), 629-636. https://doi.org/10.1021/acs.nanolett.5b04361
6. U. Chatterjee, J. Zhao, M. Iavarone, R. Di Capua, J. P. Castellan, G. Karapetrov, C. D. Malliakas, M. G. Kanatzidis, H. Claus, J. P. C. Ruff, & S. Rosenkranz et al., Emergence of coherence in the charge-density wave state of 2H-$NbSe_2$, Nat. **2015**, 6, 6313. https://doi.org/10.1038/ncomms7313

7. J. Gao, J. W. Park, K. Kim, S. K. Song, H. R. Park, J. Lee, J. Park, F. Chen, X. Luo, Y. Sun, and H. W. Yeom, Pseudogap and Weak Multifractality in 2D Disordered Mott Charge-Density-Wave Insulator, Nano Lett. **2020**, 20 (9), 6299-6305. https://doi.org/10.1021/acs.nanolett.0c01607
8. S. Baraghani, Z. Barani, Y. Ghafouri, A. Mohammadzadeh, T. T. Salguero, F. Kargar, and A. A. Balandin, Charge-Density-Wave Thin-Film Devices Printed with Chemically Exfoliated 1T-TaS_2 Ink, ACS Nano **2022**, 16 (4), 6325-6333. https://doi.org/10.1021/acsnano.2c00378
9. A. W. Tsen, R. Hovden, D. Wang, Y. D. Kim, J. Okamoto, K. A. Spoth, Y. Liu, W. Lu, Y. Sun, J. C. Hone, L. F. Kourkoutis, P. Kim, and A. N. Pasupathy, Structure and control of charge density waves in two-dimensional 1T-TaS_2, PNAS **2015**, 112 (49), 15054-15059. https://doi.org/10.1073/pnas.1512092112
10. M. Xue, G. Chen, H. Yang, Y. Zhu, D. Wang, J. He, and T. Cao, Superconductivity in Potassium-Doped Few-Layer Graphene, J. Am. Chem. Soc. **2012** 134 (15), 6536-6539. https://doi.org/10.1021/ja3003217
11. B. M. Ludbrook, G. Levy, P. Nigge, M. Zonno, M. Schneider, D. J. Dvorak, C. N. Veenstra, S. Zhdanovich, D. Wong, P. Dosanjh, C. Straßer, A. Stöhr, S. Forti, C. R. Ast, U. Starke, and A. Damascelli, Evidence for superconductivity in Li-decorated monolayer graphene, PNAS **2015**, 112 (38), 11795-11799. https://doi.org/10.1073/pnas.1510435112
12. S. Ichinokura, K. Sugawara, A. Takayama, T. Takahashi, and S. Hasegawa, Superconducting Calcium-Intercalated Bilayer Graphene, ACS Nano **2016**, 10 (2), 2761-2765. https://doi.org/10.1021/acsnano.5b07848
13. J. Chapman, Y. Su, C. A. Howard, D. Kundys, A. N. Grigorenko, F. Guinea, A. K. Geim, I. V. Grigorieva & R. R. Nair, Superconductivity in Ca-doped graphene laminates, Sci Rep **2016,** 6, 23254. https://doi.org/10.1038/srep23254
14. K.C. Rahnejat, C.A. Howard, N.E. Shuttleworth, S.R. Schofield, K. Iwaya, C.F. Hirjibehedin, Ch. Renner, G. Aeppli & M. Ellerby, Charge density waves in the graphene sheets of the superconductor CaC_6, Nat. Commun. **2011**, 2, 558. https://doi.org/10.1038/ncomms1574

15. R. Shimizu, K. Sugawara, K. Kanetani, K, Iwaya, T. Sato, T. Takahashi, and T. Hitosugi, Charge-Density Wave in Ca-Intercalated Bilayer Graphene Induced by Commensurate Lattice Matching, Phys. Rev. Lett. **2015**, 114, 146103. https://doi.org/10.1103/PhysRevLett.114.146103
16. D. S. Inosov, V. B. Zabolotnyy, D. V. Evtushinsky, A. A. Kordyuk, B. Büchner, R. Follath, H. Berger and S. V. Borisenko, Fermi surface nesting in several transition metal dichalcogenides, New. J. Phys. **2008**, 10, 125027. https://doi.org/10.1088/1367-2630/10/12/125027
17. S. V. Borisenko, A. A. Kordyuk, A. N. Yaresko, V. B. Zabolotnyy, D. S. Inosov, R. Schuster, B. Büchner, R. Weber, R. Follath, L. Patthey, and H. Berger, Pseudogap and Charge Density Waves in Two Dimensions, Phys. Rev. Lett. **2008,** 100, 196402. https://doi.org/10.1103/PhysRevLett.100.196402
18. S. V. Borisenko, A. A. Kordyuk, V. B. Zabolotnyy, D. S. Inosov, D. Evtushinsky, B. Büchner, A. N. Yaresko, A. Varykhalov, R. Follath, W. Eberhardt, L. Patthey, and H. Berger, Two Energy Gaps and Fermi-Surface "Arcs" in $NbSe_2$, Phys. Rev. Lett. **2009**, 102, 166402. https://doi.org/10.1103/PhysRevLett.102.166402
19. M. D. Johannes and I. I. Mazin, Fermi surface nesting and the origin of charge density waves in metals, Phys. Rev. B **2008**, 77, 165135. https://doi.org/10.1103/PhysRevB.77.165135
20. C. M. Varma and A. L. Simons, Strong-Coupling Theory of Charge-Density-Wave Transitions, Phys. Rev. Lett. **1983**, 51, 138. https://doi.org/10.1103/PhysRevLett.51.138
21. A. Sanna, C. Pellegrini, E. Liebhaber, K. Rossnagel, K. J. Franke & E. K. U. Gross, Real-space anisotropy of the superconducting gap in the charge-density wave material 2H-$NbSe_2$, npj Quantum Mater. **2022**, 7, 6. https://doi.org/10.1038/s41535-021-00412-8
22. T. E. Kidd, T. Miller, M. Y. Chou, and T.-C. Chiang, Electron-Hole Coupling and the Charge Density Wave Transition in $TiSe_2$, Phys. Rev. Lett. 2002 88, 226402. https://doi.org/10.1103/PhysRevLett.88.226402
23. A. Kogar, M. S. Rak, S. Vig, Ali A. Husain, F. Flicker, Y. I. Joe, L. Venema, G. J. Macdougall, T. C. Chiang, E. Fradkin, J. V. Wezel, P. Abbamonte, Signatures of exciton condensation in a transition metal dichalcogenide, SCIENCE **2017**, 358 (6368), 1314-1317.

https://doi.org/10.1126/science.aam6432

24. D. Jérome, T. M. Rice, and W. Kohn, Excitonic Insulator, Phys. Rev. **1967**, 158, 462. https://doi.org/10.1103/PhysRev.158.462
25. J. van Wezel, P. Nahai-Williamson, and S. S. Saxena, Exciton-phonon-driven charge density wave in $TiSe_2$, Phys. Rev. B **2010**, 81, 165109. https://doi.org/10.1103/PhysRevB.81.165109
26. H. Watanabe, K. Seki, and S. Yunoki, Charge-density wave induced by combined electron-electron and electron-phonon interactions in 1T−$TiSe_2$: A variational Monte Carlo study, Phys. Rev. B **2015**, 91, 205135. https://doi.org/10.1103/PhysRevB.91.205135
27. I. Jang, G. Duvjir, B. K. Choi, J. Kim, Y. J. Chang, and K-S. Kim, Universal renormalization group flow toward perfect Fermi-surface nesting driven by enhanced electron-electron correlations in monolayer vanadium diselenide, Phys. Rev. B **2019**, 99, 014106. https://doi.org/10.1103/PhysRevB.99.014106
28. B. Horovitz and J. Sólyom, Charge-density waves with electron-electron interactions Phys. Rev. B **1985**, 32, 2681(R). https://doi.org/10.1103/PhysRevB.32.2681
29. T. Valla, A. V. Fedorov, P. D. Johnson, P-A. Glans, C. McGuinness, K. E. Smith, E. Y. Andrei, and H. Berger, Quasiparticle Spectra, Charge-Density Waves, Superconductivity, and Electron-Phonon Coupling in 2H−$NbSe_2$, Phys. Rev. Lett. **2004**, 92, 086401. https://doi.org/10.1103/PhysRevLett.92.086401
30. F. Weber, S. Rosenkranz, J.-P. Castellan, R. Osborn, R. Hott, R. Heid, K.-P. Bohnen, T. Egami, A. H. Said, and D. Reznik, Extended Phonon Collapse and the Origin of the Charge-Density Wave in 2H−$NbSe_2$, Phys. Rev. Lett. **2011**, 107, 107403. https://doi.org/10.1103/PhysRevLett.107.107403
31. C.-S. Lian, C. Heil, X. Liu, C. Si, F. Giustino, and W. Duan, Coexistence of Superconductivity with Enhanced Charge Density Wave Order in the Two-Dimensional Limit of $TaSe_2$, J. Phys. Chem. Lett. **2019**, 10 (14), 4076-4081. https://doi.org/10.1021/acs.jpclett.9b01480
32. H. Ryu, Y. Chen, H. Kim, H.-Z. Tsai, S. Tang, J. Jiang, F. Liou, S. Kahn, C. Jia, and S.-K. Mo et al., Persistent Charge-Density-Wave Order in Single-Layer $TaSe_2$, Nano Lett. **2018**, 18 (2), 689-694.

https://doi.org/10.1021/acs.nanolett.7b03264

33. G. Profeta, M. Calandra, & F. Mauri, Phonon-mediated superconductivity in graphene by lithium deposition, Nat. Phys. **2012**, 8, 131–134. https://doi.org/10.1038/nphys2181
34. C. Attaccalite, L. Wirtz, M. Lazzeri, F. Mauri, and A. Rubio, Doped Graphene as Tunable Electron−Phonon Coupling Material, Nano Lett. **2010**, 10 (4), 1172-1176. https://doi.org/10.1021/nl9034626
35. Y. A. Kim, K. Fujisawa, H. Muramatsu, T. Hayashi, M. Endo, T. Fujimori, K. Kaneko, M. Terrones, J. Behrends, A. Eckmann, C. Casiraghi, K. S. Novoselov, R. Saito, and M. S. Dresselhaus, Raman Spectroscopy of Boron-Doped Single-Layer Graphene, ACS Nano **2012** 6 (7), 6293-6300. https://doi.org/10.1021/nn301728j
36. S. Sarkar, R. Roy, B. K. Das, K. K. Chattopadhyay, Temperature-dependent site selection of boron doping in chemically derived graphene, Carbon **2021**, 184, 253-265. https://doi.org/10.1016/j.carbon.2021.08.017
37. F. Banhart, J. Kotakoski, and A. V. Krasheninnikov, Structural Defects in Graphene, ACS Nano **2011**, 5 (1), 26-41. https://doi.org/10.1021/nn102598m
38. L. Tsetseris, B. Wang, and S. T. Pantelides, Substitutional doping of graphene: The role of carbon divacancies, Phys. Rev. B **2014**, 89, 035411. https://doi.org/10.1103/PhysRevB.89.035411
39. G. Csányi, P. B. Littlewood, A. H. Nevidomskyy, C. J. Pickard & B. D. Simons, The role of the interlayer state in the electronic structure of superconducting graphite intercalated compounds, Nat. Phys. **2005**, 1, 42–45. https://doi.org/10.1038/nphys119
40. S. Gao, F. Flicker, R. Sankar, H. Zhao, Z. Ren, B. Rachmilowitz, S. Balachandar, F. Chou, K. S. Burch, Z. Wang, J. van Wezel, and I. Zeljkovic, Atomic-scale strain manipulation of a charge density wave, PNAS **2018,** 115 (27) 6986-6990. https://doi.org/10.1073/pnas.171893111
41. M. J. Wei, W. J. Lu, R. C. Xiao, H. Y. Lv, P. Tong, W. H. Song, and Y. P. Sun, Manipulating charge density wave order in monolayer 1T−$TiSe_2$ by strain and charge doping: A first-principles investigation, Phys. Rev. B **2017**, 96, 165404. https://doi.org/10.1103/PhysRevB.96.165404

42. D. Zhang, J. Ha, H. Baek, Y.-H. Chan, F. D. Natterer, A. F. Myers, J. D. Schumacher, W. G. Cullen, A. V. Davydov, Y. Kuk, M. Y. Chou, N. B. Zhitenev, and J. A. Stroscio, Strain engineering a $4a\times\sqrt{3}a$ charge-density-wave phase in transition-metal dichalcogenide 1T−VSe_2, Phys. Rev. Materials **2017**, 1, 024005. https://doi.org/10.1103/PhysRevMaterials.1.024005
43. B. Sharma, M. Singh, B. Ahmed, B. Yu, P. Walmsley, I. R. Fisher, and M. C. Boyer Interplay of charge density wave states and strain at the surface of $CeTe_2$, Phys. Rev. B **2020**, 101, 245423. https://doi.org/10.1103/PhysRevB.101.245423
44. E. Lee, G. Ahn, J. Shim, Y. S. Lee, and S. Ryu, Optical separation of mechanical strain from charge doping in graphene, Nat. Commun. **2012**, 3, 1024. https://doi.org/10.1038/ncomms2022
45. D. Yoon, Y.-W. Son, and H. Cheong, Negative Thermal Expansion Coefficient of Graphene Measured by Raman Spectroscopy, Nano Lett. **2011**, 11 (8), 3227-3231. https://doi.org/10.1021/nl201488g
46. H. H. Weitering, J. M. Carpinelli, A. V. Melechko, J. Zhang, M. Bartkowiak and E. W. Plummer, Defect-Mediated Condensation of a Charge Density Wave, SCIENCE **1999**, 285 (5436), 2107-2110. https://doi.org/10.1126/science.285.5436.2107
47. L. G. Cançado, A. Jorio, E. H. M. Ferreira, F. Stavale, C. A. Achete, R. B. Capaz, M. V. O. Moutinho, A. Lombardo, T. S. Kulmala, and A. C. Ferrari, Quantifying Defects in Graphene via Raman Spectroscopy at Different Excitation Energies, Nano Lett. **2011**, 11, 3190. https://doi.org/10.1021/nl201432g
48. A. Kogar, G. A. de la Pena, Sangjun Lee, Y. Fang, S. X.-L. Sun, D. B. Lioi, G. Karapetrov, K. D. Finkelstein, J. P. C. Ruff, P. Abbamonte, and S. Rosenkranz, Observation of a Charge Density Wave Incommensuration Near the Superconducting Dome in Cu_xTiSe_2, Phys. Rev. Lett. **2017**, 118, 027002. https://doi.org/10.1103/PhysRevLett.118.027002
49. S. Yan, D. Iaia, E. Morosan, E. Fradkin, P. Abbamonte, and V. Madhavan, Influence of Domain Walls in the Incommensurate Charge Density Wave State of Cu Intercalated 1T−$TiSe_2$, Phys. Rev. Lett. **2017**, 118, 106405. https://doi.org/10.1103/PhysRevLett.118.106405

50. B. Sipos, A. F. Kusmartseva, A. Akrap, H. Berger, L. Forró & E. Tutiš, From Mott state to superconductivity in 1T-TaS_2, Nature Mater **2008**, 7, 960–965. https://doi.org/10.1038/nmat2318
51. L. Stojchevska, I. Vaskivskyi, T. Mertelj, P. Kusar, D. Svetin, S. Brazovskii And D. Mihailovic, Ultrafast Switching to a Stable Hidden Quantum State in an Electronic Crystal, SCIENCE **2014**, 344 (6180), 177-180. https://doi.org/10.1126/science.1241591
52. I. Suarez-Martinez, A.A. El-Barbary, G. Savini, M.I. Heggie, First-principles simulations of boron diffusion in graphite, Phys. Rev. Lett. **2007**, 98, 015501, https://doi.org/10.1103/PhysRevLett.98.015501.
53. A. K. Geremew, S. Rumyantsev, F. Kargar, B. Debnath, A. Nosek, M. A. Bloodgood, M. Bockrath, T. T. Salguero, R. K. Lake, and A. A. Balandin, Bias-Voltage Driven Switching of the Charge-Density-Wave and Normal Metallic Phases in 1T-TaS_2 Thin-Film Devices, ACS Nano **2019**, 13 (6), 7231-7240. DOI: 10.1021/acsnano.9b02870
54. D. A. Zocco, J. J. Hamlin, K. Grube, J.-H. Chu, H.-H. Kuo, I. R. Fisher, and M. B. Maple, Pressure dependence of the charge-density-wave and superconducting states in $GdTe_3$, $TbTe_3$, and $DyTe_3$, Phys. Rev. B **2015**, 91, 205114. http://dx.doi.org/10.1103/PhysRevB.91.205114
55. N. Ru, C. L. Condron, G. Y. Margulis, K. Y. Shin, J. Laverock, S. B. Dugdale, M. F. Toney, and I. R. Fisher, Effect of chemical pressure on the charge density wave transition in rare-earth tritellurides RTe_3, Phys. Rev. B **2008**, 77, 035114. http://dx.doi.org/10.1103/PhysRevB.77.035114

56. A. L. Efros and B. I. Shklovskii, Coulomb gap and low temperature conductivity of disordered systems, J. Phys. C: Solid State Phys. **1975**, 8 (4), L49. https://doi.org/10.1088/0022-3719/8/4/003
57. D. Joung and S. I. Khondaker, Efros-Shklovskii variable-range hopping in reduced graphene oxide sheets of varying carbon sp^2 fraction, Phys. Rev. B **2012**, 86, 235423. https://doi.org/10.1103/PhysRevB.86.235423
58. G. Duvjir, B. K. Choi, I. Jang, S. Ulstrup, S. Kang, T. T. Ly, S. Kim, Y. H. Choi, C. Jozwiak, A. Bostwick, E. Rotenberg, J.-G. Park, R. Sankar, K.-S. Kim, J. Kim, and Y. J. Chang, Emergence of a Metal–Insulator Transition and High-Temperature

Charge-Density Waves in VSe_2 at the Monolayer Limit, Nano Lett. **2018**, 18 (9), 5432-5438.
https://doi.org/10.1021/acs.nanolett.8b01764

59. K. Fujita, M.H. Hamidian, S.D. Edkins, C.K.Kim, Y. Kohsaka, M. Azuma, M. Takano, H. Takagi, H. Eisaki, and J. C. S. Davis et al., Direct phase-sensitive identification of a d-form factor density wave in underdoped cuprates, PNAS **2014**, 111(30), E3026-E3032.
https://doi.org/10.1073/pnas.1406297111
60. X. Zhu, Y. Cao, J. Zhang, E. W. Plummer, and J. Guo, Classification of charge density waves based on their nature, PNAS **2015**, 112 (8), 2367-2371.
https://doi.org/10.1073/pnas.1424791112
61. F. Alzina, H. Tao, J. Moser, Y. García, A. Bachtold, and C. M. Sotomayor-Torres, Probing the electron-phonon coupling in ozone-doped graphene by Raman spectroscopy, Phys. Rev. B **2010**, 82, 075422
https://doi.org/10.1103/PhysRevB.82.075422

Grand Conclusion and Future scope

6

6.1 Grand conclusion

In this comprehensive analysis, we embarked on a fascinating journey into the realm of boron-doped graphene, where we meticulously investigated the intricate interplay of doping density, configurations, and annealing temperature on these extraordinary materials' electronic structure and properties. Our research has illuminated various facets of BG, offering profound insights into its potential applications in future research and technology.

Foremost among our discoveries is the precise control we achieved over the synthesis of BG sheets. Through precise adjustment of annealing temperatures, we achieved distinct configurations, including the coveted BC_3 configuration achieved through graphitic substitution. Moreover, we successfully accessed other configurations like BCO_2 and BC_2O, predominantly located at the edges or out-of-plane lattice sites. This remarkable tunability of boron configurations opens up some possibilities for tailoring graphene's properties to deal with specific applications.

Spectroscopic techniques played a pivotal role in our characterization efforts, enabling us to discern the impact of boron doping on reduced graphene. Notably, we pinpointed the C=O and -O-C=O groups as highly favourable sites for out-of-plane boron attachments among the oxygen-functionalized groups (OFGs). Additionally, we unveiled a remarkable 'squeezing' of the bandgap in BG samples, particularly pronounced in cases of substitutional doping at higher temperatures. This intriguing phenomenon underscores the complex and intricate relationship between doping and graphene's electronic structure.

Our investigation also unveiled a striking contrast between undoped (TG) and doped (BG) samples, particularly concerning C sp^2 and π-conjugated domains. This contrast became particularly prominent in the context of substitutional doping, owing to the heightened prevalence of C-B bonds in BG samples prepared at higher temperatures. Further analyses, including estimations of in-plane crystallite sizes and d-spacing, corroborated the low defect concentration within these samples. Additionally, Raman spectroscopy provided compelling evidence supporting the p-type charge contribution of the doped samples, offering invaluable insights into their electronic properties.

Apart from charge carriers, our study shed light on the emergence of point defects as an additional effect, intricately linked to the increased incorporation of boron into the lattice. These findings lay the foundation for future research and the exploration of novel applications. We anticipate that aspects such as band structure, phonon dispersion, and defect profiles can be methodically tailored using p-type BG systems with point defects, offering a rich and fertile ground for further exploration and innovation.

In conclusion, our research has uncovered the existence of quantum-mechanical collective phenomena within out-of-plane boron-doped few-layer graphene. These phenomena are characterized by a periodic distribution of correlated charges within the lattice. We have elucidated the origins of this lattice reconstruction, primarily attributing it to enhanced electron-phonon coupling and interactions of interlayer states with π electron density. Our spectroscopic findings have provided compelling evidence to explain the CDW phase in BG systems, and theoretical simulations have bolstered our comprehension of these systems' electronic behaviour. This work not only advances our understanding of the fascinating world of BG but also sets the stage for exciting future research endeavours and innovative applications in a myriad of scientific and technological domains.

6.2 Future scope

The future scope in the realm of BG (BG) is both promising and far-reaching. Here, we elaborate on the potential directions and implications of this research:

1. **Electric Field Control of CDW Phase**: One of the most intriguing findings of our study is the dependency of the charge density wave (CDW) phase on applied electric fields. This discovery opens up a novel avenue for research where scientists can investigate the precise mechanisms and dynamics of how electric fields influence CDW transitions in BG. Understanding this phenomenon at a fundamental level could lead to the development of advanced materials with tunable CDW properties. Researchers may explore different types of electric field configurations, intensities, and durations to gain deeper insights into this intriguing behaviour.

2. **Nanoelectronics**: The ability to manipulate CDW phases in BG using electric fields holds great promise for nanoelectronics. Future research could focus on designing and engineering electronic devices that leverage this phenomenon. These devices could

potentially operate with lower power consumption, enhanced performance, and new functionalities. Such innovations could revolutionize the field of nanoelectronics and pave the way for energy-efficient and high-speed electronic components.

3. **Quantum Technologies**: BG's unique electronic properties, coupled with its sensitivity to CDW transitions, make it an attractive candidate for quantum technologies. Quantum computing, in particular, stands to benefit from this research. By exploiting the CDW phase as a quantum state variable, scientists might develop novel quantum gates and qubit architectures. These advancements could accelerate the development of practical quantum computers, which have the potential to solve complex problems currently beyond the reach of classical computers.

4. **Sensor and Detector Applications**: The sensitivity of BG to external stimuli, including electric fields, makes it a promising material for sensor and detector applications. Researchers could explore the development of highly responsive sensors capable of detecting minute changes in environmental conditions, such as temperature, humidity, or the presence of specific molecules. Additionally, BG-based detectors could find use in scientific instruments for precise measurements and data collection.

5. **Energy Conversion and Storage**: Harnessing the unique properties of BG could lead to innovations in energy conversion and storage technologies. For instance, the ability to manipulate CDW phases might enable more efficient energy harvesting from waste heat. BG-based materials could also play a role in next-generation batteries and supercapacitors, offering higher energy densities and faster charge/discharge rates.

6. **Materials Science Advancements**: Research into BG is likely to advance our understanding of 2D materials and their interactions with external factors. This knowledge could have implications beyond BG and benefit the broader field of materials science. Insights gained from studying BG's response to electric fields may be applicable to other 2D materials, expanding the toolkit of materials available for various applications.

In summary, the future of BG research is incredibly promising. The ability to control CDW phases with electric fields opens doors to a wide range of technological advancements, from nanoelectronics to quantum technologies and beyond. As scientists continue to explore and innovate in this field, we can anticipate exciting discoveries that will shape the next generation of cutting-edge technologies and contribute to our understanding of fundamental physics and materials science. The journey into the world of BG is poised to yield transformative advancements with profound implications for numerous industries and scientific disciplines.

Appendix A

1. Results

1.1. XRD analysis

XRD Spectra for all samples are shown at Figure A3. Observable broad x-ray diffraction peaks near $2\theta=25.9^{\circ}$ corresponding to the (002) plane of the TG and BG samples, ensure the desired degree of reduction from graphene oxide. Broader peaks around $2\theta=25.8°$, found in the BG lattices are assumed to be consequences of the turbostratic interaction [1,2] and sharp additional shoulders having $2\theta= 26.9°$ indicate the perfectly-ordered graphitic layers [2] obtained at higher annealing temperatures only (BG900 and BG1000 samples). For TG lattices, those peaks are blue shifted with respect to the BG lattices at $2\theta= 26.1°$, which can be considered as well-oriented few-layer graphene. Broadness of these peaks corresponding to the (002) plane is due to lack of crystallinity along that direction. In basal plane, crystallinity of those lattices were measured by fitting the peaks around $2\theta=43^{\circ}$ found in both doped and undoped graphene samples. Fitted peaks centered at around $2\theta=42.5^{\circ}$ and $2\theta=43.2^{\circ}$ are assigned to the (100) and (101) planes respectively, which lie in graphene plane [Figure A4(b)]. As per our interest, these values of the in-plane crystallite sizes have been correlated with the values of same obtained from intensity ratio of D and G peaks of Raman spectra of the corresponding samples, discussed later in Raman Analysis. Apart from the correlation, primary investigation reveals that the in-plane crystallite sizes of TG samples increase with annealing temperature and for BG samples it is decreasing with temperature.

For the BG samples, the XRD peaks assigned to (002) turbostratic plane shift towards higher diffraction angle in as shown in figure A3. This implies the decrement of interlayer distance, termed as d_{002} spacing, in doped samples at higher annealing temperature.

2. Tables

Table A1: Binding energies and Full Width Half Maxima of all components found in C1s Peaks of all samples

B.E. in eV (FWHM)	**C-B (eV)**	**C=C (eV)**	**C-C (eV)**	**C-O-C (eV)**	**C-OH (eV)**	**C=O (eV)**	**-COOH (eV)**	**π-π* (eV)**
Sample Name								
BG500	282.9 (1.1)	284.0 (1.1)	284.7 (1.1)	285.5 (1.5)	286.3 (1.4)	287.4 (1.5)	288.8 (1.7)	290.5 (1.7)
BG700	282.9 (1.1)	284.0 (1.1)	284.7 (1.1)	285.7 (1.5)	286.5 (1.4)	287.6 (1.5)	289.1 (1.7)	290.5 (1.8)
BG900	283.2 (1.1)	284.0 (1.1)	284.7 (1.1)	285.6 (1.4)	286.1 (1.3)	287.2 (1.4)	288.8 (1.8)	290.3 (1.9)
BG1000	283.0 (1.1)	284.0 (1.1)	284.7 (1.1)	285.6 (1.4)	286.3 (1.3)	287.3 (1.4)	288.8 (1.7)	290.4 (1.7)
TG500	--	284.1 (1.1)	284.8 (1.1)	285.6 (1.5)	286.3 (1.5)	287.3 (1.5)	289.0 (1.7)	290.4 (1.7)
TG700	--	284.0 (1.1)	284.7 (1.1)	285.4 (1.5)	286.1 (1.4)	287.2 (1.4)	288.7 (1.7)	290.4 (1.7)
TG900	--	284.0 (1.1)	284.8 (1.1)	285.6 (1.3)	286.3 (1.3)	287.3 (1.4)	288.9 (1.8)	290.3 (1.8)
TG1000	--	284.0 (1.1)	284.8 (1.1)	285.7 (1.3)	286.4 (1.3)	287.4 (1.4)	288.9 (1.7)	290.4 (1.8)

Table A2: Binding energies and Full Width Half Maxima of all components found in B1s Peaks of BG samples

B.E. in eV (FWHM)	**B-B (eV)**	**BC_3 (eV)**	**BC_2O (eV)**	**BCO_2 (eV)**	**B-O (eV)**
Sample Name					
BG500	-- (--)	188.8 (1.7)	190.2 (2.3)	192.1 (2.5)	194.1 (2.4)
BG700	186.8 (1.8)	188.7 (1.8)	190.1 (2.2)	191.8 (2.4)	193.9 (2.4)
BG900	186.9 (1.8)	188.5 (1.8)	189.7 (2.2)	192.1 (2.4)	-- (--)
BG1000	186.8 (1.9)	188.5 (1.9)	189.8 (2.1)	191.7 (2.4)	-- (--)

Table A3: Atomic percentages of carbon, boron, oxygen present in BG samples

Amounts (%)	**C**	**B**	**O**	**B/C (%)**
Samples				
BG500	82.3 ± 0.7	1.2 ± 0.3	16.5 ± 0.4	1.5 ± 0.4
BG700	85.1 ± 0.4	1.6 ± 0.2	13.3 ± 0.3	1.9 ± 0.2
BG900	80.8 ± 0.6	3.6 ± 0.3	15.6 ± 0.4	4.5 ± 0.3
BG1000	80.4 ± 0.7	4.3 ± 0.4	15.3 ± 0.3	5.3 ± 0.5

3. Figures

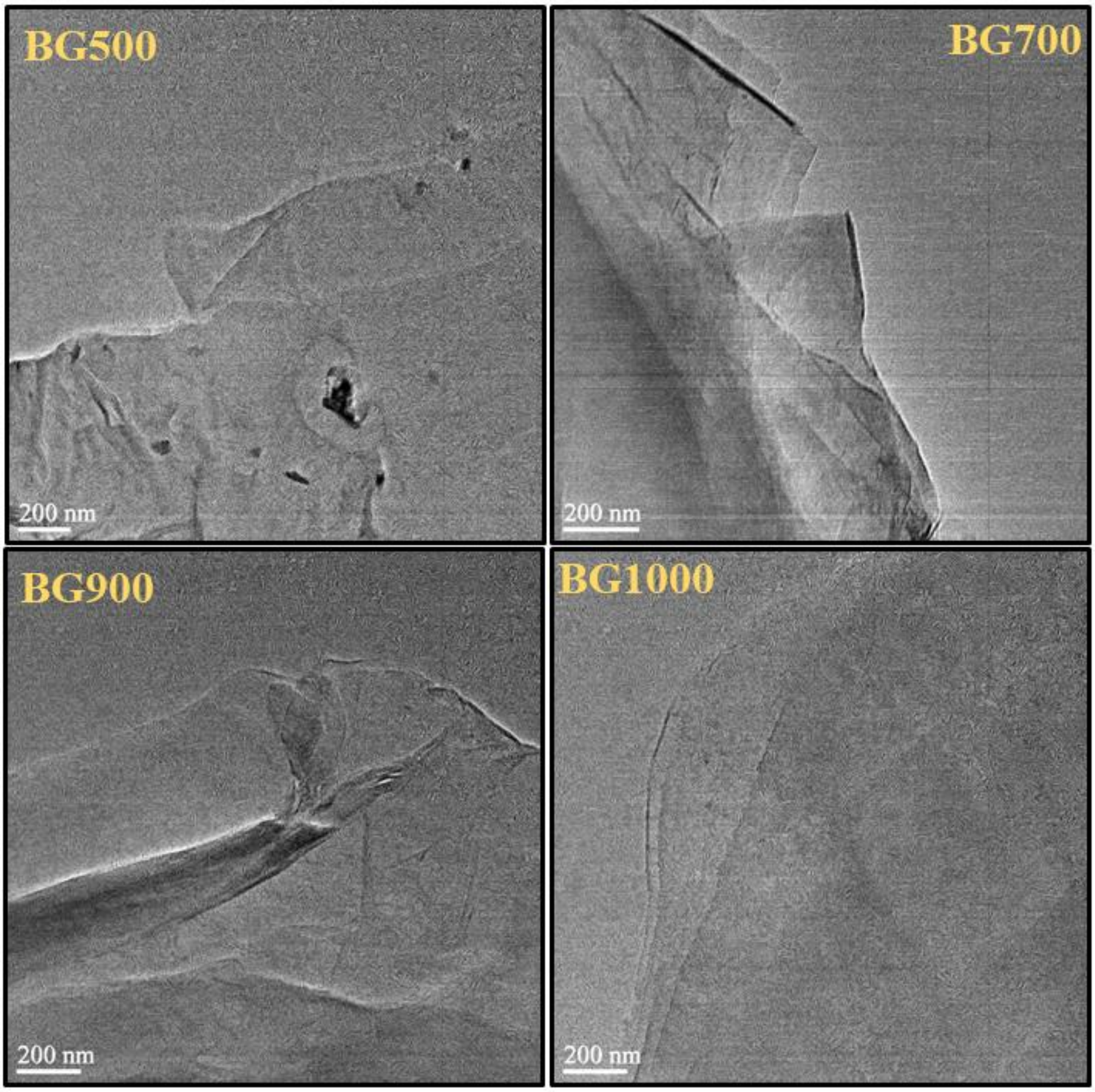

Figure A1. Transmission Electron Microscope image for all BG samples.

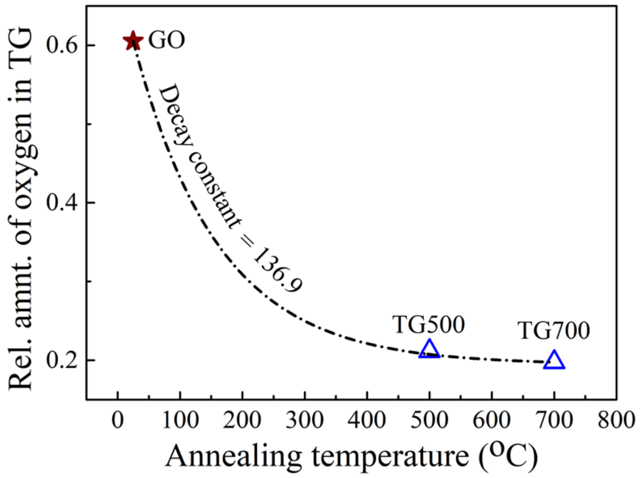

Figure A2. Relative amount of oxygen in TG samples. Oxygen containing groups are reduced exponentially (fitted with exponential function ; black dashed line) starting from graphene oxide.

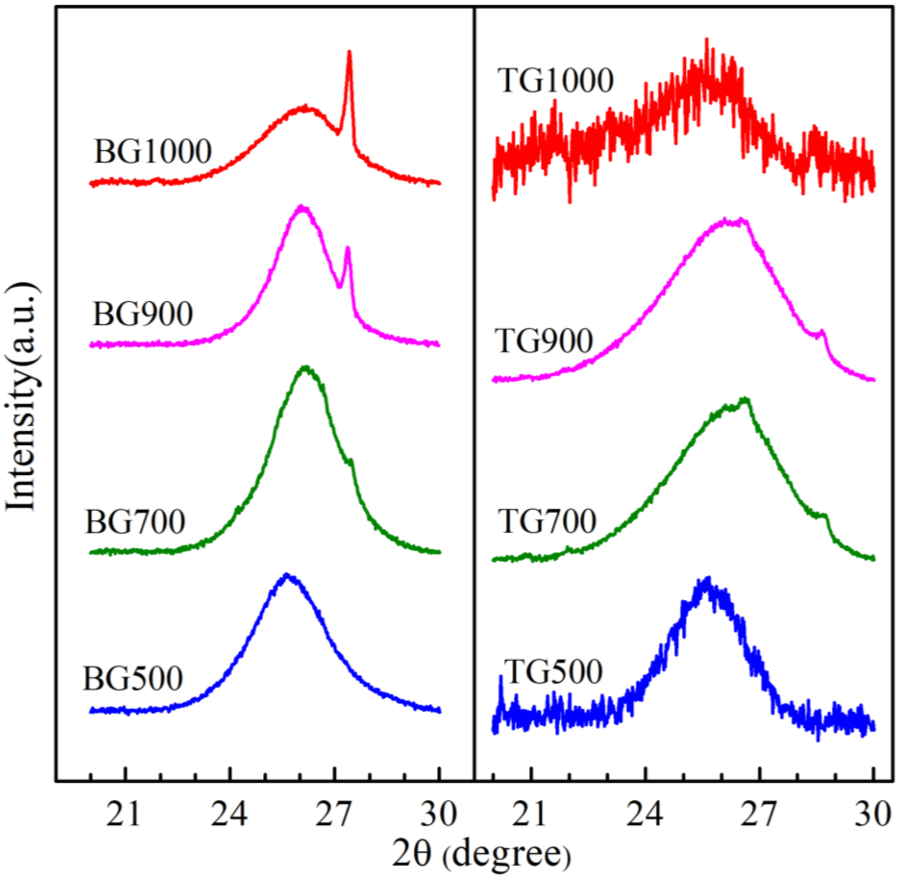

Figure A3. XRD spectra for BG and TG samples

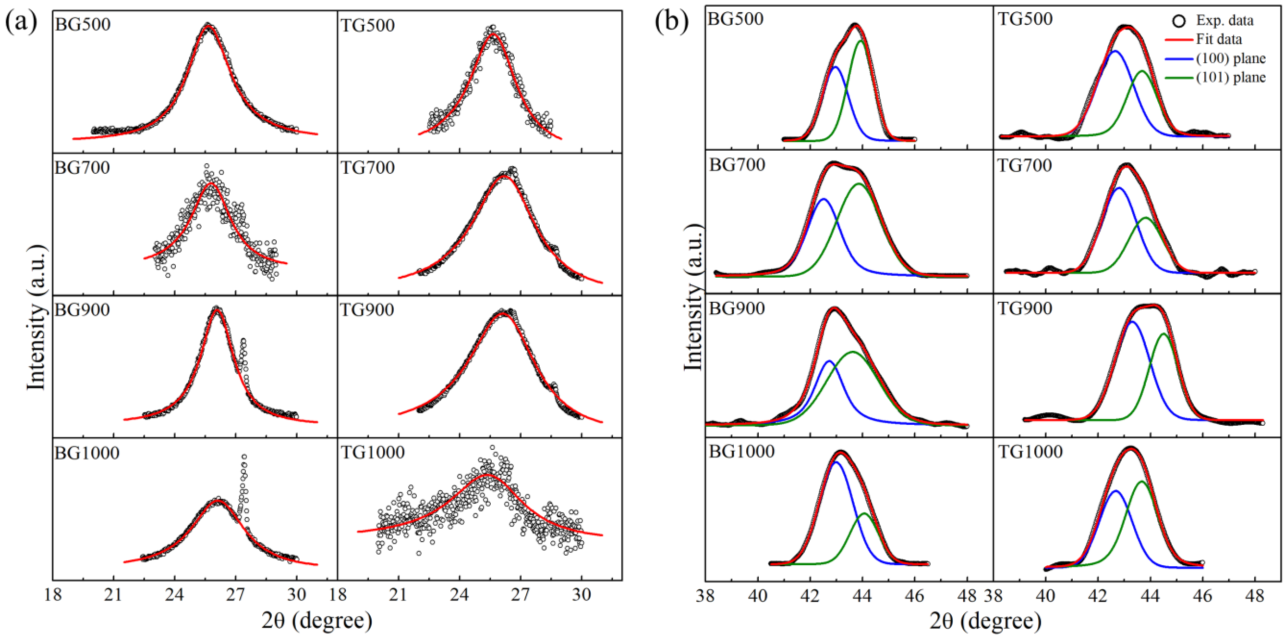

Figure A4. (a) Fitted XRD peaks, ascribed to the (002) plane of BG and TG samples. Peaks are fitted using Voigt function. (b) Deconvoluted XRD peaks corresponding to (100) and (101) planes of all samples. Deconvolutions are done with Voigt functions.

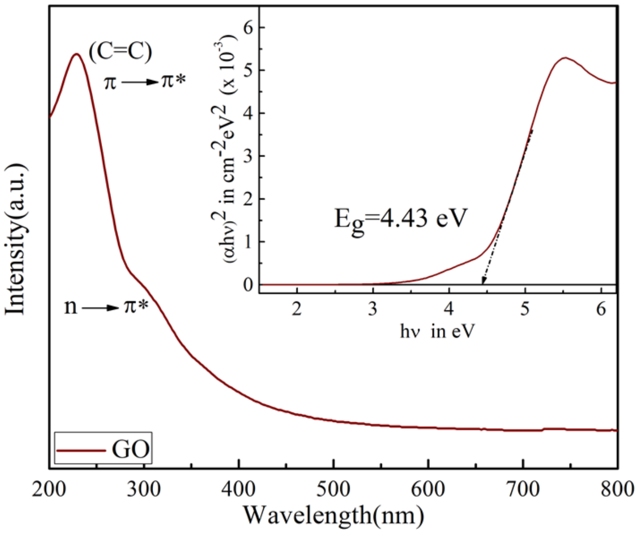

Figure A5. UV-VIS absorbance spectra for few layer graphene oxide and corresponding Tauc plots (inset).

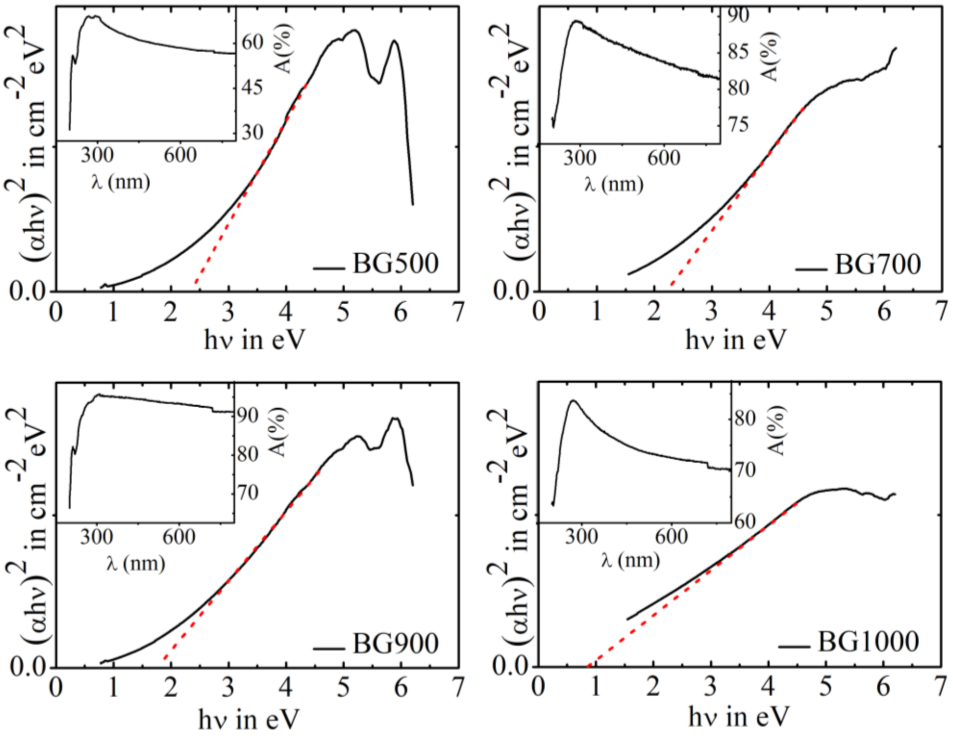

Figure A6. UV-VIS absorbance spectra for BG samples and corresponding Tauc plots (inset) λ (nm) and A(%) represent wavelength in nanometer and Absorbance in percentage.

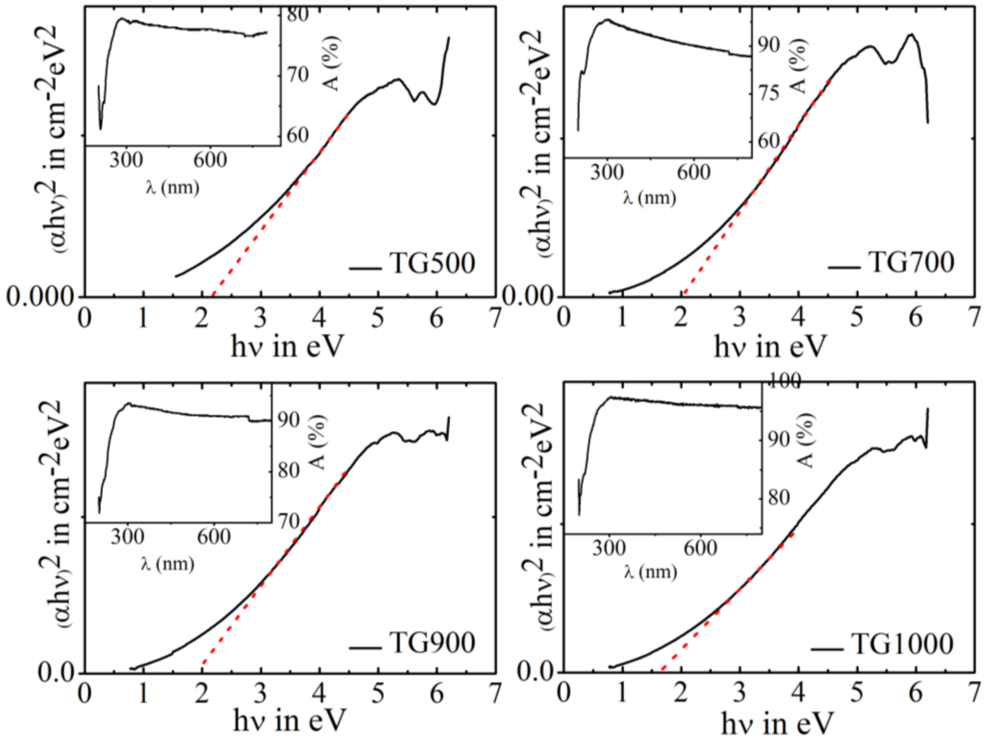

Figure A7. UV-VIS absorbance spectra for TG samples and corresponding Tauc plots (inset) ; λ (nm) and A(%) represent wavelength in nanometer and Absorbance in percentage.

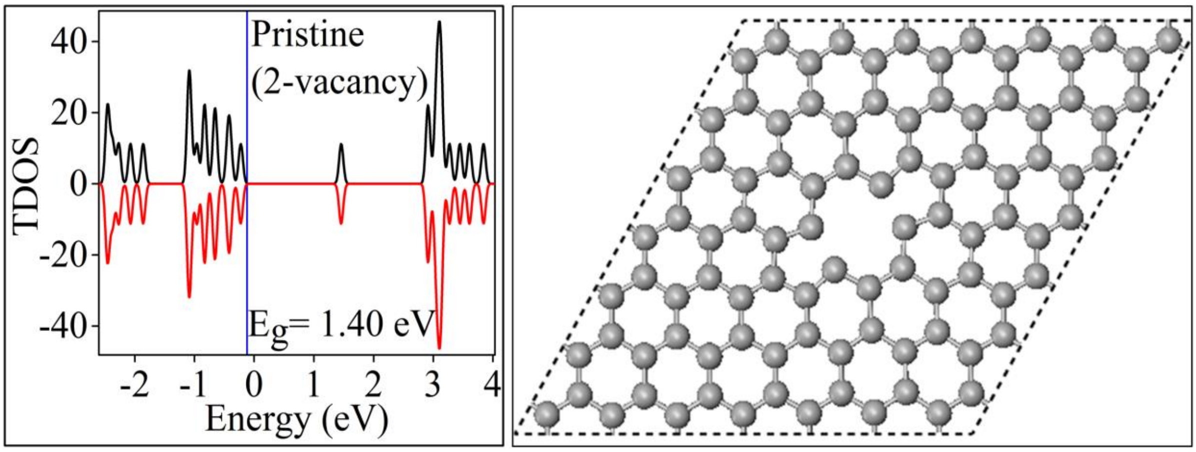

Figure A8. DOS study of single layer graphene optimized with double vacancy site. E_g is band gap here (Left). Structure taken of graphene without doping of boron atoms where each grey sphere represents the carbon atom (Right).

References

[1] W. D. Tennyson, M. Tian, A. B. Papandrew, C. M. Rouleau, A. A. Puretzky, B. T. Sneed, K. L. More, G. M. Veith, G. Duscher, T. A. Zawodzinski *et al.* Bottom up synthesis of boron-doped graphene for stable intermediate temperature fuel cell electrodes, Carbon **123**, 605 (2017).

[2] J. A. Garlow, L. K. Barrett, L. Wu, K. Kisslinger, Y. Zhu, and J. F. Pulecio, Large-Area Growth of Turbostratic Graphene on Ni(111) via Physical Vapor Deposition, Sci. Rep. **6**, 19804 (2016).

Appendix B

Theoretical methods:

In the current work, the first principles calculations were performed within the scope of density functional theory (DFT) using the Vienna ab-initio simulation package (VASP) [1-3]. All the calculations were carried out with the projector augmented wave (PAW) [4] method. The exchange-correlation terms were treated at the level of generalized gradient approximation (GGA) by means of the Perdew−Burke−Ernzerhof (PBE) [5] functional. The structural optimizations were allowed to continue until the difference in the energy of the system in two consecutive iteration steps reached below 10^{-5} eV/ atom. The calculations were performed at the Γ point with an energy cut-off value of 500 eV. The Brillouin zone integration was done for a k-point mesh of (4×4×1). A vacuum slab of length 20 Å was implemented in the direction perpendicular to the two-dimensional surfaces to ward-off spurious interaction between the periodic images. The DFT+D2 (Grimme's) method [6] was utilized to take into account the effect of the dispersive forces. In order to evaluate the band gap value with higher accuracy, the Heyd-Scuseria-Ernzerhof (HSE06) hybrid functional [7] was used during the density of states (DOS) calculations [Figure 1], whereas the band structures and their orbital decomposed versions were computed within GGA-PBE level calculation in order to save computational time [Figure B8].

Other interfering factors which could enhance EPC more efficiently in graphene is the density of states at Fermi level, introduced as N(E_F) in equation (1). After realizing the shift of E_F into the VB, from figure 1, edge of the VB is further realized by inspecting the valance band spectra (VBS) [Figure B4]. Figure 2(f) indicates the positions of the VBM from Fermi energy level are elevated since greater number of the O/P boronic groups are introduced in the lattice. Hence, BG500 and BG700 are more hole doped and have greater DOS at E_F compared to the BG900 and BG1000 samples. The outcomes of the VBS analysis are also comprehended through the electronic band structure for the corresponding out-of-plane boron configurations. (a) demonstrate the band dispersion of graphene containing different boron groups. For BC_3 and BCO_2 configurations, lowering of the associated Fermi levels from VBM are clearly seen, which signify the hole doping nature. For BC_2O configuration, the Fermi level separates the VB and CB by opening a gap near itself. Another intriguing fact is that for BCO_2, the VB and CB resemble the shape of free electron configuration or p_z electron as seen in pure graphene. In decomposed band structures of graphene with BCO_2 configuration, a large contribution from carbon p_z orbital for construction of the VB is detected (figure B8 (b)). Figure B8 (c) represents the orbital decomposed band structure for the boron atoms in the formation of bands. For BC_3 groups, charge transfer from carbon to boron populates the p_z orbitals and it becomes responsible for the formation of the bands near Fermi level. For BC_2O groups, outermost p_y electrons are involved to make up the VB, but for BCO_2 neither of these p-electrons are engaged in the band formation.

Theoretically, amounts of strain produced in BG samples due to boron inclusion were evaluated by measuring the B-C bond length. Length of different bonds for three standard boron configurations are given in table B3. Theoretical strain for a particular boron groups are compared with the strain in experimental BG systems associated with the most populated boron groups in the system.

Experimental methods:

1. **XPS analysis:** X-ray photoelectron spectra (XPS) for B1s peaks of BG samples were obtained by X-ray Photoelectron Spectrometer (SPECS, HSA 3500). Samples were kept under a monochromatic Al-K_α X-ray source of 1486.61 eV at ultra-high vacuum (10^{-9} mbar) chamber. Highly resolved B1s spectra were deconvoluted with Lorentzian asymmetric line shape with tail damping, $LF(\alpha, \beta, w, m)$, which is equivalent to asymptotic theoretical Doniach-Sunjic

asymmetric line shape. Backgrounds were subtracted with Shirley algorithm. Contributions from each type of boron-carbon bonds were properly quantified using appropriate Relative Sensitivity factor (R.S.F.) value for boron as 0.482 to get accurate. High resolution scan for B1s were achieved by lowering the pass energy and regulating the step size, dwell time to count electrons that were coming to the hemispherical analyzer during measurement.

Binding energies and Full Width Half Maxima of all components found in B1s Peaks for all BG samples are provided in table B1. Amounts of different doping configurations of boron atoms are given in table B2. Deconvolution of B1s spectra for BG700 sample is shown in figure S1.

2. **VBS analysis:** Valance band spectra (VBS) for all samples, as described in figure B4, were studied using the same XPS instrument configured by SPECS. To maintain the Fermi level (E_F) at zero binding energy, work functions (W_f) of samples were set using a standard graphite sample and calibrate the W_f value to 4.4 eV. Further energy correction was required due to screening effect of accumulation of the surface electrons. So, the final values were adjusted considering the peak for C *sp*^{2} at 284.6 eV. Valance band maxima (VBM) were visualized at the edge to the filled-up valance states from where electrons were released.
3. **XRD analysis:** Powder X-ray diffraction (XRD) patterns of the BG samples were collected by Bruker D8 diffractometer with Cu-K_α radiation at room temperature. An X-ray of wavelength, λ =1.5404 Å (Cu-Kα) was used for X-ray diffraction. Interlayer distance along (002) plane, d_{002}, for BG samples were calculated using the Bragg's equation: $2d_{002}\sin\theta = n\lambda$, where $n = 1$ for first order diffraction pattern and λ is the wavelength of the applied X-ray. Voigt functions were used to fit for the assessment of in-plane and crystallite size (L_a) as shown in figure B3. Employing deconvoluted parameters such as values of 2θ, Full width half maxima

(β) values were used to evaluate this crystallite size by applying Debye-Scherrer equation as, $L = \frac{K\lambda}{\beta \cos\theta}$, where, K is Debye-Scherrer constant with the value of 1.84 for the in-plane crystallite of samples.

4. **Raman spectra analysis:** Raman Spectra of all samples were characterized by Raman Spectrometer (WITEC, alpha 300 R) with an argon laser of wavelength, $\lambda = 532$ nm and a 100X objective with 600 grooves/mm. All first and second order peaks for different vibrational modes present in the samples were deconvoluted using nine Lorentzian functions. Total integrated area of first order D and G peaks were considered to calculate the $\frac{I_D}{I_G}$ ratio. To get $\frac{I_{2D}}{I_{2D'}}$ ratio for equation (S-5), integrated area of 2D and 2D' peaks were measured.

Crystallite size (L_a) and defect length (L_D) of the samples, mentioned in Figure 2(e), were calculated using the equations [8,9],

$$L_a(nm) = \frac{(2.4\times10^{-10})\lambda^4}{I_D/I_G} \qquad \text{(S-1)}$$

$$L_D^2(nm^2) = \frac{[(1.8\pm0.5)\times10^{-9}]\lambda^4}{I_D/I_G} \qquad \text{(S-2)}$$

In figure 2(d) and 2 (f), measurements of the values strain and doping are performed through Raman analyses using ref. 10; figure 9. Individual contributions of strain and doping in shifting of the G and 2D bands for each sample were estimated by deriving the component of the "shift" along tensile strain and hole doping axes respectively. Lee et al. conjectured about the contributions of the strain and doping in band shifts, as mapped with two axes, could be realized through vector method [11].

5. **Electrical properties measurement:** 0.8 mm thick circular pellets of the BG samples having 2.8 mm of radius were prepared to measure the temperature dependent resistance by applying current (I) through the standard four terminal electrode system in Cryogenics (UK) Physical Property Measurement System from 200K to 4.2K. Other geometrical specifications, those are measured in a travelling microscope having least count of 0.01mm, are supplied in figure B6. To find a suitable mechanism for temperature-dependent transport in our samples, resistance vs. temperature (R-T) data are fit, as depicted in figure B7, following Arrhenius model [12], Variable range hopping (VRH) conduction model proposed by Mott [13-15], VRH model proposed by Efros-Shklovskii (ES-VRH) [16]. Carrier transport processes in BG samples are found to be best competent with ES-VRH model of conduction. Finally, R-T data for all samples are fitted [Figure 4(b); inset] using the following equation,

$$R(T) = R(0)\ \exp\left[\left(\frac{T_{ES}}{T}\right)^{1/2}\right] \tag{S-3}$$

, where R(T) is the resistance of the samples at T K, R(0) is a pre-exponential factor and T_{ES} is the characteristics temperature. Localization length (ξ), as described in figure 4(b), is another inferential phenomenon linked with VRH mechanism of charge conduction, and this can be derived from T_{ES} as [17],

$$\xi = \frac{\beta_1 e^2}{k_\beta T_{ES} \epsilon'} \tag{S-4}$$

, where $\beta_1 = 6.2$ for 3D ES-VRH and $\beta_1 = 2.8$ for 2D ES-VRH, k_β is Boltzmann constant and ϵ' is the permittivity of of the boron doped graphene system.

6. **EPC parameter calculations:** To gauge the strength of electron-phonon coupling (EPC), we put more focus on the deformation potential, which is strictly related to the EPC strength, as given in equation (1) in the main text. Now, the square of the average of the deformation potentials, precisely related to the vibration of phonons near higher symmetry points, are directly proportional to the integrated peak intensity of $2D$ and $2D'$ peaks as they are generated after scattering with phonons near K and Γ points. Rise of $2D$ and $2D'$ peaks consists of fully-resonant four-step process, where photoexcited electron-hole $(e-h)$ pairs undergo intra-valley and inter-valley scattering with phonons. Now, the rate of overall inelastic scattering (γ) of $e-h$ pairs includes the electron-electron/hole-hole $(e-e)$ or $(h-h)$ scattering rate (γ_{e-e}) or (γ_{h-h}) and the electron-phonon $(e-ph)$ scattering rate (γ_{e-ph}), among which γ_{e-e} or γ_{h-h} depends linearly with Fermi energy level. The $e-ph$ scattering contribution comes from the phonons at K and Γ points, assigned as γ_{K} and γ_{Γ} respectively. Hence the integrated intensities of $2D$ and $2D'$ can be expressed in terms of scattering rate as: $I(2D) = 2C(\gamma_{\mathrm{K}}/\gamma)^2$ and $I(2D') = C(\gamma_{\Gamma}/\gamma)^2$, where C is the constant. Again, the scattering rate due to the K and Γ phonons are directly proportional to the corresponding dimensionless EPC parameters termed as λ_{K} and λ_{Γ}. Therefore, the ratio of EPC parameters assigned with K and Γ phonons, λ_K/λ_Γ, can be calculated in terms of ratio of integral intensities of second order Raman peaks near K and Γ points i.e., $I(2D)/I(2D')$ [18]. Taking all these relations into account, λ_K/λ_Γ can be formulated as,

$$\frac{\lambda_K}{\lambda_\Gamma} = \frac{1}{\sqrt{2}}\sqrt{\frac{I(2D)}{I(2D')}\frac{E_L-2\omega_\Gamma}{E_L-2\omega_K}} \qquad \text{(S-5)}$$

, where E_L is the energy of incident photon, ω_{K} and ω_{Γ} are the frequency of scattered photon at K and Γ point respectively. Ratio of the average of the square of deformation potential, averaged on the Fermi surface, associated with the K and Γ points can also be calculated as,

$$\frac{\langle D_K^2\rangle_F}{\langle D_\Gamma^2\rangle_F} = \sqrt{2}\sqrt{\frac{I(2D)}{I(2D')}\frac{\omega_K(E_L-2\omega_\Gamma)}{\omega_\Gamma(E_L-2\omega_K)}} \qquad \text{(S-6)}$$

Where, $\langle D_K^2\rangle_F$ and $\langle D_\Gamma^2\rangle_F$ are the deformation potentials allied with K and Γ phonons [19]. However, some authors recognized these as the EPC matrix elements for the respective higher symmetry points [18]. Here, considering the very straightforward dependency of deformation potential to EPC strength as shown in eq. (1) in the main article, we simply call it as EPC parameters. Above calculations reveals that the EPC near K point is higher compared to Γ point for all the BG samples, described in figure 4(a).

TABLES:

Table B1: Binding energies and Full Width Half Maxima of all components found in B1s Peaks

B.E. in eV (FWHM)	B-B (eV)	BC_3 (eV)	BC_2O (eV)	BCO_2 (eV)	B-O (eV)
Sample Name					
BG500	-- (--)	188.8 (1.7)	190.2 (2.3)	192.1 (2.5)	194.1 (2.4)
BG700	186.8 (1.8)	188.7 (1.8)	190.1 (2.2)	191.8 (2.4)	193.9 (2.4)

BG900	186.9 (1.8)	188.5 (1.8)	189.7 (2.2)	192.1 (2.4)	-- (--)
BG1000	186.8 (1.9)	188.5 (1.9)	189.8 (2.1)	191.7 (2.4)	-- (--)

Table B2: Amounts of different doping configurations of boron atoms

Doping configuration Sample Name	BC_3 (%)	BC_2O (%)	BCO_2 (%)	Total Out-of-plane boron (%)
BG500	22 ± 3	63 ± 3	4 ± 1	89 ± 7
BG700	43 ± 4	32 ± 4	4 ± 1	79 ± 9
BG900	30 ± 4	9 ± 1	0	39 ± 5
BG1000	23 ± 5	5 ± 2	0	27 ± 7

Table B3: Calculation of strain for differently configured BG samples.

Doping configuration	Bond type	Bond length in Å	Pristine C-C in Å	Strain (ε) in %	Max. Tensile Strain in %
BC_3	B-C1(B)	1.52	1.424	6.74157	10.95506
	B-C2(B)	1.58	1.424	10.95506	
	C1(B)-C	1.381	1.424	-3.01966	
	C1(B)-C	1.4	1.424	-1.68539	
	C2(B)-C	1.423	1.424	-0.07022	
	C2(B)-C	1.49	1.424	4.63483	
BC_2O	B-C1(B)	1.525	1.424	7.0927	13.76404
	B-C2(B)	1.567	1.424	10.04213	
	C1(B)-C	1.62	1.424	13.76404	
	C1(B)-C	1.48	1.424	3.93258	

	C2(B)-C	1.462	1.424	2.66854	
	C2(B)-C	1.528	1.424	7.30337	
BCO_2	B-C(B)	1.639	1.424	15.09831	15.09831
	C(B)-C	1.491	1.424	4.70506	
	C(B)-C	1.583	1.424	11.16573	

FIGURES:

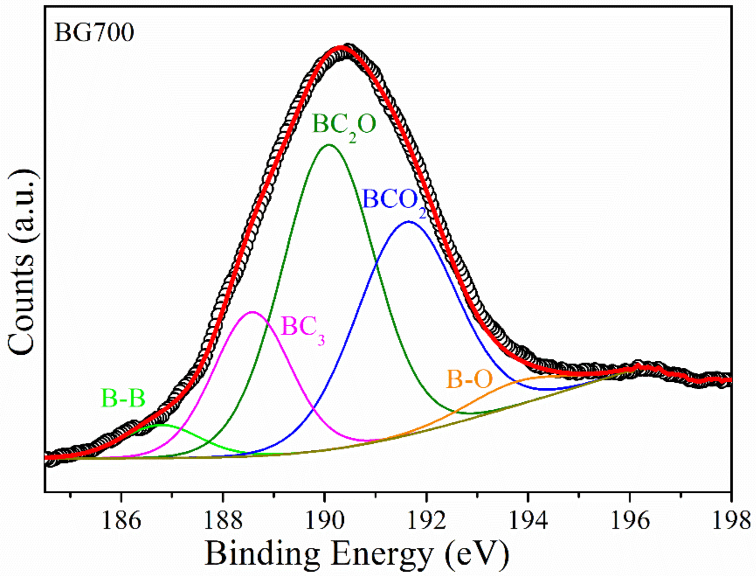

Figure B1. Deconvolution of B1s spectra of BG700 sample into different configurations.

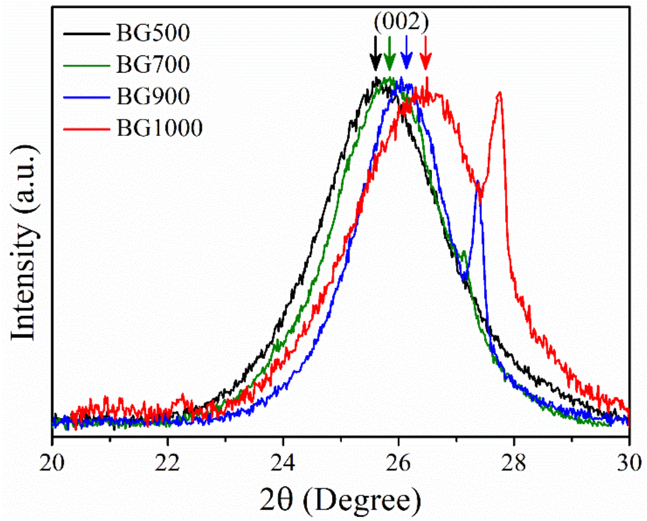

Figure B2. XRD peaks for (002) plane of all BG samples

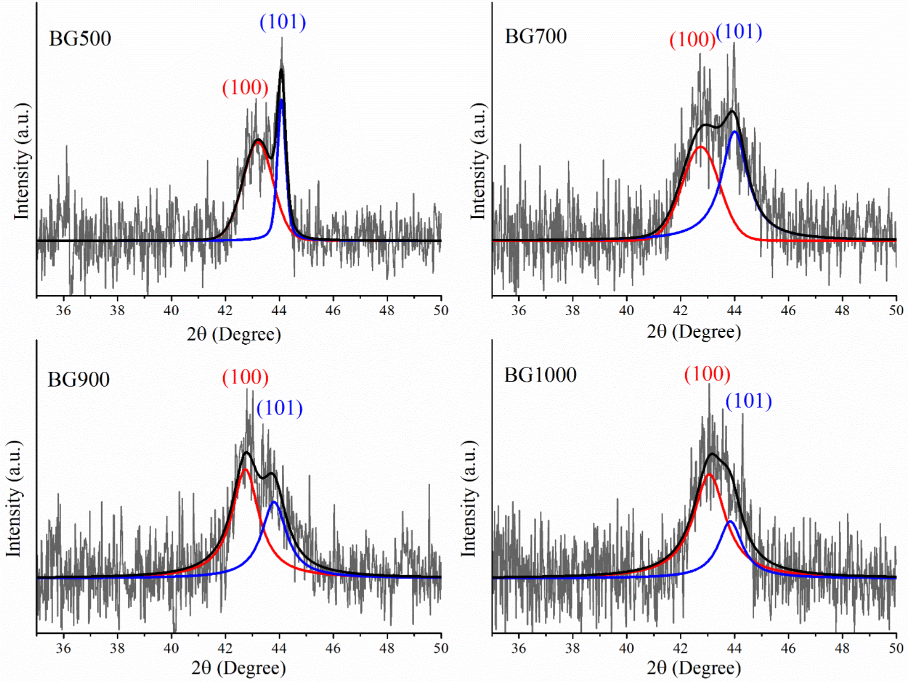

Figure B3. XRD peaks for (100) and (101) planes of all BG samples

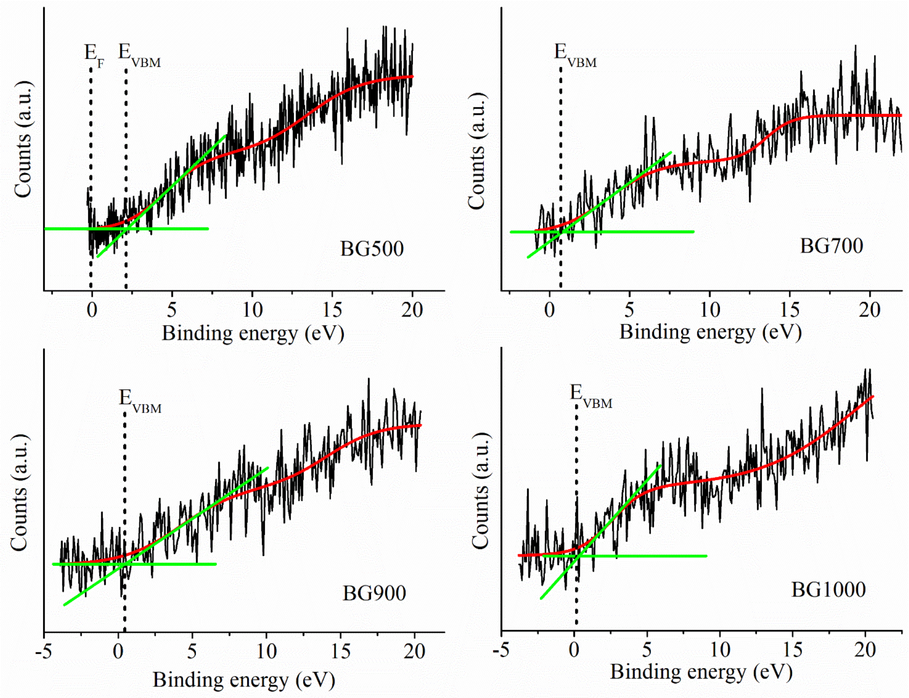

Figure B4. Valance band spectra for all BG samples.

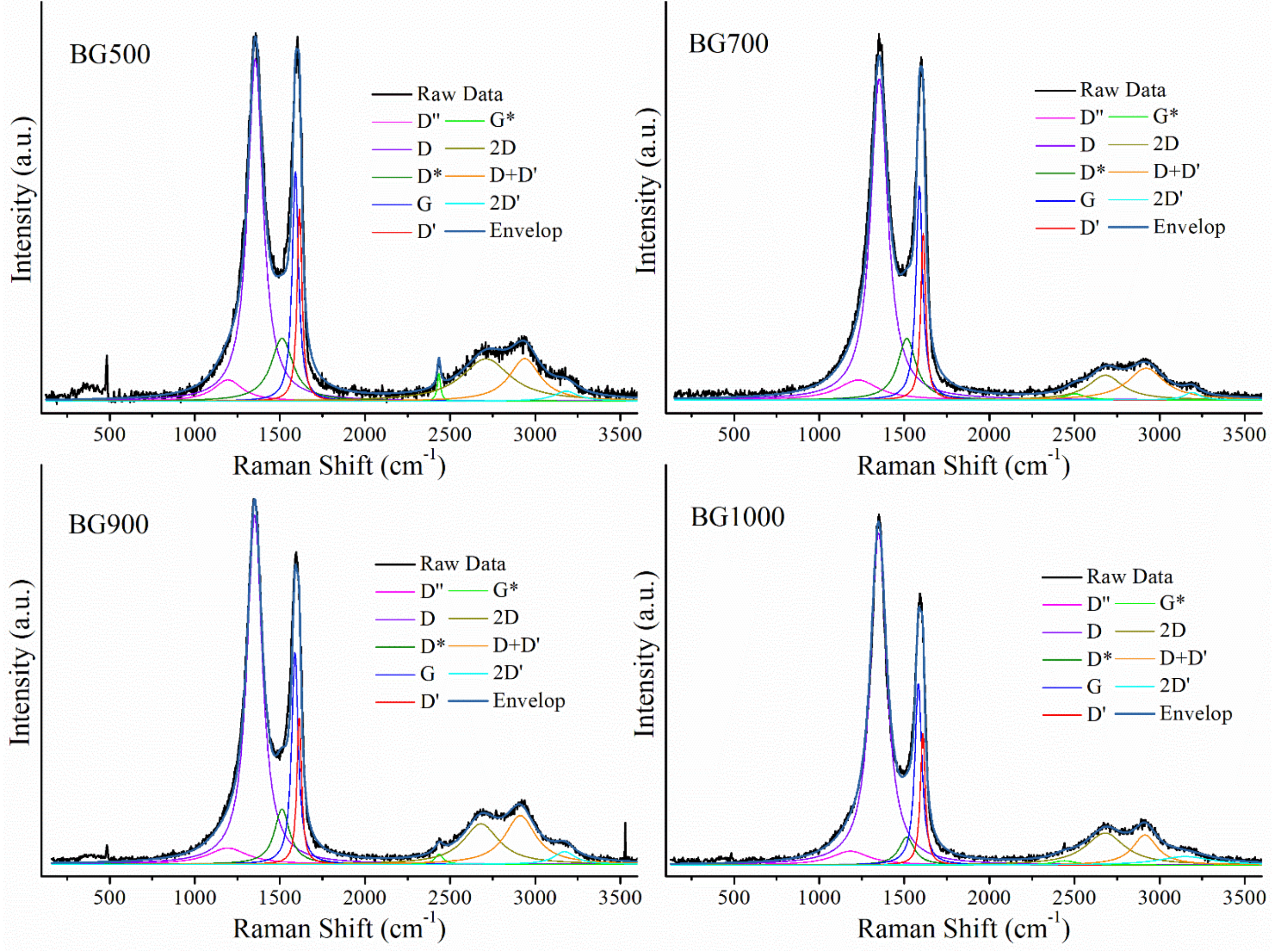

Figure B5. Deconvoluted Raman spectra for all BG samples.

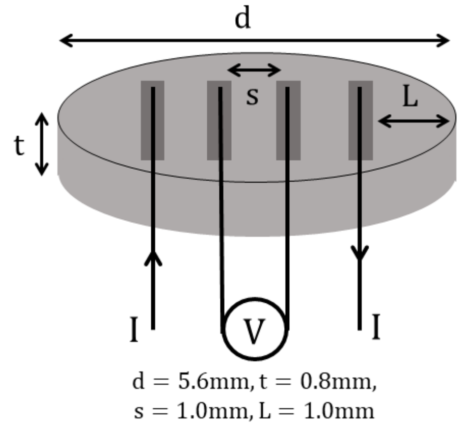

Figure B6. Schematic for low temperature resistance measurement.

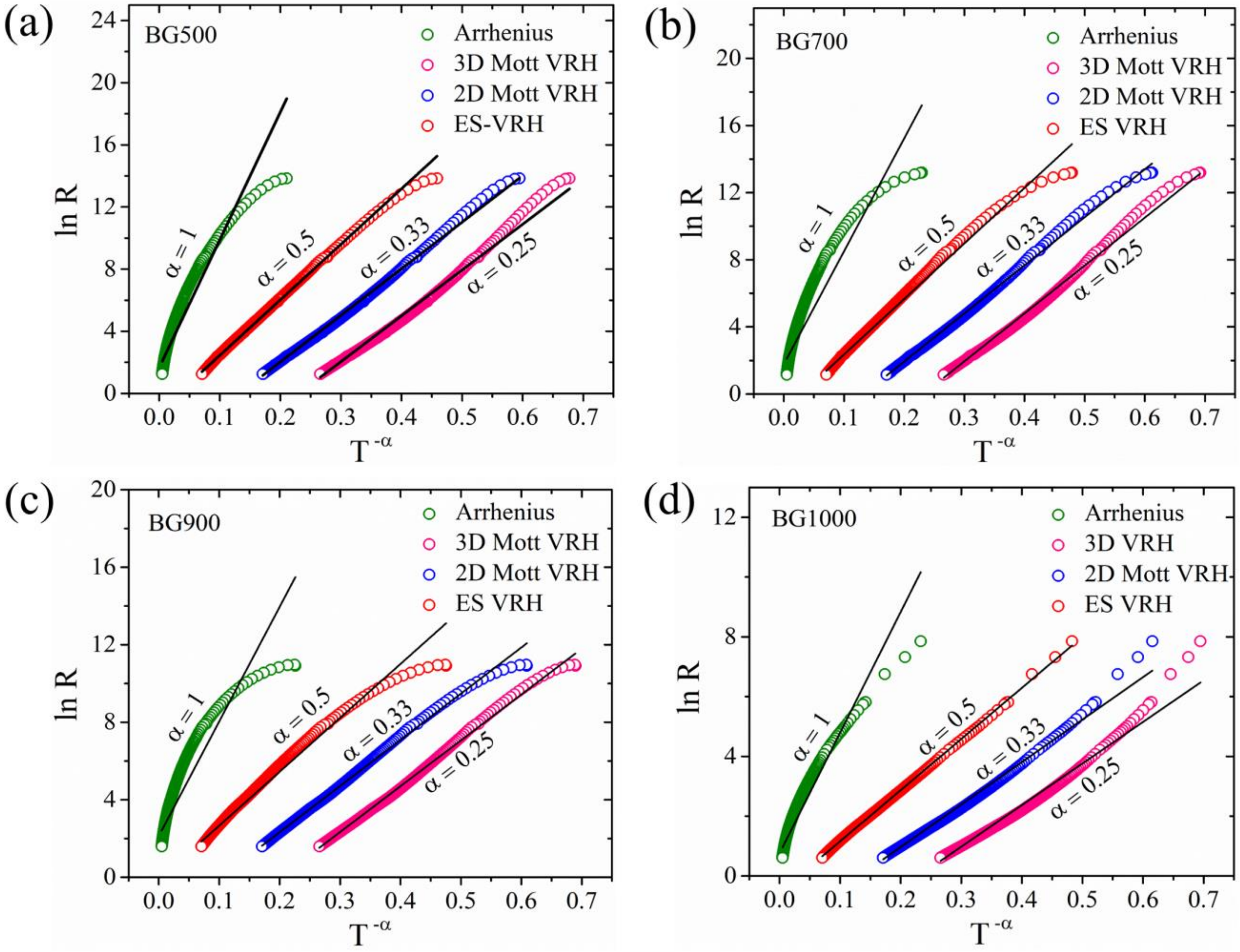

Figure B7. Fit for possible mechanisms of carrier transport in BG samples as obtained from electrical R-T measurements.

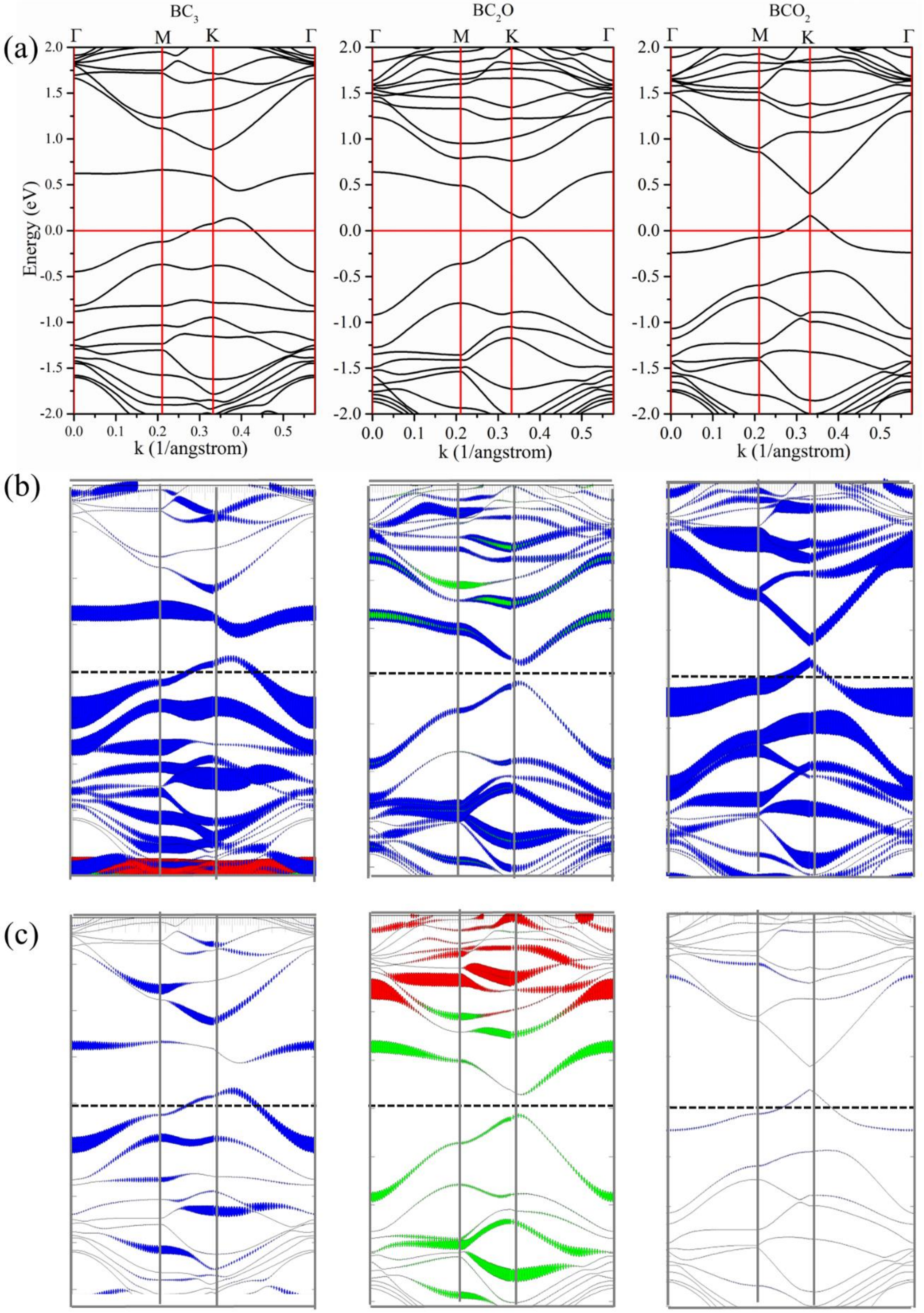
BC$_3$
BC$_2$O
BCO$_2$
(a)
(b)
(c)
Γ
M
K
Γ
Energy (eV)
2.0
1.5
1.0
0.5
0.0
-0.5
-1.0
-1.5
-2.0
0.0
0.1
0.2
0.3
0.4
0.5
k (1/angstrom)

Figure B8. Electronic band dispersion: (a) Band structure of graphene consists with BC_3 (left), BC_2O (middle) and BCO_2 (right) configurations. (b) Decomposed band structure for Carbon atoms showing individual contributions of p_x(red), p_y(green), p_z(blue) orbitals for formation of bands. Thickness of the band lines indicates weightage of the contributions. (c) Decomposed band structure for boron atoms showing individual contributions of p_x(red), p_y(green), p_z(blue) orbitals for formation of bands. Thickness of the band lines indicates weightage of the contributions.

REFERENCES:

[1] G. Kresse and J. Hafner, Ab Initio Molecular Dynamics for Liquid Metals, Phys. Rev. B **1993**, 47, 558−561.

[2] G. Kresse and J. Hafner, Ab Initio Molecular-Dynamics Simulation of the Liquid-Metal-Amorphous-Semiconductor Transition in Germanium, Phys. Rev. B **1994**, 49, 14251−14269.

[3] G. Kresse, J. Furthmüller, Efficiency of ab-initio total energy calculations for metals and semiconductors using a plane-wave basis set, Computational Materials Science **1996**, 6 (1), 15-50.

[4] P.E. Blochl, Projector augmented-wave method, Phys. Rev. B **1994**, 50, 17953.

[5] J.P. Perdew, K. Burke, M. Ernzerhof, Generalized gradient approximation made simple, Phys. Rev. Lett. **1996**, 77, 3865.

[6] S. Grimme, Semiempirical GGA-type density functional constructed with a long-range dispersion correction, J. Comput. Chem. **2006**, 27, 1787.

[7] A.V. Krukau, O.A. Vydrov, A.F. Izmaylov, G.E. Scuseria, Influence of the exchange screening parameter on the performance of screened hybrid functionals, J. Chem. Phys. **2006**, 125, 224106.

[8] L. G. Cançado, K. Takai, T. Enoki, M. Endo, Y. A. Kim, H. Mizusaki, A. Jorio, L. N. Coelho, R. Magalhães-Paniago, and M. A. Pimenta, General equation for the determination of the crystallite size La of nanographite by Raman spectroscopy, Appl. Phys. Lett. **2006**, 88, 163106.

[9] L. G. Cançado, A. Jorio, E. H. M. Ferreira, F. Stavale, C. A. Achete, R. B. Capaz, M. V. O. Moutinho, A. Lombardo, T. S. Kulmala, and A. C. Ferrari, Quantifying Defects in Graphene via Raman Spectroscopy at Different Excitation Energies, Nano Lett. **2011**, 11, 3190.

[10] S. Sarkar, R. Roy, B. K. Das, K. K. Chattopadhyay, Temperature-dependent site selection of boron doping in chemically derived graphene, Carbon **2021**, 184, 253-265.

[11] J. E. Lee, G. Ahn, J. Shim, Y. S. Lee, and S. Ryu, Optical separation of mechanical strain from charge doping in graphene, Nat. Commun. **2012**, 3, 1024.

[12] L. Ci, L. Song, C. Jin, D. Jariwala, D. Wu, Y. Li, A. Srivastava, Z. F. Wang, K. Storr, L. Balicas, F. Liu & P. M. Ajayan, Atomic layers of hybridized boron nitride and graphene domains, Nature Mater. **2010**, 9, 430–435.

[13] N. F. Mott and E. A. Davis, Electronic Processes in Non-Crystalline Materials, **1979** (Oxford: Clarendon Press).

[14] N. F. Mott, Conduction in non-crystalline materials, The Philosophical Magazine: A Journal of Theoretical Experimental and Applied Physics **1969**, 19(160), 835-852.

[15] N. F. Mott, Electrons in glass, Rev. Mod. Phys. **1978**, 50, 203.

[16] A. L. Efros and B. I. Shklovskii, Coulomb gap and low temperature conductivity of disordered systems, J. Phys. C: Solid State Phys. **1975**, 8 (4), L49.

[17] D. Joung and S. I. Khondaker, Efros-Shklovskii variable-range hopping in reduced graphene oxide sheets of varying carbon sp^2 fraction, Phys. Rev. B **2012**, 86, 235423.

[18] F. Alzina, H. Tao, J. Moser, Y. García, A. Bachtold, and C. M. Sotomayor-Torres, Probing the electron-phonon coupling in ozone-doped graphene by Raman spectroscopy, Phys. Rev. B **2010**, 82, 075422.

[19] C. Attaccalite, L. Wirtz, M. Lazzeri, F. Mauri, and A. Rubio, Doped Graphene as Tunable Electron−Phonon Coupling Material, Nano Lett. **2010**, 10 (4), 1172-1176.

“You can never cross the ocean unless you have courage to lose sight of the shore”

Christopher Columbus